EUROPEAN COMMISSION

Community research

PEBS

(Contract Number: FP7 249681)

PROYECT DERIVERABLE 3.5-3:

Report on long-term THC(m) predictions of a HLW repository in granite

Author(s):

Javier Samper, Acacia Naves, Luis Montenegro, Alba Mon, Bruno Pisani.

University of Coruña
Spain

Reporting period: 01/03/10 – 28/02/14

Date of issue of this report: 03/2013

Start date of project: 01/03/10 Duration: 48 Months

Project co-funded by the European Commission under the Seventh Euratom Framework Programme for Nuclear Research &Training Activities (2007-2011)		
Dissemination Level		
	Public	PU
	Restricted to a group specified by the partners of the [acronym] project	
	Confidential, only for partners of the [acronym] project	

EURATOM

DISTRIBUTION LIST

Name	Number of copies	Comments

Report on long-term THC(m) predictions of a HLW repository in granite

Summary

The canister corrosion, the interactions of corrosion products with bentonite and the pH buffering mechanisms have been simulated during 10^6 years at a constant temperature of 25ºC for a spent-fuel carbon-steel canister repository in granite.

Canister corrosion causes an increase in the concentration of dissolved Fe^{2+} and pH, and a decrease in Eh. Conservative species such as Cl^- present a pattern of decreasing concentration with time in the bentonite because they diffuse from the bentonite into the granite. Dissolved cations, Ca^{2+}, Mg^{2+}, Na^+ and K^+ and show trends similar to those of conservative species but they are also subjected to mineral dissolution/precipitation and cation exchange processes. Most of the released Fe^{2+} diffuses from the canister into the bentonite where it precipitates or sorbs. The largest pH in the bentonite is almost 9.5 at $2 \cdot 10^5$ years. The concentration of dissolved Fe^{2+}, the pH and the Eh are determined by the generation of corrosion products, the precipitation of magnetite and Fe sorption on weak sites. Magnetite is the main corrosion product in the bentonite. Its precipitation progresses as Fe^{2+} diffuses into the bentonite. Siderite precipitation is much smaller than magnetite precipitation due to the limited availability of dissolved bicarbonate. The thickness of the bentonite zone where siderite precipitates is similar to that of the magnetite. Calcite dissolves in most of the bentonite except near the canister where it precipitates due to the increase in pH induced by canister corrosion. Dissolution/precipitation of quartz and gypsum are not significant. The computed concentrations of exchanged cations in the bentonite vary with time due to changes in cation porewater concentration. The concentration of exchanged Ca^{2+} increases after 1 Ma while those of Na^+ and Mg^+ decrease. Only a small part of the Fe released by canister corrosion is sorbed at exchanged sites. The evolution of the concentration of exchanged Fe^{2+} is related to that of sorbed and dissolved Fe^{2+}. Model results show that sorption play a very relevant role in the geochemical evolution of bentonite. Fe^{2+} and H^+ compete for the weak 1 sorption sites near the canister. Such competition leads to the several sorption fronts and is relevant only at distances smaller than 8 cm from the canister. There is no competition between Fe^2 and H^+ for weak 2 sorption sites because the model does not consider for sorption of Fe on weak 2 sites. The time evolution of the $H_2(g)$ pressures generated has been

calculated from computed the computed activities. The partial pressure of $H_2(g)$ increases while the canister is being corroded until 16200 atm and decreases once the canister has been fully corroded. The effects of mineral dissolution and precipitation in porosity have been evaluated. The precipitation of the corrosion products close to the canister leads to a very large decrease of bentonite porosity in a zone of ≈ 6 cm of thickness. A negligible increase of the porosity is observed in the rest of the buffer.

The main conclusions of the sensitivity analysis to the corrosion rate are: 1) The increase in pH takes place sooner the larger the corrosion rate; 2) The larger the corrosion rate, the larger the magnetite concentration close to the canister/bentonite interface but the smaller its penetration in the bentonite; 3) Similar to magnetite, the larger the corrosion rate the smaller the penetration of the siderite front into the bentonite.; 4) The thickness of the zone where calcite precipitates in the bentonite decreases with the corrosion rate and ranges from 4 to 10 cm for corrosion rates from 5 to 0.5 μm/y. For the smallest corrosion rate calcite precipitates everywhere in the bentonite; 5) The computed concentrations of exchanged cations in the bentonite are not sensitive to changes in the corrosion rate; and 6) The larger the corrosion rate, the faster the porosity reduction near the canister interface. The larger the corrosion rate, the smaller the thickness of bentonite affected by pore clogging.

The main conclusions of the sensitivity analysis to the D_e of the bentonite include: 1) The computed concentrations of most dissolved species, except for the dissolved Fe^2 are not sensitive to the changes in D_e. The larger the D_e, the smoother is the increase of the curve if the concentration of dissolved Fe^{2+}; 2) The computed pH is not very sensitive to the change in the D_e of the bentonite; 3) The larger the D_e, the larger the thickness of the zone where magnetite, siderite and calcite precipitate. The thickness of magnetite precipitation increases from 4 to 9 cm when the D_e increases from $0.5D_e$ to $2D_e$; 4) The computed concentrations of exchanged cations in the bentonite and the $H_2(g)$ partial pressure are not sensitive to changes in the D_e of the bentonite; and 5) The larger the D_e of the bentonite, the larger the zone affected by the porosity reduction and the larger the thickness of bentonite affected by pore clogging.

The sensitivity analysis to the groundwater flow Q indicate that: 1) The computed concentrations of most dissolved species are very sensitive to the changes in the water flow Q because the solute flux from the bentonite into the granite is controlled mostly by the advective transport of the granite water flow. The larger the Q, the faster the decrease of the concentrations; 2) The computed pH is slightly sensitive to the change in Q after 400 years.

The larger the *Q* the larger the pH from 400 to $6 \cdot 10^4$ years. After $6 \cdot 10^4$ years, the computed pH is largest for the smallest groundwater flow; 3) The computed Eh is not sensitive to changes in Q; 4) The concentration of precipitated magnetite in the bentonite is strongly sensitive to the increase in Q. The larger the Q, the smaller the concentration of precipitated magnetite and the smaller the thickness of the zone where magnetite precipitates; 5) The concentration of precipitated siderite is very sensitive to Q. The larger the Q, the larger the precipitation of siderite and the smaller the thickness of the zone where siderite precipitates; 6) The concentration of precipitated calcite near the canister/bentonite interface is very sensitive to the changes in Q. The larger the Q, the smaller the zone where calcite precipitates; 7) The concentration of the exchanged Fe^{2+} is sensitive to Q after $t = 4 \cdot 10^3$ years. The larger the Q, the lager the concentration of the exchanged Fe^{2+}; 8) Sorption fronts are less pronounced when the groundwater flow increases; 9) The $H_2(g)$ partial pressure is very sensitive to the groundwater flow. The larger the Q, the smaller the $H_2(g)$ partial pressure; and 10) The larger the groundwater flow Q, the smaller the zone affected by the porosity reduction and the smaller the thickness of bentonite affected by pore clogging.

The change in the cation selectivities affect mostly the concentrations of exchanged cations, especially Mg^{2+} and Ca^{2+}. However, the computed pH, Eh and the concentrations of dissolved and precipitated species lack sensitivity to the selectivities.

The conclusions of the sensitivity analysis to the change in the chemical compositions of the bentonite and granite porewaters are:1) The initial concentration of Cl^- in the sensitivity run is smaller than that in the base run and therefore, the computed Cl^- concentration in the sensitivity run is smaller and decreases slower than in the base run; 2) The initial concentration of dissolved Fe^{2+} is smaller than that of the base run and the initial pH in the sensitivity run is larger than that of the base run; 3) The computed pH for the sensitivity run is generally larger than of the base run; 4) The computed concentration of magnetite in the sensitivity run near the canister/bentonite interface is much larger than in the base run while the thickness of the zone where magnetite penetrates ($\approx$ 2.5 cm) is half of that computed for the base run; 5) Siderite precipitation in the sensitivity run starts much later than in the base run. The thickness of the zone of siderite precipitation in the sensitivity run is always smaller than 4 cm and half of that of the base run. All the precipitated siderite is subsequently dissolved and no siderite remains in the bentonite at the end of the simulation; 6) The concentration of sorbed Fe^2 and the thickness of the zone of sorption fronts in the sensitivity run are much smaller than those of the base run; 7) The peak pressure of $H_2(g)$ for the

sensitivity run is smaller than that of the base run; and 8) The thickness of the bentonite zone affected by pore clogging in the sensitivity run with the modified chemical composition is smaller than that of the base run.

The results of the long-term geochemical evolution of the EBS presented in this report could be improved by: 1) Considering different types of waters: internal, external and free waters; 2) Allowing for the canister void space to have properties other than those of the bentonite; 3) Allowing for the dynamic update of bentonite porosity to account for the possible pore clogging. This will require the use of kinetics for mineral precipitation; 4) Accounting for silicate aqueous complexes; 5) Allowing for different effective diffusion coefficients for each chemical species; 6) Accounting for bentonite hydration and the thermal field across the EBS; 7) Taking into account kinetic magnetite precipitation; and 8) Incorporating smectite kinetic dissolution and the neoformation of Fe-clay minerals.

Content

List of Figures

List of Tables

1. Introduction

1.1. Background

The objectives of the WP 3.5 of the PEBS Project are to use the data and improved models from Task 3.1 – Task 3.4 for extrapolation to long-term evolution of the repository taking into account the scenarios defined in PEBS WP1, and to investigate model uncertainty and its impact on long-term prediction, thus providing input to PEBS WP4.

The models developed in the Tasks 3.1 to 3.4 will be applied to the simulation and prediction of the likely long-term evolution of the engineered barrier in the repository. However, this extrapolation to long term will not be a blind extension of the model to different space and time scales but it will require a careful assessment of the key long-term processes as well as an evaluation of the resulting uncertainty and its consequences. Coupled analyses of varying degree of complexity, extending to long time scales, will be performed by the different partners.

For most THM considerations, long-term extrapolation means to extrapolate from the time-scale that can be covered by experiments to the end of the resaturation phase of the buffer in a repository. The time span considered will possibly be several hundred to 1000 years. After this, THM processes will be of minor importance, although processes like thermo-osmosis may play a role. Chemical processes, on the other hand, may take place at all temporal scales. Chemical reactions induced by canister corrosion take place during time scales much larger than that of buffer resaturation. It is understood that the gas production by corrosion can also have an effect on THM behaviour, if production rates are so high that not all gas can be transported by dissolution and diffusion in the liquid phase.

As a consequence of this consideration, there are two levels of extrapolation in time:

1. Extrapolation to the end of the resaturation phase is of special importance, because it defines the conditions of the buffer during the successive hundreds of thousand years after buffer resaturation and feeds the necessary input to PA. It is the period which is especially interesting in terms of THM behaviour, because it involves temperature and saturation gradients as driving forces for physical and chemical processes.
2. Extrapolation to the end of PA-considered time (usually from 10^5 to 10^6 years). Some THM phenomena such as thermo-osmosis and the high density of adsorbed water may become patent at this time scale. On the other hand, chemical processes

such as canister corrosion and chemical interactions of bentonite with canister corrosion products will occur also during this period of time.

The use of physically-based models, as opposed to empirical models, allows the straightforward extrapolation in time for long-term evaluation, provided that model assumpt D_e ons hold over the entire calculation period. A careful analysis will be made to review the validity of model assumptions at different time scales. This is the case for the local equilibrium assumption (LEA) versus a kinetically-controlled reaction. Some chemical reactions must be treated with kinetics at short time scales while they can be modelled with the LEA at large time scales.

1.2. Objectives

Within the WP3.5, UDC has performed long-term THC(m) predictions of the geochemical evolution of the conditions in a HLW repository in granite. The model accounts for canister corrosion, the interactions of the corrosion products with bentonite and the diffusion of solutes from (to) the EBS to (from) the surrounding granitic rock. The model starts after the dissipation of the thermal pulse and extends over 1 Ma.

1.3. Scope

Chapter 2 describes the reference concept of a high-level radioactive waste repository in granite according to the Spanish reference concept. The conceptual and numerical models used to perform the long-term predictions are described in Chapter 3. Numerical results for the base or reference model are presented and discussed in Chapter 4. Prediction uncertainties have been evaluated by means of sensitivity runs. The results of the sensitivity runs are described in Chapter 5. There are open questions and remaining uncertainties which will need to be addressed in future studies. They are discussed in Chapter 6. The main conclusions of this study are presented in Chapter 7.

2. Reference concept

High-level radioactive waste disposal (HLW) in deep geological formations is based on a multi-barrier concept which includes natural and engineered barriers. The natural barrier is the host rock while the engineered barriers include the waste form, the canister, and the bentonite buffer. This chapter describes the reference concept for the Spanish HLW repository in granite rock and presents a general description of its expected early time evolution with an indication of the most relevant time and space scales of the engineered barrier. This description is based on the ENRESA performance assessment project, named ENRESA 2000 (ENRESA, 2000b) and the results of the FEBEX project (ENRESA 2000a, 2004; 2006).

The Spanish reference concept for a repository in granite is based on the disposal of spent fuel in carbon steel canisters in long horizontal disposal drifts. Canisters are surrounded by blocks of compacted bentonite. Access is accomplished by means of "main drifts" which are perpendicular to the disposal drifts. The main drifts meet at a central area, which includes the required underground infrastructure. Communications between the surface and the central underground area are accomplished by means of 3 access shafts and a ramp. Figure 2.1 shows a view of the underground installations.

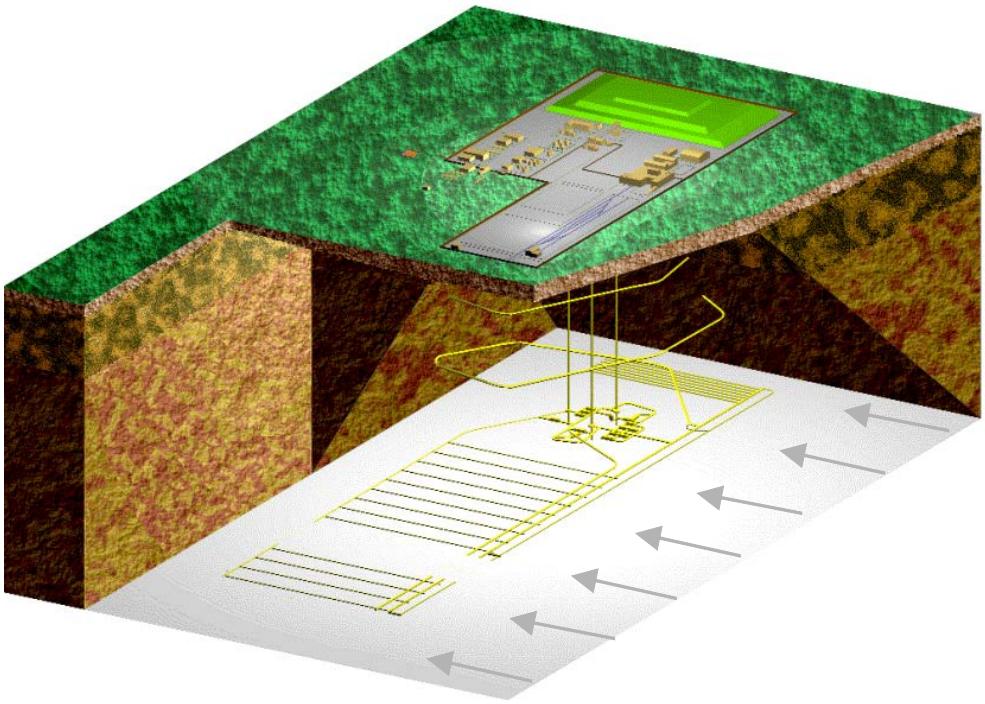

Figure 2.1. ENRESA repository concept: underground installations (ENRESA, 2005).

A canister contains 4 PWR or 12 BWR fuel elements in a subcritical configuration. After being unloaded from the reactor, the fuel elements are temporarily stored for their thermal power to decay to a level at which they may be disposed of with a total thermal power of 1,220 W per canister. A total of 3,600 canisters will be required for the final waste inventory of spent fuel estimated for the Spanish nuclear power programme.

Canisters are cylindrical and measure 4.54 m in length and 0.90 m in diameter (Figure 2.3). Their thickness of 0.10 m at the cylindrical wall and 0.12 m at the ends is capable of withstanding the pressures to which it is subjected under disposal conditions and providing a minimum period of containment of 1000 years. Canisters are disposed in cylindrical disposal cells, constructed with blocks of pre-compacted bentonite (Figure 2.2). Pre-compacted bentonite blocks, of 1,700 kg/m^3 dry density are used in order to achieve a final dry density of 1,600 kg/m^3. The blocks are initially unsaturated with a degree of saturation of 66%.

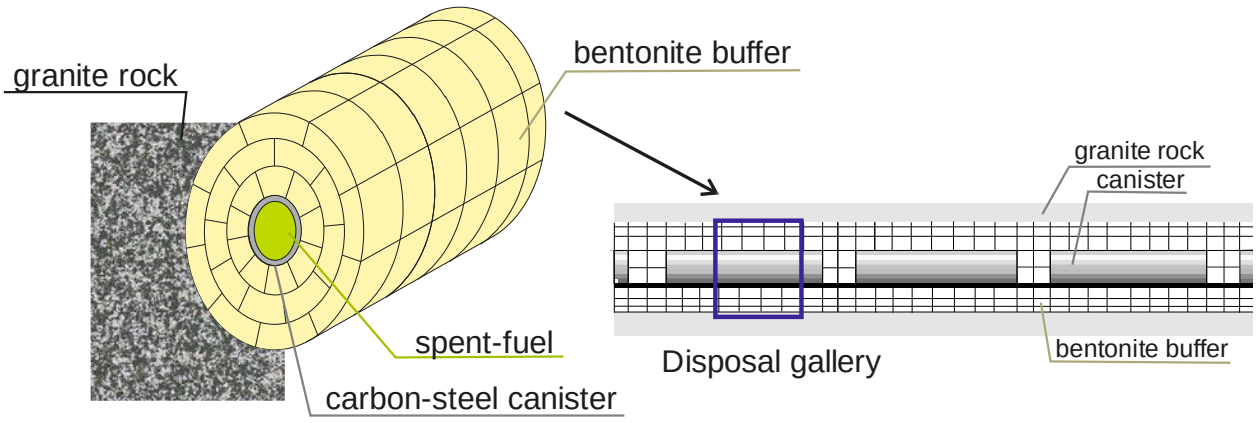

Figure 2.2. Sections of a disposal drift.

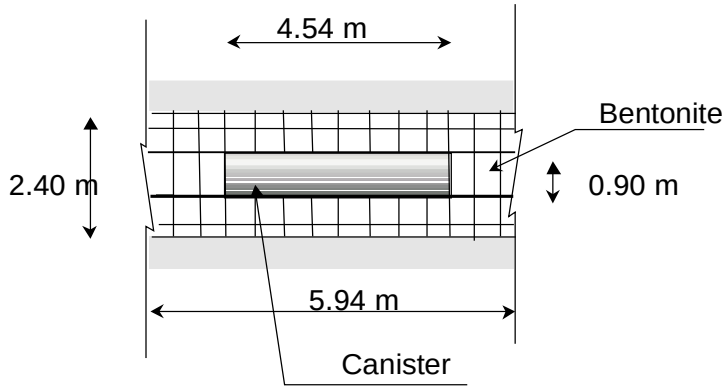

Figure 2.3. Dimensions of the canister and the individual disposal cell (ENRESA, 2000b).

The disposal drifts, having 500 m in length and 2.4 m in diameter (see Figure 2.3), are located at a depth of 500 m in the host rock formation. The separation between canisters along a drift and between drifts is determined mainly by thermal constraints. Separations of 2 m between canisters and 35 m between disposal drifts have been established in order not to exceed a temperature of 100 ºC in the bentonite. Actual separation is a function of the properties of the host rock. The thermal calculations have been made for a reference generic site.

The disposal drift will be sealed with a 6 m long seal made of bentonite blocks and closed with a concrete plug at its entry. After completion of all the disposal drifts, main drifts, ramp, shafts and other remaining rock cavities will be backfilled with a mixture of bentonite and natural sand or an appropriate crushed material. The backfilling material will consist of 10 % bentonite (increasing up to 20 % at the top of the drifts) and suitably graded sand.

The lifetime of the canister retaining the high-radioactive waste is related to the corrosion rate of carbon steel. Once the canister fails and the water enters to it, radionuclides may migrate into the bentonite buffer. Canister corrosion may affect the chemistry of the bentonite porewater and thus result in changes in the migration behaviour of the radionuclides. Furthermore, the corrosion products may also induce buffer alterations which may result in changes in parameters such as porosity, permeability, sorption and swelling.

More details about the reference concept, the phenomenological description of the main processes and their time evolution can be found in ENRESA (2005).

3. Conceptual and numerical model

3.1. Introduction

This chapter presents the conceptual and numerical reactive transport models for canister corrosion that take into account the interactions of corrosion products with bentonite and the pH buffering mechanisms. The geometry of the model corresponds to the Spanish reference concept of a spent-fuel carbon-steel canister repository in granite (Chapter 2). An individual disposal cell is modelled by assuming radial symmetry of the system and by neglecting the canister border effects. The simulations are performed at a constant temperature of 25ºC for a time horizon of 1 Ma.

3.2. Computer code

Coupled hydrogeochemical calculations of the interactions of corrosion with bentonite have been performed with CORE^{2D}V4 (Samper et al., 2003; 2011), a code for transient saturated and unsaturated water flow, heat transport and multicomponent reactive solute transport under both local chemical equilibrium and kinetic conditions in heterogeneous and anisotropic media. Flow and transport equations are solved with Galerkin triangular finite elements and an Euler scheme for time discretization. CORE^{2D}V4 solves problems with a wide range of geochemical reactions such as acid–base, aqueous complexation, redox, mineral dissolution/precipitation, gas dissolution/ex-solution, cation exchange and surface complexation. The chemical formulation is based on the ion association theory and uses an extended version of Debye–Hückel equation (B-dot) for the activity coefficients of aqueous species. CORE^{2D}V4 relies on thermodynamic data from EQ3/6 (Wolery, 1992). It uses the sequential iteration approach to solve for chemical reactive solute transport. The whole iterative cycle is repeated until prescribed convergence criteria are attained (Xu et al., 1999; Samper et al., 2009; 2011).

CORE^{2D} has been widely used to model laboratory and in situ experiments performed for HLW disposal (Molinero and Samper 2006; Samper et al., 2008b; Zheng and Samper, 2008; Zheng et al., 2008; 2010), evaluate the long-term geochemical evolution of radioactive waste repositories in clay (Yang et al., 2008), model the transport of corrosion products and their geochemical interactions with bentonite (Samper et al., 2008a; 2011) and evaluate the long-term transport and sorption of radionuclides through the bentonite barrier (Samper et al., 2010).

3.3. Model domain and discretization

A 1D radial model of a disposal cell has been used to simulate canister corrosion and the long term evolution of the bentonite. It considers the canister and the bentonite (Figure 3.1). Both of them are assumed to be homogeneous. The canister external radius is 0.45 m and its thickness is 0.10 m. The external radius of the bentonite barrier is 1.2 m. Water flow and solute transport through the granite has been simulated with a prescribed water flux of granite water parallel to the axis of the gallery.

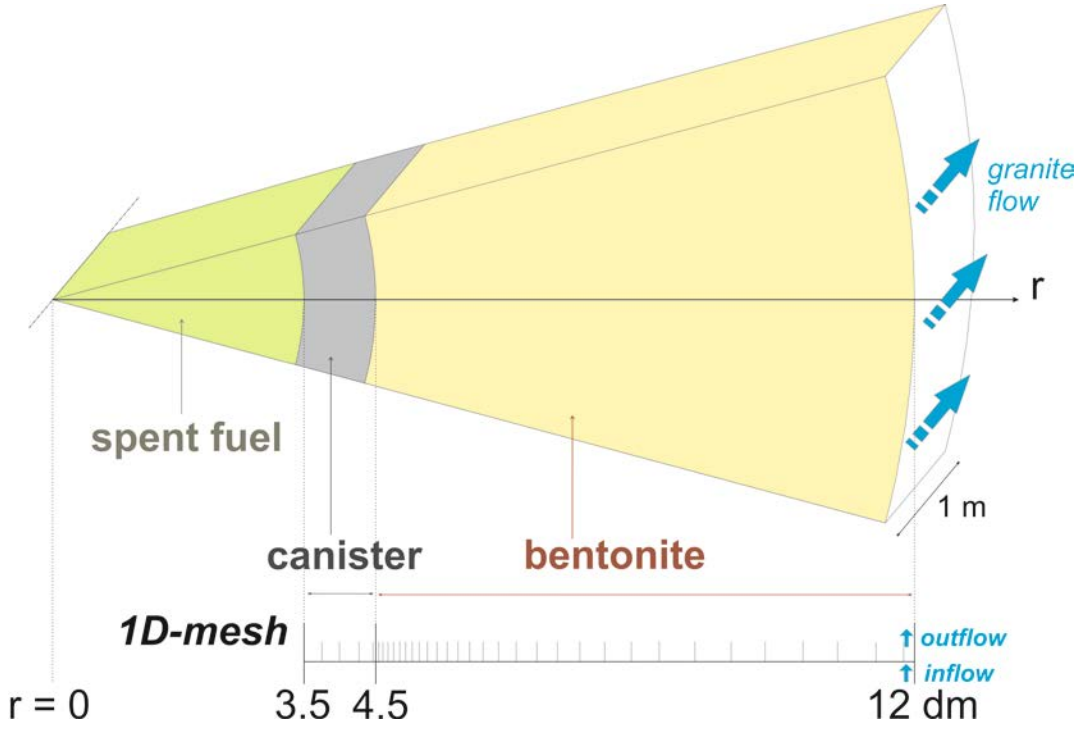

Figure 3.1. Sketch and finite element grid of the 1D axi-symmetric model.

A 1-D axi-symmetric finite element mesh has been used which has 93 nodes and 92 one-dimensional elements. The grid is shown in Figure 3.1. The mesh is especially refined close to the canister/bentonite interface where the interaction between the corrosion products and the bentonite are strongest. The spatial discretization decreases with the distance to the canister.

Simulations are carried out for 1Ma by using around 30.000 time steps.

3.4. Flow and transport

According to (ENRESA, 2005; 2006) the bentonite barrier will become fully saturated after 20 to 30 years for the Spanish reference concept. Therefore, the model assumes that the bentonite is initially water-saturated.

Flow and transport parameters are similar to those reported by Samper et al. (2008a; 2011). Advection in the bentonite is negligible because its hydraulic conductivity is extremely low ($6 \cdot 10^{-14}$ m/s). Therefore, solute diffusion is the main solute transport mechanism in the engineered barrier. All dissolved chemical species are assumed to have the same effective diffusion of $4.07 \cdot 10^{-11}$ m^2/s. Bentonite porosity is 0.407. It is assumed that all water is accessible. The canister is assumed to have the same transport properties of the bentonite. The uncertainties caused by these simplifying assumptions should be evaluated in future studies.

Samper et al. (2008a) showed that the changes in the bentonite porosity caused by mineral dissolution/precipitation are less than 0.1 for a corrosion rate of 0.2 μm/y after 0.3 Ma. Therefore, those changes are disregarded in all the simulations in order to reduce computation time.

No flow boundaries are considered in the model except for the bentonite/granite interface. A flow rate of 0.1 L/y is imposed at the outer element of the model to simulate the washing of that surface by groundwater water through the granite. The inflow water has the chemical composition of the granite porewater. This boundary condition has a significant effect on the geochemical evolution of the EBS.

3.5. Geochemical model

The geochemical model accounts for the following geochemical reactions:

- Aqueous complexation reactions,
- Acid/base reactions
- Redox reactions
- Mineral dissolution/precipitation
- Cation exchange
- Protonation/deprotonation by surface complexation
- Canister corrosion

The model starts after the thermal pulse has dissipated. Therefore, all the chemical reactions are modelled at a constant temperature of 25ºC.

The chemical system is defined in terms of the follow primary species: H_2O, $O_2(aq)$, H^+, Na^+, K^+, Ca^{2+}, Mg^{2+}, Fe^{2+}, HCO_3^-, Cl^-, SO_4^{2-} and $SiO_2(aq)$. Relevant aqueous complexes were identified from speciation runs performed with EQ3/6 (Wolery, 1992). The homogeneous chemical reactions considered in the model and their equilibrium for aqueous complexes are listed in Table 3.1. All these reactions are assumed at local chemical equilibrium.

Table 3.1. Homogeneous chemical reactions considered in the model and their equilibrium constants at 25ºC (Wolery, 1992).

Reaction	Log K (25°C)
$OH^- + H^+ \rightleftarrows H_2O$	$1.3832 \cdot 10^1$
$CO_3^{2-} + H^+ \rightleftarrows HCO_3^-$	$1.0284 \cdot 10^1$
$CaCO_3(aq) + H^+ \rightleftarrows Ca^{2+} + HCO_3^-$	6.9197
$CaHCO_3^+ \rightleftarrows Ca^{2+} + HCO_3^-$	-1.0493
$CaSO_4(aq) \rightleftarrows Ca^{2+} + SO_4^{2-}$	-2.1186
$CaOH^+ + H^+ \rightleftarrows Ca^{2+} + H_2O$	$1.2666 \cdot 10^1$
$MgCO_3(aq) + H^+ \rightleftarrows Mg^{2+} + HCO_3^-$	7.2869
$MgHCO_3^+ \rightleftarrows Mg^{2+} + HCO_3^-$	-1.0412
$MgSO_4(aq) \rightleftarrows Mg^{2+} + SO_4^{2-}$	-2.4449
$MgOH^+ + H^+ \rightleftarrows Mg^{2+} + H_2O$	$1.1607 \cdot 10^1$
$NaOH + H^+ \rightleftarrows Na^+ + H_2O$	$1.3998 \cdot 10^1$
$NaCO_3^- + H^+ \rightleftarrows Na^+ + HCO_3^-$	9.8367
$NaHCO_3(aq) \rightleftarrows Na^+ + HCO_3^-$	$-1.2287 \cdot 10^{-1}$
$CO_2(aq) + H_2O \rightleftarrows H^+ + HCO_3^-$	-6.3161
$HS^- + 2O_2(aq) \rightleftarrows H^+ + SO_4^{2-}$	138.31
$Fe^{3+} + 0.5H_2O \rightleftarrows H^+ + 0.25O_2 + Fe^{2+}$	-8.2077
$FeHCO_3^+ \rightleftarrows Fe^{2+} + HCO_3^-$	-1.98
$FeCO_3(aq) + H^+ \rightleftarrows Fe^{2+} + HCO_3^-$	5.67
$FeCl^+ \rightleftarrows Fe^{2+} + Cl^-$	$1.54 \cdot 10^{-1}$

Reaction	Log K (25°C)
$FeCl^{2+} + 0.5H_2O \rightleftarrows Fe^{2+} + H^+ + 0.25O_2(aq) + Cl^-$	-7.50
$FeOH^+ + H^+ \rightleftarrows Fe^{2+} + H_2O$	$1.07 \cdot 10^1$
$FeOH^{2+} \rightleftarrows Fe^{2+} + 0.5H_2O + 0.25O_2$	-3.95
$Fe(OH)_2(aq) + 2H^+ \rightleftarrows Fe^{2+} + 2H_2O$	$2.02 \cdot 10^1$
$Fe(OH)_3(aq) + 2H^+ \rightleftarrows Fe^{2+} + 0.25O_2 + 2.5H_2O$	3.96
$Fe(OH)_4^- + 3H^+ \rightleftarrows Fe^{2+} + 0.25O_2 + 3.5H_2O$	$1.30 \cdot 10^1$
$Fe(OH)_2^+ + H^+ \rightleftarrows Fe^{2+} + 0.25O_2 + 1.5H_2O$	-2.7424
$Fe(SO_4)_2^- + 0.5H_2O \rightleftarrows Fe^{2+} + H^+ + 2SO_4^{2-} + 0.25O_2$	$-1.14 \cdot 10^1$
$FeSO_4(aq) \rightleftarrows Fe^{2+} + SO_4^{2-}$	$-2.19 \cdot 10^1$
$FeHSO_4^{2+} + 0.5H_2O \rightleftarrows Fe^{2+} + 2H^+ + SO_4^{2-} + 0.25O_2$	-9.7477
$Fe_2(OH)_2^{4+} \rightleftarrows 2Fe^{2+} + H_2O + 0.5O_2$	-9.3067
$KOH(aq) + H^+ \rightleftarrows K^+ + H_2O$	$1.44 \cdot 10^1$
$KSO_4^- \rightleftarrows K^+ + SO_4^{2-}$	$-8.85 \cdot 10^{-1}$
$NaSO_4^- \rightleftarrows Na^+ + SO_4^{2-}$	$-8.25 \cdot 10^{-1}$
$HSO_4^- \rightleftarrows H^+ + SO_4^{2-}$	-2.0366
$H_{2(aq)} + 0.5O_{2(aq)} \rightleftarrows H_2O$	$4.610 \cdot 10^1$

The model accounts for the dissolution/precipitation of calcite, gypsum, quartz, magnetite, siderite and goethite. The initial volume fractions of calcite and quartz in the bentonite are similar to those reported by Samper et al. (2008a). Gypsum, magnetite, siderite and goethite are minerals which are not initially present in the system, but are allowed to precipitate.

Table 3.2 lists the mineral dissolution/precipitation reactions and their equilibrium constants at 25ºC. Carbon-steel canister corrosion is simulated in a manner similar to mineral dissolution by using a constant kinetic rate (see Section 3.6).

Table 3.2. Dissolution/precipitation reactions considered in the model and their equilibrium constants at 25ºC (Wolery, 1992).

	Reaction	Log K (25°C)
Calcite	$CaCO_3 + H^+ \rightleftarrows Ca^{2+} + HCO_3^-$	1.8487
Gypsum	$CaSO_4 \cdot 2H_2O \rightleftarrows Ca^{2+} + SO_4^{2-} + 2H_2O$	-4.4823
Quartz	$SiO_2(s) \rightleftarrows SiO_2(aq)$	-3.9993
Magnetite	$Fe_3O_4(s) + 6H^+ \rightleftarrows 3Fe^{2+} + 0.5O_2(aq) + 3H_2O$	-6.5076
Siderite	$FeCO_3^-(s) + H^+ \rightleftarrows Fe^{2+} + HCO_3^-$	-0.1920
Goethite	$FeOOH + 2H^+ \rightleftarrows Fe^{2+} + 1.5H_2O + 0.25O_2(aq)$	-7.9555

The model accounts for the cation exchange of Na^+, Ca^{2+}, Mg^{2+}, K^+ and Fe^+ in the bentonite. The cation exchange capacity (CEC) is 102 meq/100g (Fernández et al., 2004). Table 3.3 lists the cation exchange reactions and their selectivity coefficients at 25ºC. The Gaines-Thomas convection is used in which Na is adopted as the reference cation (Gaines and Thomas, 1953). Exchange reactions are written so that exchanged Na^+ is on the left side of the reaction with a unit stoichiometric coefficient. Cation selectivity coefficients for exchanged Ca^{2+}, Mg^{2+} and K^+ were calibrated so that the computed concentrations of exchanged cations of the FEBEX bentonite are within the range of those reported by Fernández et al. (2004) and ENRESA (2004) (see Table 3.3). The selectivity coefficient for the exchange of iron was taken from Tournassat (2003). The base run was performed with the selectivities used by Samper et al. (2008a). The simulation results obtained with the calibrated selectivities are presented in Chapter 5 as part of the sensitivity analyses.

Table 3.3. Cation exchange reactions and selectivity coefficients at 25ºC taken from Samper et al. (2008a) and calibrated for this study.

Reaction	$K_{Na\text{-}cation}$ Used for base run (from Samper et al., 2008a)	Calibrated $K_{Na\text{-}cation}$ Used for a sensitivity run
$Na^+ + 0.5Ca-X_2 \rightleftarrows 0.5Ca^{2+} + Na-X$	0.282	0.292
$Na^+ + 0.5Mg-X_2 \rightleftarrows 0.5Mg^{2+} + Na-X$	0.344	0.280
$Na^+ + K-X \rightleftarrows K^+ + Na-X$	0.091	0.138
$Na^+ + 0.5Fe-X_2 \rightleftarrows 0.5Fe^{2+} + Na-X$	0.5	0.5

Surface complexation reactions in the bentonite are modelled with a triple sorption site model similar to that of Bradbury and Baeyens (1997; 2005). The total concentration of sorption sites is 0.322 mol/L. There are 3 types of sorption sites. The first type of sites corresponds to the strong sites which have a large binding affinity but a small concentration (0.0079 mol/L). The other two types are the weak sites (the so-called weak 1 and weak 2) have binding constants weaker than those of the strong sites although their concentrations (0.16 mol/L) are larger than those of the strong sites. Table 3.4 lists the protolysis constants at 25ºC. According to Samper et al. (2008a; 2011), proton surface complexation plays a major role in controlling the pH of the bentonite porewater. Surface complexation and cation exchange reactions are not considered in the canister.

Table 3.4. Protolysis constants for surface complexation reactions for a triple-site model (Bradbury and Baeyens, 2005) at 25ºC.

Reaction	**Log K_{int}**
$\equiv S^{S}OH_2^{+} \rightleftarrows \equiv S^{S}OH + H^{+}$	-4.5
$\equiv S^{S}O^{-} + H^{+} \rightleftarrows \equiv S^{S}OH$	7.9
$\equiv S^{S}OFe^{+} + H^{+} \rightleftarrows \equiv S^{S}OH + Fe^{2+}$	0.6
$\equiv S^{S}OFeOH + 2H^{+} \rightleftarrows \equiv S^{S}OH + Fe^{2+} + H_2O$	10.0
$\equiv S^{S}OFe(OH)_2^{-} + 3H^{+} \rightleftarrows \equiv S^{S}OH + Fe^{2+} + 2H_2O$	20.0
$\equiv S^{W1}OH_2^{+} \rightleftarrows \equiv S^{W1}OH + H^{+}$	-4.5
$\equiv S^{W1}O^{-} + H^{+} \rightleftarrows \equiv S^{W1}OH$	7.9
$\equiv S^{W1}OFe^{+} + H^{+} \rightleftarrows \equiv S^{W1}OH + Fe^{2+}$	3.3
$\equiv S^{W2}OH_2^{+} \rightleftarrows \equiv S^{W2}OH + H^{+}$	-6.0
$\equiv S^{W2}O^{-} + H^{+} \rightleftarrows \equiv S^{W2}OH$	10.5

Table 3.5 lists the chemical composition of the initial bentonite porewater and the boundary water at the bentonite/granite interface similar to granite porewater (Samper et al., 2008a; 2011). The initial canister porewater is assumed to have the same chemical composition of the bentonite which is the chemical equilibrium with respect to calcite and quartz, proton surface complexation and cation exchange. This table includes the values reported by Samper et al. (2008a; 2011) as initial values and those computed with the code at the first time step which corresponds to t = $5 \cdot 10^{-4}$ years. There are some differences in the concentrations of some chemical species which are especially relevant for dissolved iron,

bicarbonate and silica. Such differences are caused by the lack of equilibrium with respect to calcite, quartz and goethite. In fact, the numerical model computes the following concentrations of mineral species after t = $5 \cdot 10^{-4}$ years: 1) The dissolution of $5.92 \cdot 10^{-3}$ mol/L of calcite; 2) The precipitation of $7.45 \cdot 10^{-4}$ mol/L of quartz; and 3) The precipitation of $1.05 \cdot 10^{-9}$ mol/L of goethite.

Table 3.5. Chemical composition of the initial bentonite porewater and the boundary water at the bentonite/granite interface (Samper et al., 2008a).

Species	**Initial bentonite porewater**	**Bentonite porewater computed at t = $5 \cdot 10^{-4}$ years**	**Boundary water (granite porewater)**
pH	6.43	6.46	7.825
Eh (V)	-0.059	-0.078	-0.188
Ca^{2+} (mol/L)	$3.10 \cdot 10^{-2}$	$3.32 \cdot 10^{-2}$	$1.522 \cdot 10^{-4}$
Mg^{2+} (mol/L)	$3.47 \cdot 10^{-2}$	$3.67 \cdot 10^{-2}$	$1.604 \cdot 10^{-4}$
Na^{+} (mol/L)	$1.84 \cdot 10^{-1}$	$1.88 \cdot 10^{-1}$	$4.350 \cdot 10^{-3}$
K^{+} (mol/L)	$1.50 \cdot 10^{-3}$	$1.55 \cdot 10^{-3}$	$5.371 \cdot 10^{-5}$
Fe^{2+} (mol/L)	$6.58 \cdot 10^{-5}$	$1.43 \cdot 10^{-4}$	$1.791 \cdot 10^{-8}$
Cl^{-} (mol/L)	$2.75 \cdot 10^{-1}$	$2.75 \cdot 10^{-1}$	$3.949 \cdot 10^{-4}$
HCO_3^{-} (mol/L)	$1.69 \cdot 10^{-3}$	$7.59 \cdot 10^{-3}$	$5.049 \cdot 10^{-3}$
SO_4^{2-} (mol/L)	$2.05 \cdot 10^{-2}$	$2.05 \cdot 10^{-2}$	$1.561 \cdot 10^{-5}$
SiO_2 (aq) (mol/L)	$8.42 \cdot 10^{-4}$	$9.67 \cdot 10^{-5}$	$3.761 \cdot 10^{-4}$

3.6. Canister corrosion

The available oxygen in the repository will be consumed after its closure and anaerobic conditions will prevail. Corrosion under reducing conditions will occur according to thermodynamic predictions. Carbon-steel canister corrosion can be represented as:

$$Fe(s) + 2H_2O \rightleftarrows Fe(OH)_2(s) + H_2(g) \qquad (3.1)$$

where Fe(s) denotes an idealized mineral phase for carbon-steel and H_2O is assumed to be the oxidizing agent of the canister. The concentration of ferrous iron, Fe^{2+}, in the vicinity of carbon-steel canister is controlled by the solubility product of ferrous hydroxide, $Fe(OH)_2$(s). This metastable mineral can form magnetite, Fe_3O_4(s), according to:

$$3Fe(OH)_2(s) \rightleftarrows Fe_3O_4(s) + 2H_2O + H_2(g) \qquad (3.2)$$

Since magnetite is thermodynamically more stable than ferrous hydroxide, corrosion will lead to:

$$3Fe(s) + 4H_2O \rightleftarrows Fe_3O_4(s) + 4H_2(g) \qquad (3.3)$$

In addition to $Fe(OH)_2(s)$ and $Fe_3O_4(s)$, siderite and green rusts could form as corrosion products of carbon-steel canister under anaerobic conditions depending on the bentonite porewater composition. Siderite precipitation proceeds according to:

$$Fe^{2+} + CO_3^{2-} \rightleftarrows FeCO_3(s) \qquad (3.4)$$

However, the low concentration of carbonate in the bentonite porewater restricts siderite precipitation. As indicated by ENRESA (2005), siderite is not the main corrosion product because bentonite limits the carbonate flux reaching the canister surface.

Green rusts are Fe(II)–Fe(III) hydroxyl compounds containing anions such as CO_3^{2-}, SO_4^{2-} and Cl^-. The redox potential of carbonate green rust, GR1, has been thermodynamically predicted by Drissi et al. (1995). Refait et al. (1997) reported that the formation of GR1 is unlikely if the initial concentration of CO_3^{2-} is smaller than 0.005 mol/L. This is the case for bentonite porewater. The redox potential of sulphate green rust, GR2, is out of the expected range of redox potentials of bentonite porewater, and therefore its formation is also unlikely (Génin et al., 1996). Furthermore, chloride green rust GR3 formation is even more unlikely than that of GR1 and GR2 because the typical sequence of affinity of green rust compounds is GR1 > GR2 > GR3 (Miyata, 1983).

Goethite precipitation is not expected to occur based on thermodynamic grounds. However, the model accounts for the precipitation of goethite according to:

$$Fe^{2+} + 1.5H_2O + 0.25O_2(aq) \rightleftarrows FeOOH(s) + 2H^+ \qquad (3.5)$$

The following kinetic rate expression has been used for mineral dissolution/precipitation:

$$r_m = k_m(\Omega_m^{\theta} - 1)^{\eta} \qquad (3.6)$$

where r_m is the dissolution/precipitation rate (mol/m^2/s), k_m is the kinetic rate constant (mol/m^2/s), Ω_m is the ratio between the ion activity product and the equilibrium constant (dimensionless) and Θ and η are parameters of the kinetic law.

Carbon-steel corrosion is modelled by using a kinetic formulation in a manner similar to mineral dissolution. The canister is treated as a porous material made of 100% metallic iron, Fe(s), which dissolves at a constant rate according to:

$$Fe(s) + 2H_2O \rightleftarrows Fe^{2+} + 2OH^- + H_2(g) \qquad (3.7)$$

which can be written in terms of primary species as:

$$Fe(s) + 2H^+ + 0.5O_2(aq) \rightleftarrows Fe^{2+} + H_2O \qquad (3.8)$$

This is the chemical reaction used in the numerical model to simulate the canister corrosion. According to it, corrosion consumes protons and forces the reduction of water which in turn releases $H_{2(aq)}$ according to:

$$H_{2(aq)} + 0.5O_{2(aq)} \rightleftarrows H_2O \qquad (3.9)$$

Hydrogen is simulated as a dissolved species, $H_{2(aq)}$. The model does not account for $H_{2(g)}$. Assuming that the $H_{2(g)}$ is in equilibrium with the $H_{2(aq)}$, one has:

$$H_2(g) \rightleftarrows H_2(aq) \qquad (3.10)$$

From the results of the simulation for H_2(aq) it is possible to calculate the partial pressure of H_2(aq) according to:

$$P_P(H2(g)) = \frac{K_{H_2(g)\rightleftarrows H_2(aq)}}{[H_2(aq)]} \qquad (3.11)$$

were $K_{H2(g)\leftrightarrow H2(aq)}$ is the equilibrium constant at 25ºC of the Eq. (3.10) and [H_2(aq)] is the computed activity of H_2(aq).

The corrosion rate, r_c, in μm/year is calculated as:

$$r_c = \frac{r_m M_w}{\rho} \qquad (3.12)$$

where ρ is the density of the carbon steel (7.860 kg/m^3), M_w is its molecular weight (55.85 g/mol) and r_m is the corrosion rate per unit mineral surface (mol/m^2/year). A constant corrosion rate of 2 μm/year, which amounts to 0.281 mol/m^2/year, is assumed for the base run. It should be noticed that η = 0 for canister corrosion.

The corrosion products formed at the canister–bentonite interface migrate into the bentonite where they undergo chemical interactions with the aqueous and the solid phases.

4. Results for the base run

4.1. Canister corrosion

Figure 4.1 shows the computed time evolution of canister Fe(s) corrosion. The canister is fully corroded after $5 \cdot 10^4$ years for a corrosion rate of 2 μm/y. After full canister corrosion, ≈ 350 mol/L of Fe(s) are dissolved. It should be noticed that the cumulative amount of corroded Fe(s) remains constant once the canister has corroded entirely.

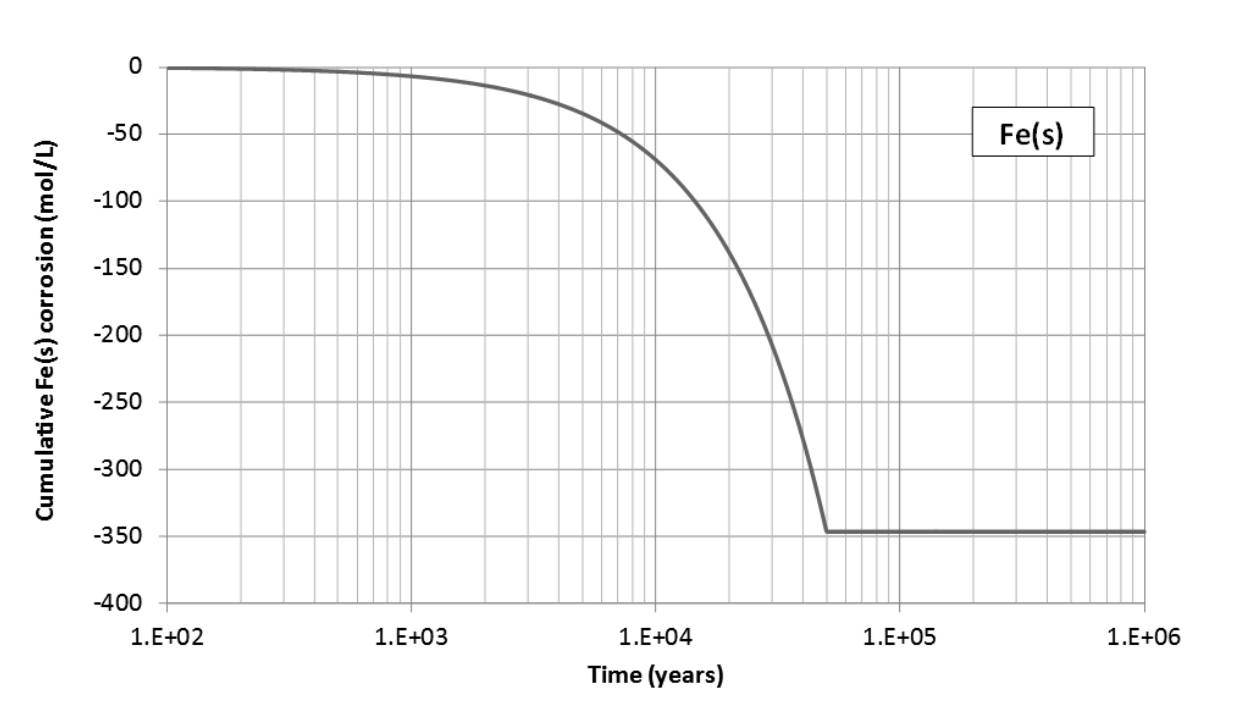

Figure 4.1. Time evolution of the computed cumulative canister corrosion.

4.2. Aqueous species

According to Equation (3.8), canister corrosion causes an increase in Fe^{2+} concentration and pH, and a decrease in Eh. Most of the released Fe^{2+} diffuses from the canister into the bentonite where it precipitates or sorbs.

Figure 4.2 shows the time evolution of the computed concentration of dissolved Fe in the bentonite at radial distances, r, equal to 4.6, 5.3 and 9.5 dm where r is measured from the axis of the disposal cell. Such radial distances correspond to the points located at 0.1, 0.8 and 5 dm from the canister/bentonite interface. Figure 4.3 shows the radial distribution of the computed concentration of dissolved Fe in the bentonite at several times. The time trends in the concentration of dissolved Fe are directly related to those of the sorbed species which are

shown in Figure 4.24, Figure 4.25 and Figure 4.27. For instance, the sudden decrease in dissolved Fe concentration after 80 years at r = 4.6 dm is associated with a sudden increase in Fe sorbed in weak 1 sites. The concentration of dissolved Fe after 100.000 years becomes smaller than $5 \cdot 10^{-6}$ mol/L due to the aqueous diffusion of dissolved Fe from the bentonite to the granite.

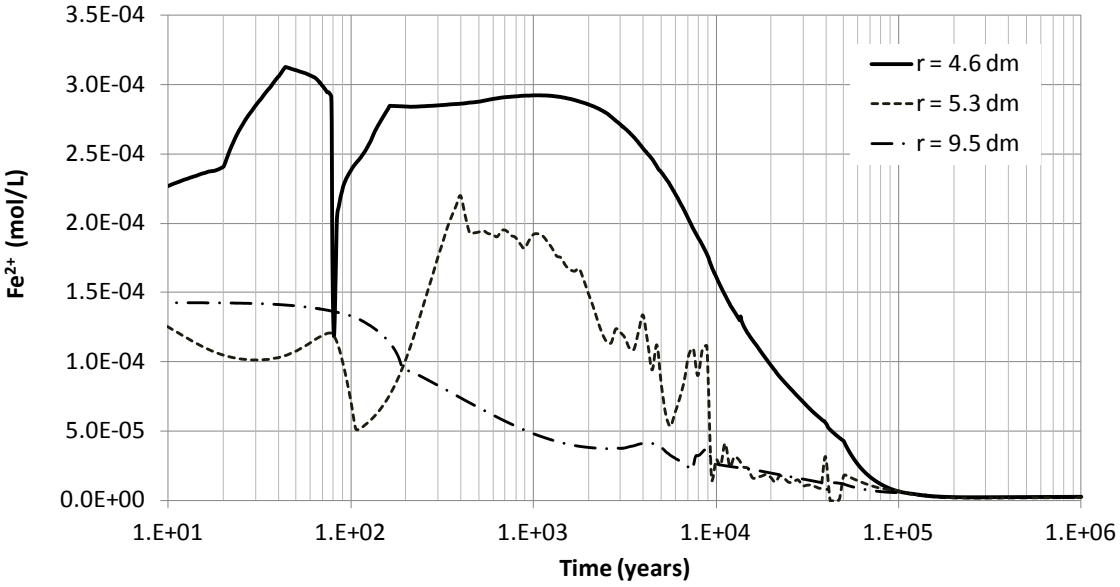

Figure 4.2. Time evolution of the computed concentration of dissolved Fe in the bentonite at r = 4.6, 5.3 and 9.5 dm.

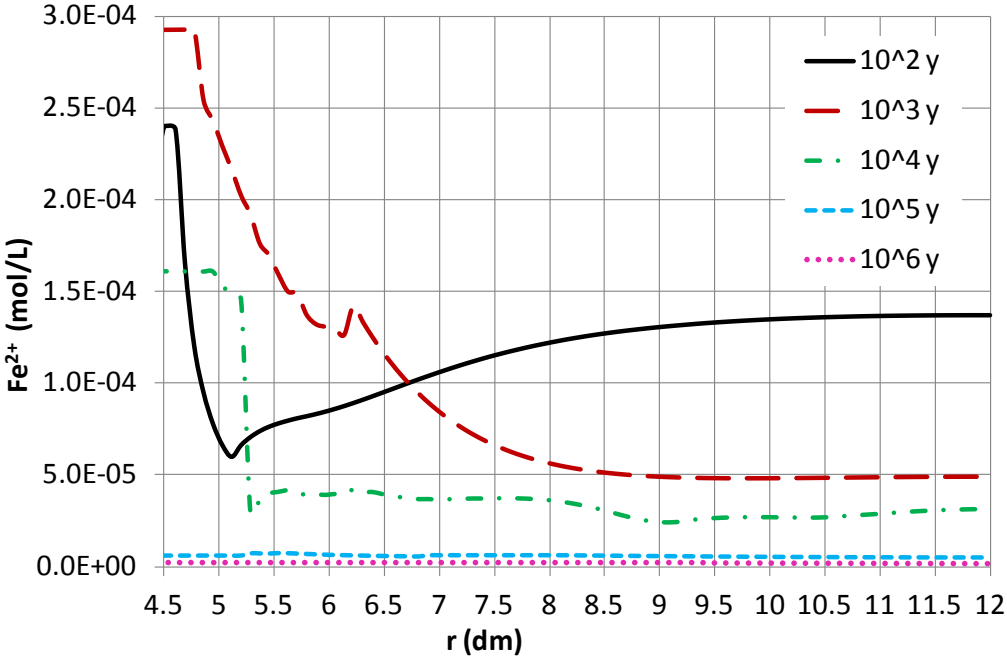

Figure 4.3. Radial distribution of the computed concentration of dissolved iron in the bentonite at selected times (r is the radial distance from the axis of the disposal cell).

Figure 4.4 shows the time evolution of the computed pH in the bentonite at r = 4.6, 5.3 and 9.5 dm. At r = 4.6 dm the pH increases from its initial value of 6.4 to 7.1 at t = 80 years. Then, the pH increases sharply almost a unit. Such an increase in pH is caused by the sorption of Fe on weak 1 sites according to:

$$\equiv S^{W1}OH + Fe^{2+} \rightleftarrows \equiv S^{W1}OFe^{+} + H^{+} \qquad (3.13)$$

Dissolved Fe^{2+} gets sorbed and releases protons (see Figure 4.24). From 80 to $2 \cdot 10^5$ years the pH keeps increasing and reaches a peak value of 9.5 after $2 \cdot 10^5$ years. At the end of the simulation, t = 10^6 years, the computed pH gets below 9.

At r = 5.3 dm the sorption fronts (see Figure 4.25 and Figure 4.26) induce a large decrease in pH at t = 10.000 years. Figure 4.5 and Figure 4.6 show the radial distribution of the computed pH in the bentonite at selected times. One can see clearly that pH reaches a minimum value of 4.5 at r = 5.3 dm from 10.000 to 20.000 years.

At points farther away from the canister such as r = 9.5 dm, the pH increases gradually reaching its maximum at t = $2 \cdot 10^5$ years the behavior of the pH is the same all along the bentonite (see Figure 4.4).

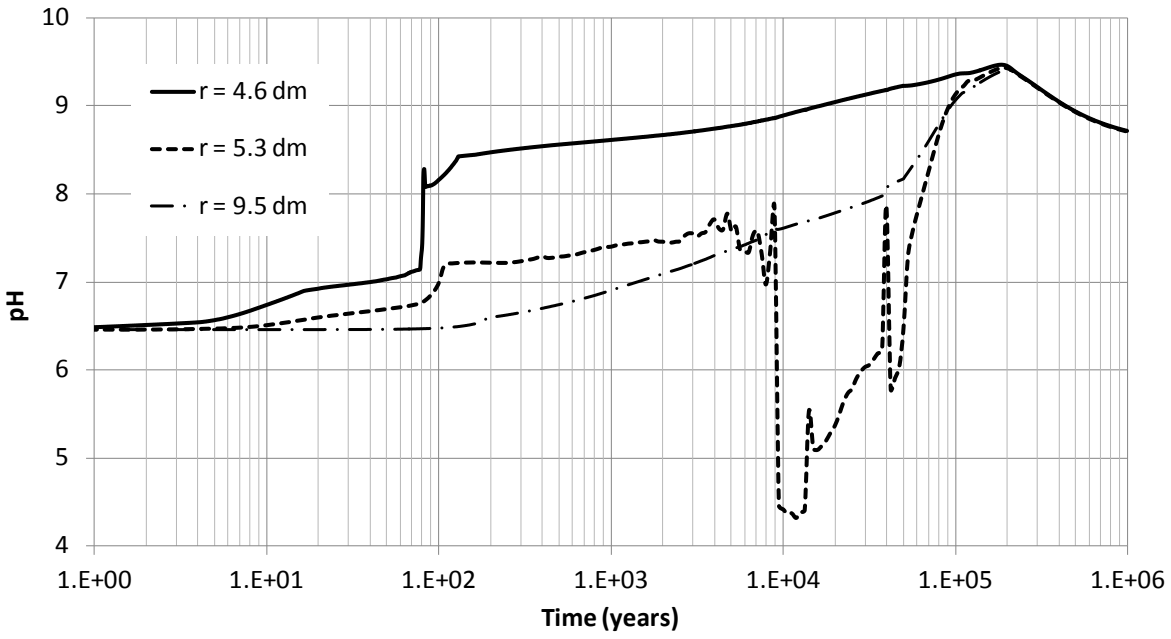

Figure 4.4. Time evolution of the computed pH in the bentonite at r = 4.6, 5.3 and 9.5 dm.

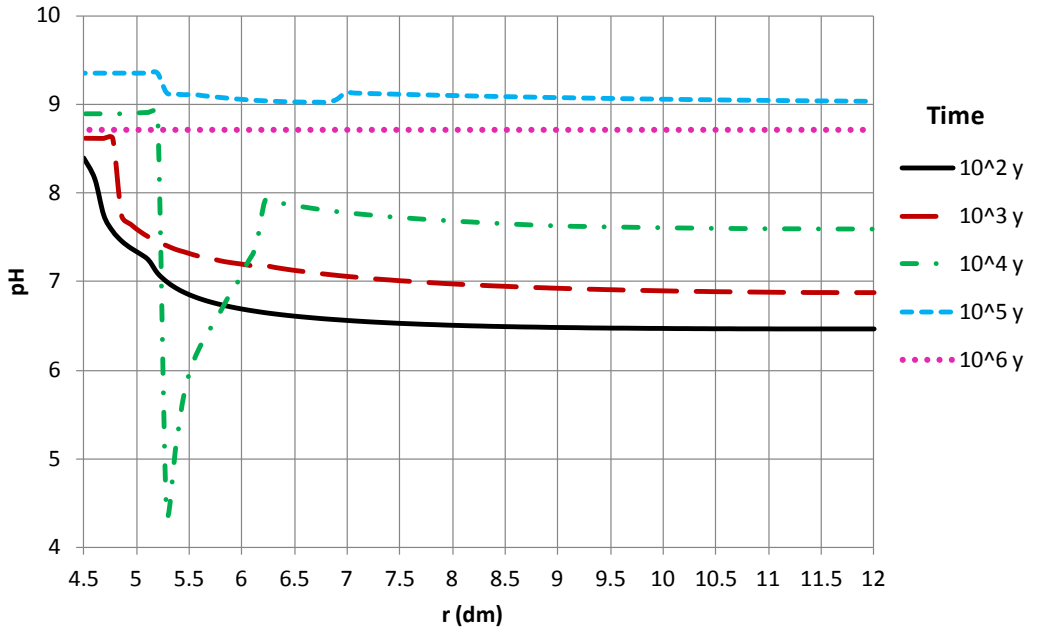

Figure 4.5. Radial distribution of computed pH in the bentonite at selected times covering the range from 10^2 to 10^6 years (r is the radial distance to the axis of the disposal cell).

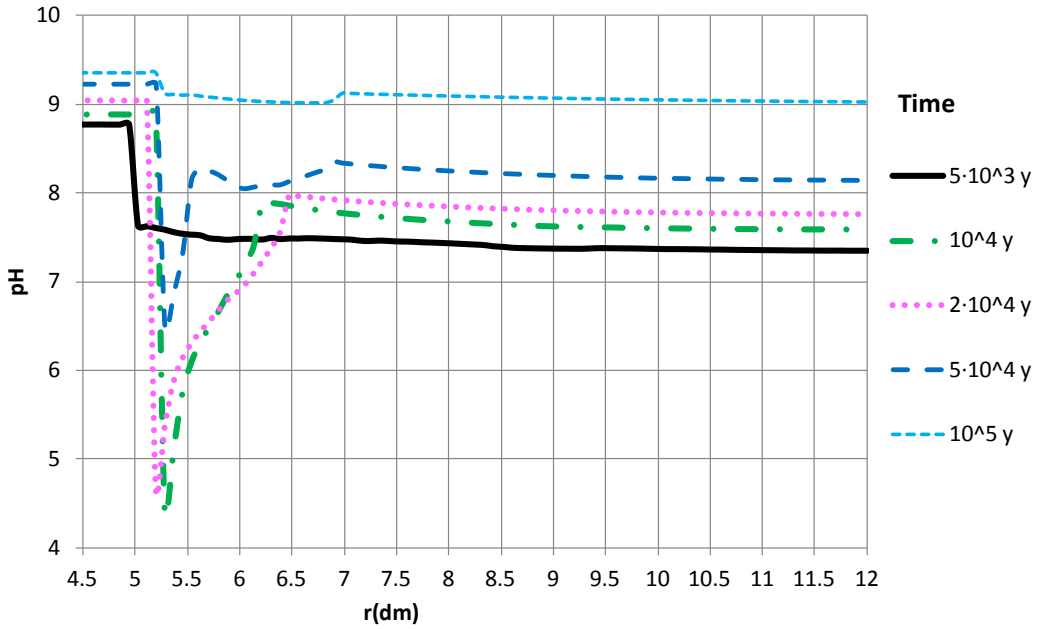

Figure 4.6. Radial distribution of computed pH in the bentonite at selected times covering the range from $5 \cdot 10^3$ to 10^5 years (r is the radial distance to the axis of the disposal cell).

Figure 4.7 shows the time evolution of the computed Eh in the bentonite at r = 4.6, 5.3 and 9.5 dm. At r = 4.6 dm, the Eh decreases sharply from -0.2 V to -0.5 V at 80 years. Later, it decreases smoothly until $5 \cdot 10^4$ years, when the canister is full corroded. Finally, Eh increases until -0.4 V. At r = 5.3 dm the sorption fronts induce an increase in Eh at 10.000 years which is related to the front of pH (see Figure 4.4).

The time evolution of the Eh after $2 \cdot 10^5$ years is the same at the three locations within the bentonite. Figure 4.8 shows the radial distribution of the computed Eh in the bentonite at several times. Eh shows a peak at r = 5.3 dm after 10.000 years. The time evolution of the Eh is directly related to that of pH and is affected by the sorption fronts.

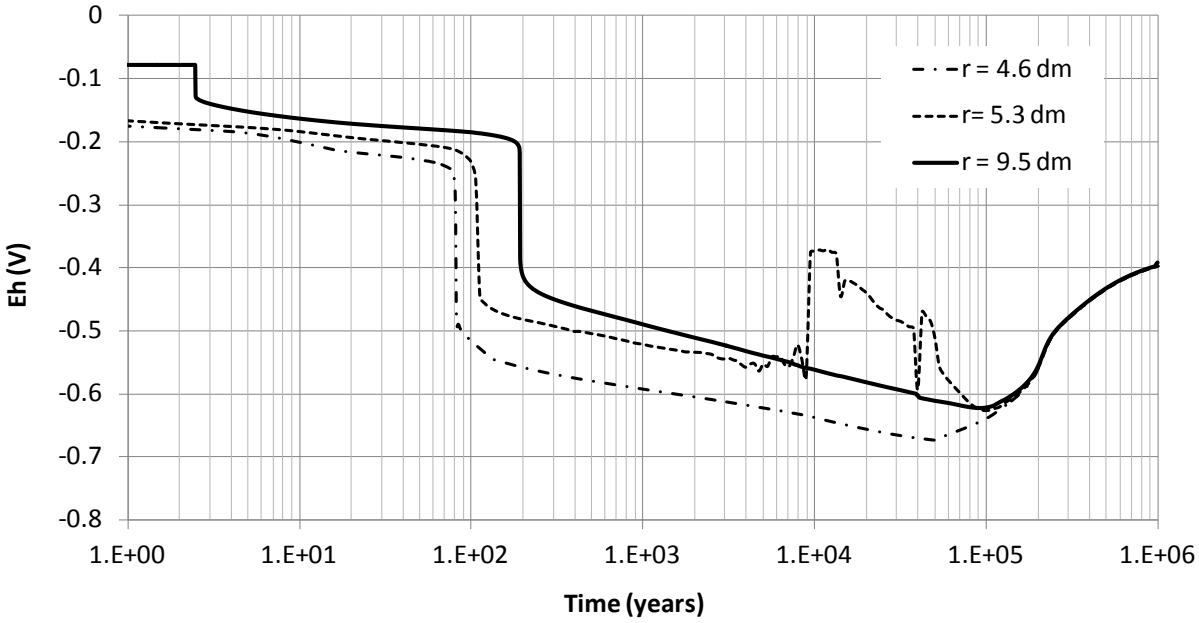

Figure 4.7. Time evolution of the computed Eh in the bentonite at r = 4.6, 5.3 and 9.5 dm.

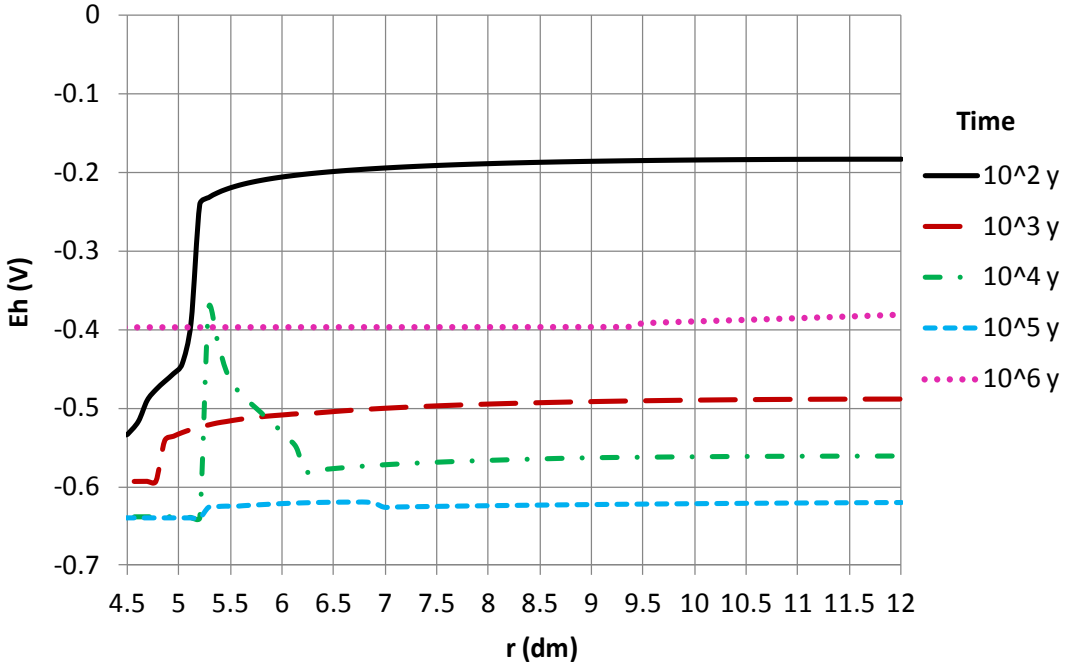

Figure 4.8. Radial distribution of the computed Eh in the bentonite at selected times (r is the radial distance to the axis of the disposal cell).

Figure 4.9 shows the time evolution of the computed concentration of dissolved Cl^- in the bentonite. The concentration of a conservative species such as Cl^- is the same everywhere in the bentonite. The decrease of the concentration is due to the out diffusion of Cl^-. The diffusive solute flux is larger than the advective flux in the granite and therefore the gradient of the concentrations in the bentonite is very small. For these conditions, it can be shown that the plot of the log concentration of Cl^- versus time is a straight-line (Figure 4.10) because the concentration, C, is given by

$$C-C_b=(C_0-C_b)\exp(-\alpha t) \qquad (3.14)$$

where C_0 is the initial concentration, C_b is the boundary concentration and α is a recession coefficient [T^{-1}] which for a water flow Q is equal to Q/V_w where V_w is the total volume of water in the bentonite and the canister (Samper et al., 2010; Ma, 2010).

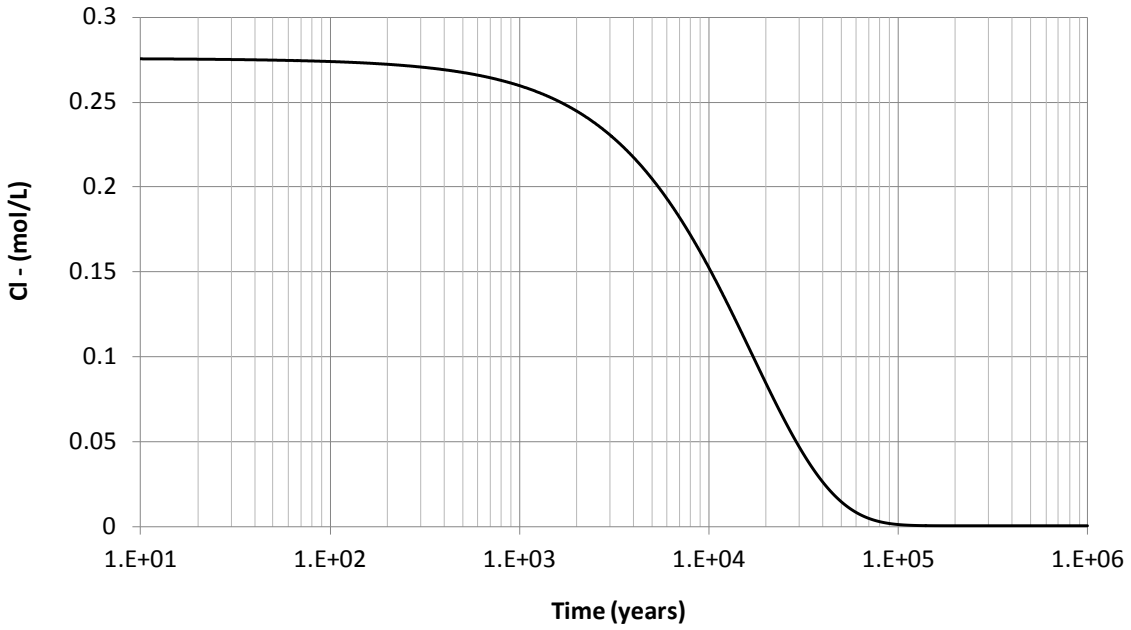

Figure 4.9. Time evolution of the computed concentration of Cl^- in the bentonite at r = 4.6, 5.3 and 9.5 dm.

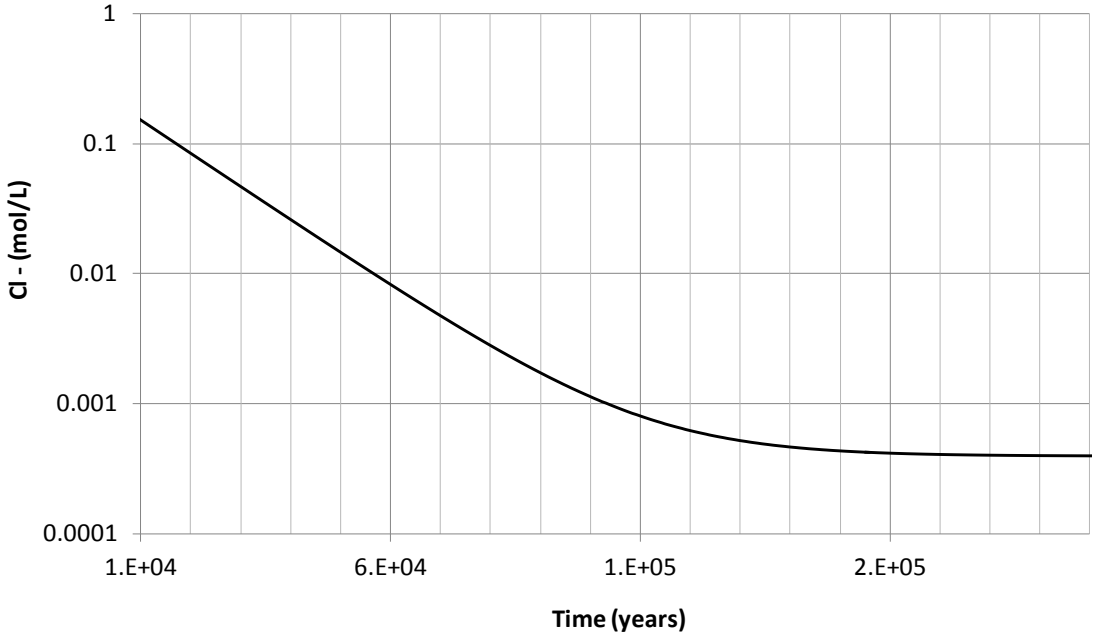

Figure 4.10. Time evolution of the computed concentration of Cl^- in the bentonite at r = 4.6, 5.3 and 9.5 dm. The log c-t plot at the bottom is a straight line for t < 110000 years, the time needed for Cl^- to diffuse out of the EBS.

The computed concentrations of the dissolved cations, Ca^{2+}, Mg^{2+}, Na^+ and K^+, show trends similar to those of Cl^-. In addition to diffusion, these species are subjected to mineral dissolution/precipitation and cation exchange reactions.

Figure 4.11 shows the time evolution of the computed concentration of dissolved Ca^{2+} in the bentonite at r = 4.6, 5.3 and 9.5 dm. There are small differences in the concentrations of Ca^{2+} in these points for t < 1000 years which are due to calcite precipitation near the canister/bentonite interface. This figure shows also the plot of the radial distribution of the concentration of dissolved Ca^{2+} at several selected times. One can see that the concentration of dissolved Ca^{2+} in the bentonite near the canister decreases due to calcite precipitation until t = 100 years. This creates a concentration gradient which induces the diffusion of dissolved Ca^{2+} towards this zone so that the concentration gradient dissipates after 3000 years. Later, the concentrations are the same everywhere throughout the bentonite.

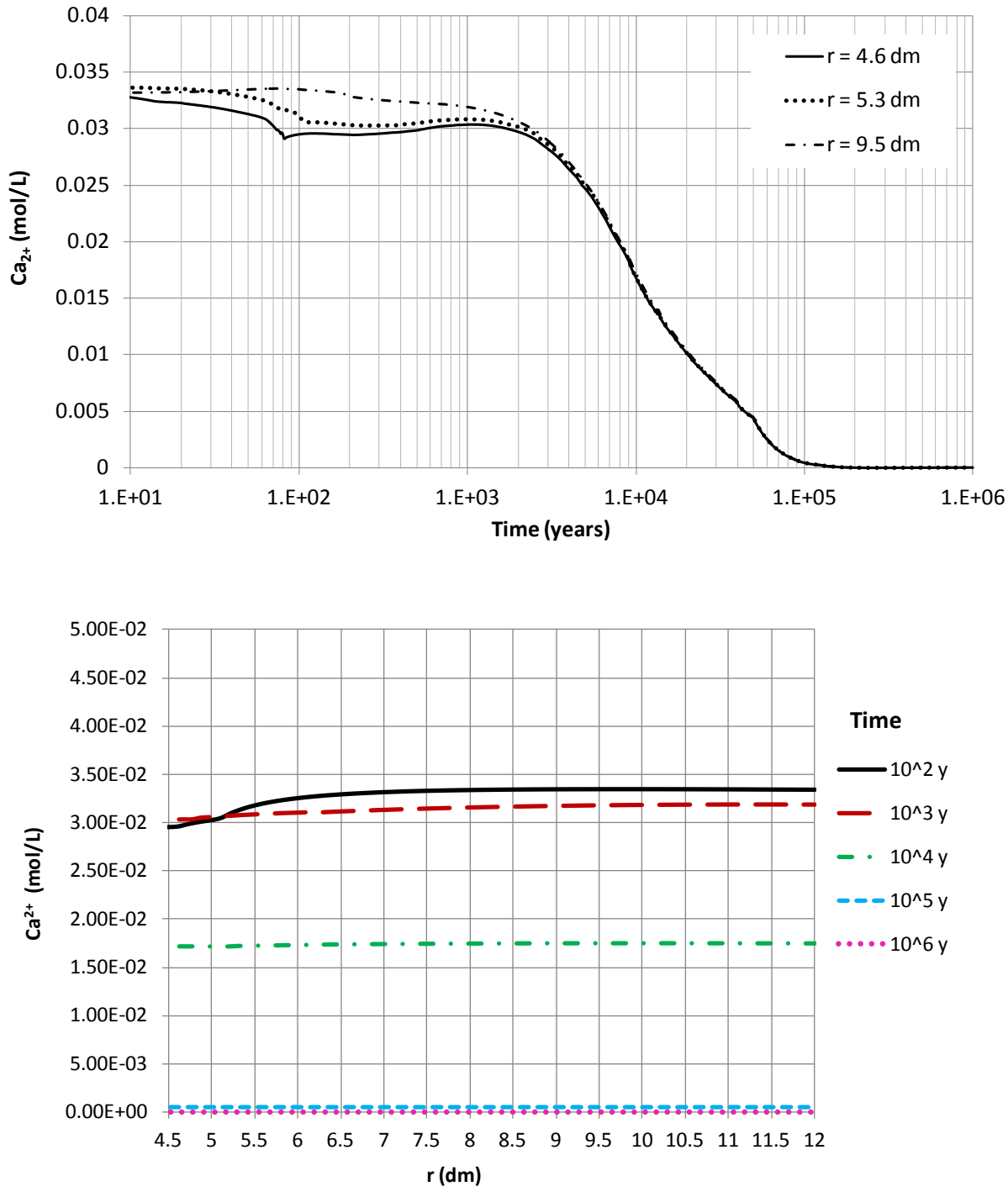

Figure 4.11. Time evolution of the computed concentration of dissolved Ca^{2+} in the bentonite at r = 4.6, 5.3 and 9.5 dm (top) and radial distribution of the concentrations at several times (bottom). r is the radial distance to the axis of the disposal cell.

Figure 4.12 shows the time evolution of the computed concentration of dissolved HCO_3^- in the bentonite at r = 4.6, 5.3 and 9.5 dm. This concentration decreases from its concentration of $7.6 \cdot 10^{-3}$ mol/L to the value at the granite boundary $5.05 \cdot 10^{-3}$ mol/L due to the solute diffusion. However, HCO_3^- is subjected to calcite and siderite dissolution/precipitation. The following stages can be established for the space-time patterns of the concentration of dissolved HCO_3^-:

1) For t < 80 years, the concentration of dissolved HCO_3^- near the canister decreases dramatically due to the rise in pH (Figure 4.4) which induces the precipitation of calcite and siderite. In fact, there is a clear coincidence in the sharp fronts of increasing pH at t = 80 years and the fronts of decreasing HCO_3^- .

2) For $80 < t < 2 \cdot 10^5$ years, the concentration of dissolved HCO_3^- keep decreasing due to calcite and siderite precipitation near the canister/bentonite interface. Then, a spatial gradient in the concentration of dissolved HCO_3^- is created which induces the diffusion HCO_3^- towards the canister (Figure 4.13).

3) For $t > 2 \cdot 10^5$ years, calcite and siderite dissolution has ceased (Figure 4.14 and Figure 4.16). The concentration of dissolved HCO_3^- is controlled by the in-diffusion of HCO_3^- from the granite porewater.

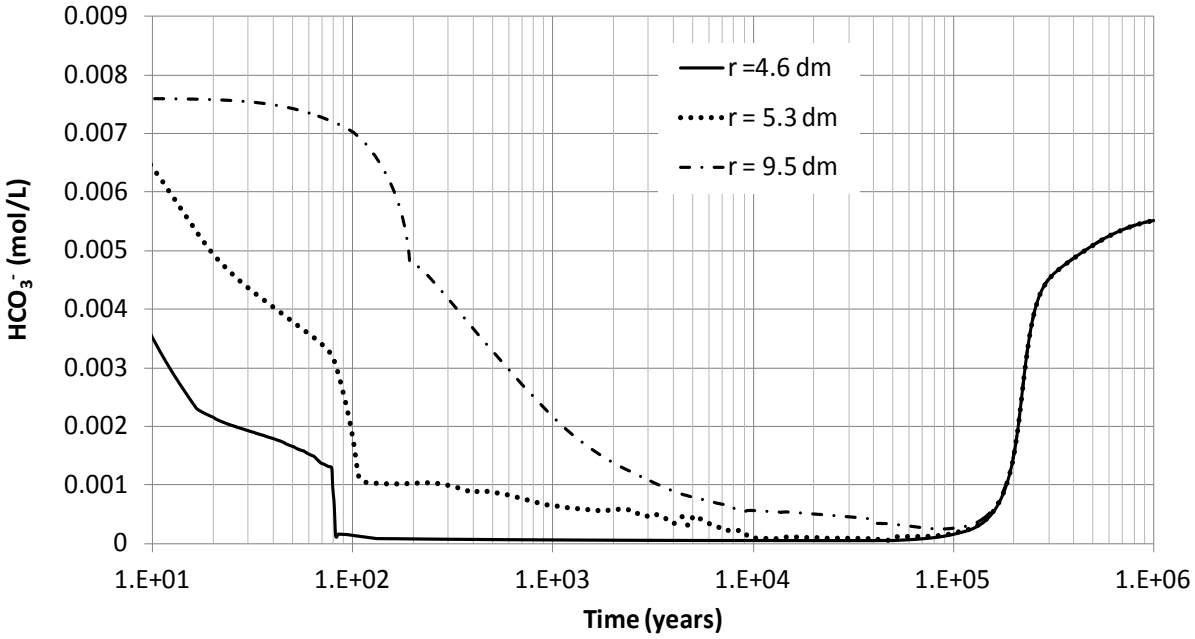

Figure 4.12. Time evolution of the concentration of dissolved HCO_3^- in the bentonite at r = 4.6, 5.3 and 9.5 dm.

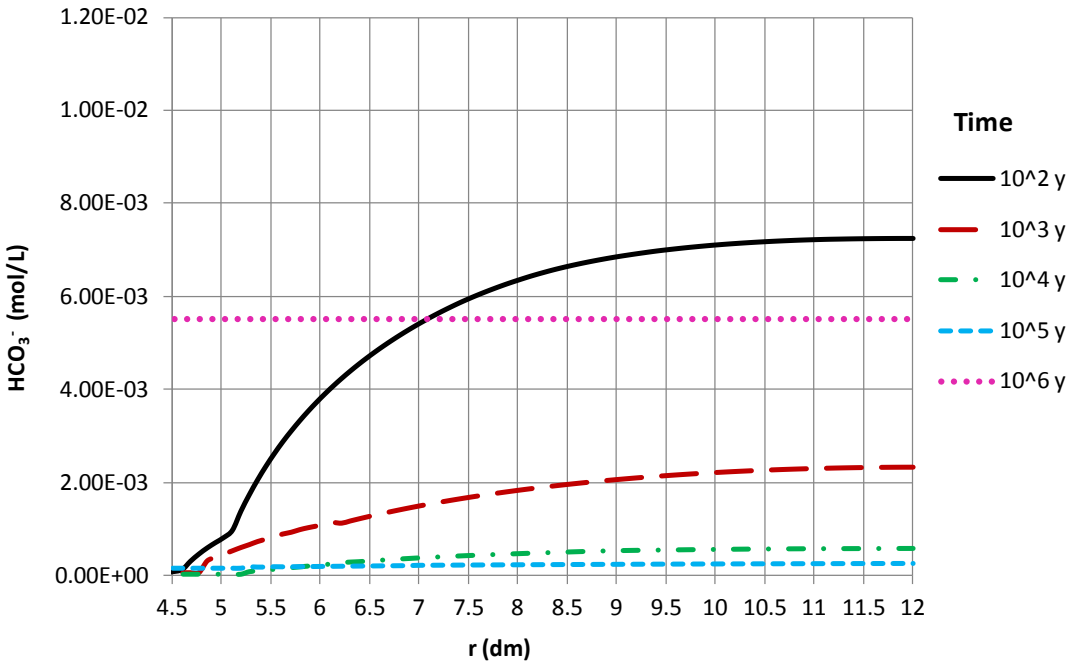

Figure 4.13. Radial distribution of dissolved HCO_3^- concentration at selected times (r is the radial distance to the axis of the disposal cell).

4.3. Mineral phases

The products of the canister corrosion, hydrogen, iron and hydroxyl anions will diffuse from the canister into the bentonite. Hydrogen does not undergo chemical reactions and is transported only by aqueous diffusion of $H_{2(aq)}$. OH^- and iron, on the other hand, may diffuse and react. Dissolved iron may precipitate as mineral phases, sorb by surface complexation and exchange with the exchanged complex.

Model results show that magnetite is the main corrosion product in the bentonite. Siderite precipitation is much smaller than magnetite precipitation due to the limited availability of dissolved carbonate. No goethite precipitation is simulated.

Figure 4.14 shows the time evolution of the concentration of cumulative precipitated magnetite in the bentonite at r = 4.6 dm. Magnetite starts to precipitate significantly after 1000 years close to the canister/bentonite interface (r = 4.5 dm). One can see that after $5 \cdot 10^4$ years, when the canister is fully corroded, magnetite precipitation stops. Figure 4.15 presents the radial distribution of the computed concentration of cumulative precipitated magnetite at several selected times. Magnetite precipitation increases with time and progresses as Fe^{+2} diffuses from the canister into the bentonite. The zone of bentonite affected by magnetite precipitation after 10^6 years has a thickness of approximately 6 cm.

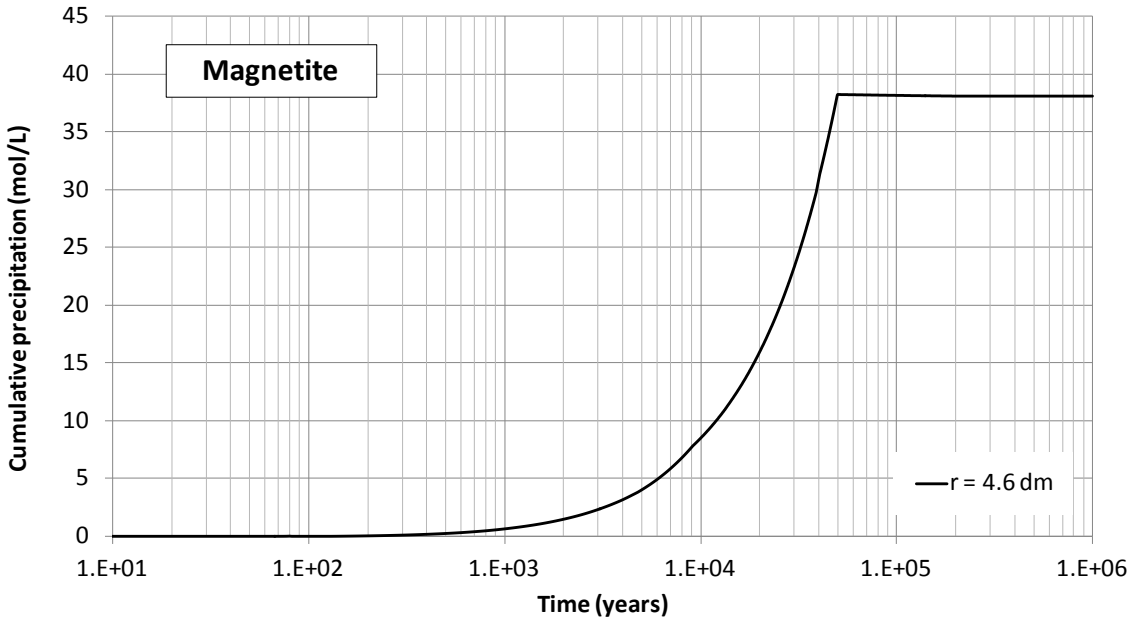

Figure 4.14. Time evolution of the concentration of cumulative precipitated magnetite at r = 4.6 dm.

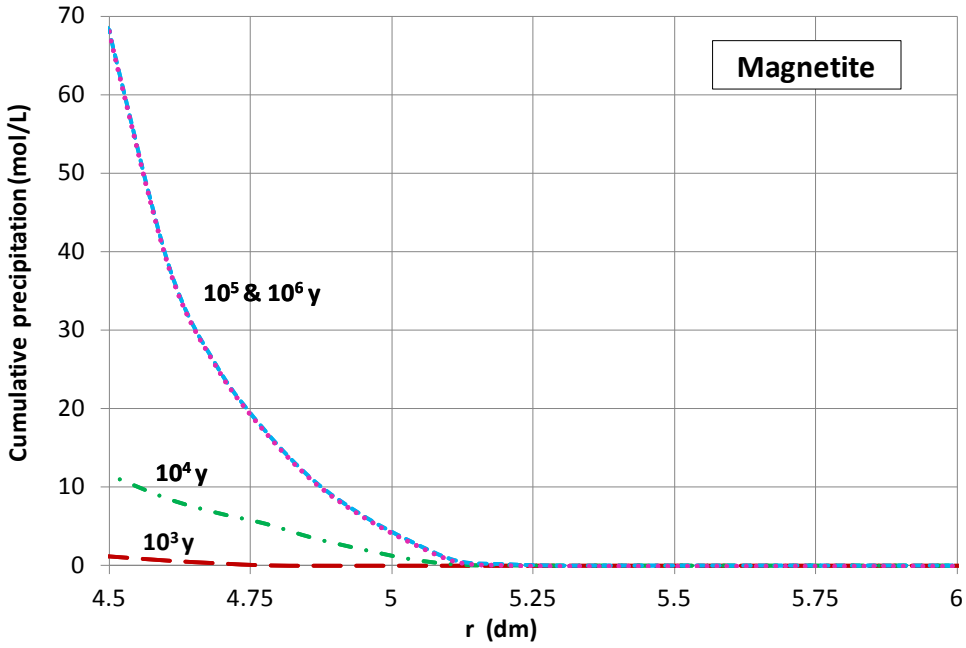

Figure 4.15. Radial distribution of the concentration of cumulative precipitated magnetite at several selected times. r is the radial distance to the axis of the disposal cell.

Figure 4.16 shows the time evolution of the computed concentration of cumulative precipitated siderite in the bentonite at several locations. Siderite starts precipitating near the canister/bentonite interface (r = 4.6 dm) after 100 years. Changes in the slope of the computed cumulative concentration are due to the competition of siderite and magnetite for the dissolved Fe^{2+} and siderite and calcite competition for dissolved bicarbonate. Siderite

precipitation increases when magnetite stops precipitating after t = $5 \cdot 10^4$ years. Siderite precipitation ceases after 200.000 years. At r = 9.5 dm siderite precipitation is negligible.

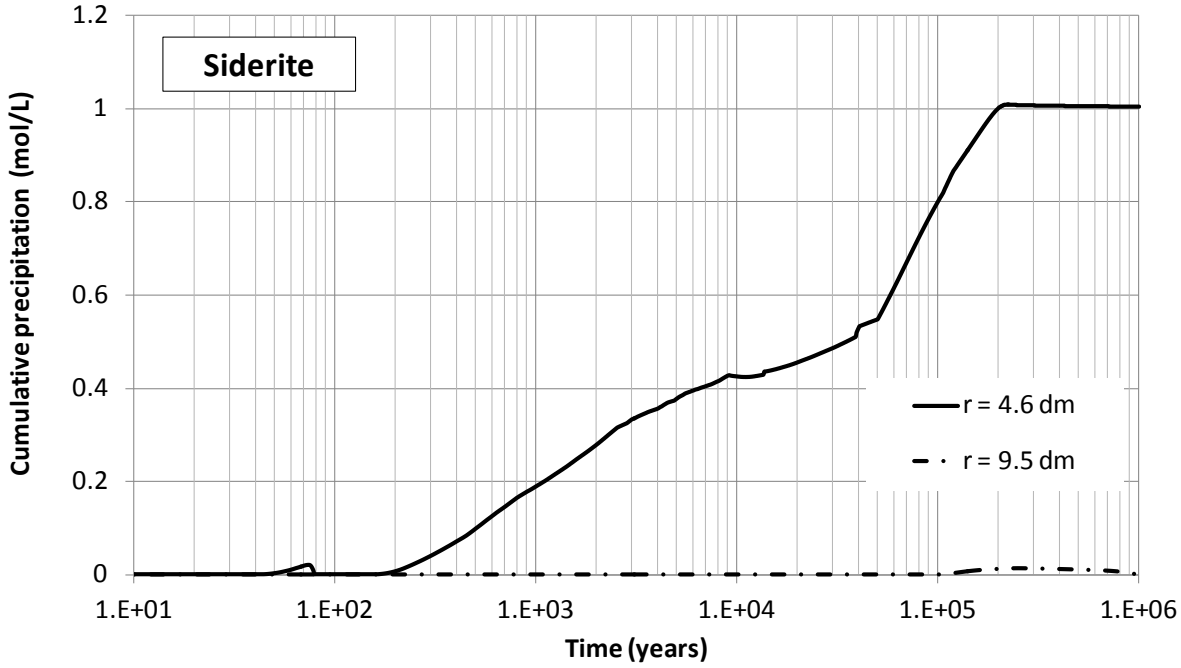

Figure 4.16. Time evolution of the concentration of cumulative precipitated siderite at r = 4.6 and 9.5 dm. r is the radial distance to the axis of the disposal cell.

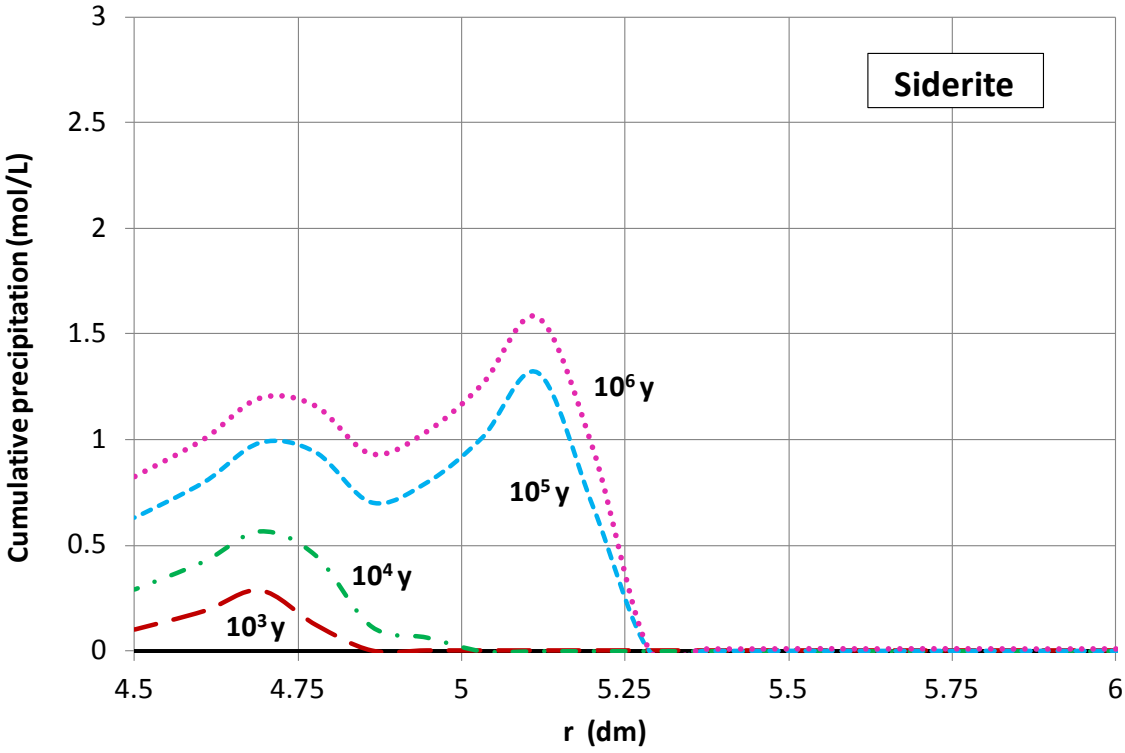

Figure 4.17. Radial distribution of the concentration of cumulative precipitated siderite at several selected times. r is the radial distance to the axis of the disposal cell.

Figure 4.17 shows the spatial distribution of the computed concentration of cumulative precipitated siderite in the bentonite at several selected times. The thickness of the siderite precipitation zone in the bentonite after 10^6 years is similar to that of magnetite precipitation (Figure 4.15). The concentration of precipitated siderite is much smaller than that of precipitated magnetite due to the limited availability of dissolved bicarbonate. While the concentration of siderite is about 1 mol/L after 10^5 years, the concentration of magnetite ranges from 5 to 70 mol/L (Figure 4.15).

The precipitation of the iron minerals contributes to a decrease in the concentration of dissolved Fe^{+2} and plays an important role on the pH evolution.

Figure 4.18 shows the time evolution of the computed concentration of precipitated calcite in the bentonite at r = 4.6, 5.3 and 9.5 dm. While calcite precipitates near the interface canister/bentonite (r = 4.6 dm), it dissolves at other locations (at r = 5.3 and 9.5 dm).

Figure 4.19 shows the radial distribution of the concentration of precipitated calcite at several times. Calcite precipitates near the interface canister/bentonite due to the rise in pH. The zone where calcite precipitates has a thickness of about 7 cm. Far from the interface, the concentrations of dissolved Ca^{2+} and HCO_3^- decrease due to solute diffusion from the bentonite into the granite. Such a decrease leads to the dissolution of calcite

The dissolution/precipitation of quartz and gypsum are not significant.

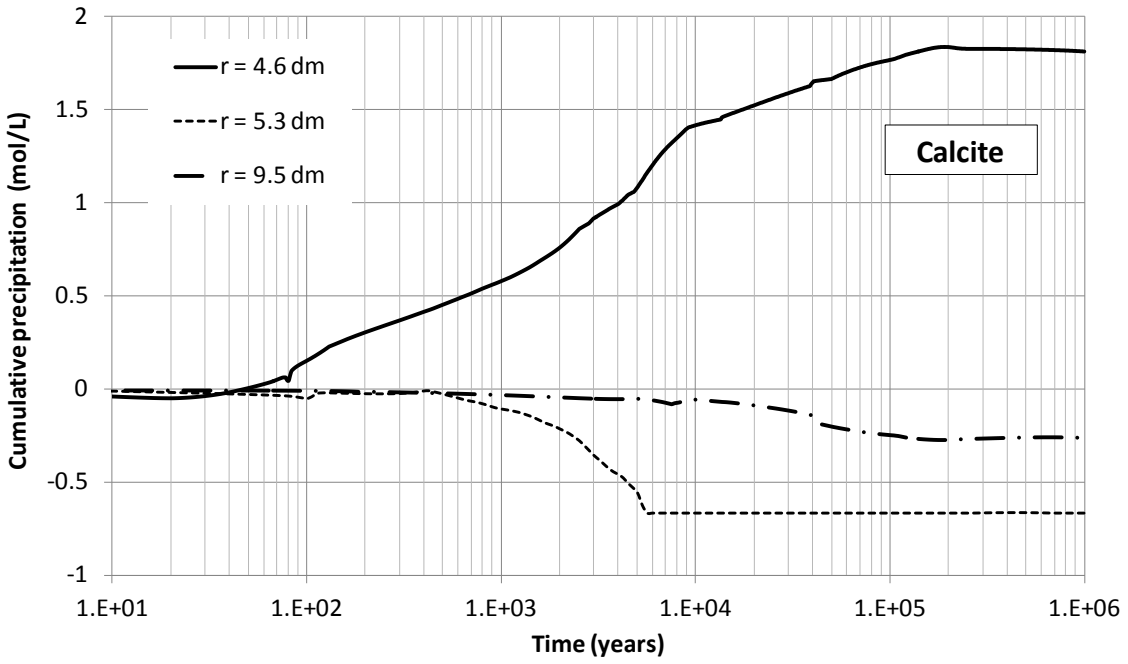

Figure 4.18. Time evolution of the concentration of cumulative precipitated calcite at r = 4.6, 5.3 and 9.5 dm. r is the radial distance to the axis of the disposal cell.

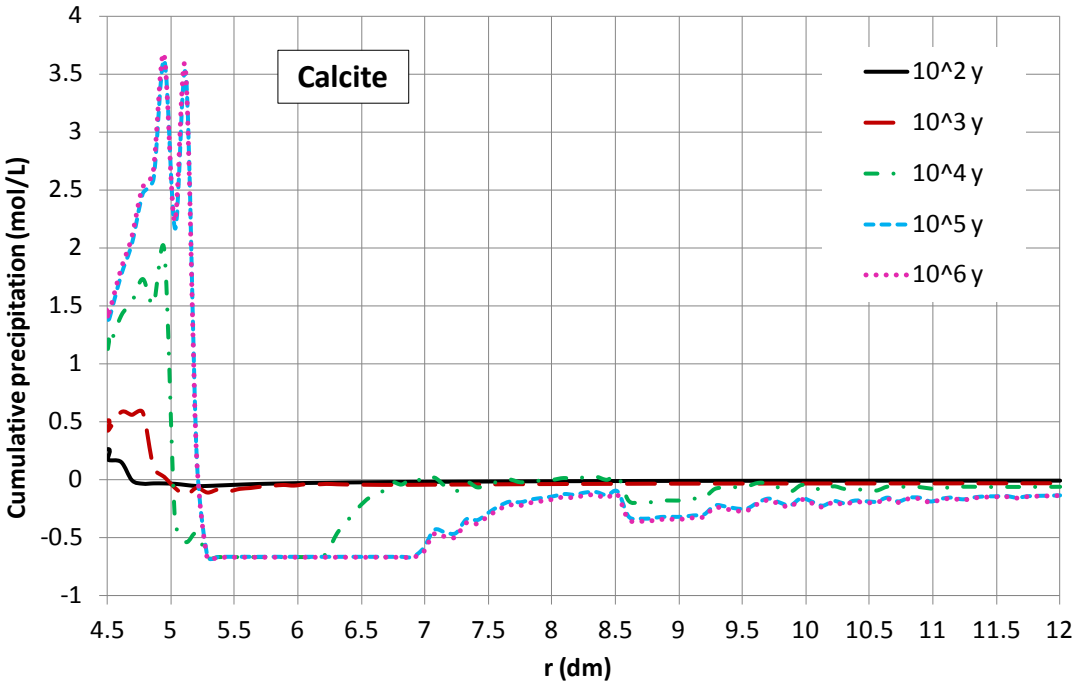

Figure 4.19. Spatial distribution of the concentration of cumulative precipitated calcite at selected times. r is the radial distance to the axis of the disposal cell.

4.4. Cation exchange

Figure 4.20 and Figure 4.21 show the time evolution of the computed concentrations of the exchanged cations in the bentonite at r = 4.6 and 9.5 dm, respectively. At r = 4.6 dm the concentration of exchanged Ca^{2+} decreases slightly from 20 to 80 years in response to the decrease in the concentration of dissolved Ca^{2+} caused by calcite precipitation. The exchanged Ca^{2+} is replaced by the dissolved Mg^{2+}. From 80 to 10.000 years the cation exchange reverses and the exchanged Mg^{2+} is replaced by the dissolved Ca^{2+}. After 10.000 years, the ratio of the concentrations of Ca^{2+} and Na^{+} increases due to calcite dissolution and therefore, the dissolved Ca^{2+} replaces the exchanged Na^{+}.

Far from the canister interface (r = 9.5 dm) the computed concentrations of the exchanged cations remain constant until t = 3.000 years. Later, the trend is similar to that computed at r = 4.6 dm, that is, the dissolved Ca^{2+} replaces the exchanged Na^{+}.

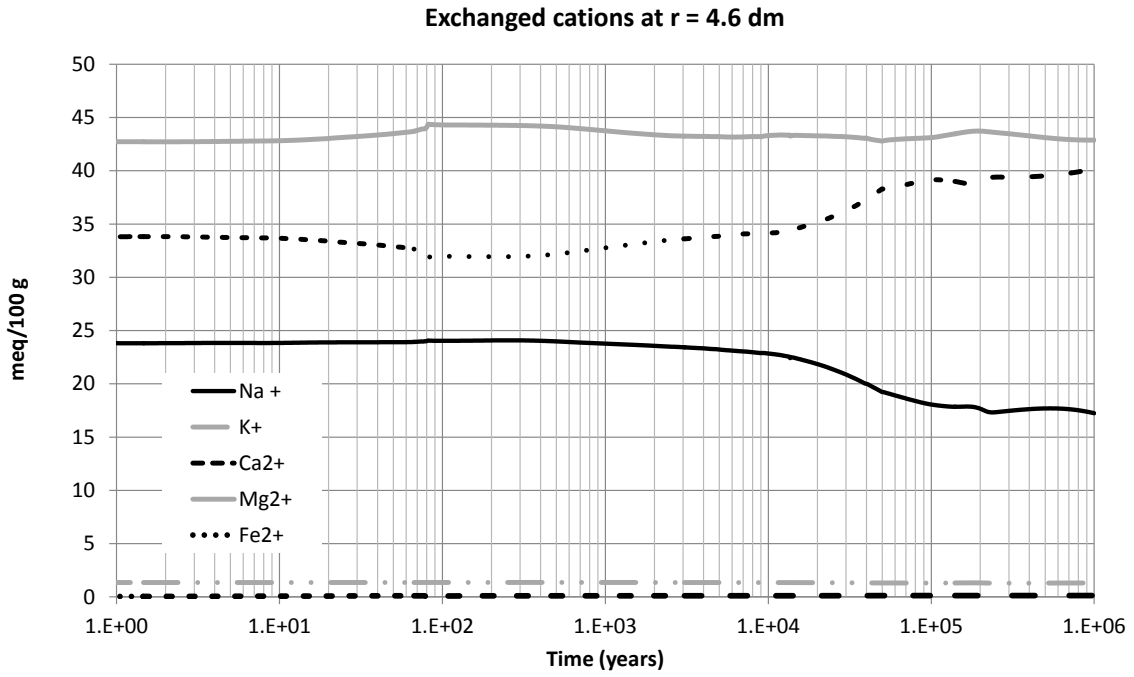

Figure 4.20. Time evolution of the computed concentrations of the exchanged cations in the bentonite at r = 4.6 dm.

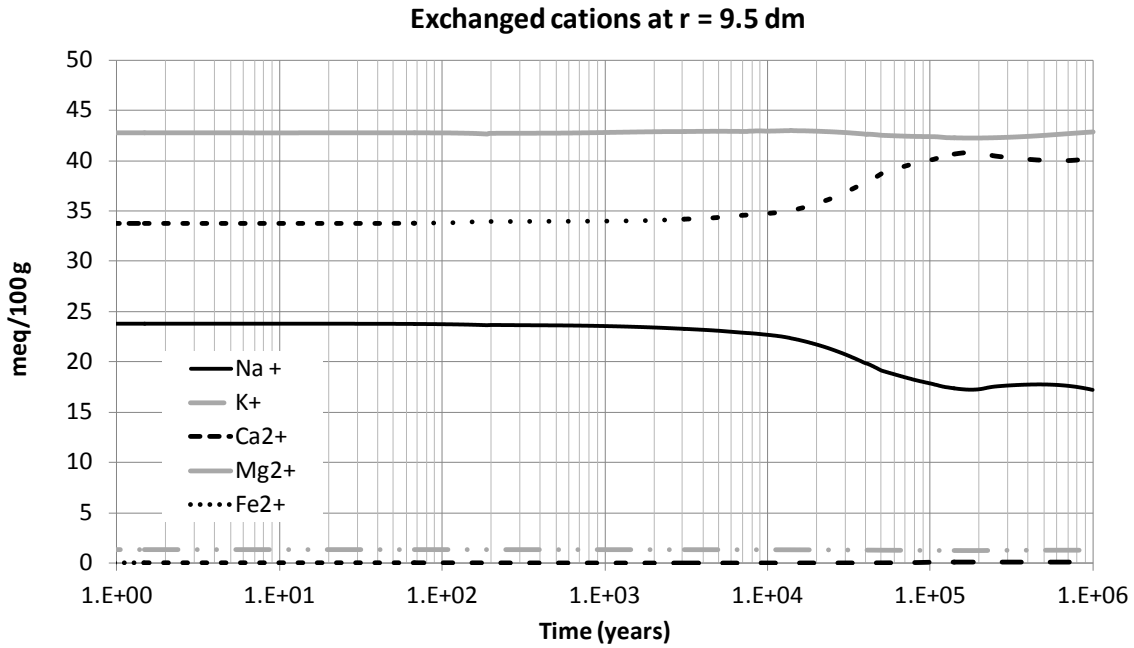

Figure 4.21. Time evolution of the the computed concentrations of the exchanged cations in the bentonite at r = 9.5 dm.

Figure 4.22 shows the time evolution of the computed concentration of exchanged Fe^{2+} in the bentonite near the interface (r = 4.6 dm) and near the centre of the bentonite buffer (r = 9.5 dm). The concentration of the exchanged Fe^{2+} follows a trend similar to that of the sorbed (see Figure 4.24, Figure 4.25 and Figure 4.27) and dissolved Fe^{2+} (see Figure 4.2 and Figure 4.3). Figure 4.23 shows the spatial distribution of the computed concentration of exchanged

Fe^{2+} at several selected times. The concentration of exchanged Fe^{2+} increases from its initial value of 0.04 meq/100 g to about 0.12 meq/100 g at the end of the simulation.

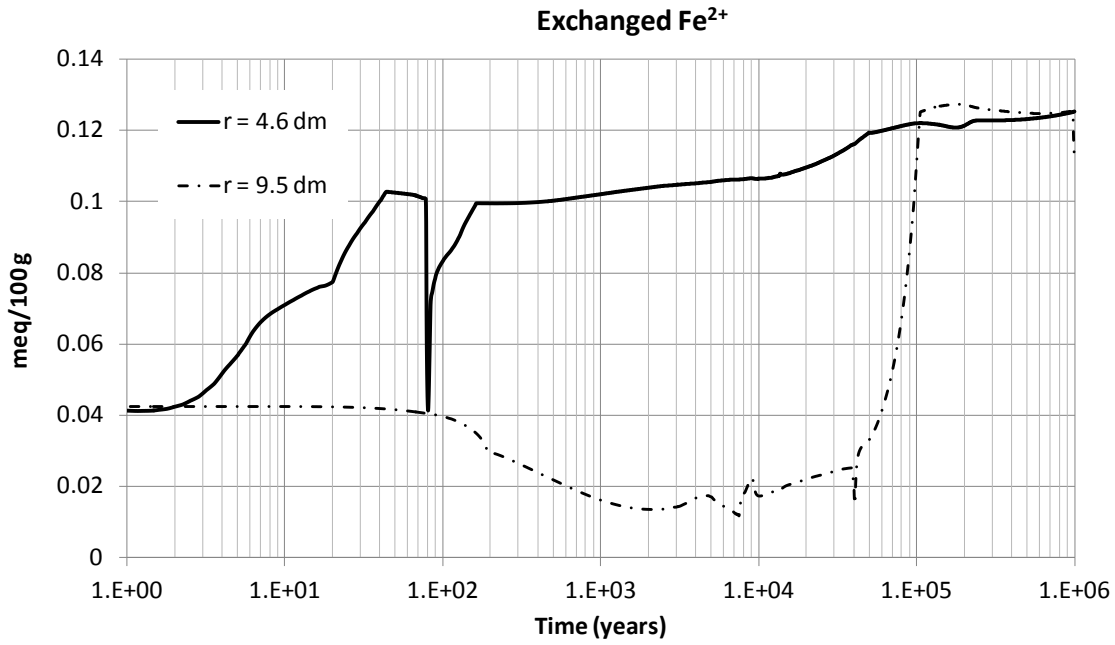

Figure 4.22. Time evolution of the computed concentration of exchanged iron in the bentonite at r = 4.6 and 9.5 dm. r is the radial distance to the axis of the disposal cell.

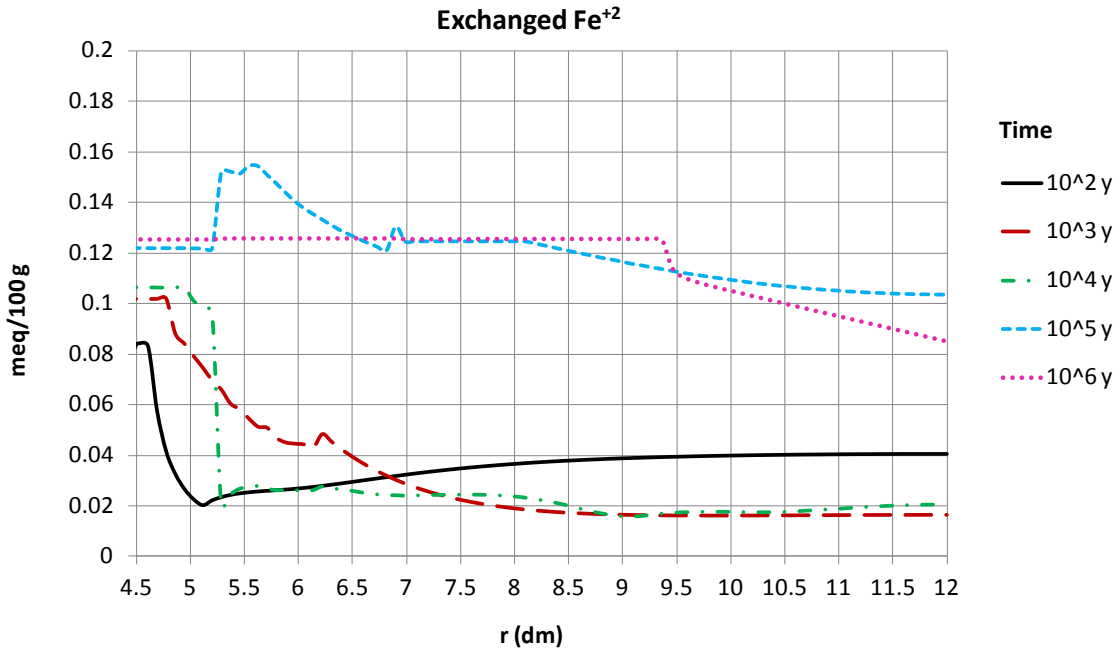

Figure 4.23. Spatial distribution of the computed concentration of exchanged iron the bentonite at several times. r is the radial distance to the axis of the disposal cell.

4.5. Sorbed species

Model results show that the competition of Fe^{2+} and H^{+} for sorption sites plays a very important role in the geochemical evolution of the bentonite.

Figure 4.24 presents the time evolution of computed concentration of sorbed species in the bentonite at r = 4.6 dm. The competition between the dissolved Fe^{2+} and H^{+} for the weak 1 sorption sites produces two sorption fronts. The first one occurs at t = 80 years when the concentration of $S^{W1}OH$ decreases while that of $S^{W1}OFe^{+}$ increases according to Eq. (3.13). The concentration of the surface complex $S^{W1}O^{-}$ of weak 1 sorption sites increases after 3000 years producing a decrease in the concentration of $S^{W1}OFe^{+}$. There is no competition between Fe^{2+} and H^{+} for the weak 2 sorption sites because the model does not consider Fe^{2+} sorption on such sites. This is the main reason why the concentration of $S^{W2}OH$ is the largest during most of the simulated time. The sorption front at t = 80 years is shown also as an increase in the concentration of $S^{W2}OH$ and a decrease of $S^{W2}OH^{2+}$. The concentration of the strong sites is much smaller than those of the complexes attached to the weak sites.

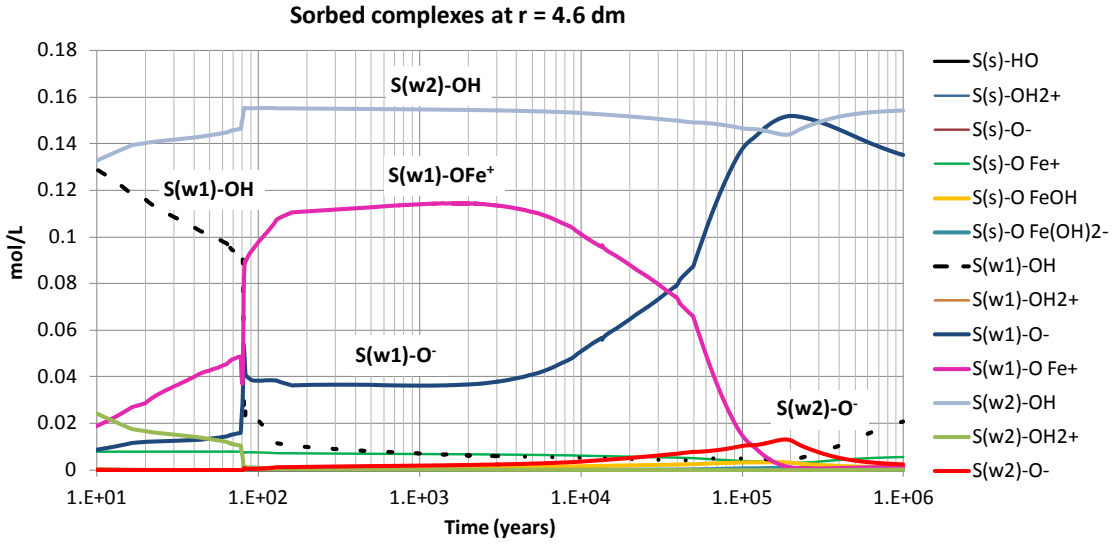

Figure 4.24. Time evolution of the computed concentrations of the sorbed in the bentonite at r = 4.6 dm.

Figure 4.25 and Figure 4.26 show the time evolution of the computed concentrations of the sorbed species in the bentonite at r = 5.3 dm. The patterns of the sorbed complexes at this location are similar to those calculated at r = 4.6 dm for $t < 10^4$ years The concentration of $S^{W1}OH$ decreases while that of $S^{W1}OFe^{+}$ increases and, at the same time, the concentration of $S^{W2}OH$ increases while that of $S^{W2}OH2^{+}$ decreases. It should be mentioned that the increase in the concentration of $S^{W1}OFe^{+}$ at r = 5.3 dm is smaller than that at r = 4.6 dm. Sorbed

species show a number of complex fronts for $10^4 < t < 7 \cdot 10^4$ years. The computed concentrations of most of the sorbed species show numerous fluctuations for which there is no clear explanation. After 10^5 years the behaviour of the sorbed complexes is similar to that computed at r = 4.6 dm.

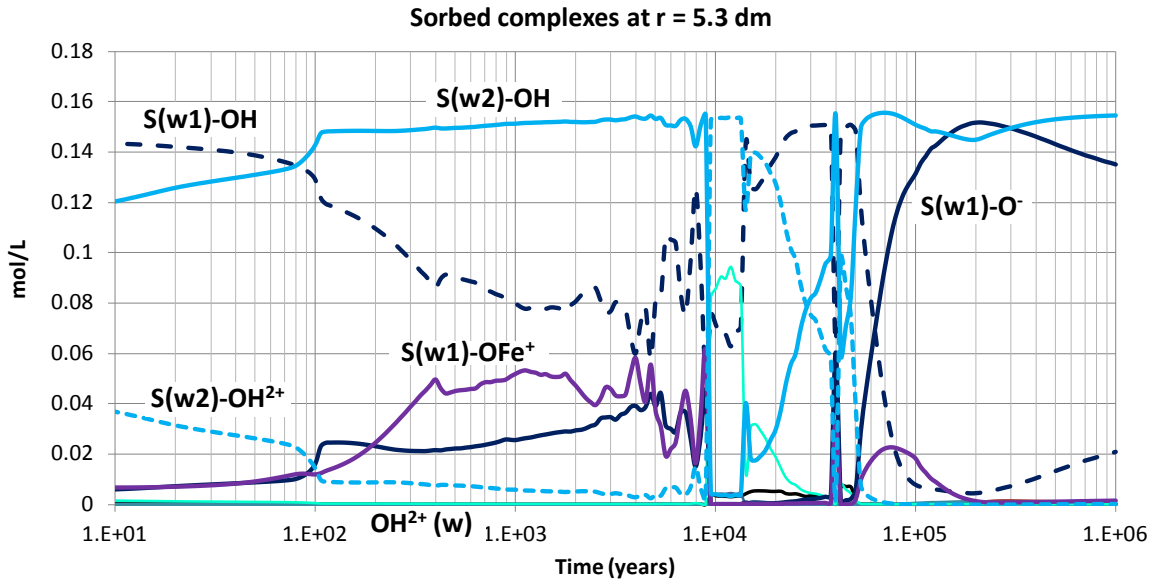

Figure 4.25. Time evolution of the computed concentrations of the sorbed species in the bentonite at r = 5.3 dm.

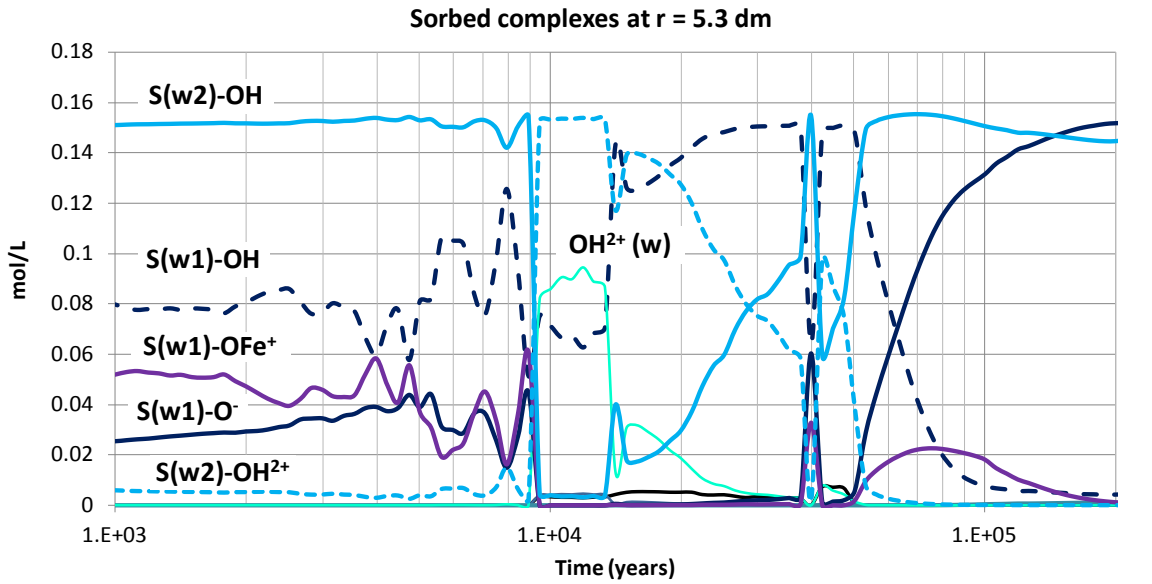

Figure 4.26. Time evolution of the computed concentrations of the sorbed species in the bentonite at r = 5.3 dm (zoom between 10^3 and 10^5 years).

Figure 4.27 and Figure 4.28 show the time evolution of the computed concentrations of the sorbed species in the bentonite at r = 9.5 and 11.9 dm, respectively. These figures show that there is no competition of Fe^{2+} and H^{+} for the sorption sites at these locations. The main changes in sorbed species involve the desorption of protons from hydroxyl groups $S^{W1}OH$ so that the concentration of $S^{W1}OH$ decreases and that of $S^{W1}O^{-}$ increases.

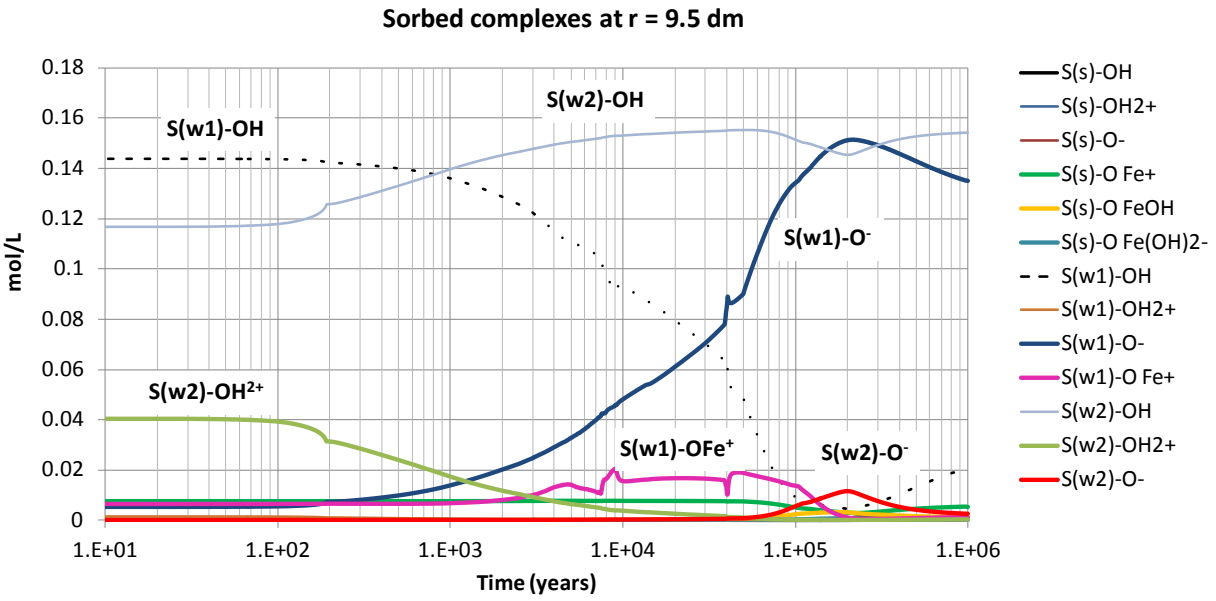

Figure 4.27. Time evolution of the computed concentrations of the sorbed species in the bentonite at r = 9.5 dm.

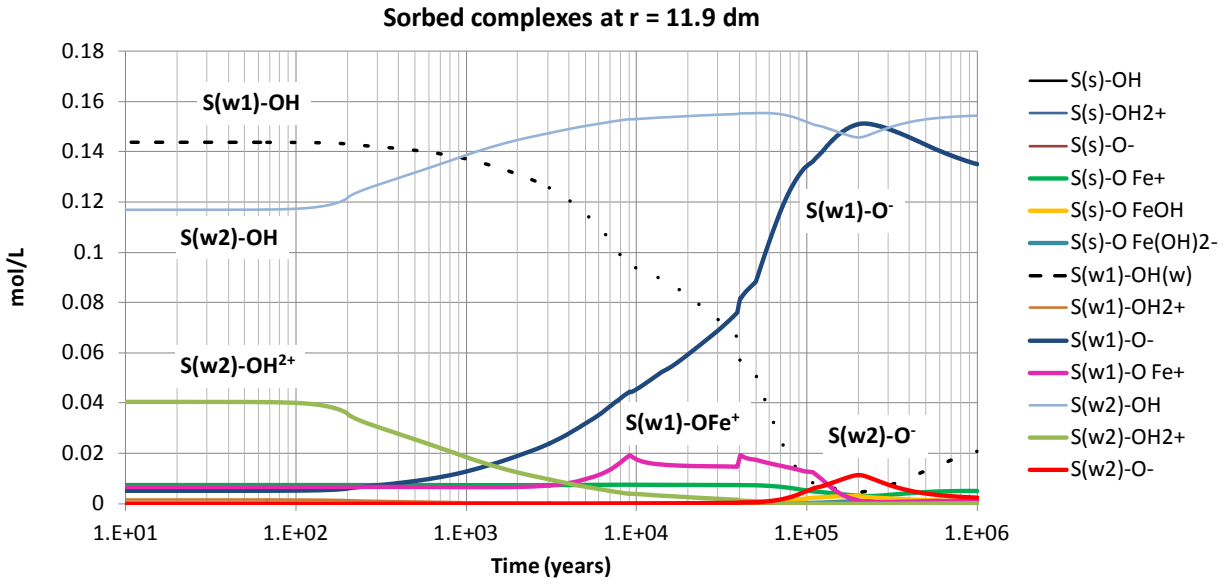

Figure 4.28. Time evolution of the computed concentrations of the sorbed species in the bentonite at r = 11.9 dm.

Figure 4.29 to Figure 4.34 shows the spatial distribution of the concentration of sorbed species in the bentonite at several times. These figures are useful to understand the time evolution of the sorbed species in the bentonite buffer. At t = 100 years (Figure 4.29) the dominant sorbed species in weak 1 sites near the canister interface (r < 4.75 dm) is $S^{W1}OFe^{+}$ as a result of the first sorption (see Figure 4.24 to Figure 4.28). The concentration of $S^{W1}OFe^{+}$ decreases for r > 4.75 dm while that of $S^{W1}OH$ increases. The dominant weak 2 sorbed species is always $S^{W2}OH$.

The computed concentrations of sorbed species at t = 10^3 years (Figure 4.30) show similar trends as those of t = 10^2 years.

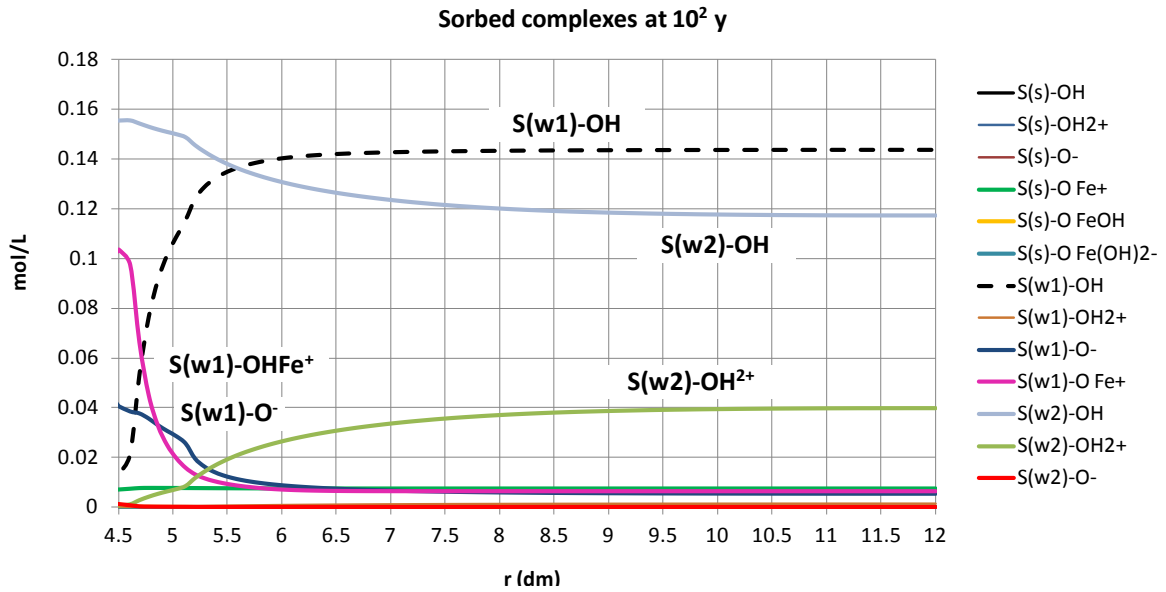

Figure 4.29. Spatial distribution of the computed concentrations of the sorbed species in the bentonite at 10^2 years. r is the radial distance to the axis of the disposal cell.

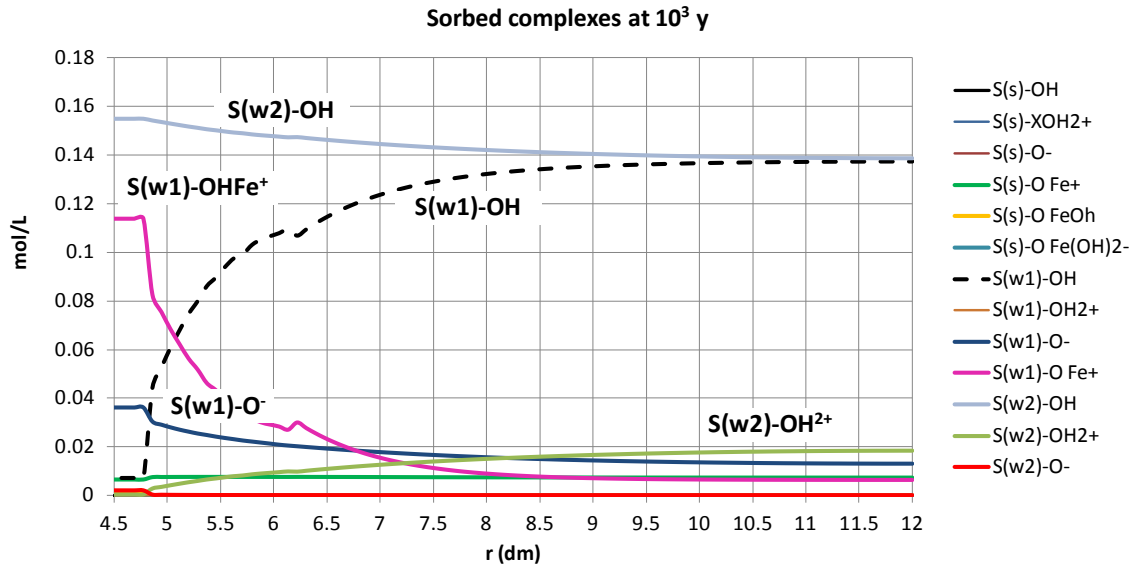

Figure 4.30. Spatial distribution of the computed concentrations of the sorbed species in the bentonite at 10^3 years. r is the radial distance to the axis of the disposal cell.

At t = 10^4 and t = $5 \cdot 10^4$ years (Figure 4.31 and Figure 4.32), the concentration curves show a front at r = 5.3 dm. The concentrations of $S^{W2}OH$, $S^{W1}OFe^+$ and $S^{W1}O^-$ decrease sharply and immediately increase again. At the same time, the concentrations of $S^{W1}OH$ and $S^{W2}OH^{2+}$ show an opposite trend. These fronts are caused by the competition of Fe^{2+} and H^+ for the weak 1 sites. For t = $5 \cdot 10^4$ years, the dominant sorbing species on weak1sorption sites for r > 5.3 dm is $S^{W1}O^-$

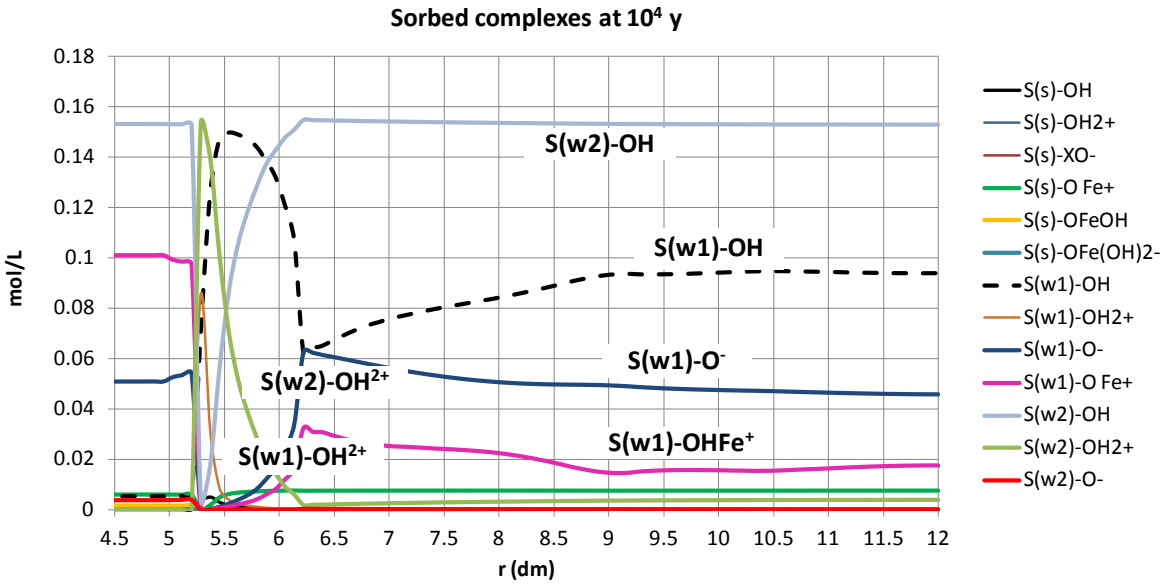

Figure 4.31. Spatial distribution of the computed concentrations of the sorbed species in the bentonite at 10^4 years. r is the radial distance to the axis of the disposal cell.

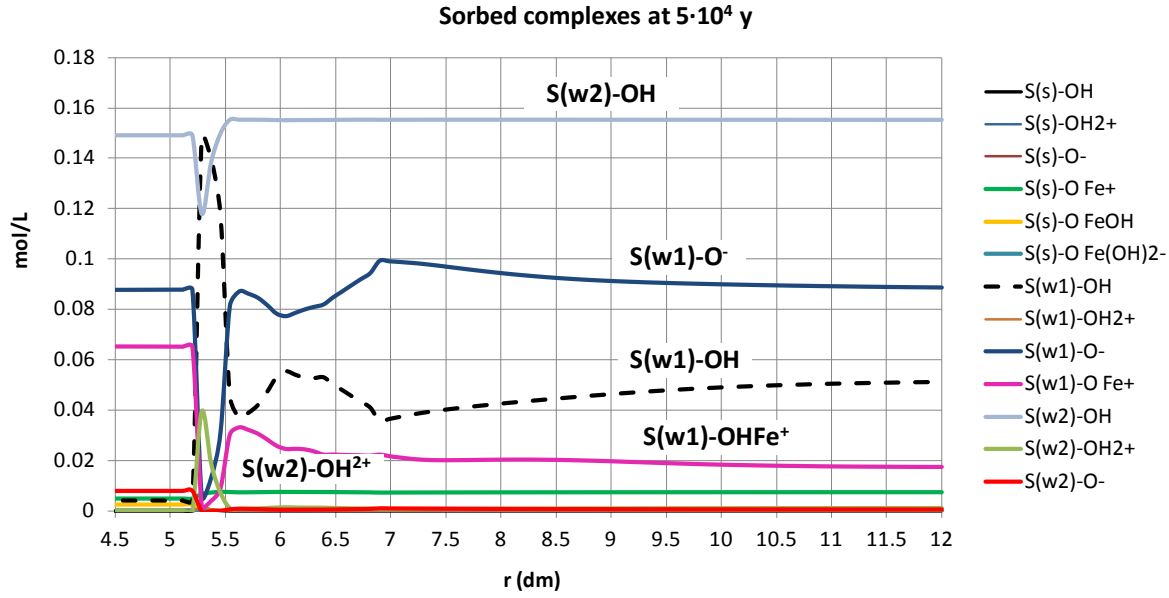

Figure 4.32. Spatial distribution of the computed concentrations of the sorbed species in the bentonite at $5 \cdot 10^4$ years. r is the radial distance to the axis of the disposal cell.

At 10^5 and 10^6 years (Figure 4.33 and Figure 4.34) sorption is controlled by $S^{W2}OH$ and $S^{w1}O^-$ sorbed complexes. At 10^5 years there is very little Fe sorption but at 10^6 years Fe sorption disappears completely.

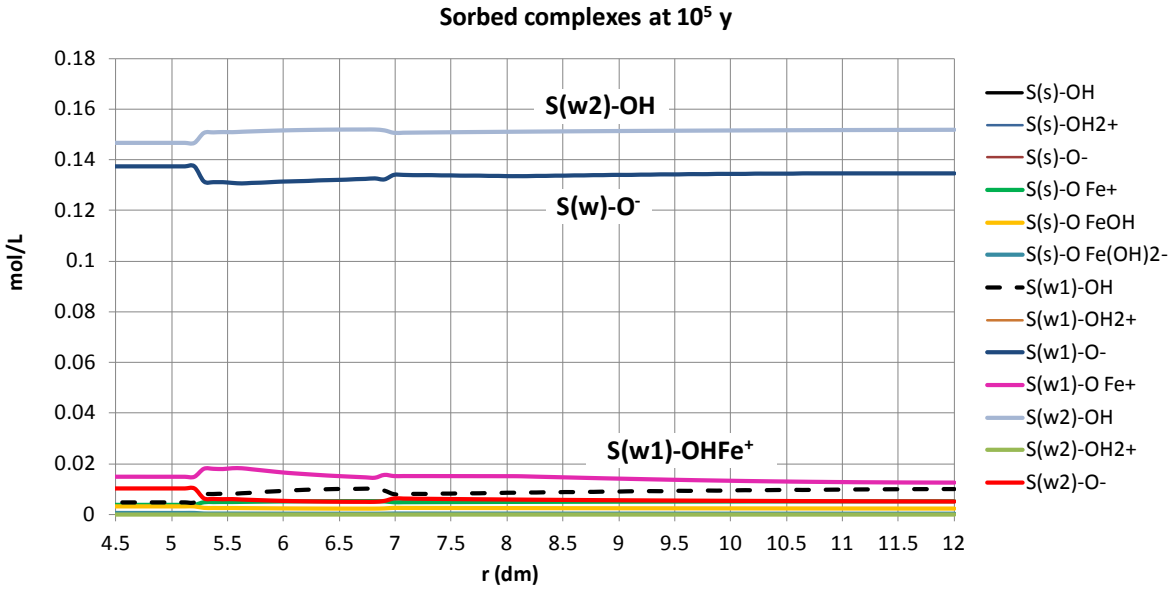

Figure 4.33. Spatial distribution of the computed concentrations of the sorbed species in the bentonite at10^5 years. r is the radial distance to the axis of the disposal cell.

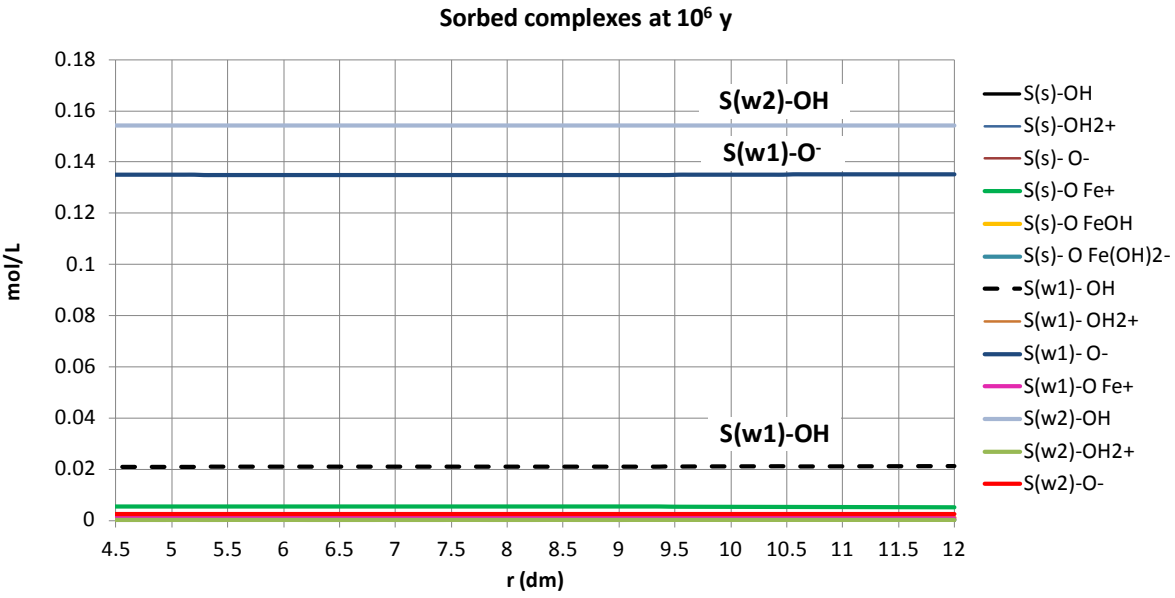

Figure 4.34. Spatial distribution of the computed concentrations of the sorbed species in the bentonite at 10^6 years. r is the radial distance to the axis of the disposal cell.

4.6. Hydrogen pressure

Figure 4.35 shows the time evolution of the computed $H_2(g)$ partial pressure in the bentonite. There are not significant differences between hydrogen partial pressures along the bentonite. $H_2(g)$ pressure keeps increasing and reaches its peak after $5 \cdot 10^4$ years. Later, it decreases once the canister is fully corroded (compare Figure 4.1 and Figure 4.35). The maximum pressure is 16200 atm for a corrosion rate of 2 μ/y. These results account for the diffusion of the dissolved hydrogen but disregards gas migration in the bentonite and the mechanical effects of high gas pressures which could be relieved by temporary cracks in the bentonite.

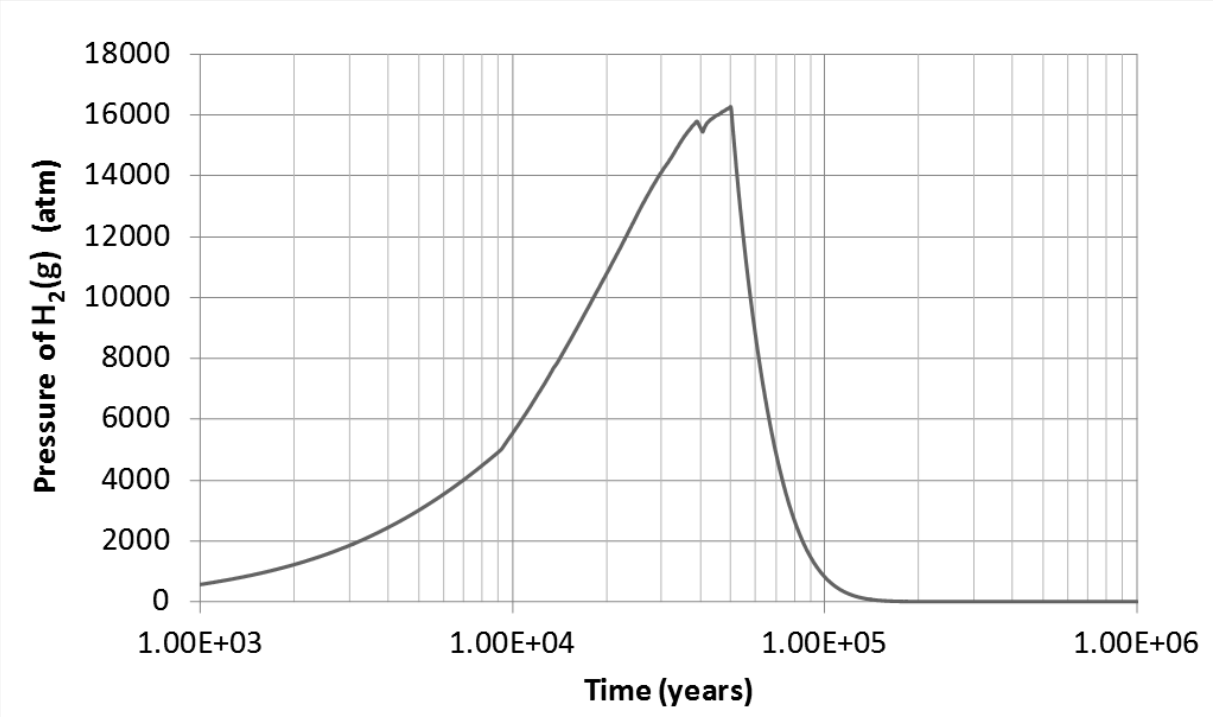

Figure 4.35. Time evolution of hydrogen partial pressure in the bentonite.

4.7. Changes in porosity

Samper et al. (2008a) showed that changes in the bentonite porosity caused by mineral dissolution/precipitation are smaller than 10% for a corrosion rate of 0.2 μm/y and after 0.3 Ma. Based on that, our model disregards porosity changes and its effects in the solute transport and geochemical processes. Our simulation accounts for a corrosion rate 10 times larger than that of Samper et al. (2008a; 2011) and therefore, porosity changes could be more significant.

The changes in bentonite porosity caused by chemical reactions have been calculated from the simulated results with a constant porosity (0.407) by adding and subtracting the

volume of the amount of dissolved and precipitated minerals. Figure 4.36 and Figure 4.37 show the time evolution and the spatial distribution of the changes in bentonite porosities at several locations and times. For a corrosion rate of 2 μm/y, the porosity at the canister/bentonite interface is half its initial value after 10.000 years. The precipitation of the corrosion products close to the canister leads to a very relevant decrease of bentonite porosity. A variable porosity would provide more accurate simulations. The reduction of porosity can up to zero in a zone of 2.5 near the canister-bentonite interface. The changes in porosity are negligible for r > 5.25 dm.

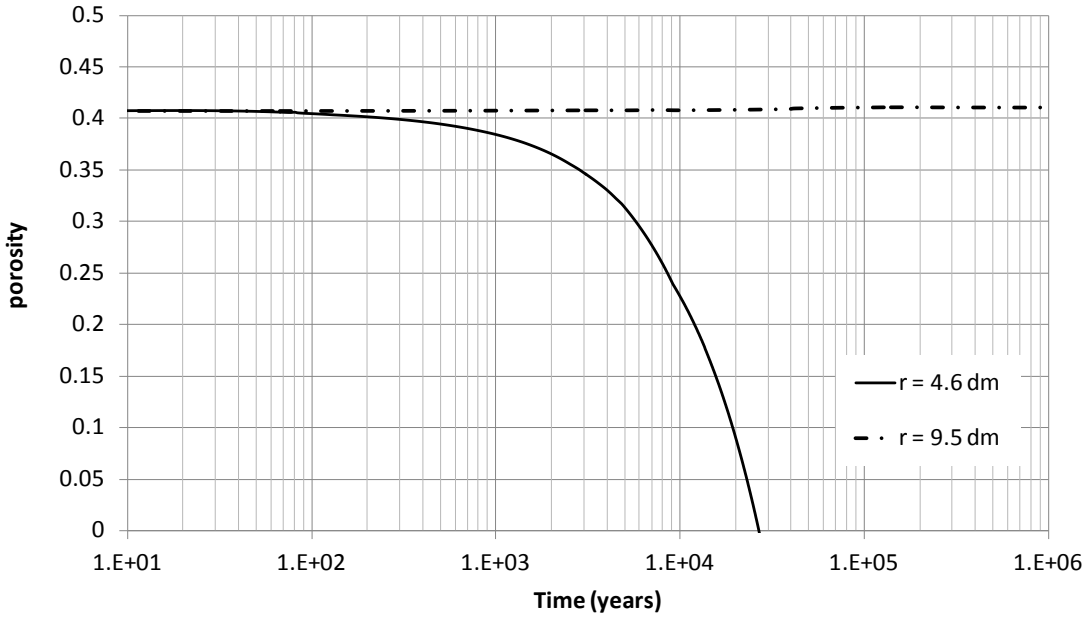

Figure 4.36. Time evolution of the change in bentonite porosity due to mineral dissolution and precipitation at r = 4.6 and 9.5 dm.

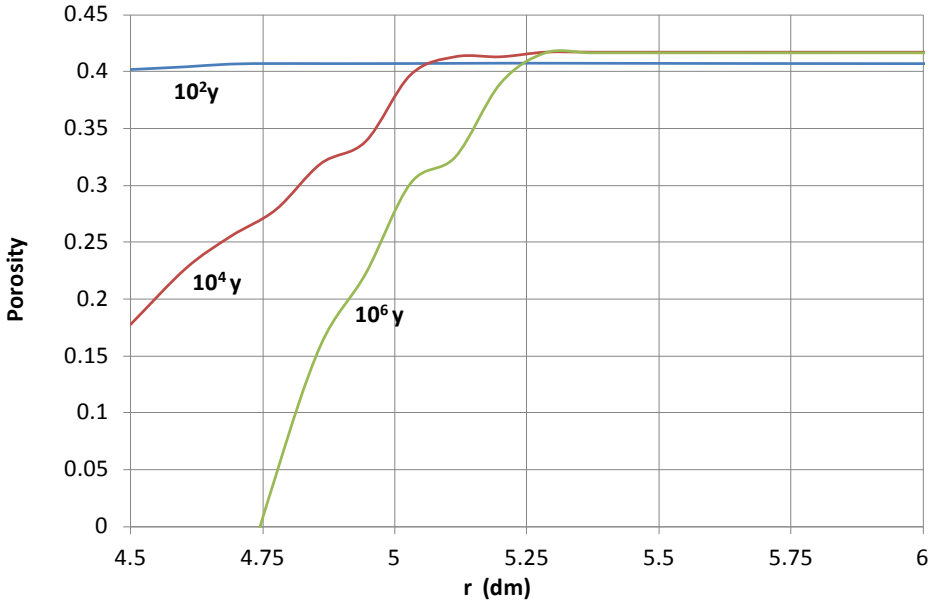

Figure 4.37. Spatial distribution of the change in bentonite porosity due to mineral dissolution and precipitation at selected times. r is the radial distance to the axis of the disposal cell.

4.8. Conclusions

The canister corrosion, the interactions of corrosion products with bentonite and the pH buffering mechanisms have been simulated during 1 Ma and at a constant temperature of 25ºC for a spent-fuel carbon-steel canister repository in granite.

The canister is fully corroded after $5 \cdot 10^4$ years for a constant corrosion rate of 2 μm/y. Canister corrosion causes an increase in the concentration of dissolved Fe^2 and pH, and a decrease in Eh. Most of the released Fe^{2+} diffuses from the canister into the bentonite where it precipitates or sorbs. The largest pH in the bentonite is almost 9.5 at $2 \cdot 10^5$ years. The evolution of the concentration of dissolved Fe^{2+}, pH and Eh are determined by the generation of corrosion products, the precipitation of magnetite and Fe sorption on weak sites.

Magnetite is the main corrosion product in the bentonite. Approximately 70 mol/L of magnetite precipitate in the canister/bentonite interface before the canister is full corroded and the precipitation stops. Its precipitation progresses as Fe^{2+} diffuses into the bentonite. Siderite precipitation is much smaller than magnetite precipitation due to the limited availability of dissolved bicarbonate (smaller than 2 mol/L). The thickness of the bentonite zone where siderite precipitates is similar to that of the magnetite. The precipitation of the corrosion products contributes to the decrease in the concentration of dissolved Fe^2 and influences the pH evolution. Calcite dissolves in most of the bentonite except near the canister where it precipitates due to the increase in pH induced by canister corrosion. Dissolution/precipitation of quartz and gypsum are not significant.

Conservative species such as Cl^- present a pattern of decreasing concentration with time in the bentonite because their diffusion to granite. Dissolved cations, Ca^{2+}, Mg^{2+}, Na^+ and K^+ and show trends similar to those of conservative species but they are also subjected to mineral dissolution/precipitation and cation exchange processes.

The computed concentrations of exchanged cations in the bentonite vary with time due to changes in cation porewater concentration. The concentration of exchanged Ca^{2+} increases after 1 Ma while those of Na^+ and Mg^+ decrease. Only a small part of the Fe released by canister corrosion is sobbed at exchanged sites. The evolution of the concentration of exchanged Fe^{2+} is related to that of sorbed and dissolved Fe^{2+}.

Model results show that sorption play a very relevant role in the geochemical evolution of bentonite. Fe^{2+} and H^+ compete for the weak 1 sorption sites near the canister. Such competition leads to the several sorption fronts and is relevant only at distances smaller than 8

cm from the canister. There is no competition between Fe^{2} and H^{+} for weak 2 sorption sites because the model does not consider for sorption of Fe on weak 2 sites.

The time evolution of the $H_2(g)$ pressures generated has been calculated from computed the computed activities. The partial pressure of $H_2(g)$ increases while the canister is being corroded until 16200 atm and decreases once the canister has been fully corroded.

Finally, the effects of mineral dissolution and precipitation in porosity have been evaluated. The precipitation of the corrosion products close to the canister leads to a very large decrease of bentonite porosity in a zone of ≈ 6 cm of thickness. A negligible increase of the porosity is observed in the rest of the buffer.

5. Sensitivity analyses

5.1. Introduction

The numerical predictions of the long term geochemical conditions of the EBS presented in the previous chapter have uncertainties due to uncertainties in the model processes and parameters. This chapter presents the sensitivity of the long term geochemical predictions of the EBS to changes in: 1) The canister corrosion rate; 2) The effective diffusion coefficient of the chemical species in the bentonite; 3) The flow rate of granite porewater at the bentonite/granite interface; 4) The selectivity coefficients of the cation exchange reactions; and 5) The chemical composition of the initial bentonite porewater and granitic boundary porewater.

5.2. Sensitivity to changes in the corrosion rate

5.2.1 Reported corrosion rates

There are reported corrosion rates for wide ranges of conditions including bulk water, compacted bentonite, oxidizing conditions, reducing conditions and water rich in sulphides. Among the published results, the most relevant are those which are representative of the reducing conditions in highly compacted bentonite. According to the reported values of King (2008) and Johnson (personal communication), the steady-state corrosion rates in compacted bentonite with Cl-rich porewater include:

- 1 μ/year at 30 °C (Smart et al. 2006), 1 M NaCl (based on gas evolution)
- 2 μ/year at 50 °C (Taniguchi et al, 2004), synthetic sea water (based on weight loss)
- 2 μ/year at 50 °C (Smart et al. 2006), 1 M NaCl (based on gas evolution)
- 2 μ/year at 60 °C (NAGRA studies, in progress for Opalinus Clay porewater after 2 years) (based on gas evolution)
- From 0.2 to 1 μ/year at 80 °C (Taniguchi et al, 2004) (based on weight loss)
- 3 μ/year at 80 °C (JNC, 2000), synthetic sea water (based on weight loss)

Although large corrosion rates are expected to take place just immediately after waste emplacement due to the presence of oxygen, the anoxic corrosion rate will be about 1 to 2 μ/year (King, 2008). A set of sensitivity runs have been performed to evaluate the uncertainty in the corrosion rate. The following values were analysed: 0.1, 0.5, 1, 3 and 5 μ/year.

5.2.2 Results of the sensitivity runs

Canister corrosion

Figure 5.1 shows the time evolution of the computed Fe(s) corrosion for several corrosion rates. It should be noticed that the cumulative amount of Fe(s) corrosion is the same for all the simulations which amounts to ~ 350 mol/L of Fe(s). The canister is fully corroded after $5 \cdot 10^4$ years for a corrosion rate of 2 µm/y while full corrosion is achieved after $2 \cdot 10^4$ years for a rate of 5 µm/y while 10^6 years are needed for a rate of 0.1 µm/y.

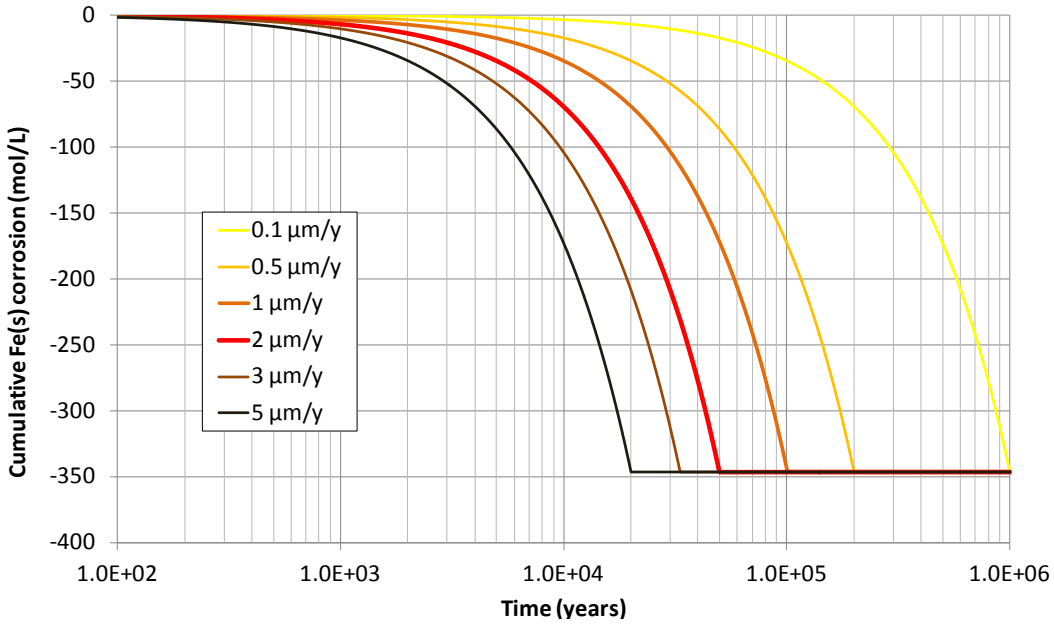

Figure 5.1. Sensitivity of the time evolution of cumulative canister corrosion for corrosion rates ranging from 0.1 to 5 µm/y.

Aqueous species

The corrosion rate determines the concentration of dissolved Fe^{2+} which diffuses into the bentonite and may then precipitate, sorb or exchange. Figure 5.2 and Figure 5.3 show the time evolution of the computed concentration of dissolved Fe^{2+} at selected locations for several corrosion rates.

The time trends in the concentration of dissolved Fe are directly related to those of the sorbed species (see Figure 5.18 and Figure 5.19). The sudden decrease of the concentration of Fe^{2+} observed at r = 4.6 dm at 80 years for a corrosion rate of 2 µm/y which is associated with a sudden increase in the concentration of sorbed Fe^{2+} in weak 1 sites is also observed for other corrosion rates, but at other times and locations and other magnitudes. The differences in magnitude are related to the different positions and migration rates of the sorption fronts.

The lower the corrosion rate the larger the penetration of the released Fe^{2+} into the bentonite (Figure 5.3). At t = 10^5 years, the concentration of dissolved Fe^{2+} becomes very small in the bentonite due to the solute diffusion from the bentonite into granite.

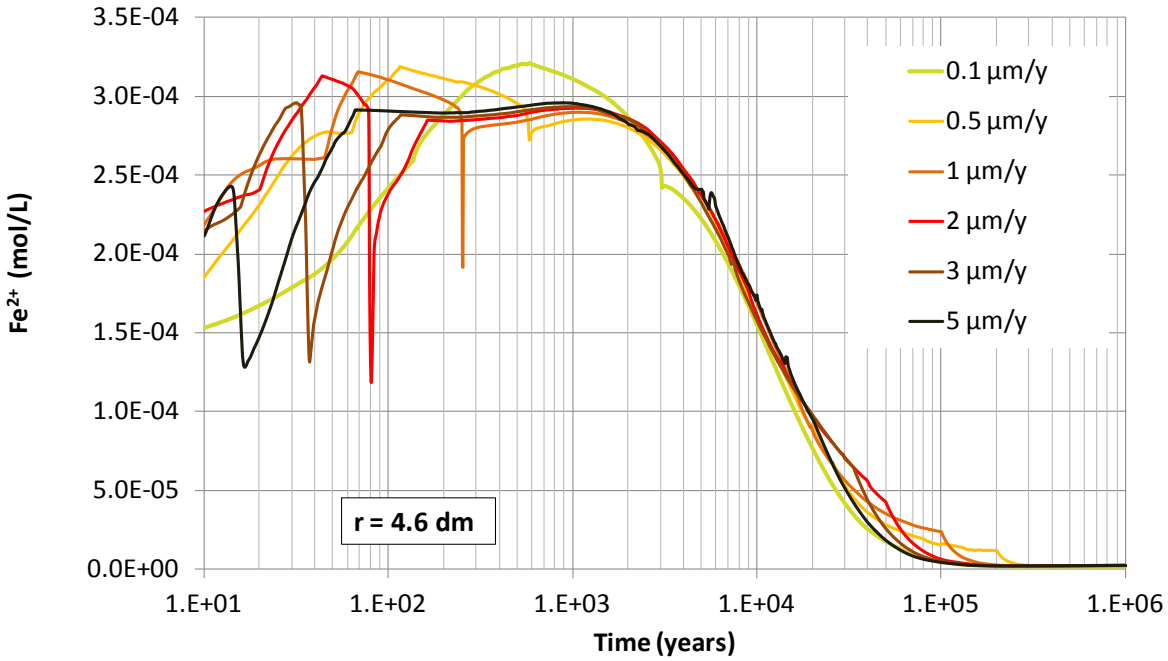

Figure 5.2. Sensitivity of the computed time evolution of dissolved Fe^{2+} in the bentonite at r = 4.6 dm to changes in the corrosion rate. r is the radial distance to the axis of the disposal cell.

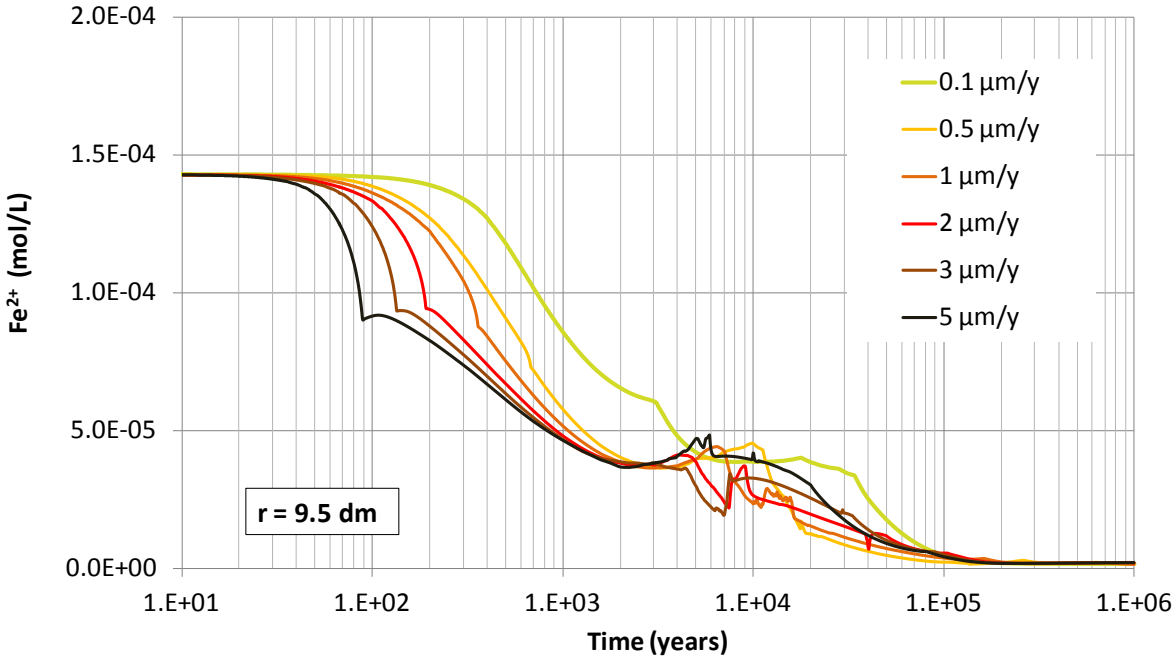

Figure 5.3. Sensitivity of the computed time evolution of dissolved Fe^{2+} in the bentonite at r = 9.5 dm to changes in the corrosion rate. r is the radial distance to the axis of the disposal cell.

Canister corrosion causes an increase in pH and a decrease in Eh. Figure 5.4 and Figure 5.5 show the time evolution of the computed pH in the bentonite at r = 4.6 and 9.5 dm. At r = 4.6 dm the pH increases gently from its initial value of 6.4 to around 7. Then, the pH increases sharply due to the sorption of Fe^{2+} on weak 1 sites. The pH increases sooner, the larger the corrosion rate. Afterwards, the pH continues increasing until it reaches its maximum of approximately 9.5 between t = 10^5 and t = $3 \cdot 10^5$ years. Then, the pH decreases and gets below 9 at 10^6 years. The larger the corrosion rate, the sooner the pH achieves its maximum. The computed pH for a corrosion rate of 0.1 μm/y shows a very different behaviour after $2 \cdot 10^5$ years because the pH keeps increasing and reaches a pH larger than 10. This behaviour is related to the sorption on weak 2 sorption sites (Figure 2.18).

In the middle of the bentonite barrier, at r = 9.5 dm, the pH increases gradually reaching its maximum at about $2 \cdot 10^5$ years for all the corrosion rates except for 0.1 μm/y (Figure 2.5). Then, it decreases until the end of the simulation. The computed pH time evolution for a corrosion rate of 0.1 μm/y presents a different behaviour. pH exceeds 10 at t = 10^6 years for this rate.

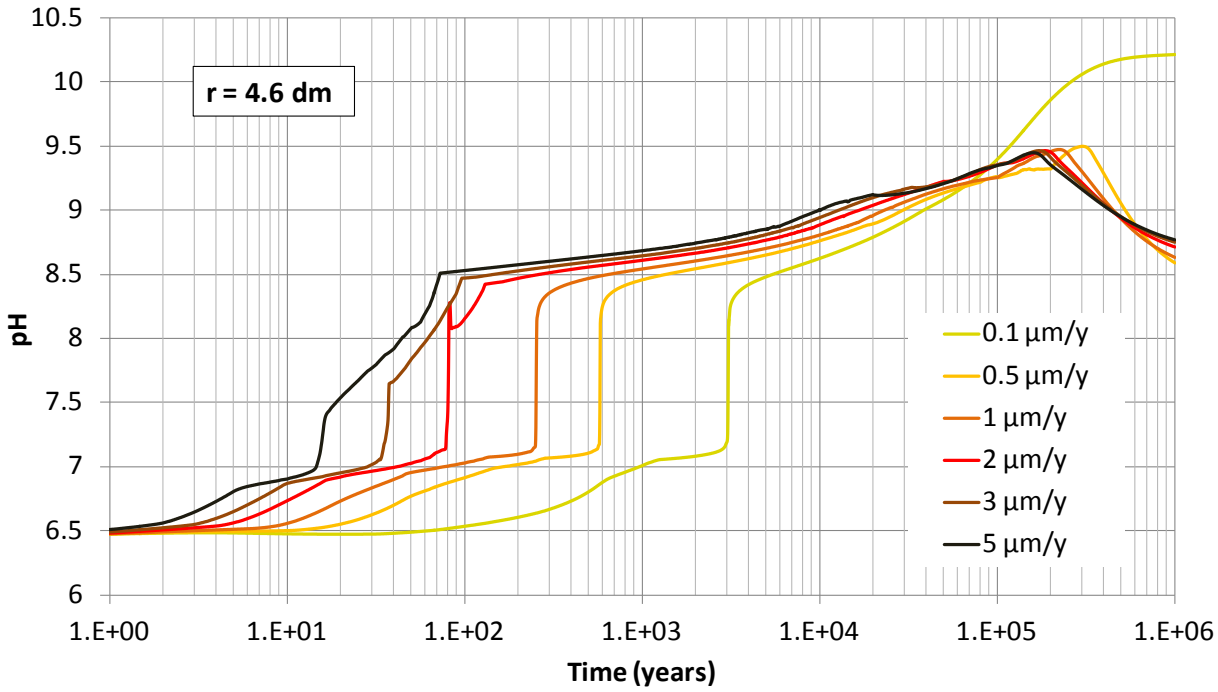

Figure 5.4. Sensitivity of the computed time evolution of the pH in the bentonite at r = 4.6 dm to changes in the corrosion rate. r is the radial distance to the axis of the disposal cell.

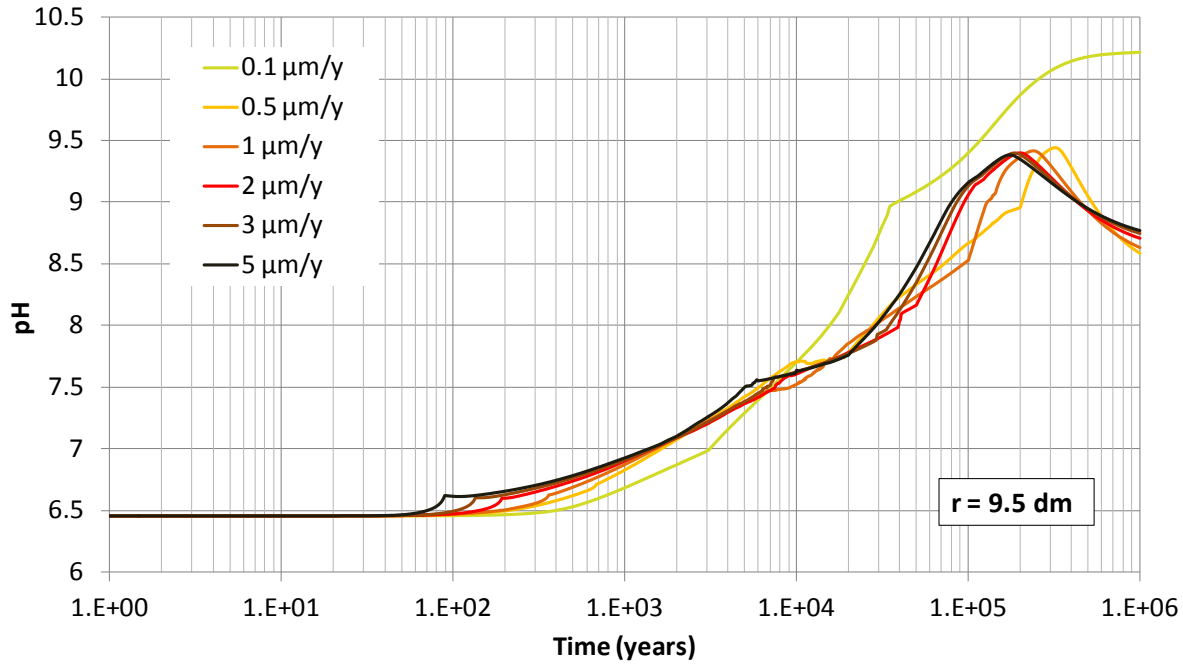

Figure 5.5. Sensitivity of the computed time evolution of the pH in the bentonite at r = 9.5 dm to changes in the corrosion rate. r is the radial distance to the axis of the disposal cell.

Figure 5.6 shows the spatial distribution of computed pH in the bentonite at t = 10^4 years for several corrosion rates. It should be noticed that the pH fronts are related to the Fe^{2+} sorption front and occur at different times and positions and reach pH values around 4. Sorption fronts dissipate and they do not show up at r = 9.5 dm.

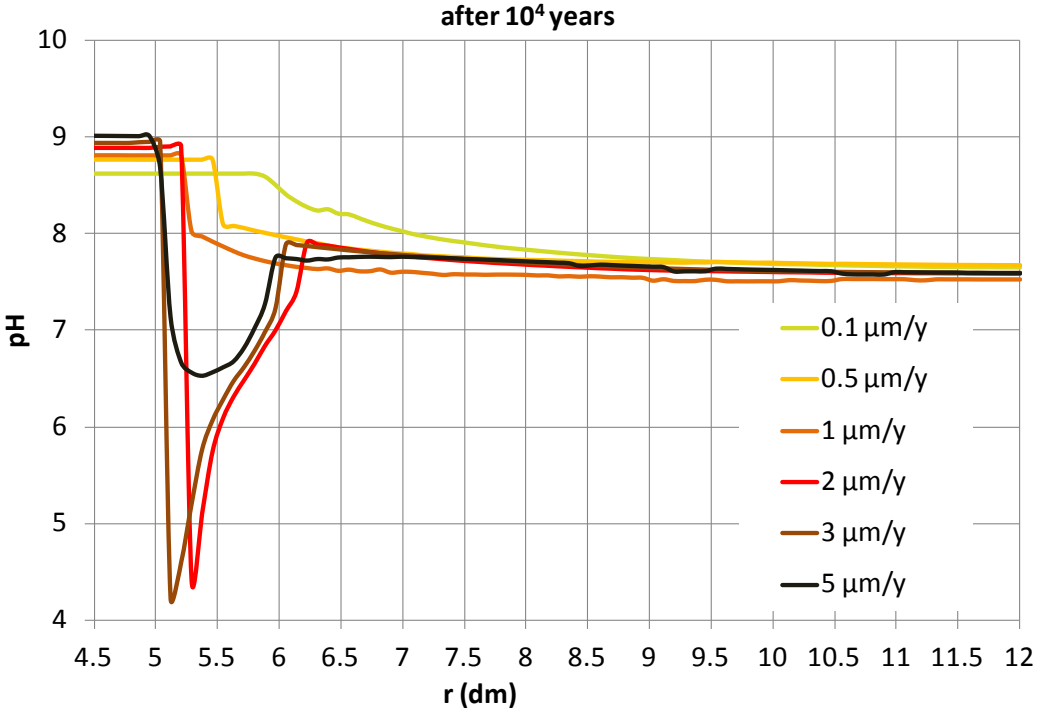

Figure 5.6. Sensitivity of the spatial distribution of the computed pH in the bentonite at t = 10^4 years to changes in the corrosion rate. r is the radial distance to the axis of the disposal cell.

Figure 5.7 shows the time evolution of computed Eh in the bentonite at r = 4.6 dm. The Eh shows similar trends to those of pH, but opposite because the Eh decreases from its initial value until it reaches its minimum between -0.65 and -0.7 V. The decrease in Eh is initially smooth and later becomes sharp from -0.2 to -0.5 V due to the Fe sorption front. After reaching its minimum, the Eh increases at the end of the simulation. Similar to pH, the results of the simulation of Eh for a corrosion rate of 0.1 μm/y show a different behaviour. The Eh keeps decreasing until the end of simulation reaching nearly -0.7 V.

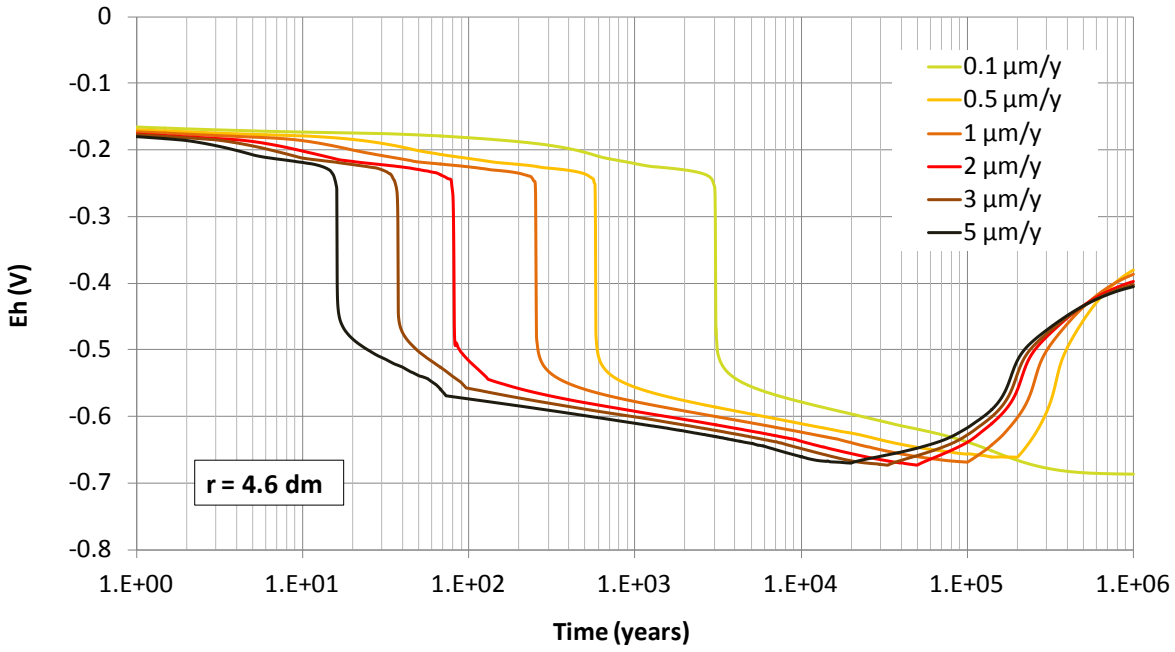

Figure 5.7. Sensitivity of the computed time evolution of the Eh in the bentonite at r = 4.6 dm to changes in the corrosion rate. r is the radial distance to the axis of the disposal cell.

Mineral phases

The results of the sensitivity runs show that magnetite is the main corrosion product regardless the corrosion rate. Siderite precipitation is much smaller than that of magnetite. Goethite never precipitates.

Figure 5.8 shows the time evolution of the concentration of cumulative precipitated magnetite in the bentonite at r = 4.6 cm computed for different corrosion rates. Figure 5.9 to Figure 5.11 show the sensitivity of the spatial distribution of the concentration of cumulative precipitated magnetite at selected times to changes in the corrosion rate. The larger the corrosion rate, the sooner magnetite precipitates significantly. At t = 10^4 years, nearly 35 mol/L of magnetite precipitate at the canister/bentonite interface for a corrosion rate of 5 μm/y. However, only 12 mol/L of magnetite precipitate for a rate 2 μm/y while magnetite precipitation is insignificant for 0.1 μm/y (Figure 5.9). Magnetite continues precipitating as

long as the canister is being corroded (compare Figure 5.1 and Figure 5.8). The larger the corrosion rate, the larger the magnetite concentration close to the canister/bentonite interface but the smaller its penetration in the bentonite. The concentration of cumulative precipitated magnetite at t = 10^6 years ranges from 62 to 75 mol/L at the canister/bentonite interface for corrosion rates from 0.5 to 5 µm/y, respectively (Figure 5.11). The thickness of the zone where magnetite precipitates at the end of the simulation is smaller than 5 cm (r < 5 dm) for a corrosion rate of 5 µm/y and reaches 10 cm (r = 5.5 dm) for 0.5 µm/y (Figure 2.10). The sensitivity run for a corrosion rate of 0.1 µm/y shows a notably smaller concentration of precipitated magnetite at the canister/bentonite interface and a much larger thickness at t = 10^6 years than those for other corrosion rates.

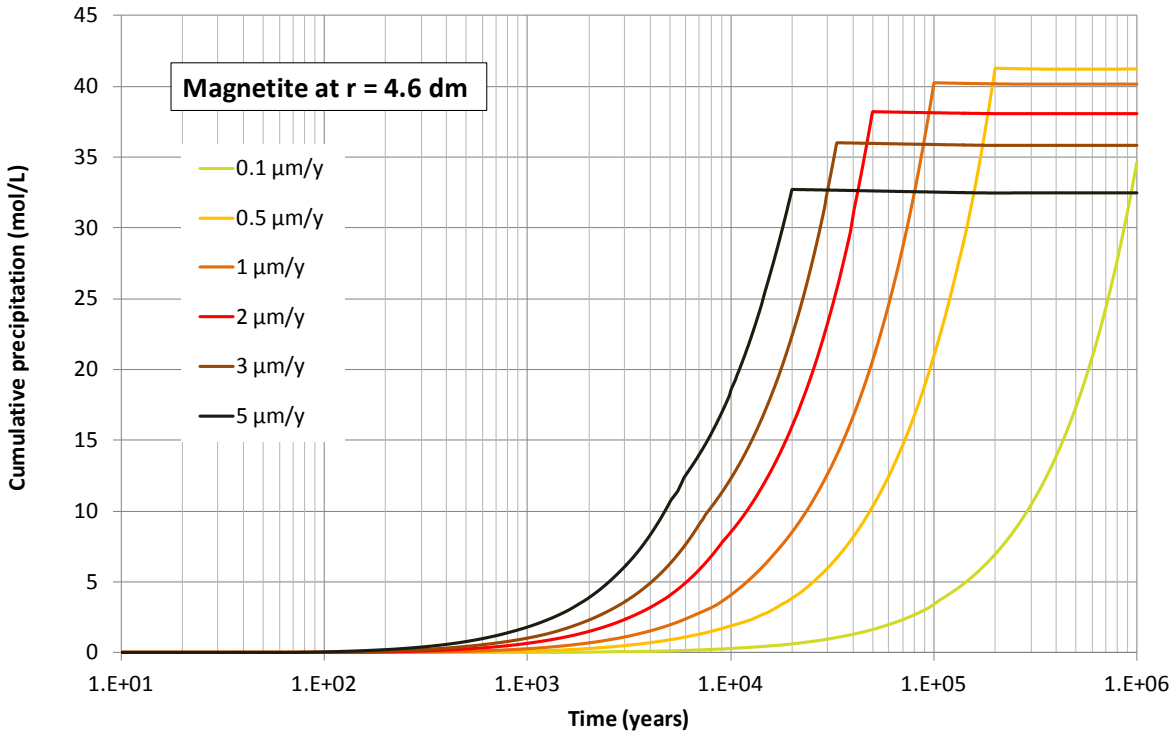

Figure 5.8. Sensitivity of the computed time evolution of the concentration of precipitated magnetite in the bentonite at r = 4.6 dm to changes in the corrosion rate. r is the radial distance to the axis of the disposal cell.

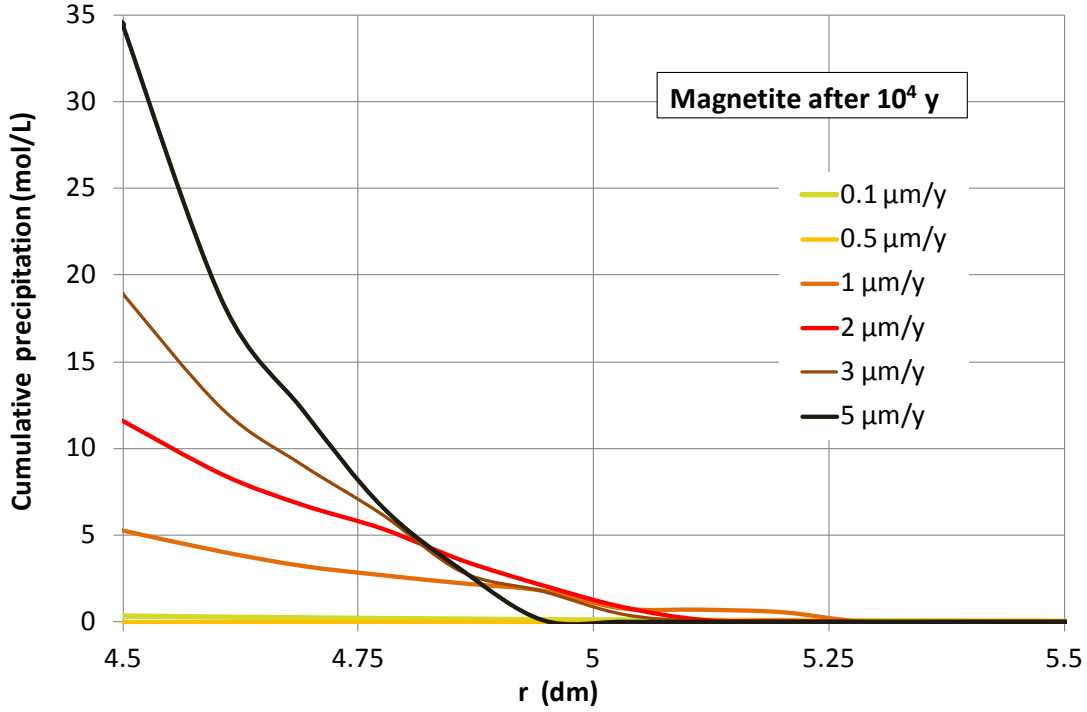

Figure 5.9. Sensitivity of the spatial distribution of the concentration of precipitated magnetite in the bentonite at t = 10^4 years to changes in the corrosion rate. r is the radial distance to the axis of the disposal cell.

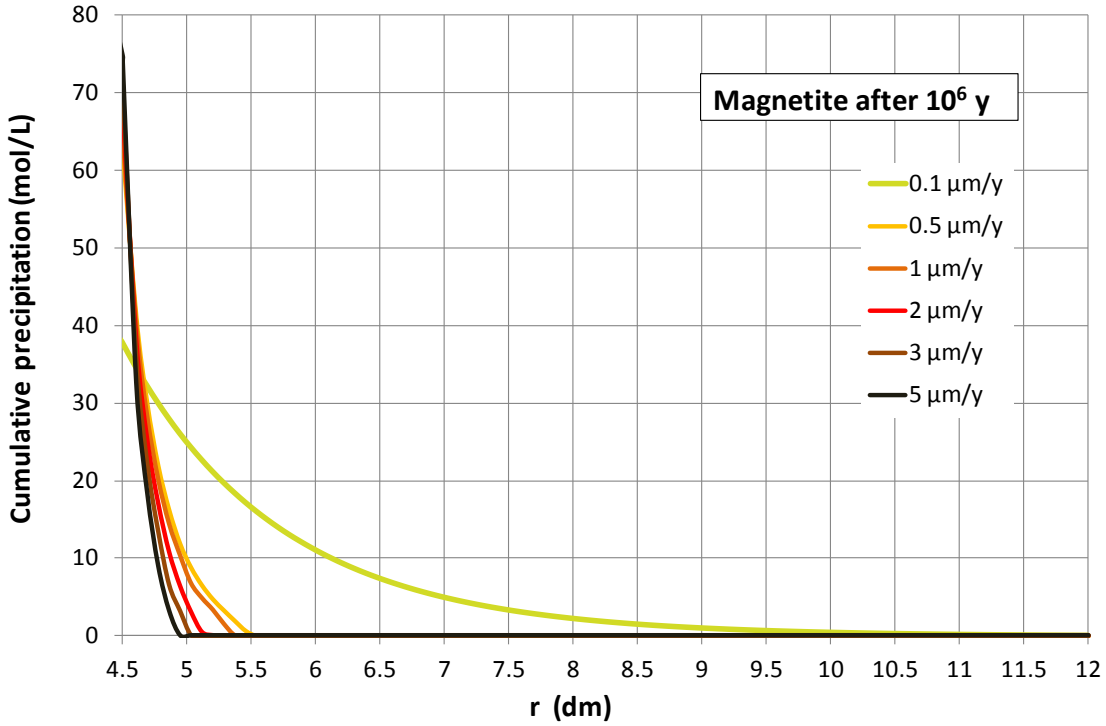

Figure 5.10. Sensitivity of the spatial distribution of the concentration of precipitated magnetite in the bentonite at t = 10^6 years to changes in the corrosion rate. r is the radial distance to the axis of the disposal cell.

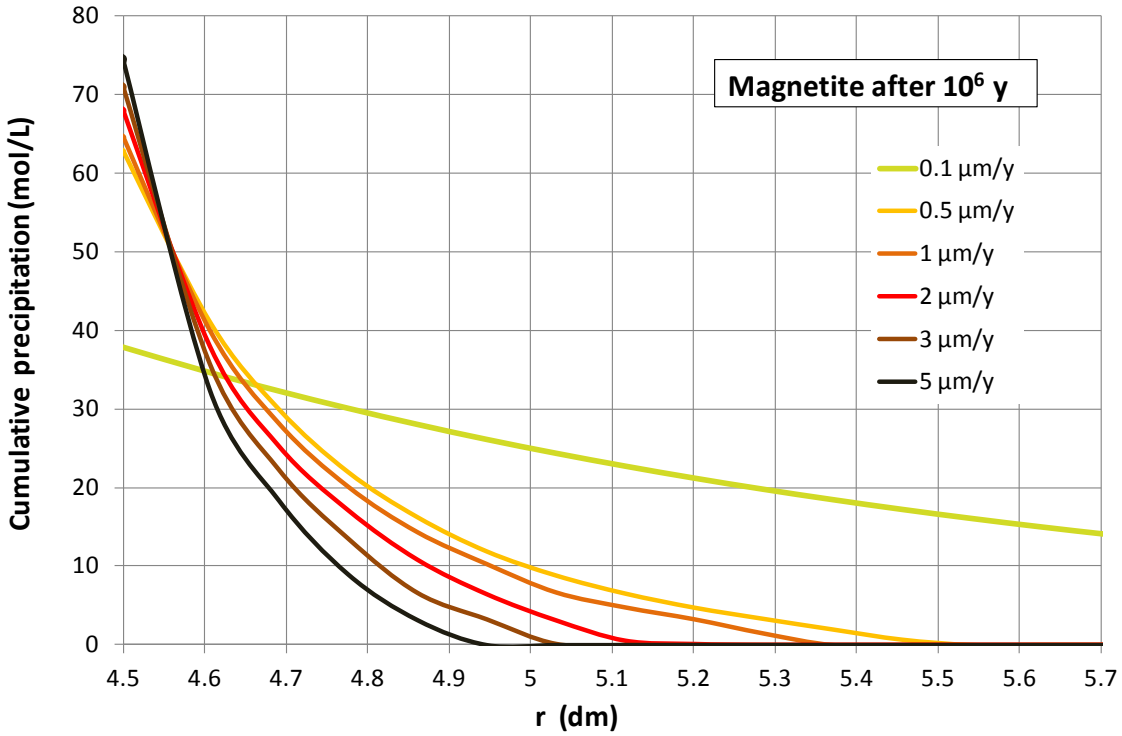

Figure 5.11. Sensitivity of the spatial distribution of the concentration of precipitated magnetite in the bentonite at t = 10^6 years to changes in the corrosion rate. Zoom of the canister/bentonite interface. r is the radial distance to the axis of the disposal cell.

Siderite precipitation/dissolution is influenced by the pH and the concentrations of dissolved Fe^{2+} and HCO_3^-. Figure 5.12 shows the time evolution of the concentration of cumulative precipitated siderite at r = 4.6 dm computed for several corrosion rates. Siderite precipitation is always much smaller than magnetite precipitation due to the limited availability of dissolved HCO_3^-. The results of the base run for 2 µm/y show that siderite precipitation rates vary with time. This is also true for most of the sensitivity runs. However, a significant siderite dissolution episode can be observed for corrosion rates of 3 and 5 µm/y. It is especially significant for a 5 µm/y for which it takes place from $5 \cdot 10^3$ to $2 \cdot 10^4$ years.

Additionally, the curves of siderite dissolution/precipitation show slight peaks which coincide with the pH and sorption fronts. Such peaks occur at 3000 years for a corrosion rate of 0.1 µm/y, at t = 600 years for 0.5 µm/y, at t = 250 years for 1 µm/y and at t = 80 years for 2 µm/y (Figure 5.12). Siderite dissolution produced by such pH fronts is not observed for the corrosion rates of 3 or 5 µm/y because they take place before siderite precipitation is significant. Such fronts produce also the precipitation of some magnetite and the dissolution of calcite (Figure 5.15). The magnetite peaks cannot be observed in the plots because they are too small. Once the magnetite precipitation stops, the siderite precipitation keeps increasing in all the cases, i.e.: at 10^5 years for the simulation assuming a corrosion rate of 1 µm/y (Figure

5.12). Therefore, siderite precipitation extends after canister full corrosion until approximately $2 \cdot 10^5$ years for corrosion rates of 2, 3 and 5 µm/y, $2.5 \cdot 10^5$ years for 1 µm/y and $3.5 \cdot 10^5$ years for 0.5 µm/y.

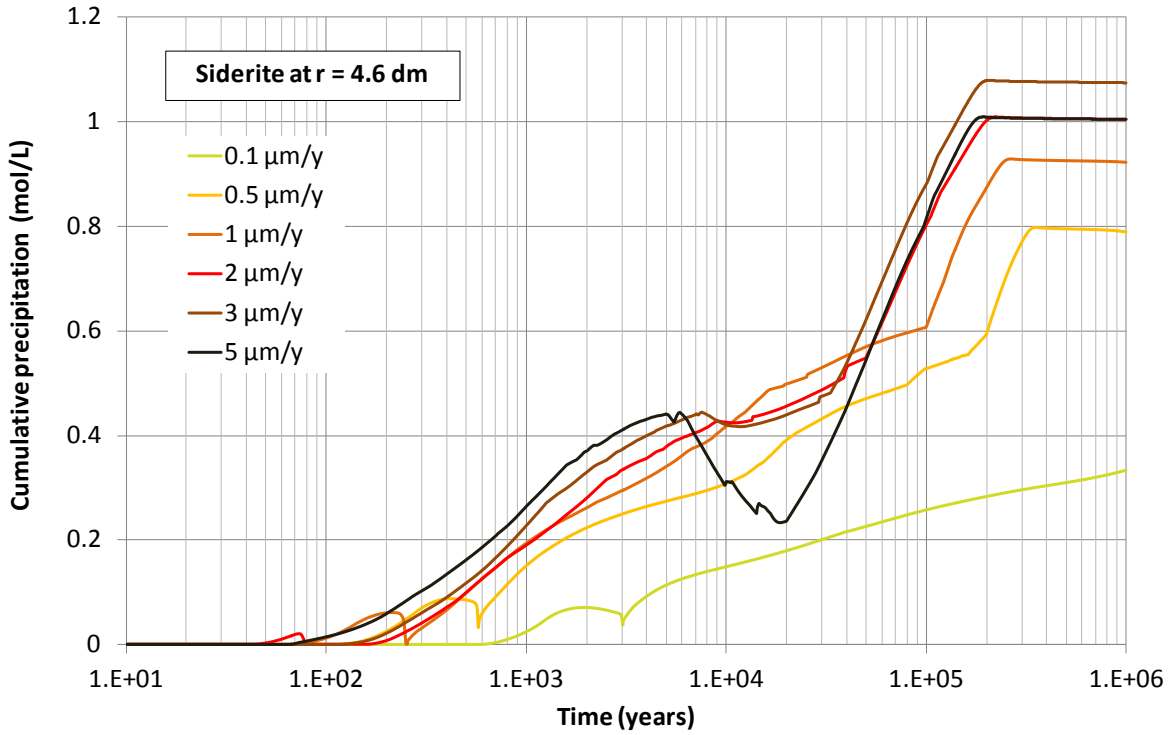

Figure 5.12. Sensitivity of the time evolution of the concentration of precipitated siderite in the bentonite at r = 4.6 dm to changes in the corrosion rate. r is the radial distance to the axis of the disposal cell.

Figure 5.13 and Figure 5.14 show the sensitivity of the radial distribution of the concentration of cumulative precipitated siderite at t = 10^6 years to changes in the corrosion rate. Similar to magnetite, the larger the corrosion rate the smaller the thickness of the zone where siderite precipitates. Siderite thickness is smaller than 5 cm (r < 5 dm) for a corrosion rate of 5 µm/y. In this case, siderite and magnetite thickness coincide. The thickness of the zone where siderite precipitates is approximately 1 cm larger than that of magnetite for corrosion rates from 0.5 to 3 µm/y.

In the canister/bentonite interface, the larger the corrosion rate the larger the amount of siderite precipitation. The largest concentration of precipitated siderite at the interface has been computed for a corrosion rate of 5 µm/y and is equal to 1 mol/L. Within the bentonite, siderite concentration increases with the distance to the interface and is largest for the smallest corrosion rate. Finally, the computed siderite precipitation for a corrosion rate of 0.1 µm/y presents a spatial distribution completely different than that of other corrosion rates. Siderite

precipitates throughout the bentonite. Its concentration is significant smaller than that of other sensitivity runs. Close to the bentonite/granite interface, the concentration of precipitated siderite increases slightly due to the diffusion of HCO_3^- from the granite.

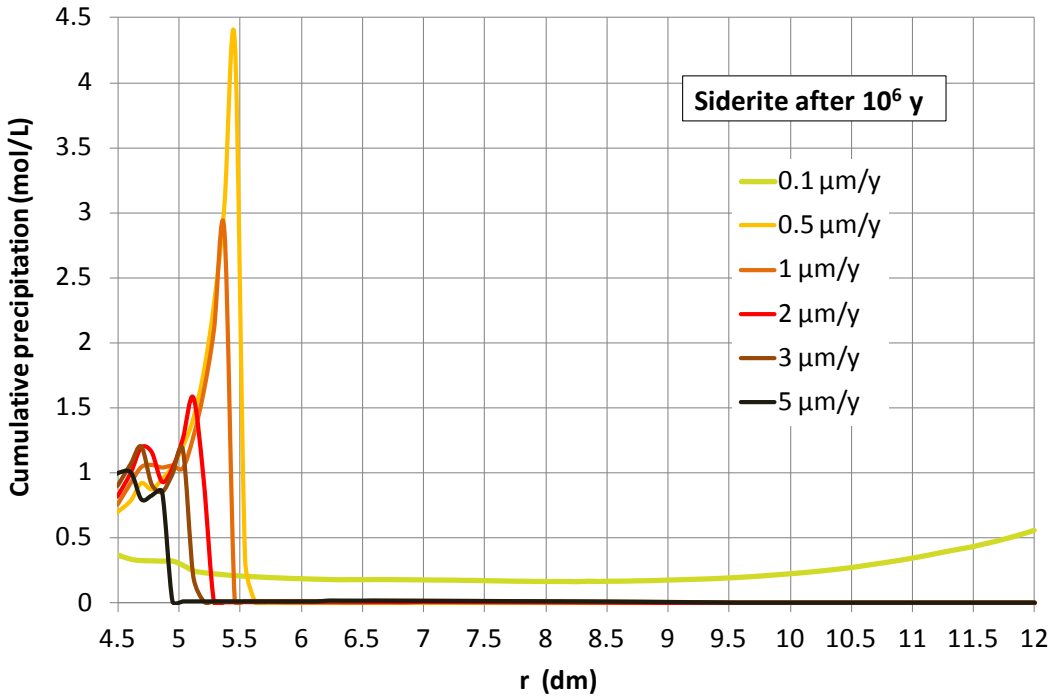

Figure 5.13. Sensitivity of the spatial distribution of the concentration of precipitated siderite in the bentonite at t = 10^6 years to changes in the corrosion rate. r is the radial distance to the axis of the disposal cell.

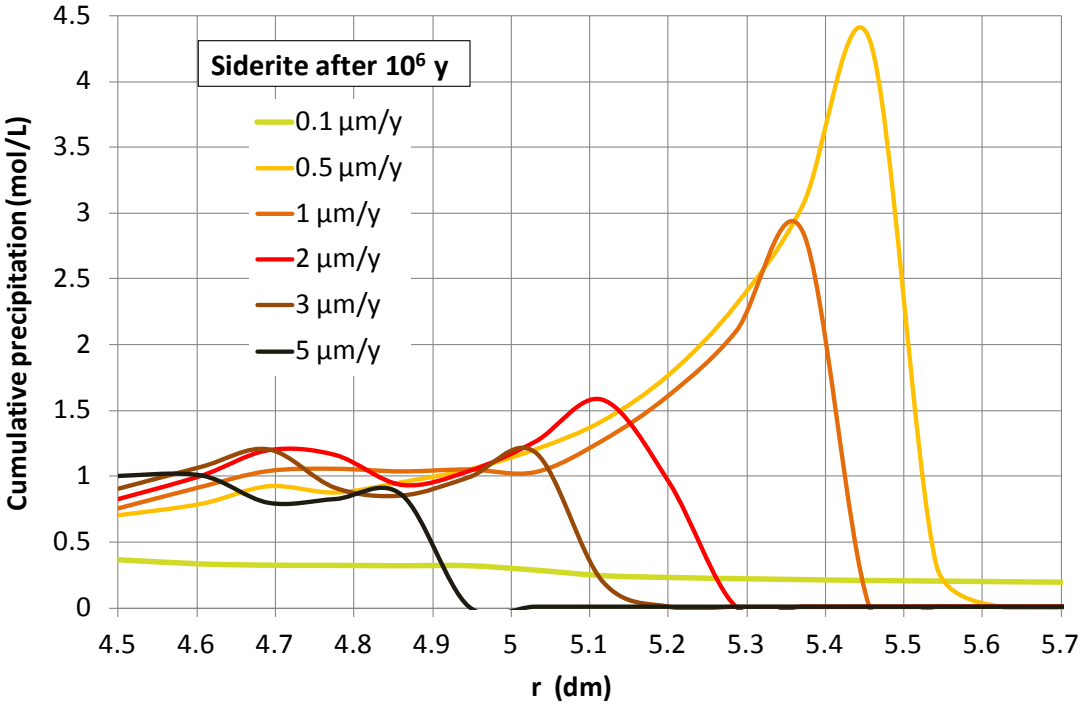

Figure 5.14. Sensitivity of the spatial distribution of cumulative siderite precipitation in the bentonite at t = 10^6 years to changes in the corrosion rate. Zoom to the canister/bentonite interface. r is the radial distance to the axis of the disposal cell.

Figure 5.15 shows the time evolution of cumulative calcite precipitation in the bentonite at r = 4.6 cm for several corrosion rates. Calcite dissolves slightly at this location from 20 to 300 years. The larger the corrosion rate, the smaller this time period. The increase in pH produced by canister corrosion near the canister/bentonite interface leads to calcite precipitation.

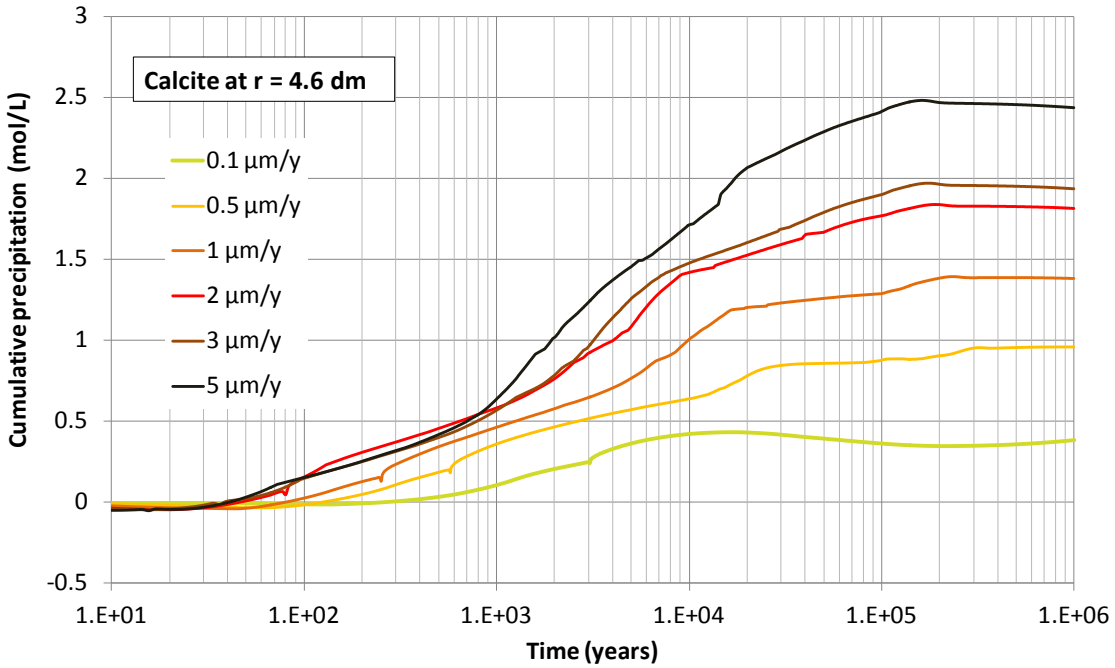

Figure 5.15. Sensitivity of the time evolution of the concentration of precipitated calcite in the bentonite at r = 4.6 dm to changes in the corrosion rate. r is the radial distance to the axis of the disposal cell.

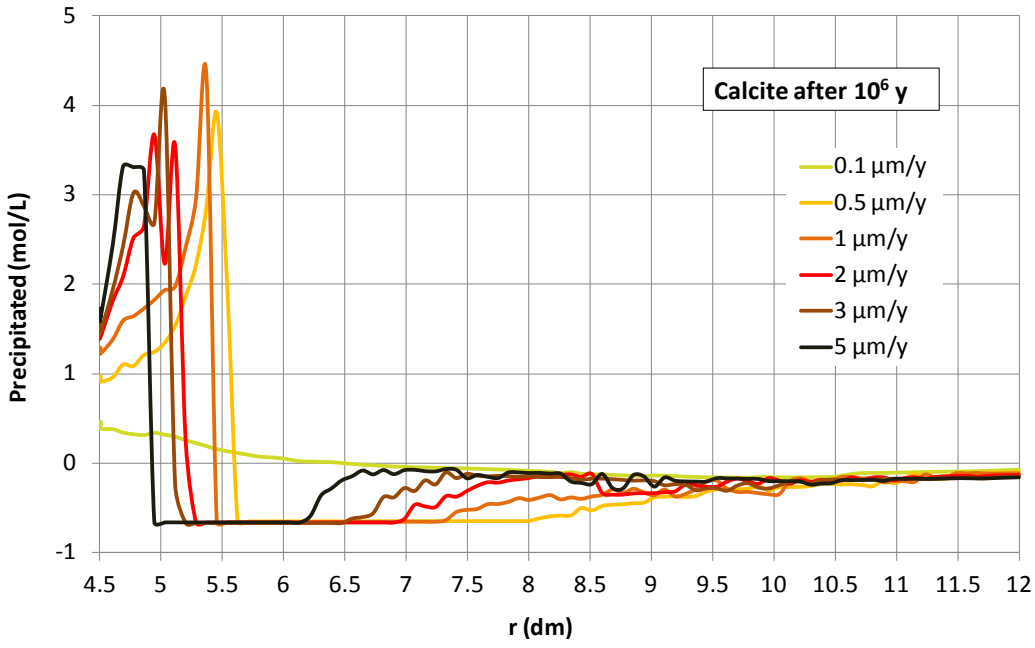

Figure 5.16. . Sensitivity of the spatial distribution of the concentration of precipitated calcite in the bentonite at t = 10^6 years to changes in the corrosion rate. r is the radial distance to the axis of the disposal cell.

Figure 5.16 shows the sensitivity of the spatial distribution of the concentration of cumulative precipitated/dissolved calcite at t = 10^6 years to changes in the corrosion rate. The thickness of the zone where calcite precipitates in the bentonite decreases with the corrosion rate and ranges from 4 to 10 cm for corrosion rates from 5 to 0.5 µm/y. Calcite precipitates everywhere in the bentonite for the smallest corrosion rate.

Cation exchange

The concentration of exchanged Fe^{2+} in the bentonite is directly related to the concentrations of dissolved and sorbed Fe^{2+}. Figure 5.17 shows the sensitivity of the time evolution of the concentration of exchanged Fe^{2+} at r = 4.6 dm to changes in the corrosion rate. There are some differences in the concentration of exchanged Fe^{2+} which do not affect the concentrations of other exchanged cations because the concentration of exchanged Fe^{2+} is more than two orders of magnitude smaller than those of Na^{+}, Ca^{2+} and Mg^{2+}. Therefore, it can be concluded that the computed concentrations of exchanged cations in the bentonite are not sensitive to changes in the corrosion rate.

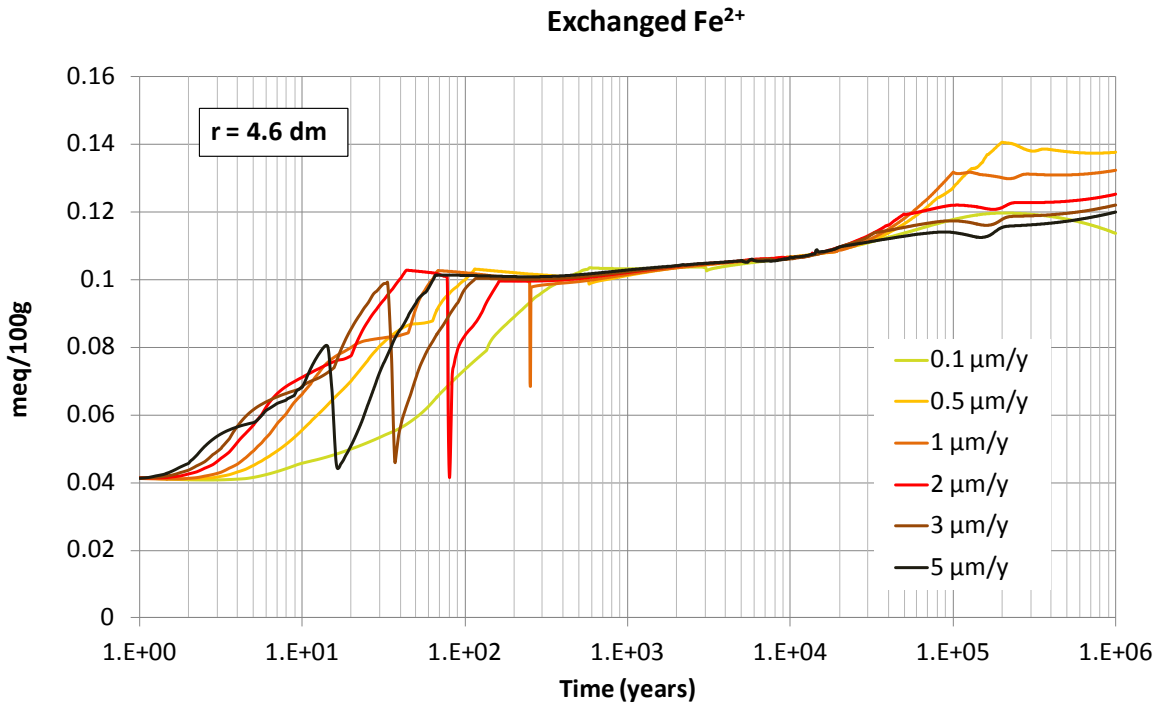

Figure 5.17. Sensitivity of the time evolution of the concentration of exchanged iron in the bentonite at r = 4.6 dm to changes in the corrosion rate. r is the radial distance to the axis of the disposal cell.

Sorbed species

The time evolution of computed concentrations of sorbed species in the bentonite has been analysed at several locations for several corrosion rates. Figure 5.18 shows the time evolution of the concentrations of sorbed species at r = 4.6 dm for the smallest and largest corrosion rates, 0.1 and 5 μm/y, respectively. These figures can be compared with those of the base run (2 μm/y) shown in Figure 4.24.

The competition of H^+ and dissolved Fe^{2+} for weak 1 sorption sites produces a sorption front at 80 years for a rate of 2 μm/y. Competition for sorption sites occurs also for other corrosion rates. However, it takes place at different times and speeds. For the slowest corrosion rate (0.1 μm/y) the sorption front is delayed until 3000 years. For the largest corrosion rate (5 μm/y) it takes place after less than 20 years. The concentration of $S^{W1}O^-$ increases from 3000 to $2 \cdot 10^5$ years while the concentration of $S^{W1}OFe^+$ decreases for all the corrosion rates. Afterwards, the concentration of $S^{W1}OH$ increases smoothly while that of $S^{W1}O^-$ decreases for all the corrosion rates except for 0.1 μm/y. Dissolved Fe^{2+} and H^+ do not compete for the weak 2 sorption sites. $S^{W2}OH$ is the main sorbed species during most of the time. A second corrosion front can be observed in which the concentration of $S^{W2}OH$ increases and that of $S^{W2}OH^{2+}$ decreases. The behaviour of the weak 2 sorption complexes at t= $2 \cdot 10^5$ years is different for the smallest corrosion rate of 0.1 μm/y because the concentration of $S^{W2}O^-$ increases and that of $S^{W2}OH$ decreases.

Figure 5.19 shows the sensitivity of the spatial distribution of the sorbed species at t = 10^4 years to changes in the corrosion rates. The sorption fronts observed at t = 10^4 years and r = 5.3 dm in the base run (Figure 4.31) are also observed in the sensitivity run of 5 μm/y at r = 5.1 dm. The oscillations of the concentrations of sorbed species for the largest corrosion rate are smaller than those of the base run, especially for the weak 2 sorbed species. The sorption front for a corrosion rate of 5 μm/y is advanced compared to that for 2 μm/y and, therefore, the spatial distribution for 5 μm/y at t = 10^4 years is comparable to that for 2 μm/y at t = $5 \cdot 10^4$ years (Figure 4.32). On the contrary, the sorption front for a corrosion rate of 0.1 μm/y is delayed with respect to that of the base run. Therefore, the spatial distribution of the concentrations for 0.1 μm/y at t = 10^4 years is comparable to that for 2 μm/y at $3 \cdot 10^4$ years.

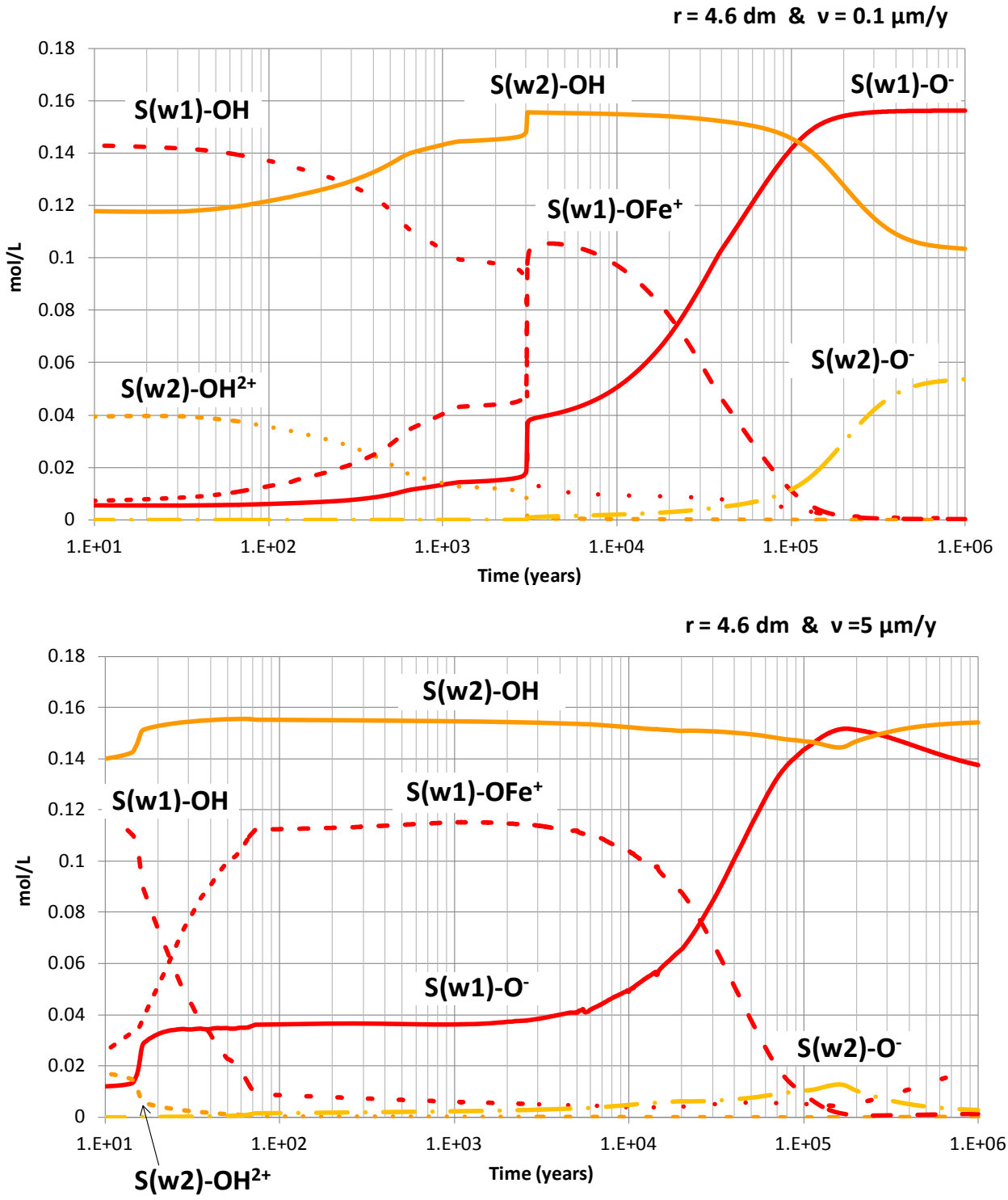

Figure 5.18. Time evolution of the computed concentrations of sorbed species in the bentonite at r = 4.6 dm for a corrosion rate of 0.1 (top) and 5 µm/y (bottom). r is the radial distance to the axis of the disposal cell.

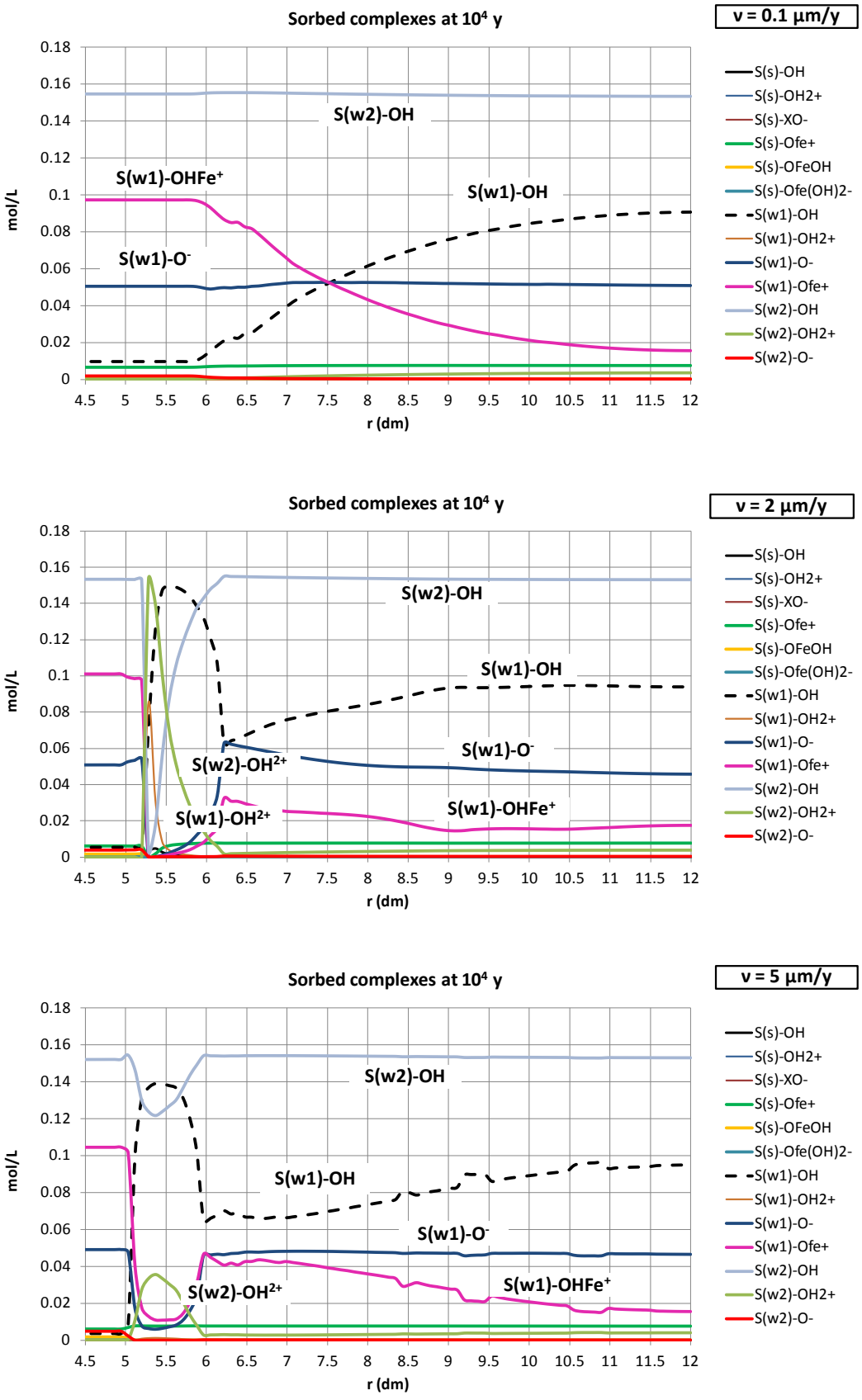

Figure 5.19. Spatial distribution of the concentrations of sorbed species in the bentonite at t = 10^4 years for corrosion rates of 0.1, 2 and 5µm/y. r is the radial distance to the axis of the disposal cell.

Hydrogen pressure

The time evolution of the $H_2(g)$ partial pressure in the bentonite has been computed for all the sensitivity runs (Figure 5.20). Pressure increases as long as corrosion is taking place (compare Figure 5.20 and Figure 5.1). Since $H_2(aq)$ diffuses from the bentonite into the granite simultaneously to its production, the slower the corrosion rate the smaller the peak hydrogen pressure in the bentonite. The maximum pressure for a corrosion rate of 2 µm/y is of 16200 atm and it is reached at $t = 5 \cdot 10^4$ years. The maximum pressure decreases to 600 atm for a corrosion rate of 0.1 µm/y. For a corrosion rate of 5 µm/y, the hydrogen pressure reaches 19200 atm between 10^4 and $2 \cdot 10^4$ years. There are no significant gradients in the calculated concentrations of $H_2(aq)$ in the bentonite.

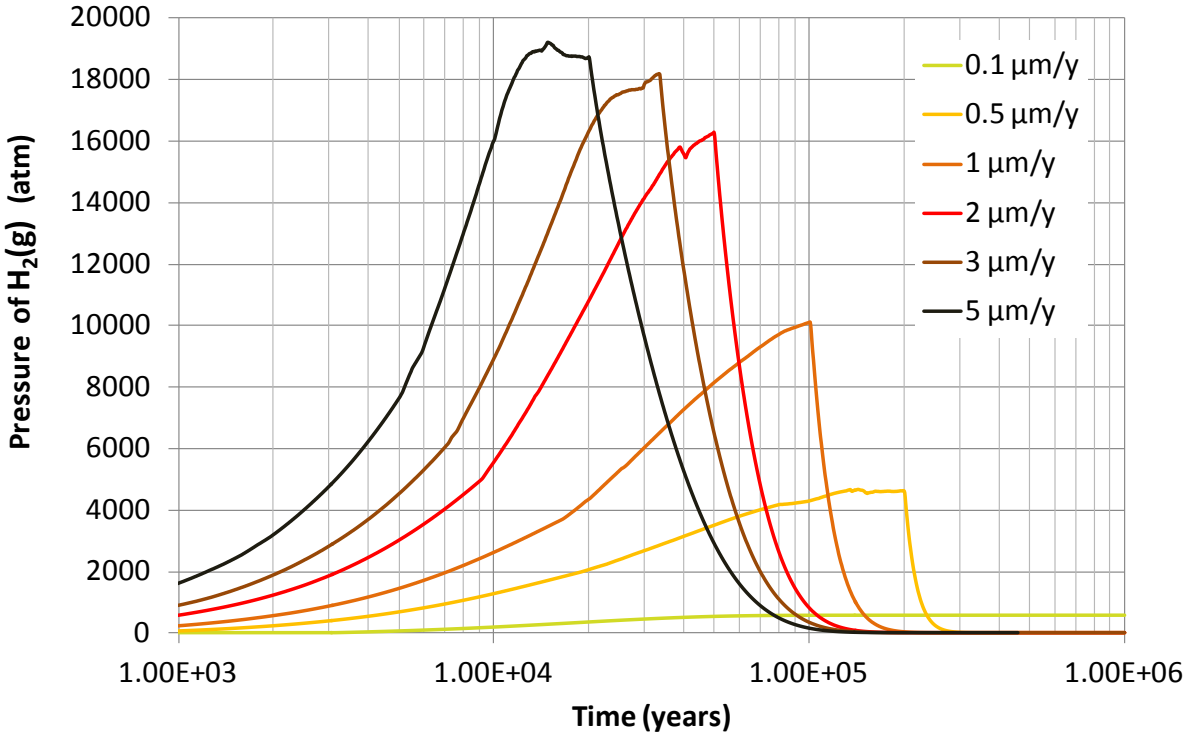

Figure 5.20. Sensitivity of the computed time evolution of the $H_2(g)$ partial pressure in the bentonite to changes in the corrosion rate.

Changes in porosity

Changes in the bentonite porosity have been calculated from the computed mineral dissolution/precipitation for each sensitivity run. Figure 5.21 and Figure 5.22 show the changes in the bentonite porosity caused by mineral dissolution/precipitation at r = 4.6 dm and their spatial distribution at $t = 10^6$ years for several corrosion rates, respectively. The precipitation of magnetite close to the canister causes a decrease in bentonite porosity for all the corrosion rates. The larger the corrosion rate the faster the porosity reduction near the

canister interface. The porosity at r = 4.6 dm is half its initial value at t = 4500 years for a corrosion rate of 5 μm/y and $2\cdot10^5$ years for 0.1 μm/y. On the other hand, the reduction in porosity is not significant in the bentonite located far from the canister. The larger the corrosion rate, the smaller the thickness of bentonite affected by pore clogging.

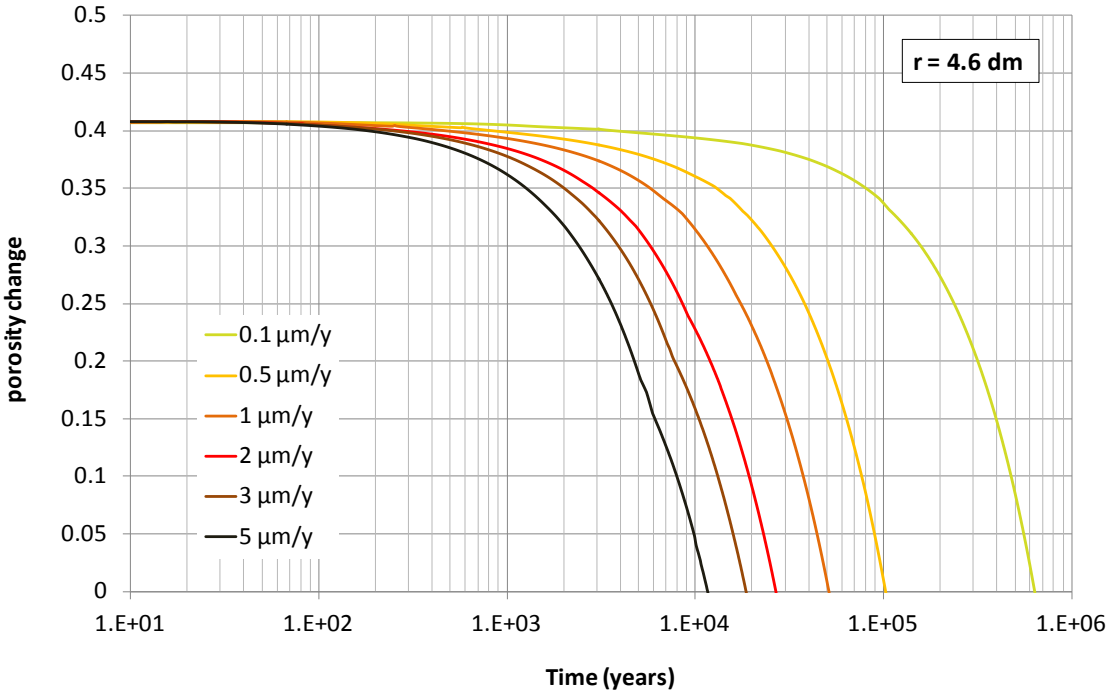

Figure 5.21. Time evolution of the computed changes in bentonite porosity at r = 4.6 dm due to mineral dissolution and precipitation for several corrosion rates.

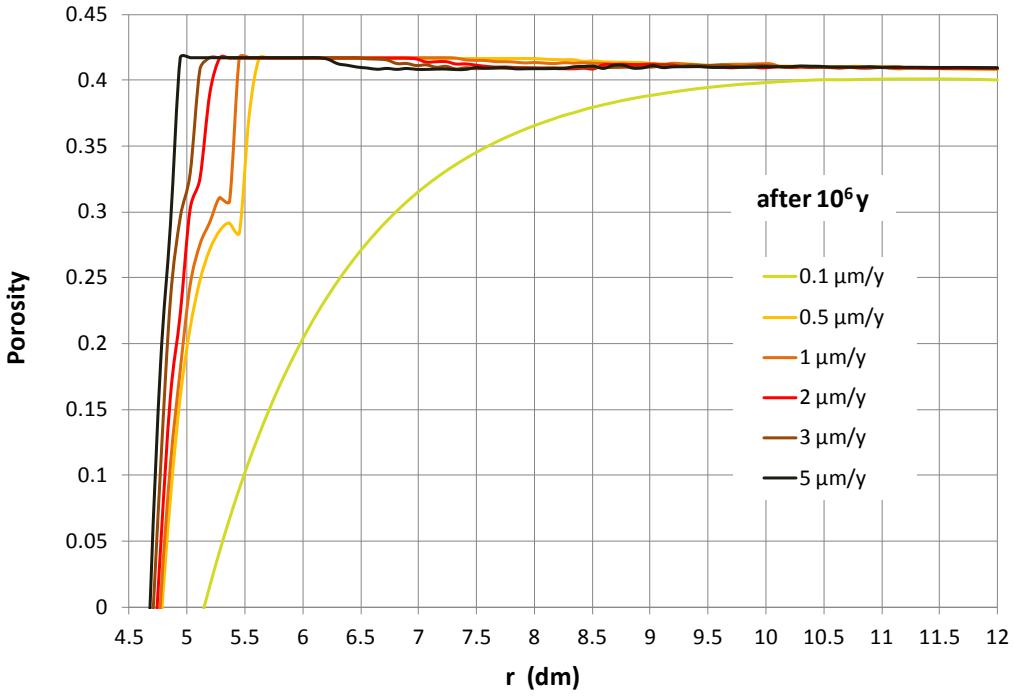

Figure 5.22. Sensitivity of the spatial distribution of the changes in bentonite porosity due to mineral dissolution and precipitation for several corrosion rates at t = 10^6 years. r is the radial distance to the axis of the disposal cell.

5.2.3 Conclusions

The main conclusions of the sensitivity analysis to the corrosion rate include:

1. The larger the corrosion rate the sooner the arrival of pH to its maximum. The computed pH for a corrosion rate of 0.1 μm/y shows a very different behaviour after $2 \cdot 10^5$ years because the pH keeps increasing and reaches a pH larger than 10. This behaviour is related to the sorption on weak 2 sorption sites.
2. The larger the corrosion rate, the larger the concentration of precipitated magnetite close to the canister/bentonite interface but the smaller the thickness of the zone where magnetite precipitates. Magnetite penetration at the end of the simulation is smaller than 5 cm (r < 5 dm) for a corrosion rate of 5 μm/y and reaches 10 cm (r = 5.5 dm) for 0.5 μm/y. The sensitivity run for a corrosion rate of 0.1 μm/y shows a notably smaller concentration of precipitated magnetite at the canister/bentonite interface and a much larger thickness of precipitation at $t = 10^6$ years than those for other corrosion rates.
3. Similar to magnetite, the larger the corrosion rate the smaller the thickness of the zone where siderite precipitates. The thickness is smaller than 5 cm (r < 5 dm) for a corrosion rate of 5 μm/y and is equal to that of siderite. The thickness of siderite is approximately 1 cm larger than that of magnetite for corrosion rates from 0.5 to 3 μm/y.
4. The thickness of the zone where calcite precipitates in the bentonite decreases with the corrosion rate and ranges from 4 to 10 cm for corrosion rates from 5 to 0.5 μm/y. For the smallest corrosion rate, calcite precipitates everywhere in the bentonite.
5. The computed concentrations of exchanged cations in the bentonite are not sensitive to changes in the corrosion rate.
6. The larger the corrosion rate, the faster the porosity reduction near the canister interface. The porosity at r = 4.6 dm is half its initial value after 4500 years for a corrosion rate of 5 μm/y and $2 \cdot 10^5$ years for 0.1 μm/y. The larger the corrosion rate, the smaller the thickness of bentonite affected by pore clogging.

5.3. Sensitivity to changes in the D_e of the bentonite

5.3.1 Introduction

All dissolved chemical species are assumed to have the same effective diffusion which is equal to $4.07 \cdot 10^{-11}$ m^2/s for the base run. Cationic species may have an effective diffusion larger than $4.07 \cdot 10^{-11}$ m^2/s while anionic species may diffuse slower. A set of sensitivity runs have been performed to evaluate the uncertainty in the value of the effective diffusion of the dissolved species. The effective diffusion for the sensitivity runs was taken equal to half and double the reference value, D_e, of $4.07 \cdot 10^{-11}$ m^2/s. The sensitivity runs will be denoted as $0.5D_e$ and $2D_e$, respectively.

5.3.2 Results of the sensitivity runs

Aqueous species

The computed concentrations of most of the dissolved species except for Fe^{2+} are not sensitive to the changes in D_e (Figure 5.23) because the solute flux from the bentonite into the granite is controlled by the advective transport of the granite water flow and not by solute diffusion through the bentonite.

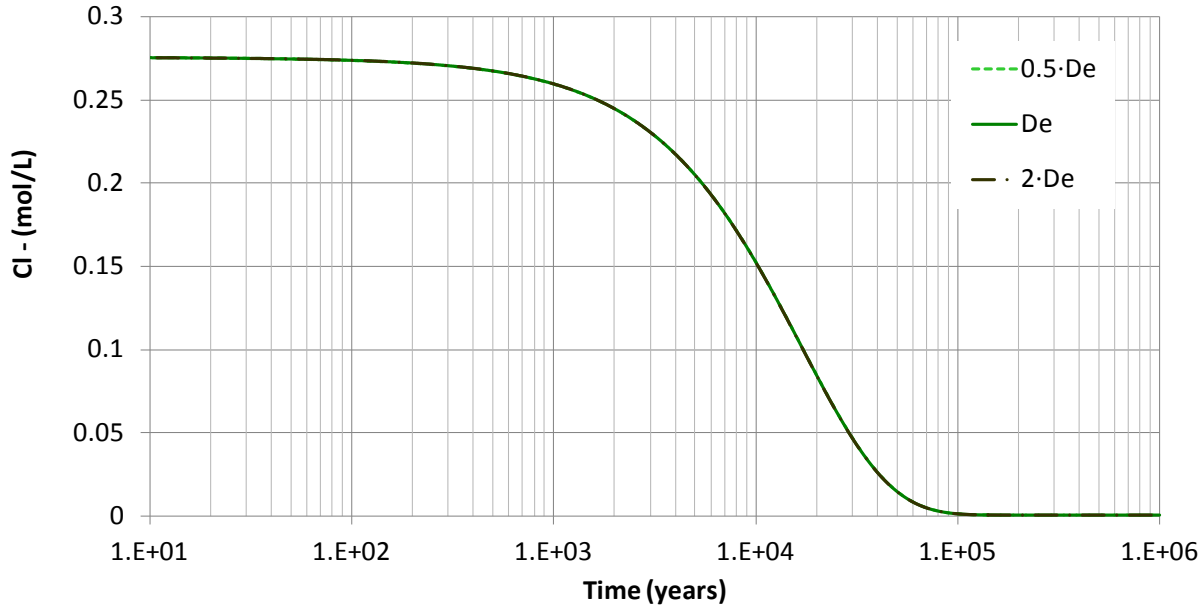

Figure 5.23. Sensitivity of the time evolution of the computed concentration of dissolved Cl^- in the bentonite at r = 4.6 dm to changes in the D_e of the bentonite. r is the radial distance to the axis of the disposal

Figure 5.24 shows the sensitivity of the time evolution of the computed concentration of the dissolved Fe^{2+} in the bentonite at r = 4.6 dm to changes in the D_e of the bentonite. The trends of the curves are similar for all the values of D_e. The larger the D_e, the smoother the increase of concentrations.

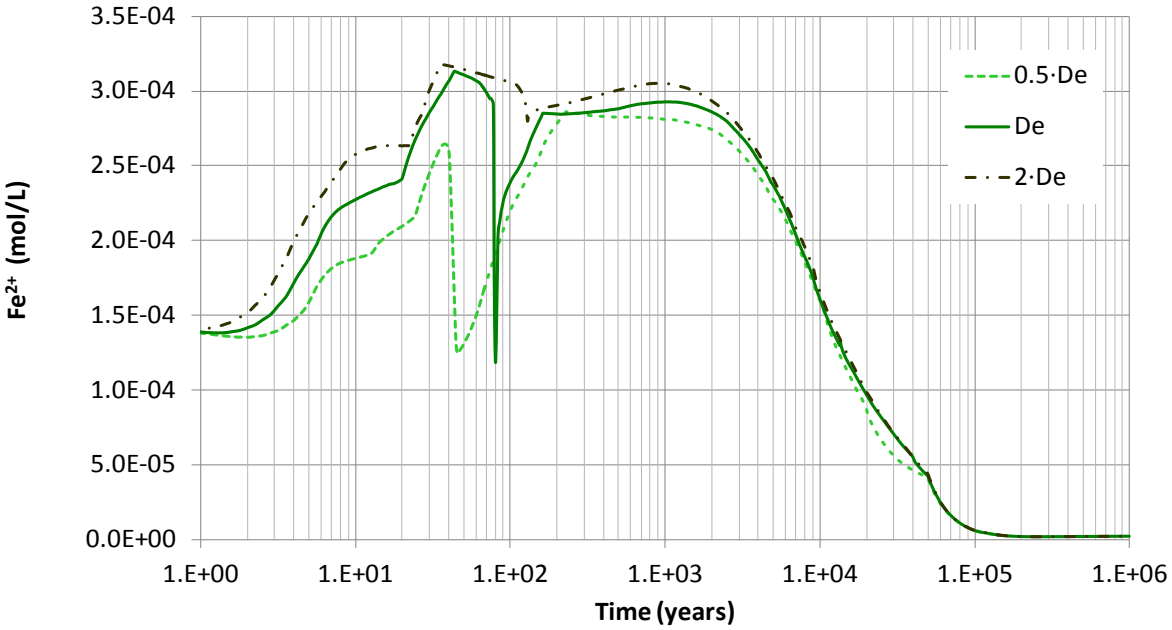

Figure 5.24. Sensitivity of the time evolution of the computed concentration of dissolved Fe^{2+} in the bentonite at r = 4.6 dm to changes in the D_e of the bentonite. r is the radial distance to the axis of the disposal cell.

Figure 5.25 and Figure 5.26 show the sensitivity of the spatial distribution of the computed concentration of dissolved Fe^{2+} at t = 10^2 and 10^6 years, respectively to changes in the D_e in the bentonite. The patterns of the curves are similar for all the values of D_e The larger the D_e, the larger the penetration of the iron front from the canister into the bentonite.

Figure 5.27 shows the sensitivity of the time evolution of the computed pH in the bentonite at r = 4.6 and r = 9.5 dm to changes in the D_e in the bentonite. The computed pH is not very sensitive to the change in the D_e in the bentonite. In fact, the curves are similar for all the values of D_e. The larger the D_e, the faster the changes in pH occur at r = 9.5 dm. Near the canister/bentonite interface (at r = 4.6 dm), the sensitivity is the opposite, the smaller the D_e, the faster the sharp increase in pH. In fact, the pH front caused by the competition of Fe^{2+} and H^+ for sorption sites is sensitive to the change in the D_e of the bentonite. Figure 5.28 shows the spatial distribution of the computed pH in the bentonite at t = 10^4 years. The smaller the D_e of the bentonite, the smaller the pH front and the smaller the penetration of the front.

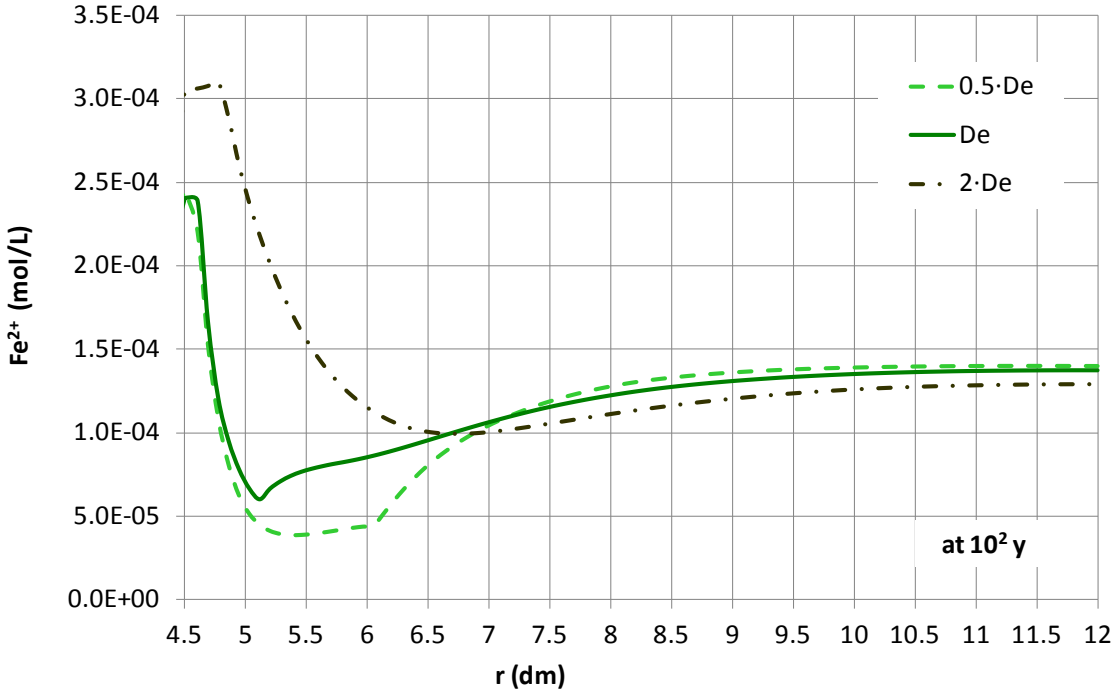

Figure 5.25. Sensitivity of the spatial distribution of the computed concentration of dissolved Fe^{2+} at t = 10^2 years to changes in the D_e of the bentonite. r is the radial distance to the axis of the disposal cell.

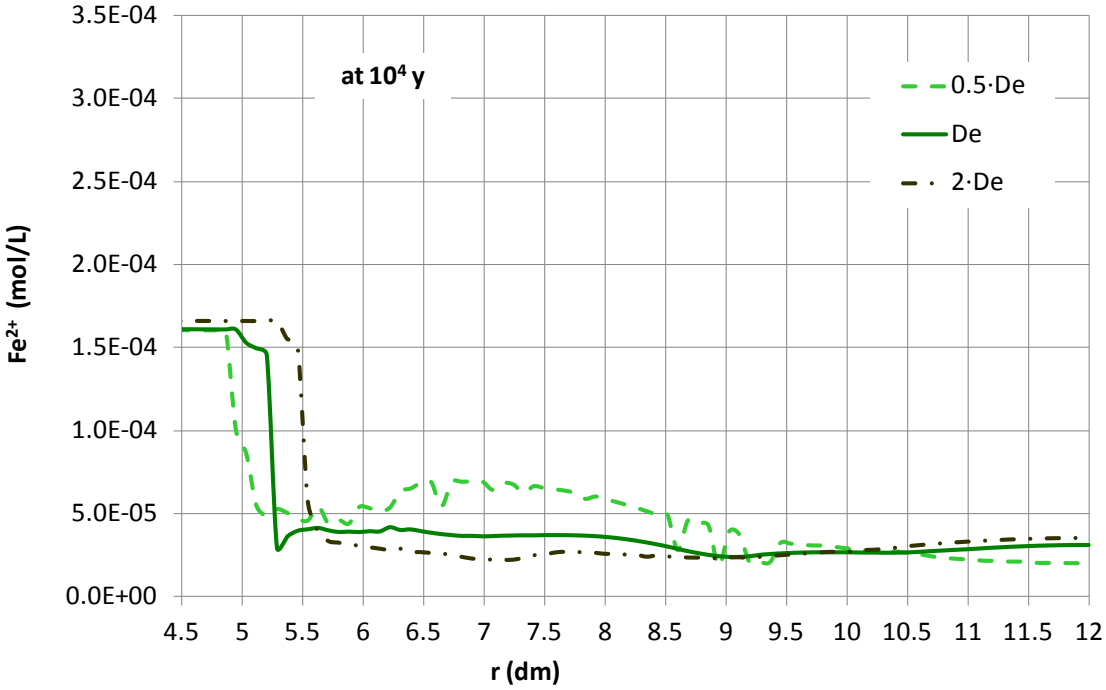

Figure 5.26. Sensitivity of the spatial distribution of the computed concentration of dissolved Fe^{2+} at t = 10^4 years to changes in the D_e of the bentonite. r is the radial distance to the axis of the disposal cell.

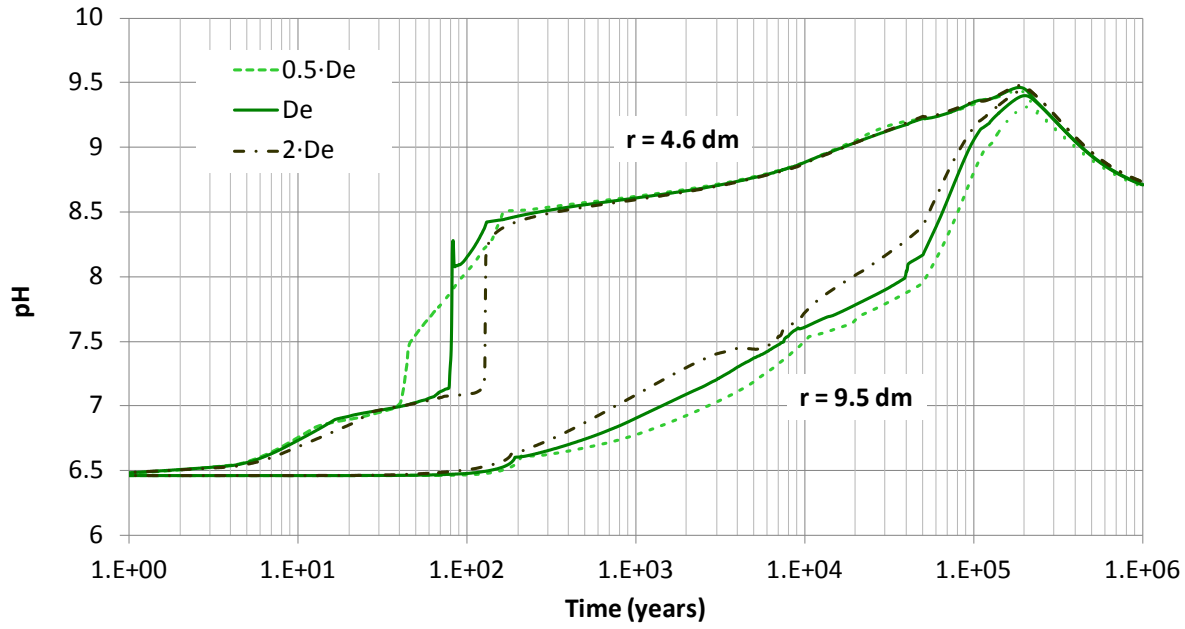

Figure 5.27. Sensitivity of the time evolution of the computed pH in the bentonite at r = 4.6 and r = 9.5 dm to changes in the D_e of the bentonite. r is the radial distance to the axis of the disposal cell.

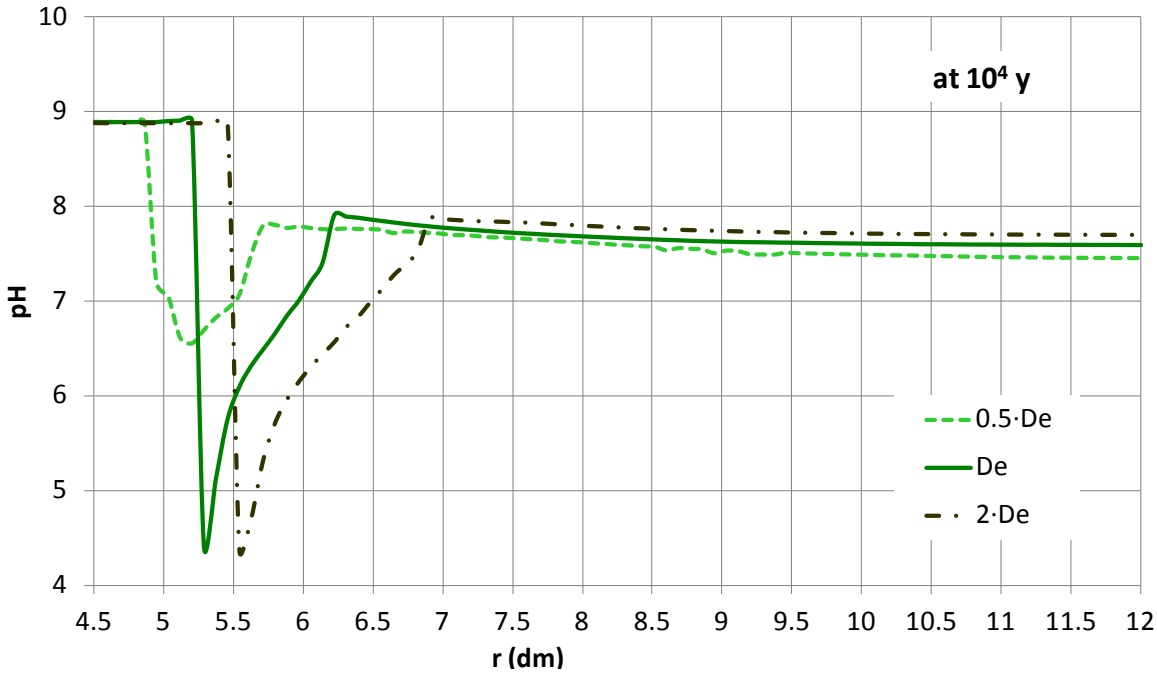

Figure 5.28. Sensitivity of the spatial distribution of the computed pH in the bentonite at t = 10^4 years to changes in the D_e of the bentonite. r is the radial distance to the axis of the disposal cell.

The computed Eh is not very sensitive to the changes in the D_e of the bentonite. In fact, the curves are similar for all the values of D_e (Figure 5.29). However, near the canister/bentonite interface (at r = 4.6 dm), the front of the Eh is sensitive to the D_e of the bentonite. The smaller the D_e, the faster the sharp increase in Eh. In fact, the Eh front associated with the pH front is sensitive to the change in the D_e of the bentonite. Figure 5.30 shows the spatial distribution of the computed Eh in the bentonite at t = 10^4 years. The smaller the D_e of the bentonite the smaller the Eh front and the smaller the penetration of the front.

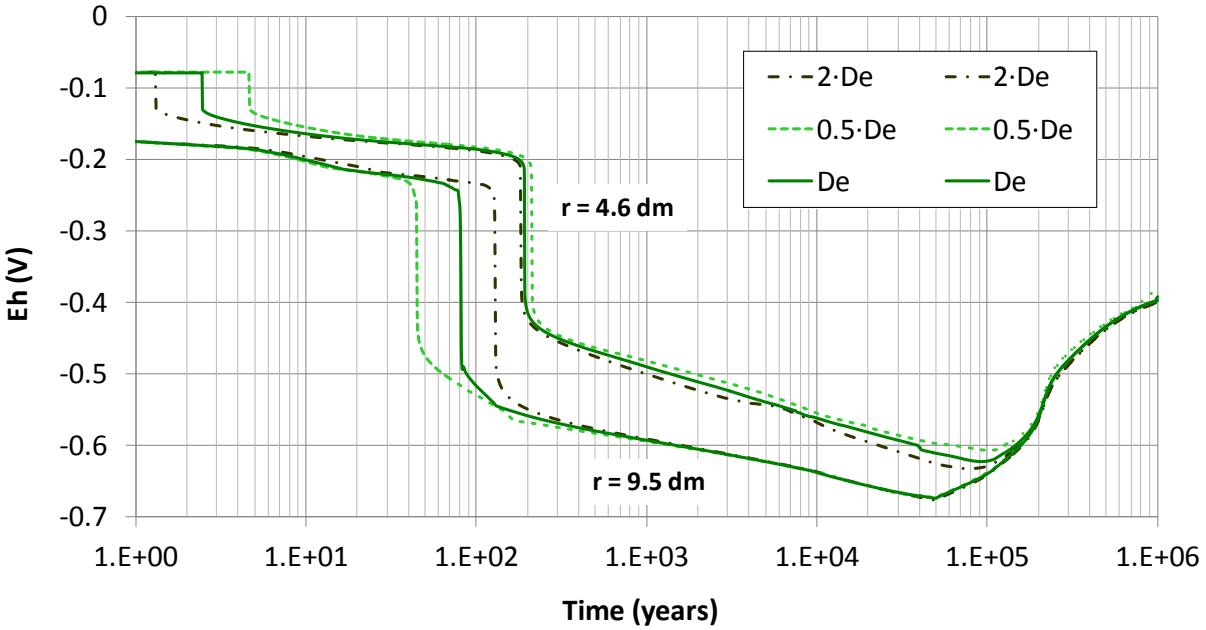

Figure 5.29. Sensitivity of the time evolution of the computed Eh in the bentonite at r = 4.6 and r = 9.5 dm to changes in the D_e of the bentonite. r is the radial distance to the axis of the disposal cell.

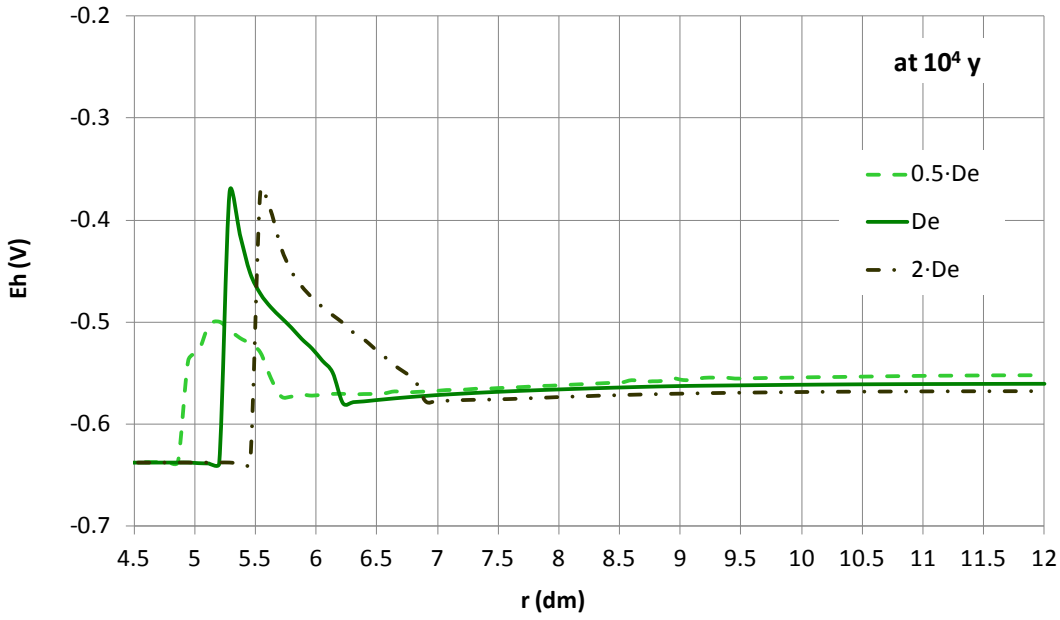

Figure 5.30. Sensitivity of the spatial distribution of the computed Eh in the bentonite at 10^4 years to changes in the D_e of the bentonite. r is the radial distance to the axis of the disposal cell.

Mineral phases

One can see in Figure 5.31 that the time evolution of the concentration of cumulative precipitated magnetite in the bentonite at r = 4.6 dm is not sensitive to an increase in the D_e of the bentonite. However, the concentration of cumulative precipitated magnetite decreases when the D_e decreases because the diffusive flux of dissolved Fe decreases when the D_e decreases. The spatial distribution of the concentration of cumulative precipitated magnetite in the bentonite at t = 10^6 years is clearly sensitive to changes in the D_e of the bentonite (Figure 5.32). The larger the D_e, the larger the thickness of the zone where magnetite precipitates. Such thickness increases from 4 to 9 cm when the D_e increases from $0.5D_e$ to $2D_e$.

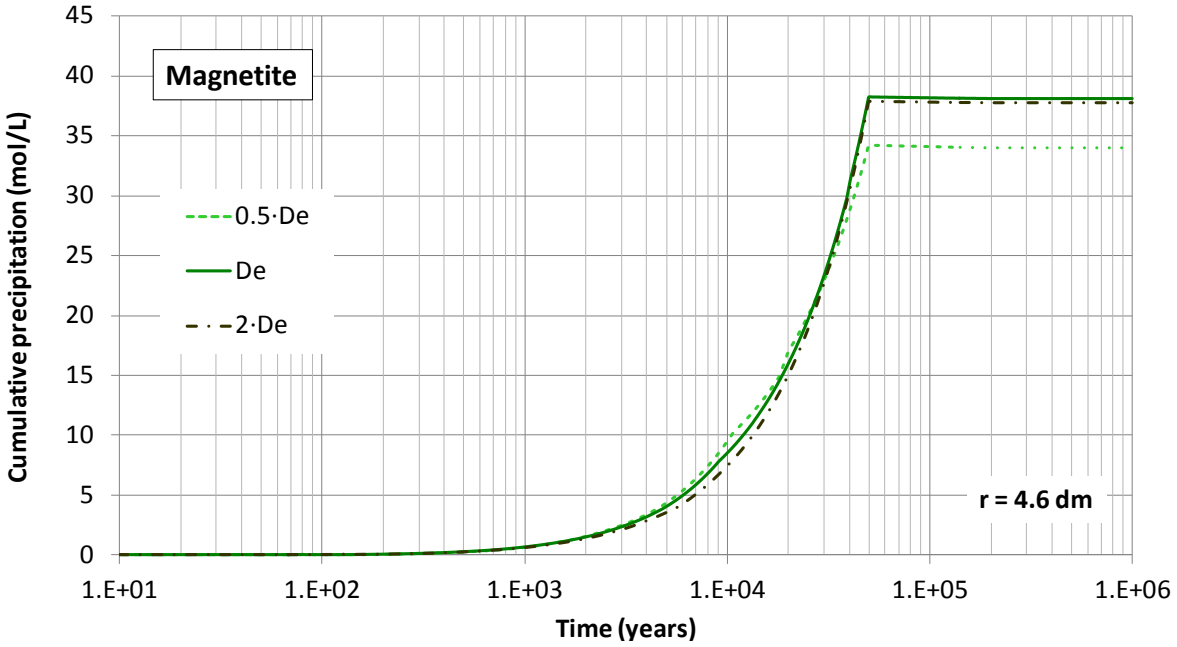

Figure 5.31. Sensitivity of the time evolution of the concentration of cumulative precipitated magnetite in the bentonite at r = 4.6 dm to changes in the D_e of the bentonite. r is the radial distance to the axis of the disposal cell.

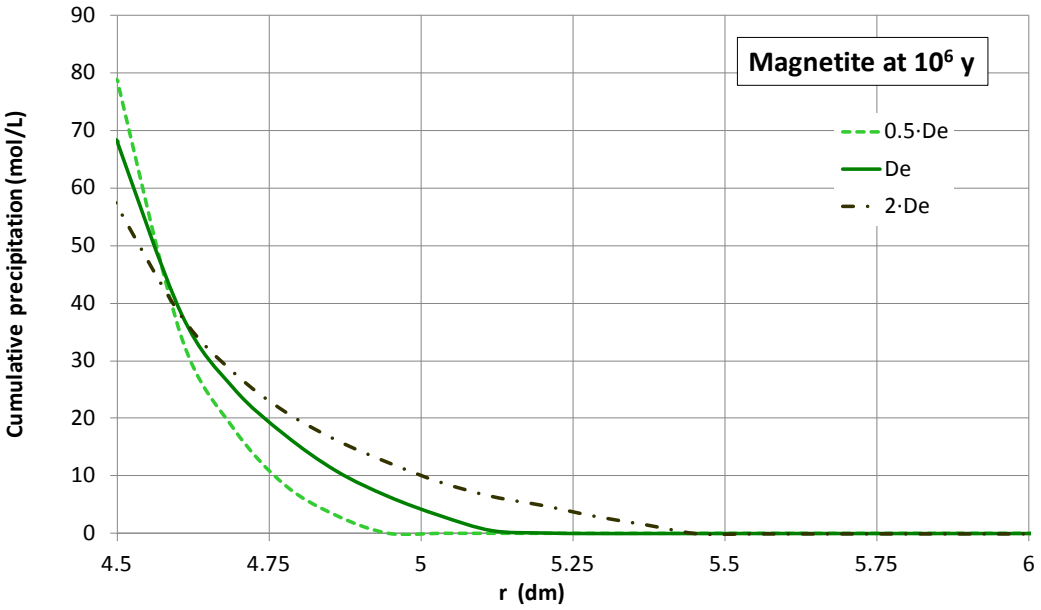

Figure 5.32. Sensitivity of the spatial distribution of the concentration of cumulative precipitated magnetite in the bentonite at t = 10^6 years to changes in the D_e of the bentonite. r is the radial distance to the axis of the disposal cell.

The time evolution of the concentration of cumulative precipitated siderite at r = 4.6 dm is sensitive to changes in the D_e of the bentonite. The larger the D_e, the sooner the precipitation starts and the smaller the steady-state concentration of siderite (Figure 5.33). The spatial distribution of the concentration of cumulative precipitated siderite in the bentonite at t = 10^6 years is clearly sensitive to changes in the D_e of the bentonite (Figure 5.34). The larger the D_e, the larger the thickness of the zone where siderite precipitates.

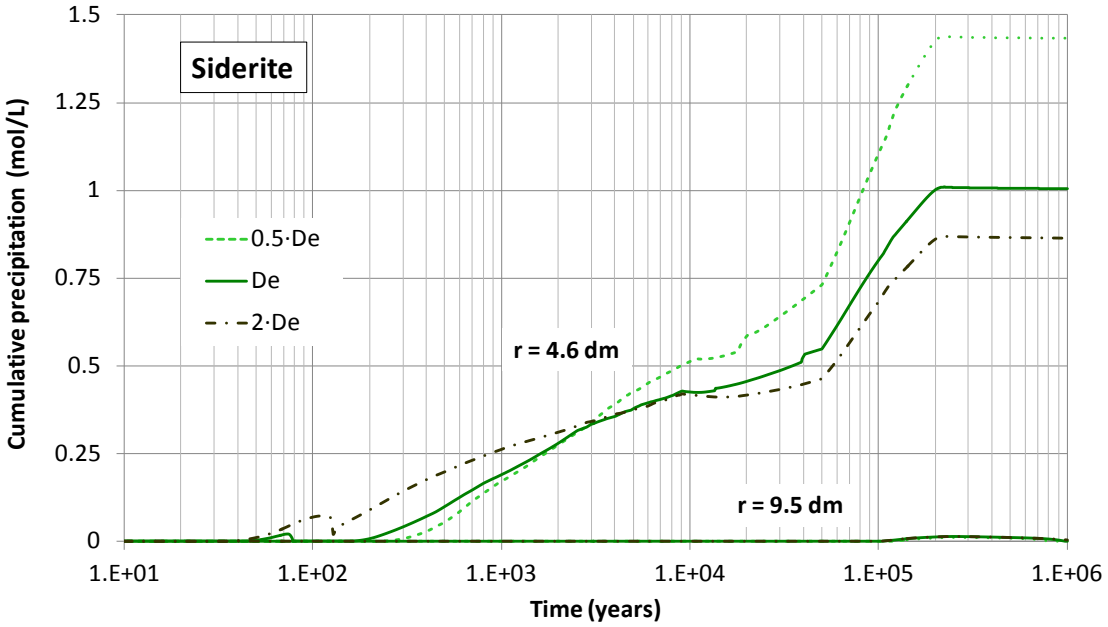

Figure 5.33. Sensitivity of the time evolution of the concentration of cumulative precipitated siderite in the bentonite at r = 4.6 dm to changes in in the D_e of the bentonite. r is the radial distance to the axis of the disposal cell.

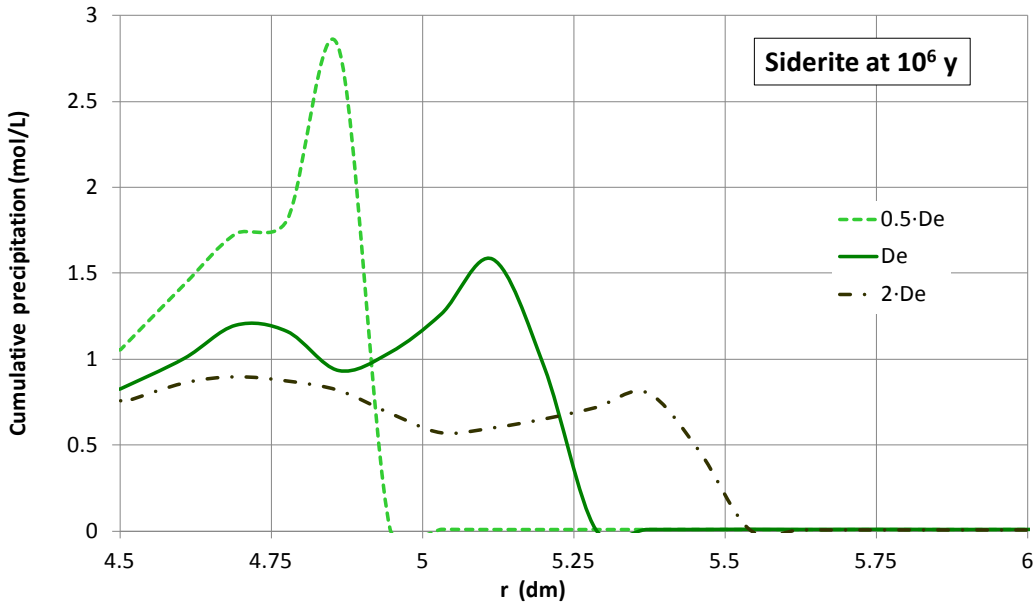

Figure 5.34. Sensitivity of the spatial distribution of the concentration of cumulative precipitated siderite in the bentonite at 10^6 years to changes in the D_e of the bentonite. r is the radial distance to the axis of the disposal cell.

One can see in Figure 5.35 that the time evolution of the concentration of cumulative precipitated calcite in the bentonite at r = 4.6 dm and r = 9.5 dm are slightly sensitive to changes in the D_e of the bentonite. The changes are larger at r = 4.6 dm. The spatial distribution of the concentration of cumulative precipitated calcite in the bentonite at t = 10^6 years is clearly sensitive to changes in the D_e of the bentonite (Figure 5.41). The larger the D_e, the larger the thickness of the zone where calcite precipitates.

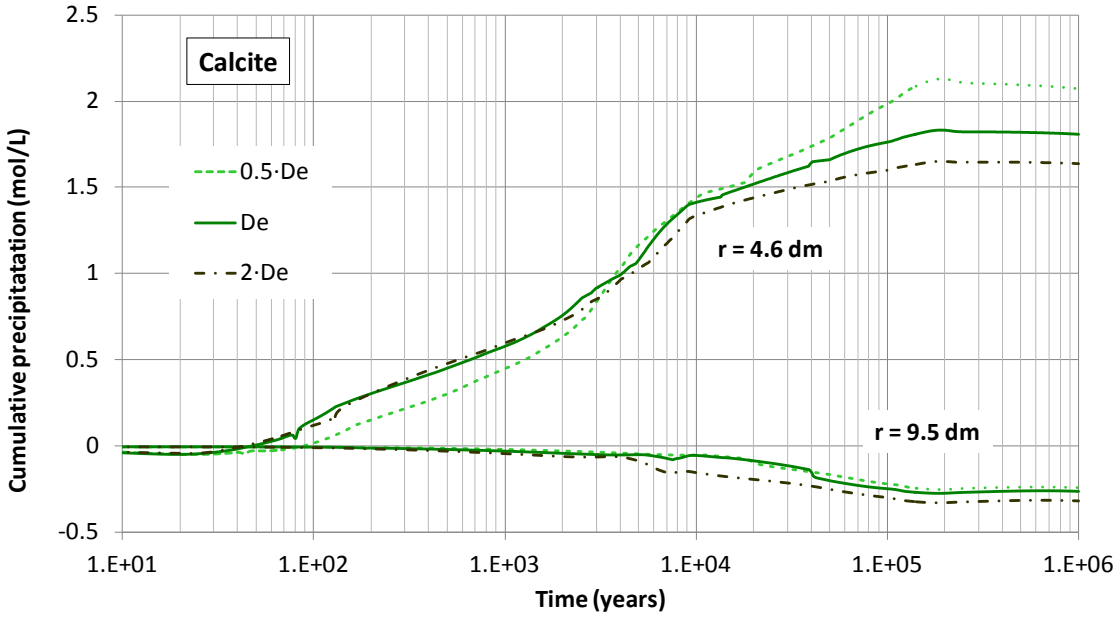

Figure 5.35. Sensitivity of the time evolution of the concentration of cumulative precipitated calcite in the bentonite at r = 4.6 dm to changes in in the D_e of the bentonite. r is the radial distance to the axis of the disposal cell.

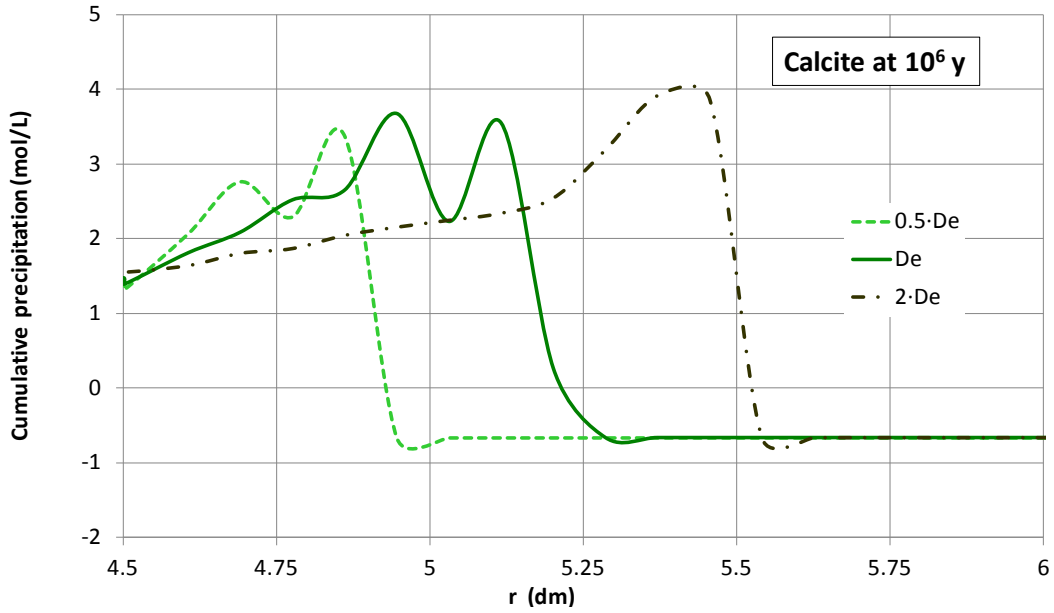

Figure 5.36. Sensitivity of the spatial distribution of the concentration of cumulative precipitated calcite in the bentonite at 10^6 years to changes in the D_e of the bentonite. r is the radial distance to the axis of the disposal cell.

Cation exchange

Figure 5.37 shows the sensitivity of the time evolution of the computed concentration of the exchanged Fe^{2+} in the bentonite at r = 4.6 and 9.5 dm to changes in the D_e of the bentonite. The sensitivity of the concentration of the exchanged Fe^{2+} is similar to that of the concentration of the dissolved Fe^{2+} (see Figure 4.24).

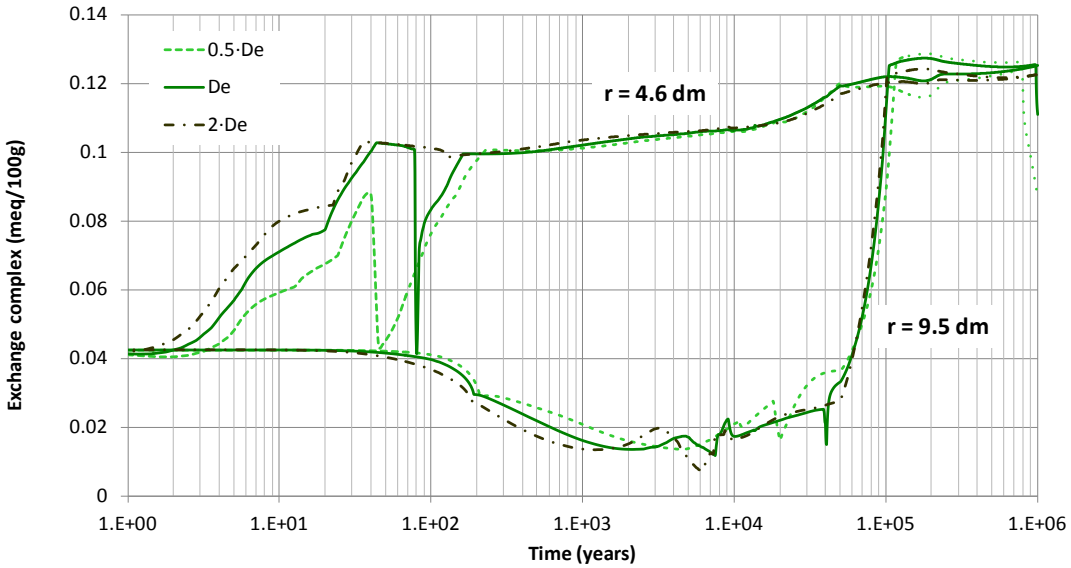

Figure 5.37. Sensitivity of the time evolution of the computed concentrations of exchanged Fe^{2+} in the bentonite at r = 4.6 dm to changes in the D_e of the bentonite. r is the radial distance to the axis of the disposal cell.

Sorbed species

The time evolution of computed concentrations of sorbed species in the bentonite has been analysed at several locations for several values the D_e of the bentonite. Figure 5.38 shows the time evolution of the concentrations of sorbed species at r = 4.6 dm for the smallest and largest values of the D_e of the bentonite, respectively. These figures can be compared with those of the base run shown in Figure 4.24. The competition of dissolved Fe^{2+} and H^+ for weak 1 sorption sites produces a sorption front at 80 years for the reference value of the D_e. Competition for sorption sites occur also for other values of the D_e of the bentonite. However, it takes place at different times and speeds. For the largest D_e, the sorption front is delayed until 120 years. For the smallest D_e, it takes place after 40 years. $S^{W2}OH$ is the main sorbed species during most of the time. A second sorption front can be observed as an increase in the concentration of $S^{W2}OH$ and a decrease of the concentration of $S^{W2}OH^{2+}$.

Figure 5.39 shows the comparison of the spatial distribution of the sorbed species at t = 10^4 years computed for different values of the D_e of the bentonite. The sorption fronts observed at t = 10^4 years and r = 5.3 dm in the base run (Figure 4.31) are also observed in the sensitivity run of the smallest D_e at r = 4.9 dm while the front occurs at r = 5.5 dm for the largest D_e.

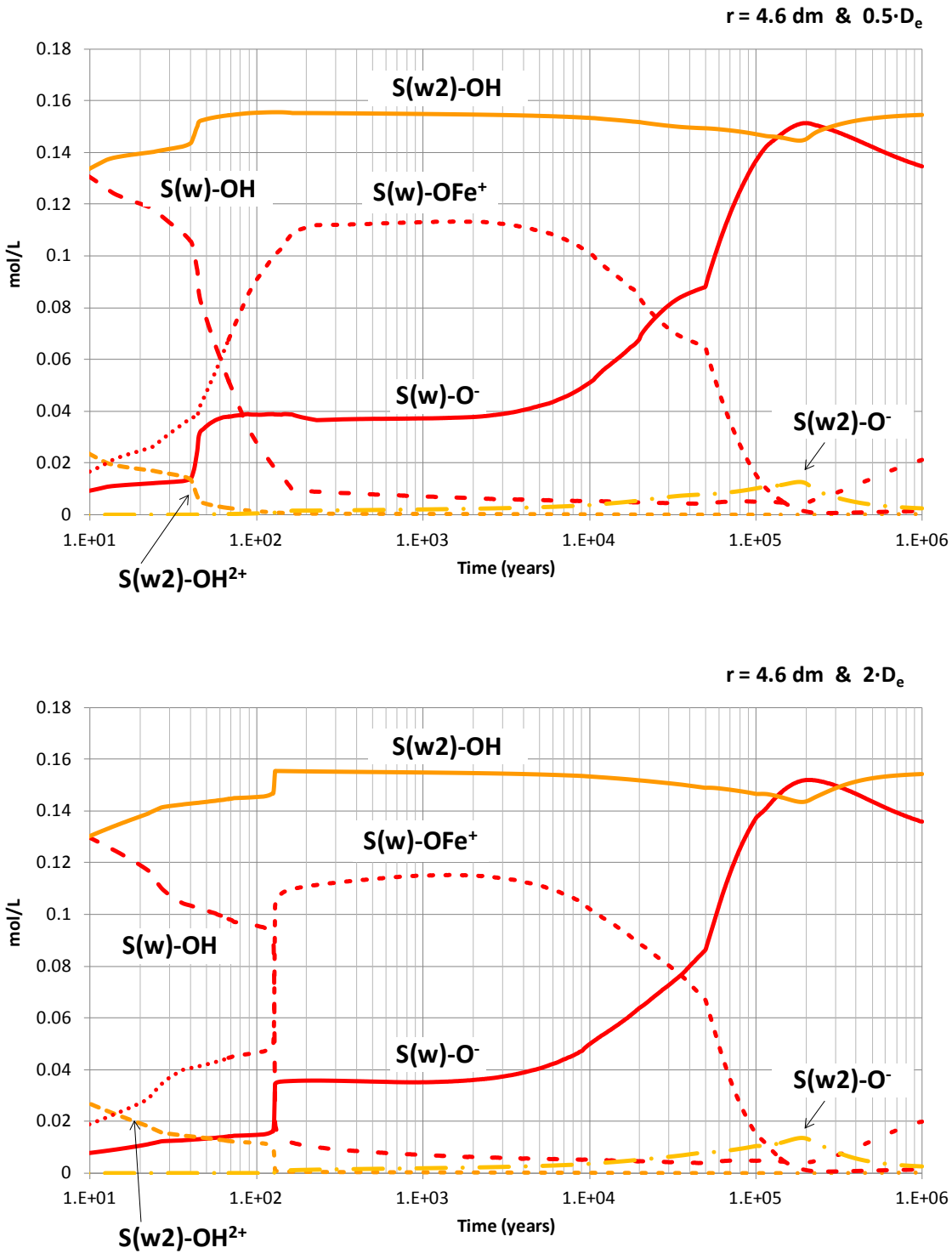

Figure 5.38. Time evolution of the concentration of sorbed species in the bentonite at r = 4.6 dm for a D_e of the bentonite equal to half (top) and twice (bottom) its reference value. r is the radial distance to the axis of the disposal cell.

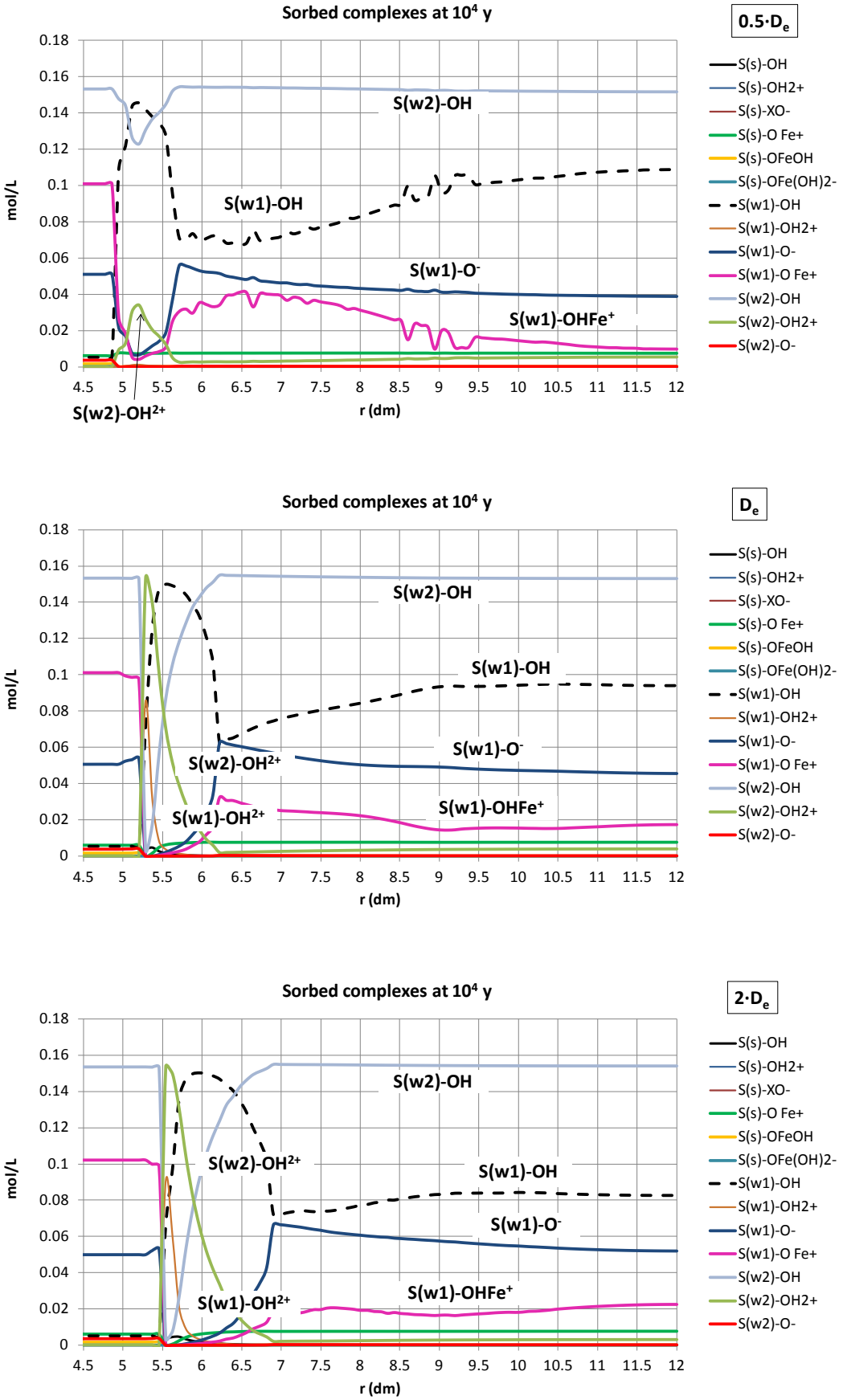

Figure 5.39. Spatial distribution of the concentration of sorbed species in the bentonite at t = 10^4 years for several values of the D_e of the bentonite. r is the radial distance to the axis of the disposal cell.

Hydrogen pressure

The time evolution of H_2(g) partial pressure in the bentonite for several values of the D_e of the bentonite is shown in Figure 5.40. The larger the D_e of the bentonite, the larger the H_2(g) partial pressure because hydrogen pressures are proportional to the concentrations of H_2(aq) which in turn depend on the diffusion coefficient. However, the changes in the H_2(g) partial pressure caused by changes in the D_e of the bentonite are generally small.

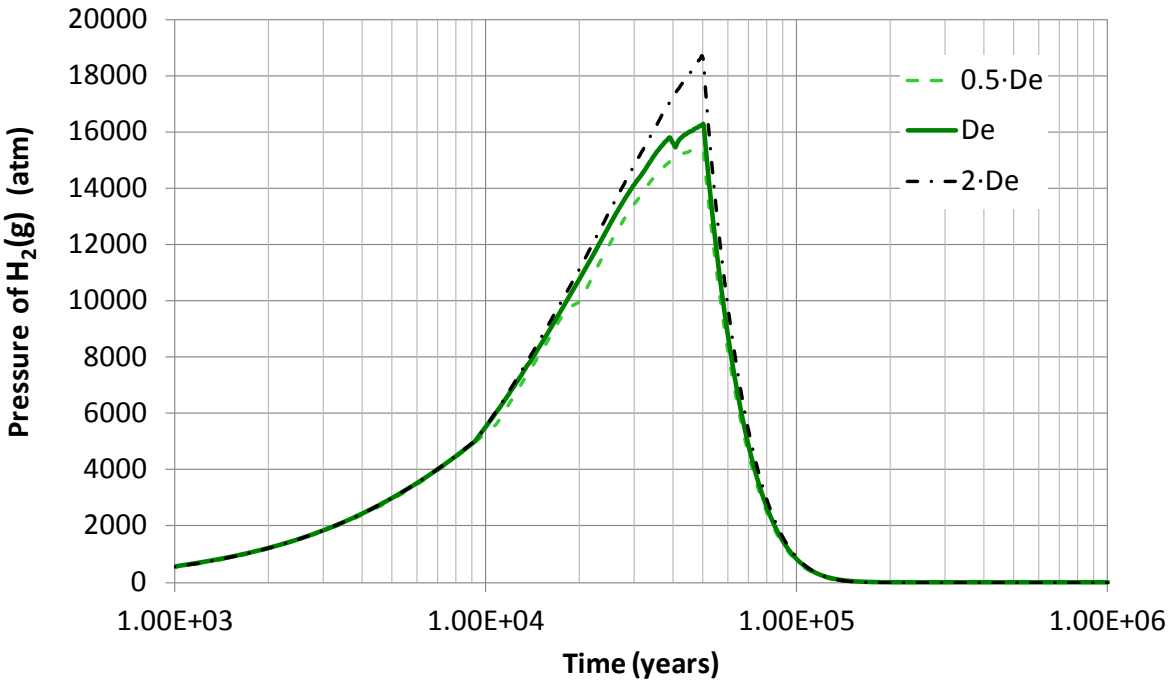

Figure 5.40. Sensitivity of the time evolution of the hydrogen partial pressure in the bentonite to changes in the D_e of the bentonite.

Changes in porosity

Changes in the bentonite porosity have been calculated from the computed mineral dissolution/precipitation for several values of the D_e of the bentonite. Figure 5.41 shows the changes in the bentonite porosity caused by mineral dissolution/precipitation at r = 4.6 and 9.5 dm. Porosity changes at r = 4.6 dm are not very sensitive to the D_e of the bentonite. The sensitivity of the spatial distribution of the porosity at t = 10^4 and 10^6 years to changes in the D_e of the bentonite are shown in Figure 5.42 and Figure 5.43, respectively. The precipitation of magnetite close to the canister causes a decrease in bentonite porosity. The larger the D_e of the bentonite, the larger the zone affected by the porosity reduction and the larger the thickness of bentonite affected by pore clogging.

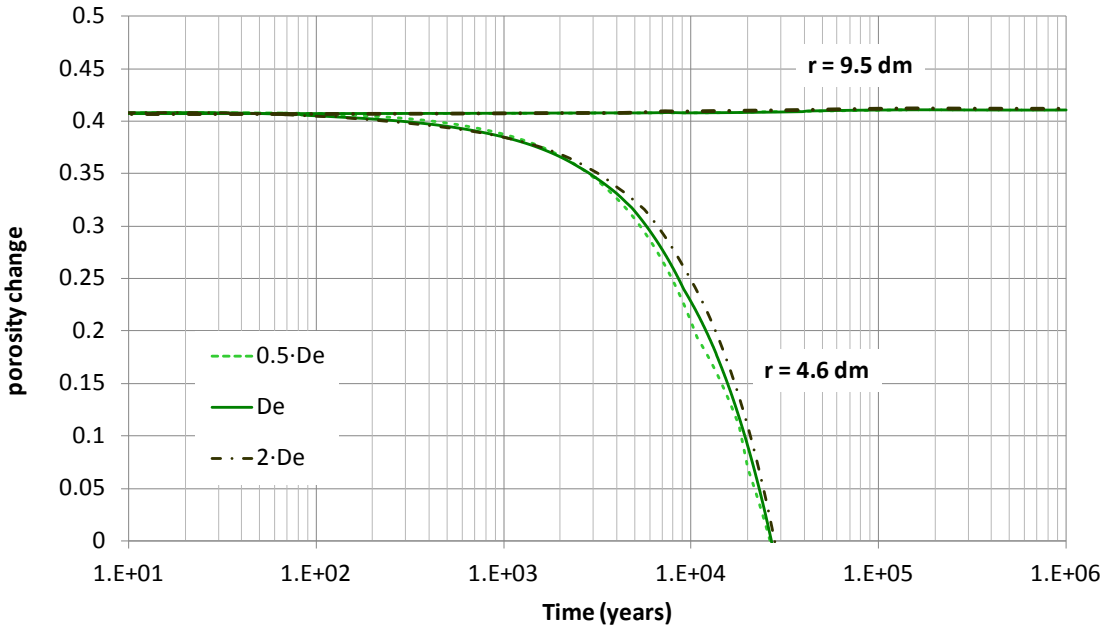

Figure 5.41. Sensitivity of the time evolution of the changes in bentonite porosity due to mineral dissolution and precipitation for several values of the D_e of the bentonite.

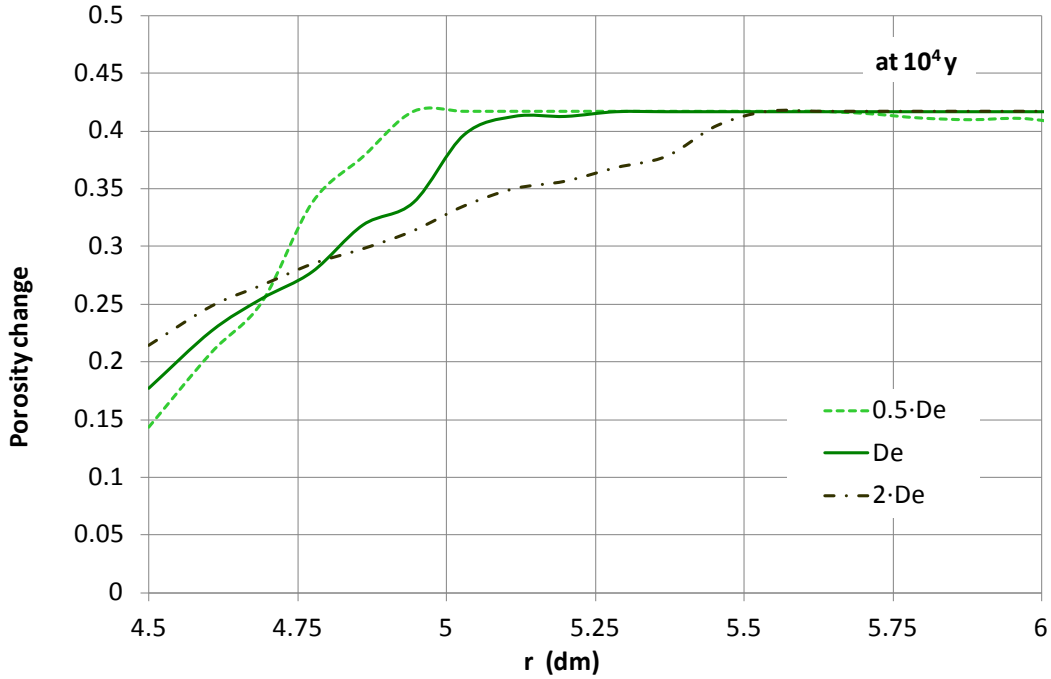

Figure 5.42. Sensitivity of the spatial distribution of the changes in bentonite porosity at t = 10^4 years due to mineral dissolution and precipitation for several values of the D_e of the bentonite. r is the radial distance to the axis of the disposal cell.

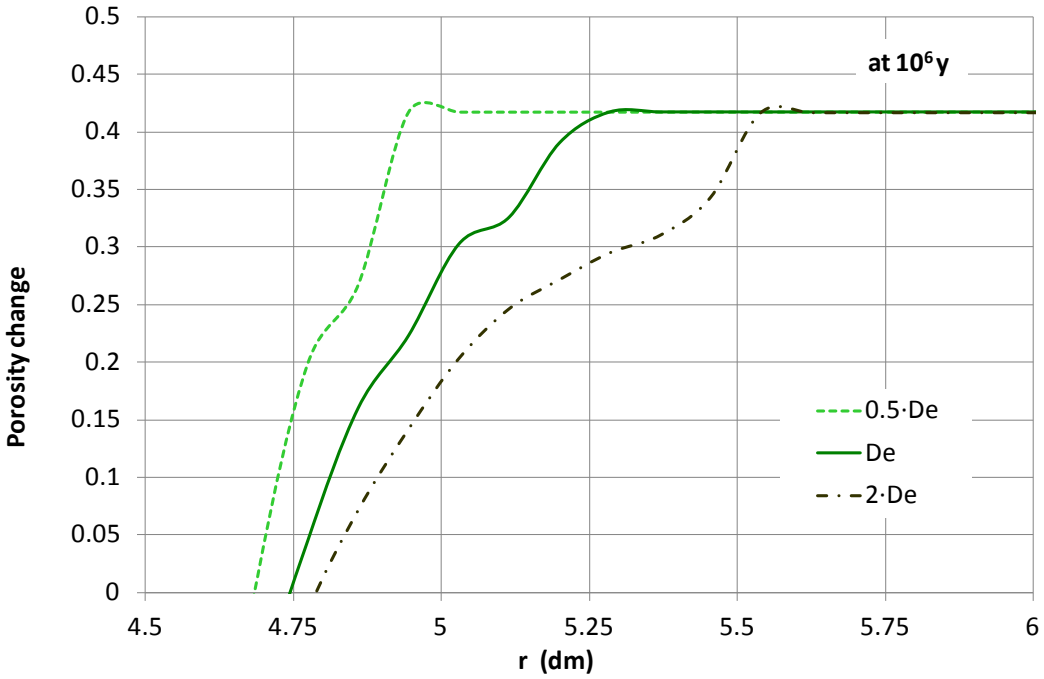

Figure 5.43. Sensitivity of the spatial distribution of the changes in bentonite porosity at t = 10^6 years due to mineral dissolution and precipitation for several values of the D_e of the bentonite. r is the radial distance to the axis of the disposal cell.

5.3.3 Conclusions

The main conclusions of the sensitivity analysis to the D_e of the bentonite include:

1. Except for the dissolved Fe^{2+}, the computed concentrations of most dissolved species are not sensitive to the changes in D_e because the solute flux from the bentonite into the granite is controlled by the advective transport of the granite water flow and not by solute diffusion through the bentonite. The larger the D_e, the smoother is the increase of the curve of the concentration of dissolved Fe^{2+}.

2. The computed pH is not very sensitive to the change in the D_e of the bentonite. In fact, the time evolution curves are similar for all the values of D_e. The larger the D_e, the faster the changes in pH occur at r = 9.5 dm. Near the canister/bentonite interface (at r = 4.6 dm), the sensitivity is the opposite, the smaller the D_e, the faster the sharp increase in pH. In fact, the pH front caused by the competition of Fe^{2+} and H^+ for sorption sites is sensitive to the change in the D_e of the bentonite. The smaller the D_e, the smaller the magnitude and the penetration of the pH front.

3. The larger the D_e, the larger the thickness of the zone where magnetite, siderite and calcite precipitate. The thickness of magnetite precipitation increases from 4 to 9 cm when the De increases from *0.5De* to *2De*.

4. The computed concentrations of exchanged cations in the bentonite are not sensitive to changes in the D_e of the bentonite.
5. The changes in the H2(g) partial pressure caused by changes in the D_e of the bentonite are generally small.
6. The larger the D_e of the bentonite, the larger the zone affected by the porosity reduction and the larger the thickness of bentonite affected by pore clogging.

5.4. Sensitivity to changes in the groundwater flow

5.4.1 Introduction

A flow rate of 0.01 L/y per canister is imposed at the outer element of the model to simulate the washing of the bentonite surface by groundwater water through the granite. This water flow could be larger than 0.01 L/year in areas where the rock is more fractured. In fact, Samper et al. (2010) and Lu et al. (2012) used a value of 0.06 L/year. Several sensitivity runs were performed to evaluate the model uncertainties caused by uncertainties in the groundwater flow through the granite. The following groundwater flows were taken for the sensitivity runs: equal to 0.05 and 0.1 L/y.

5.4.2 Results of the sensitivity runs

Aqueous species

The computed concentrations of dissolved species are very sensitive to the changes in the water flow, Q, because the solute flux from the bentonite into the granite is controlled mostly by the advective transport of the granite water flow. Figure 5.44 shows the sensitivity of the time evolution of the computed concentration of dissolved Cl^- in the bentonite at r = 9.5 dm to changes in the groundwater flow Q. The larger the Q, the faster the decrease of the concentrations. In fact, the time needed for the concentration to decrease to a half, $T_{1/2}$, is proportional to Q.

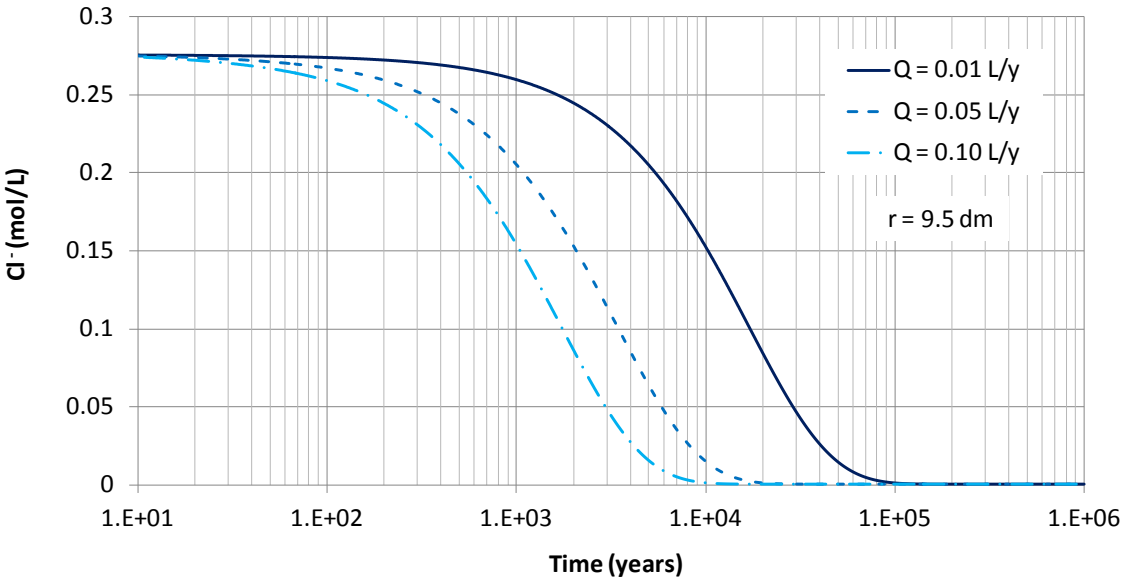

Figure 5.44. Sensitivity of the time evolution of the computed concentration of dissolved Cl^- in the bentonite at r = 9.5 dm to changes in the groundwater flow, Q (L/year). r is the radial distance to the axis of the disposal cell.

Figure 5.45 shows the sensitivity of the time evolution of the computed concentration of the dissolved Fe^{2+} in the bentonite at r = 4.6 dm and 9.5 dm to changes in the groundwater flow Q. The larger the Q the faster the concentrations decrease after 200 years. Figure 5.46 shows the sensitivity of the spatial distribution of the computed concentration of dissolved Fe^{2+} at t = 10^3 years to changes in Q. Once again, the larger the flow Q, the smaller the concentration and the faster the concentrations decrease.

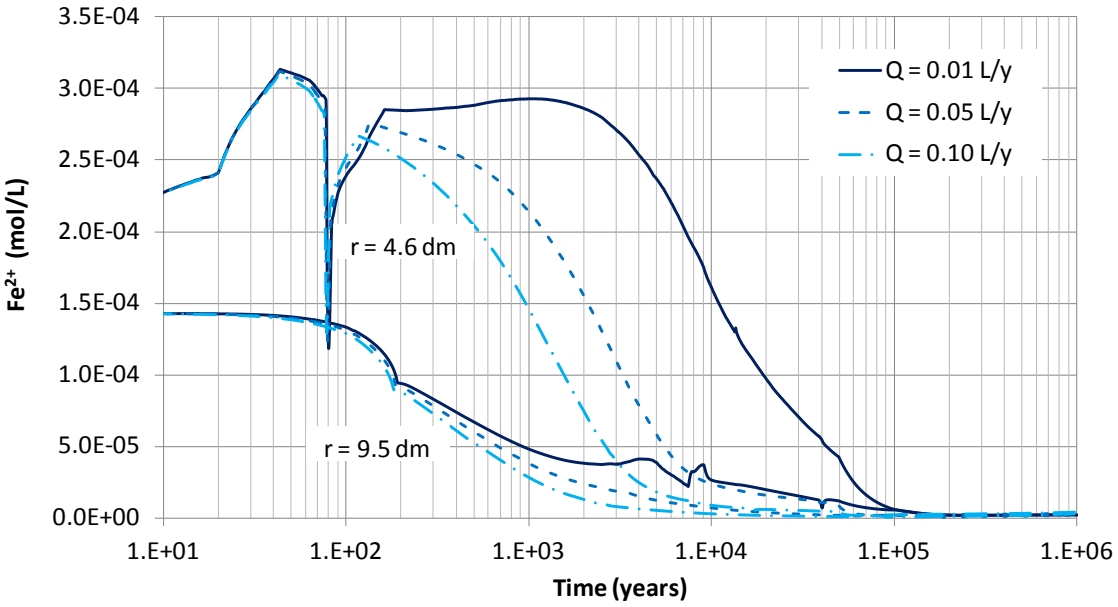

Figure 5.45. Sensitivity of the time evolution of the computed concentration of dissolved Fe^{2+} in the bentonite at r = 4.6 and r = 9.5 dm to changes in the groundwater flow, Q (L/year). r is the radial distance to the axis of the disposal cell.

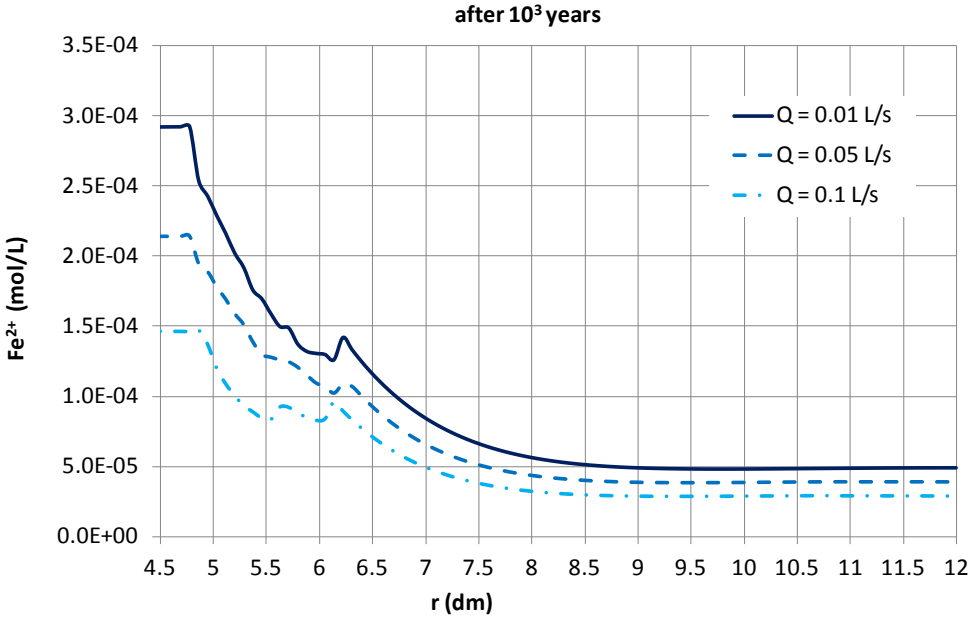

Figure 5.46. Sensitivity of the spatial distribution of the computed concentration of dissolved Fe^{2+} in the bentonite at t = 10^3 years to changes in the groundwater flow, Q (L/year). r is the radial distance to the axis of the disposal cell.

Figure 5.47 shows the sensitivity of the time evolution of the computed pH in the bentonite at r = 4.6 and r = 9.5 dm to changes in the groundwater flow, Q. The computed pH is slightly sensitive to the change in Q after 400 years. The larger the *Q* the larger the pH from 400 to $6 \cdot 10^4$ years. After $6 \cdot 10^4$ years, the computed pH is largest for the smallest groundwater flow. Figure 5.48 shows the spatial distribution of the computed pH in the bentonite at t = 10^4 years. The larger the Q, the smaller the pH front.

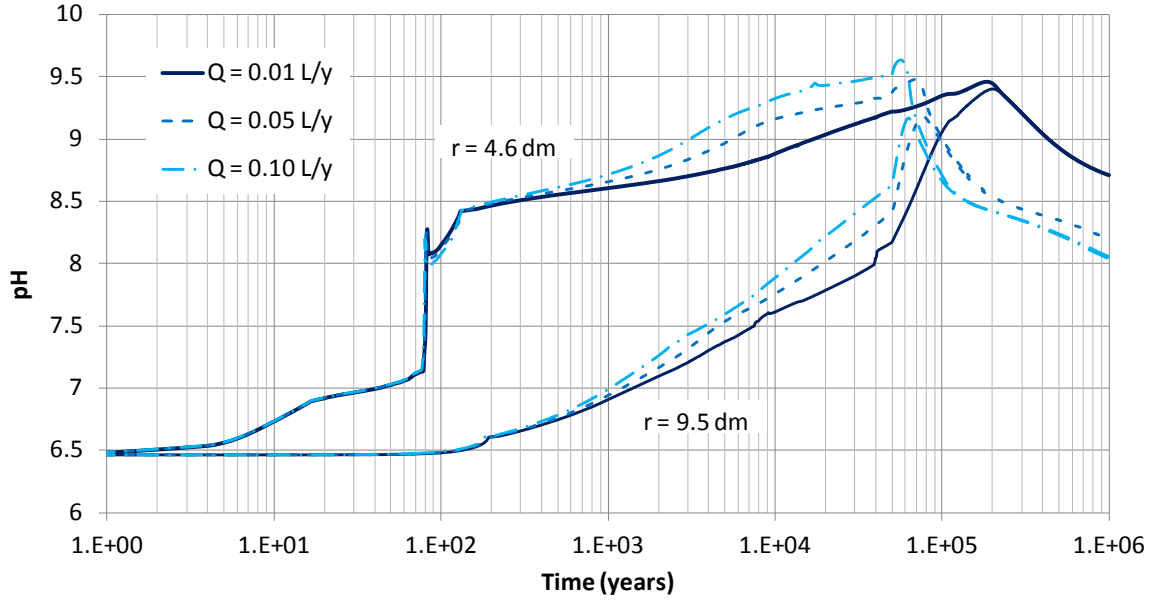

Figure 5.47. Sensitivity of the time evolution of computed pH in the bentonite at r = 4.6 and r = 9.5 dm to changes in the groundwater flow, Q (L/year). r is the radial distance to the axis of the disposal cell.

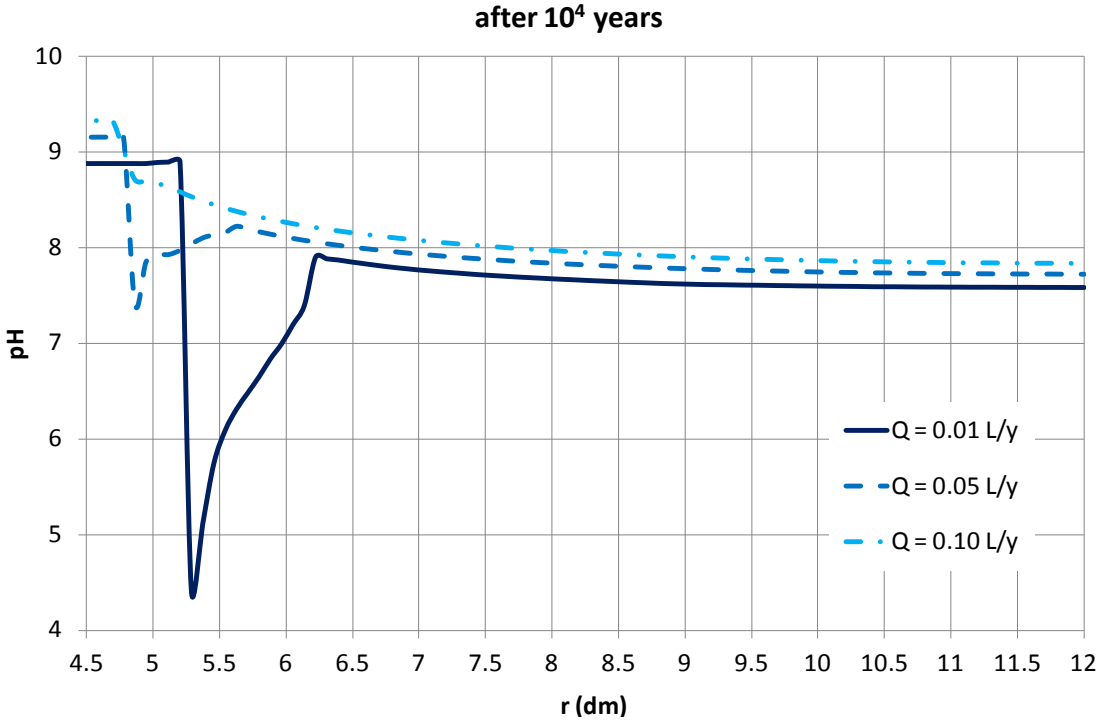

Figure 5.48. Sensitivity of the spatial distribution of computed pH in the bentonite at t = 10^4 years to changes in the groundwater flow, Q (L/year). r is the radial distance to the axis of the disposal cell.

The computed Eh is not sensitive to the change in the groundwater flow Q (Figure 5.49). However, near the canister/bentonite interface (at r = 4.6 dm), the front of the Eh is sensitive to the groundwater flow Q (Figure 5.50). The larger the Q, the smaller the Eh front.

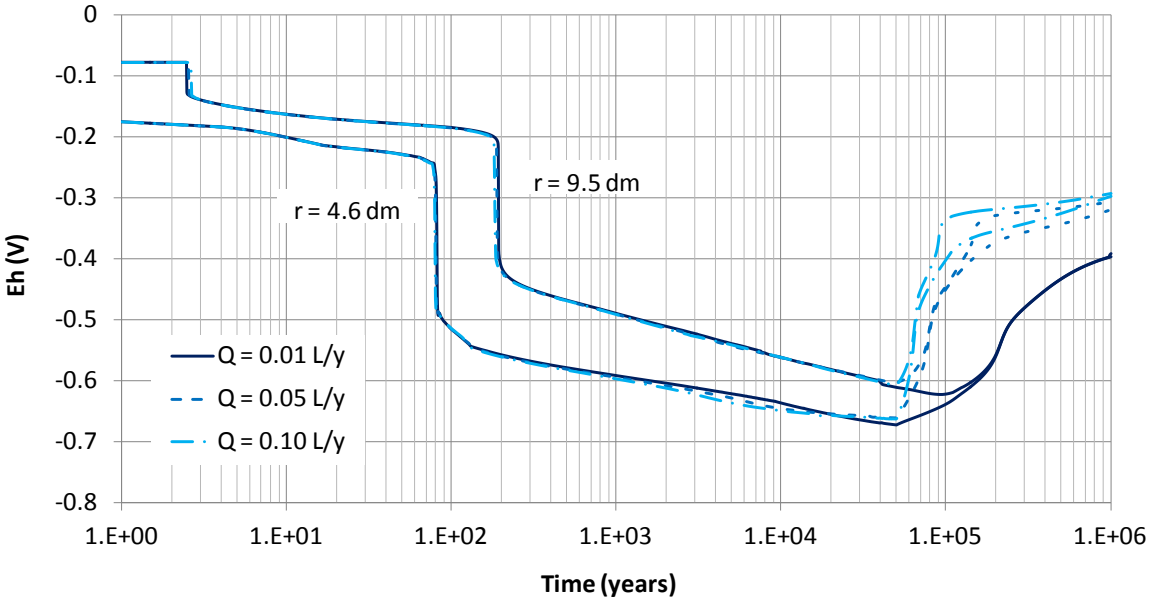

Figure 5.49. Sensitivity of the time evolution of computed Eh in the bentonite at r = 4.6 and r = 9.5 dm to changes in the groundwater flow, Q (L/year). r is the radial distance to the axis of the disposal cell.

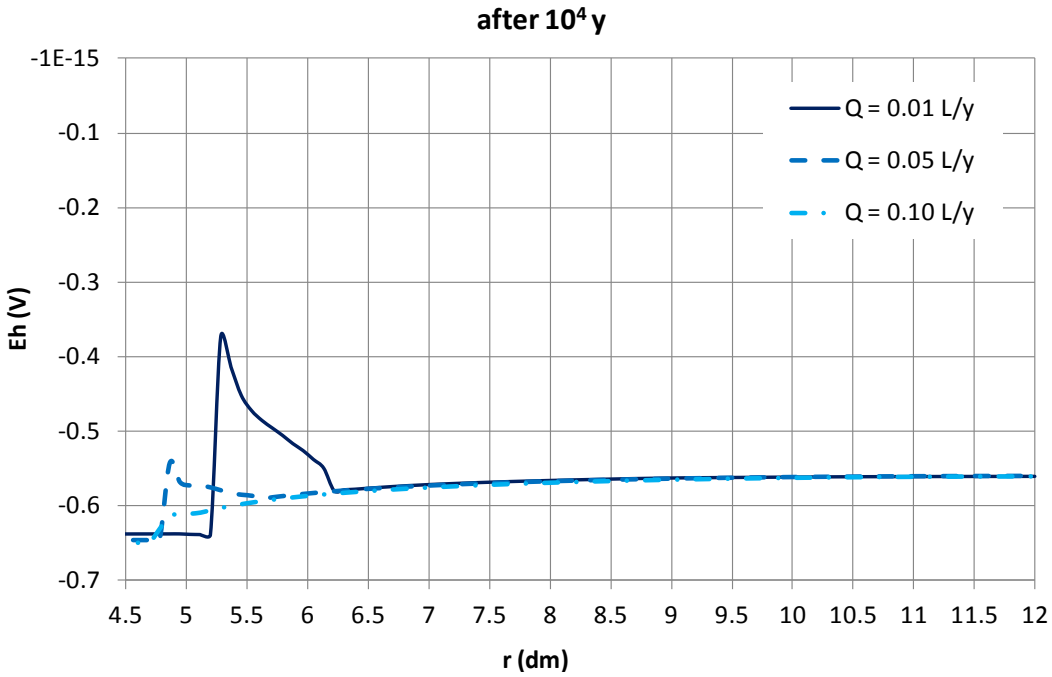

Figure 5.50. Sensitivity of the spatial distribution of computed pH in the bentonite at t = 10^4 years to changes in the groundwater flow, Q (L/year). r is the radial distance to the axis of the disposal cell.

Mineral phases

One can see in Figure 5.51 that the time evolution of the concentration of cumulative precipitated magnetite in the bentonite at r = 4.6 dm is strongly sensitive to the increase in the groundwater flow, Q. The larger the Q, the smaller the concentration of precipitated magnetite. The spatial distribution of the concentration of cumulative precipitated magnetite in the bentonite at t = 10^6 years is also very sensitive to changes in Q (Figure 5.51). The larger the Q, the smaller the thickness of the zone where magnetite precipitates. Such thickness decreases from 6 cm to less than 2 cm when Q increases by a factor of 10.

The time evolution of the concentration of cumulative precipitated siderite at r = 4.6 dm is very sensitive to Q. The larger the Q, the larger the precipitation of siderite (Figure 5.52). The spatial distribution of the concentration of cumulative precipitated siderite in the bentonite at t = 10^6 years is also sensitive to changes in Q (Figure 5.53). The larger the Q, the smaller the thickness of the zone where siderite precipitates.

One can see in Figure 5.54 that the concentration of cumulative precipitated calcite in the bentonite at r = 4.6 dm is very sensitive to the changes in groundwater flow, Q. The spatial distribution of the concentration of calcite in the bentonite at t = 10^6 years is also very sensitive to changes in Q (Figure 5.55). The larger the Q, the smaller the zone where calcite precipitates.

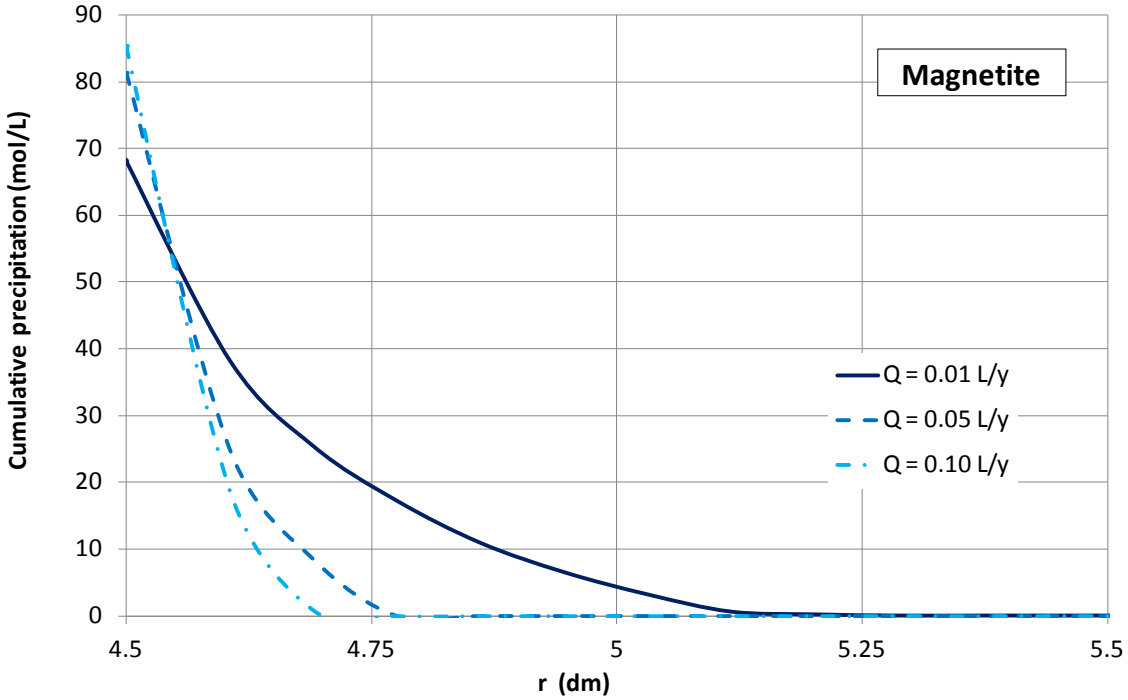

Figure 5.51. Sensitivity of the spatial distribution of computed concentration of cumulative precipitated magnetite in the bentonite at t = 10^6 years to changes in the groundwater flow, Q(L/year). r is the radial distance to the axis of the disposal cell.

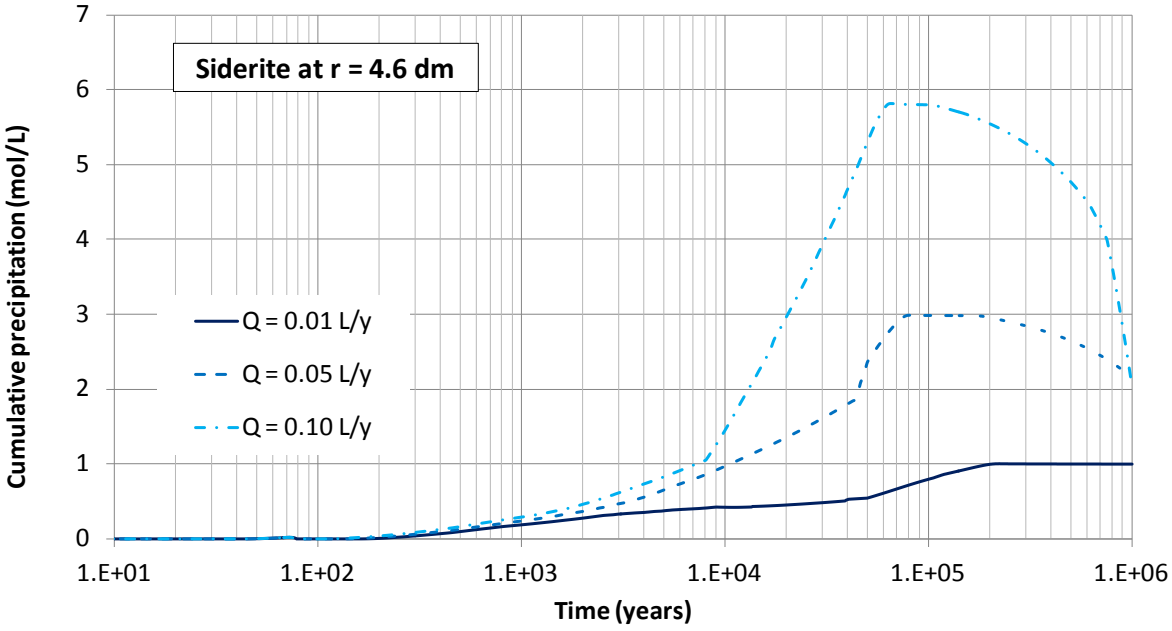

Figure 5.52. Sensitivity of the time evolution of the computed concentration of cumulative precipitated siderite in the bentonite at r = 4.6 dm to changes in the groundwater flow, Q(L/year). r is the radial distance to the axis of the disposal cell.

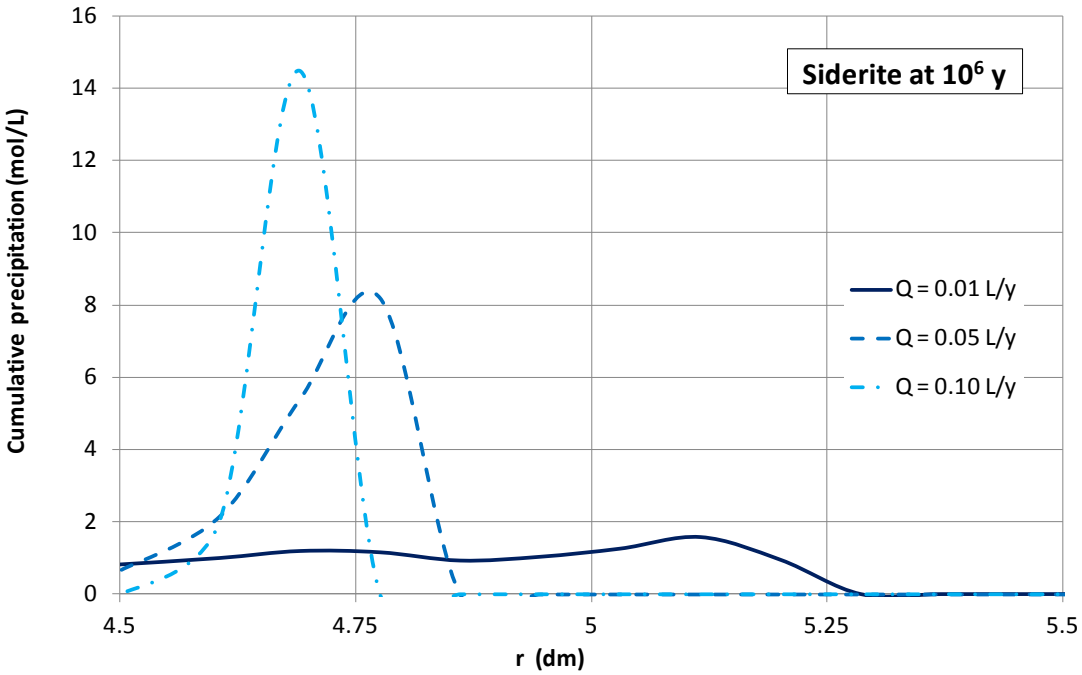

Figure 5.53. Sensitivity of the spatial distribution of computed concentration of cumulative precipitated siderite in the bentonite at t = 10^6 years to changes in the groundwater flow, Q(L/year). r is the radial distance to the axis of the disposal cell.

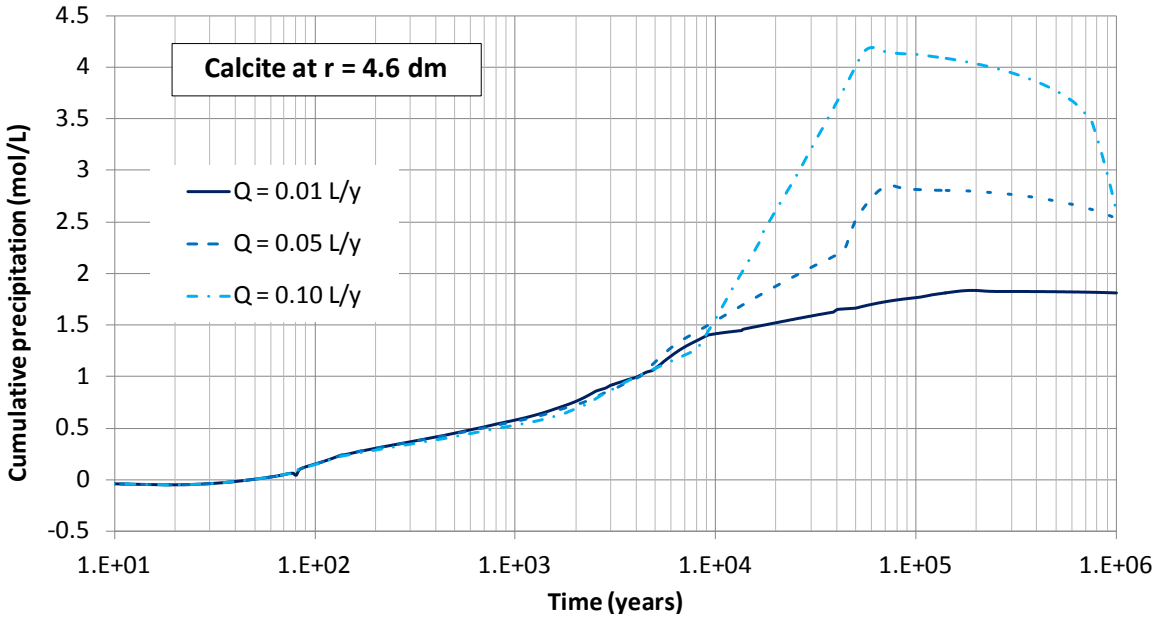

Figure 5.54. Sensitivity of the time evolution of the computed concentration of cumulative precipitated calcite in the bentonite at r = 4.6 dm to changes in the groundwater flow, Q(L/year). r is the radial distance to the axis of the disposal cell.

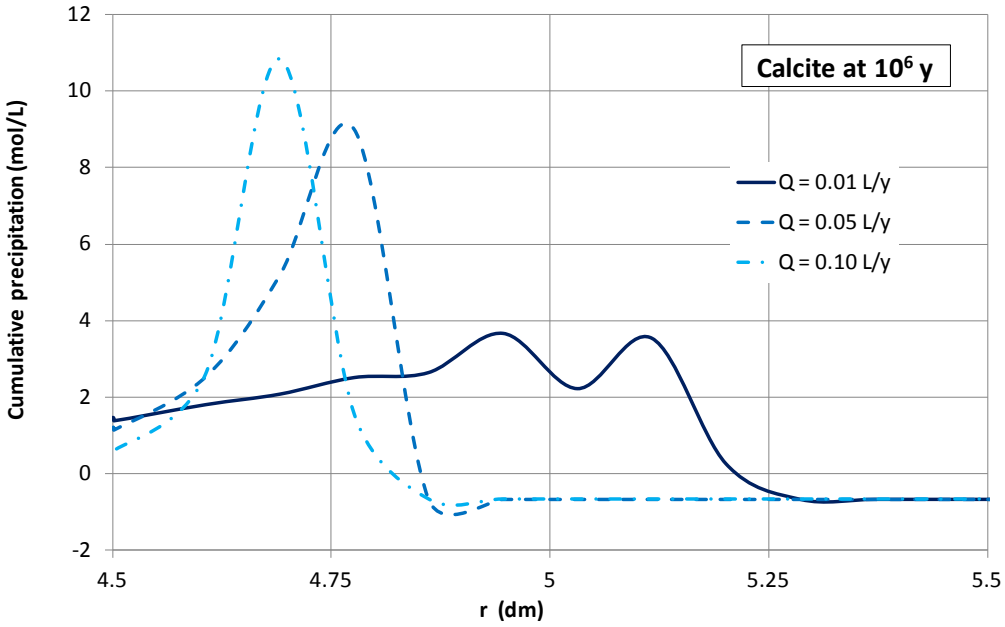

Figure 5.55. Sensitivity of the spatial distribution of computed concentration of cumulative precipitated calcite in the bentonite at t = 10^6 years to changes in the groundwater flow, Q (L/year). r is the radial distance to the axis of the disposal cell.

Cation exchange

Figure 5.56 shows the sensitivity of the time evolution of the computed concentration of the exchanged Fe^{2+} in the bentonite at r = 4.6 dm to changes in the groundwater flow Q. The concentration of the exchanged Fe^{2+} is sensitive to Q after t = $4 \cdot 10^3$ years . The larger the Q, the lager the concentration of the exchanged Fe^{2+}.

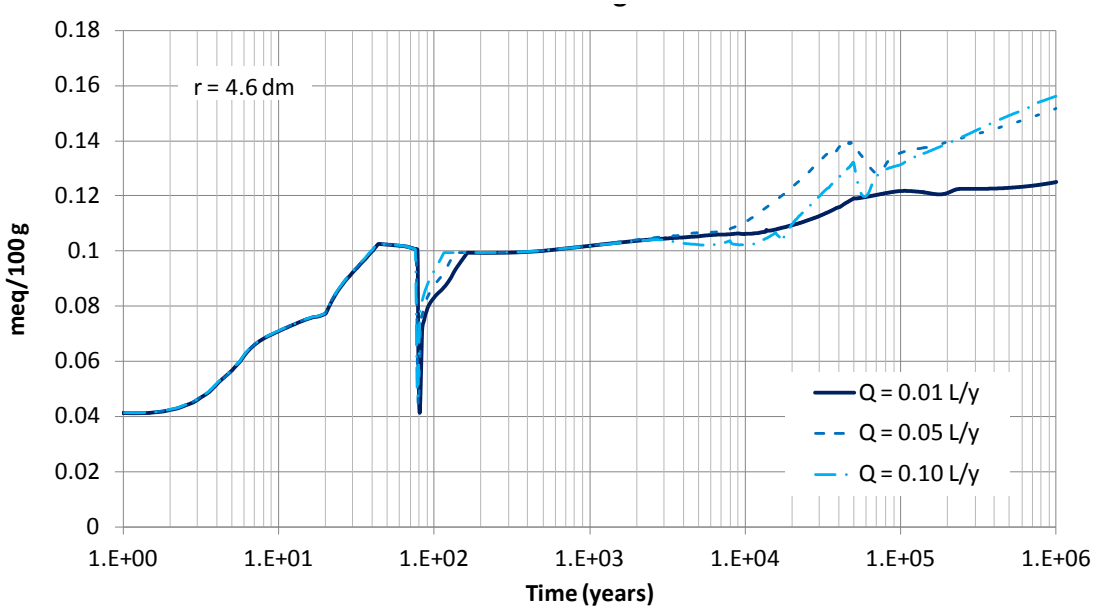

Figure 5.56. Sensitivity of the time evolution of computed concentration of exchanged Fe^{2+} in the bentonite at r = 4.6 dm to changes in the groundwater flow, Q (L/year). r is the radial distance to the axis of the disposal cell.

Sorbed species

The time evolution of computed concentrations of sorbed species in the bentonite has been analysed at several locations for several values the Q. Figure 5.57 shows the time evolution of the concentrations of sorbed species at r = 4.6 dm for Q = 0.01 and 0.05 L/year. The concentrations are sensitive to Q only after 1000 years. The sorption fronts and the patterns of the curves are similar for both values of Q.

Figure 5.58 shows the comparison of the spatial distribution of the sorbed species at t = 10^4 years computed for Q = 0.01 and 0.05 L/year. The sorption fronts observed at t = 10^4 years in the base run occur also when the groundwater flow increases. However, the fronts are less pronounced.

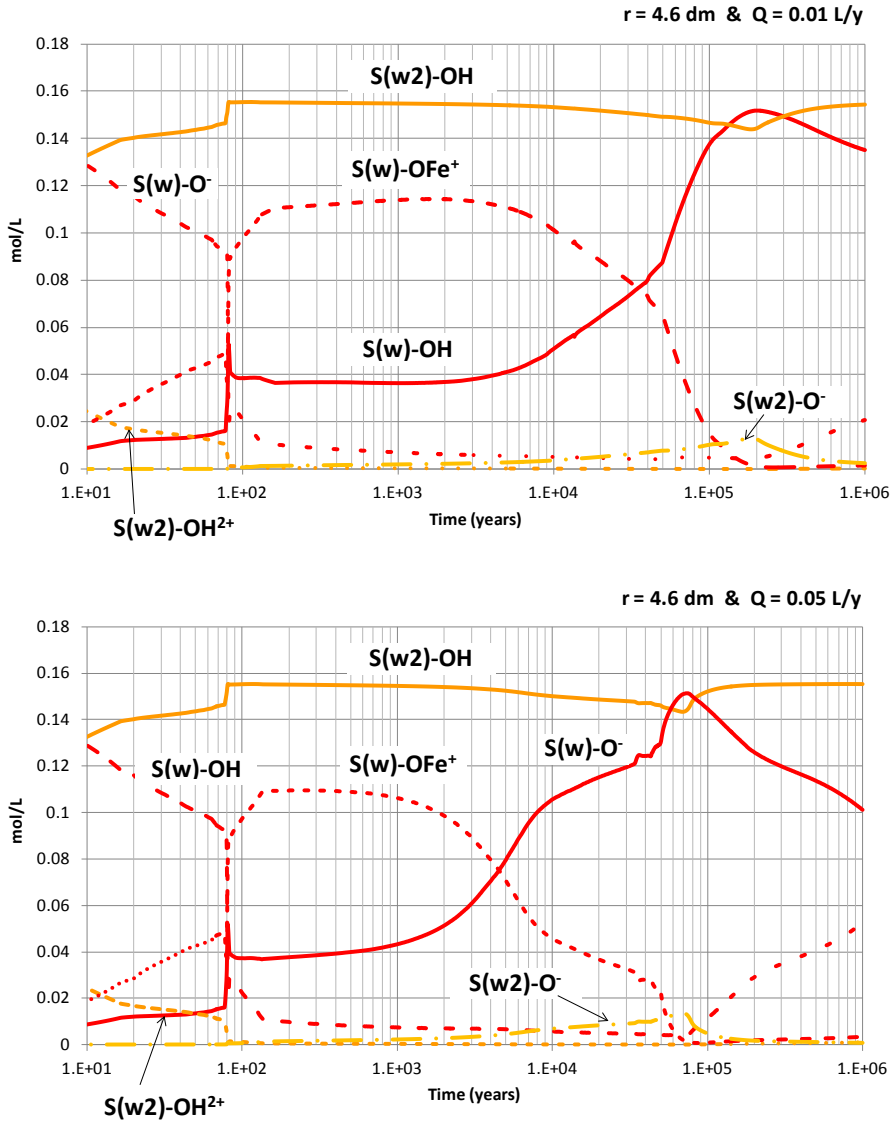

Figure 5.57. Time evolution of the concentration of sorbed species in the bentonite at r = 4.6 dm for groundwater flow Q equal to 0.01 (top) and 0.05 L/year. r is the radial distance to the axis of the disposal cell.

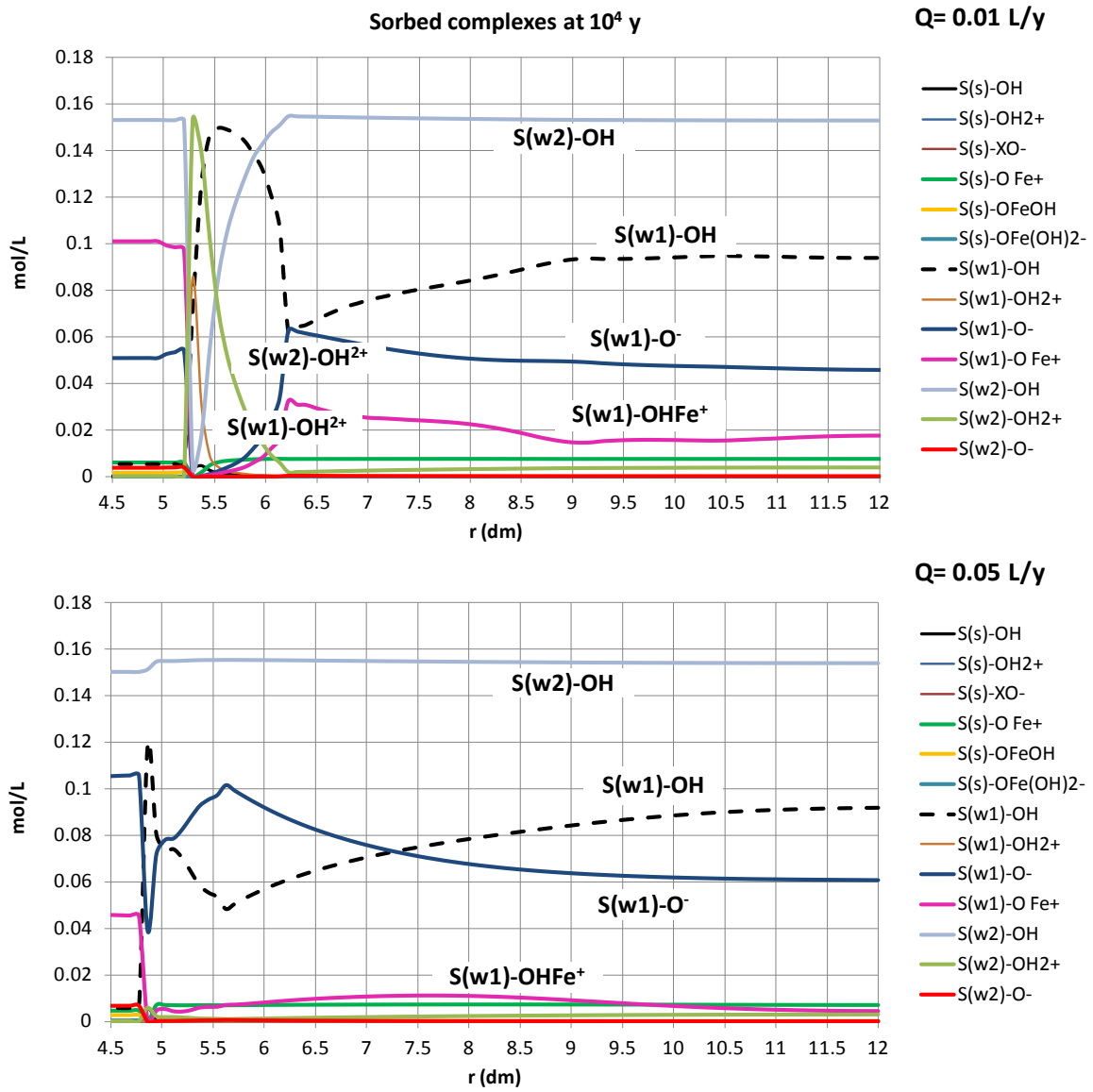

Figure 5.58. Spatial distribution of the concentrations of sorbed species in the bentonite at t = 10^4 years for groundwater flow Q equal to 0.01 and 0.05 L/year. r is the radial distance to the axis of the disposal cell.

Hydrogen pressure

The time evolution of H_2(g) partial pressure in the bentonite for several values of the groundwater flow Q is shown in Figure 5.59. H_2(g) partial pressures are very sensitive to the groundwater flow. The larger the Q, the smaller the H_2(g) partial pressure because hydrogen pressures are proportional to the concentrations of H_2(aq) which in turn decrease when Q increases.

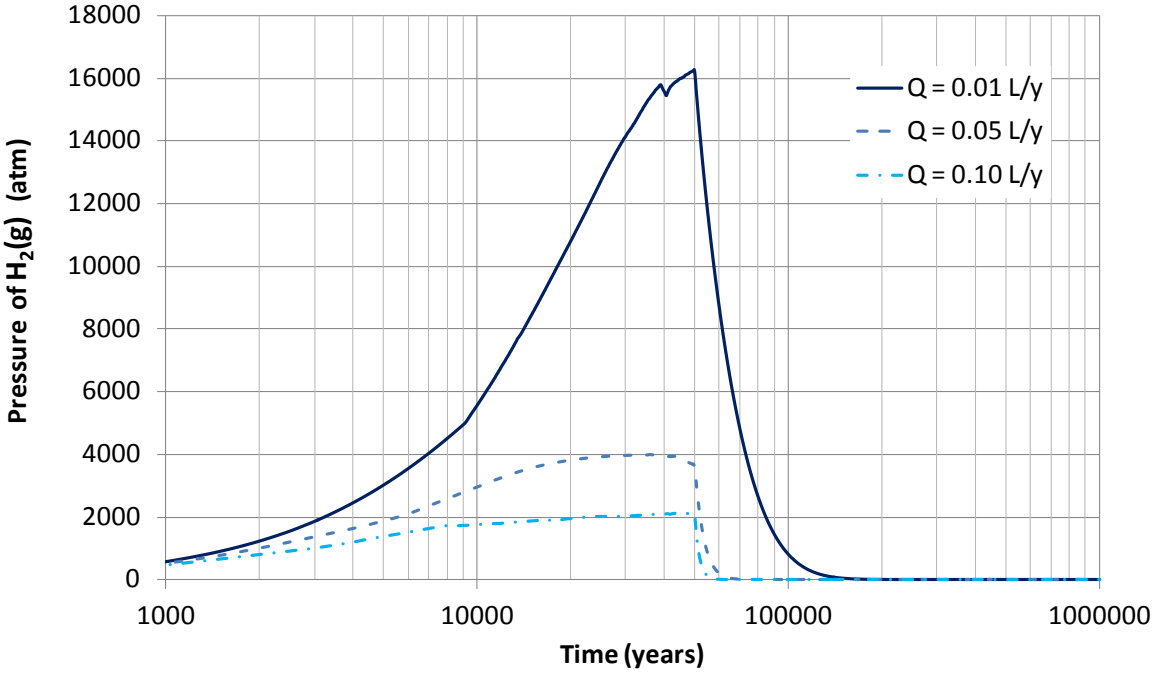

Figure 5.59. Sensitivity of the time evolution of hydrogen partial pressure in the bentonite to changes in the groundwater flow, Q (L/year).

Changes in porosity

Changes in the bentonite porosity have been calculated from the computed mineral dissolution/precipitation for several values of the groundwater flow Q. Figure 5.60 shows the changes in the bentonite porosity caused by mineral dissolution/precipitation at r = 4.6 and 9.5 dm. Porosity changes are not sensitive to Q at r = 9.5 dm. The sensitivity of the spatial distribution of the porosity at t = 10^4 and 10^6 years to changes in Q bentonite are shown in Figure 5.61 and Figure 5.62, respectively. The precipitation of magnetite close to the canister causes a decrease in bentonite porosity. The larger the groundwater flow Q, the smaller the zone affected by the porosity reduction and the smaller the thickness of bentonite affected by pore clogging.

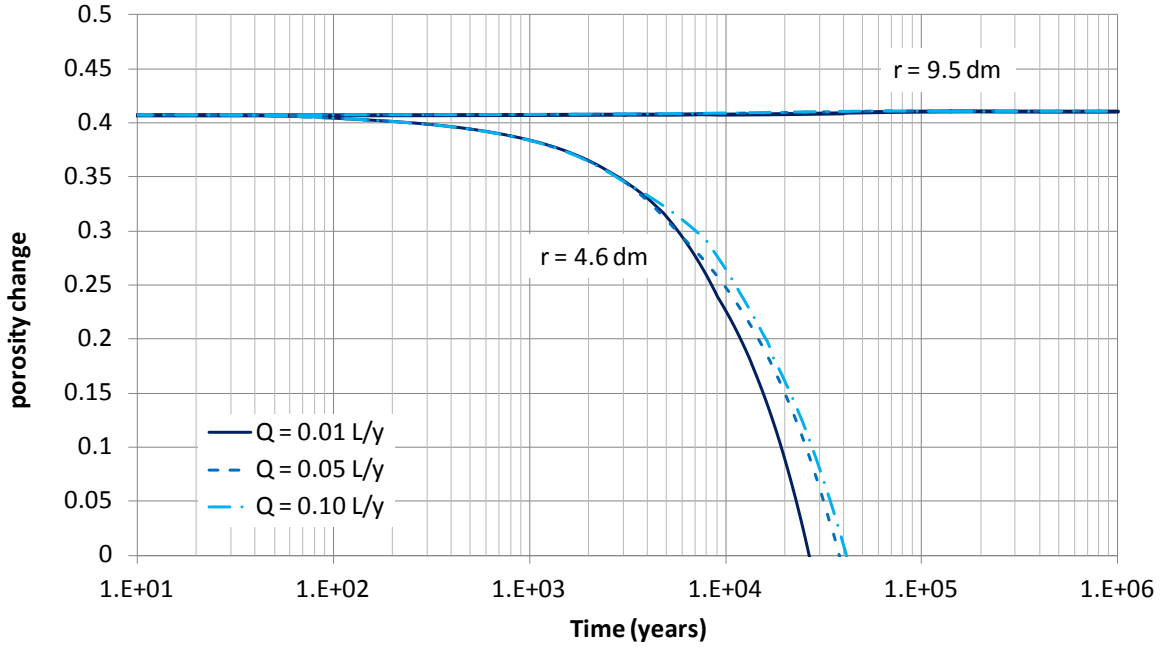

Figure 5.60. Time evolution of the changes in the bentonite porosity due to mineral dissolution/precipitation for several values of the groundwater flow, Q (L/year).

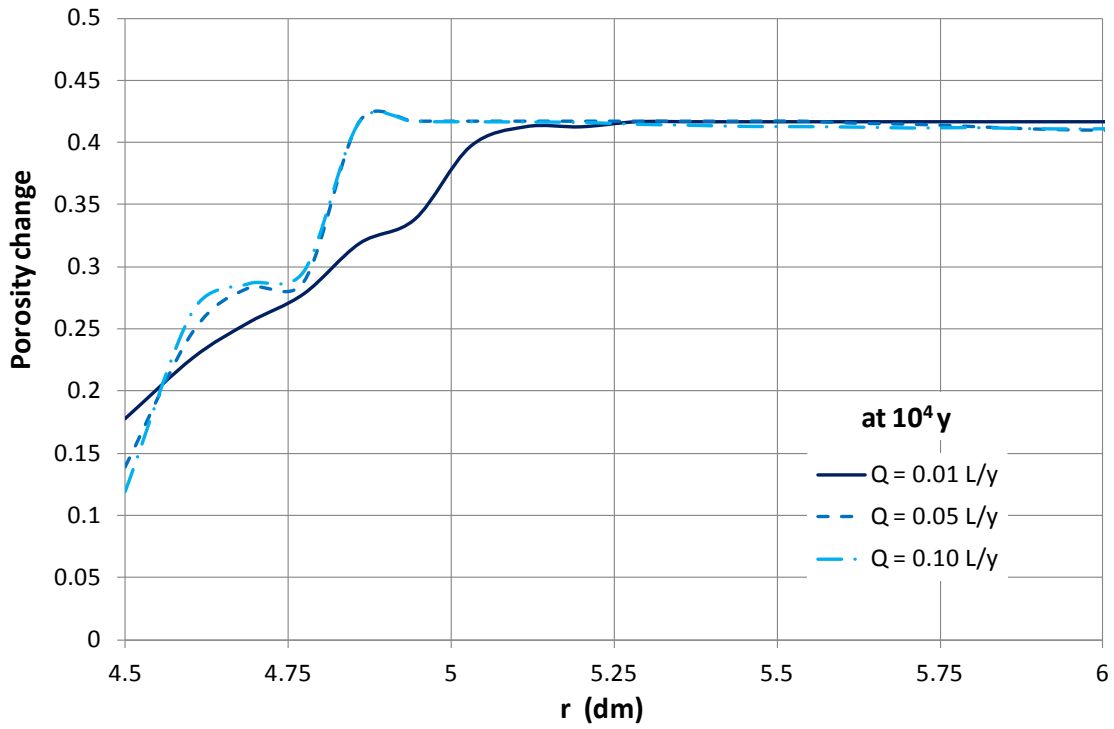

Figure 5.61. Spatial distribution of the changes in bentonite porosity at t = 10^4 years due to mineral dissolution/precipitation for several values of the groundwater flow, Q (L/year). r is the radial distance to the axis of the disposal cell.

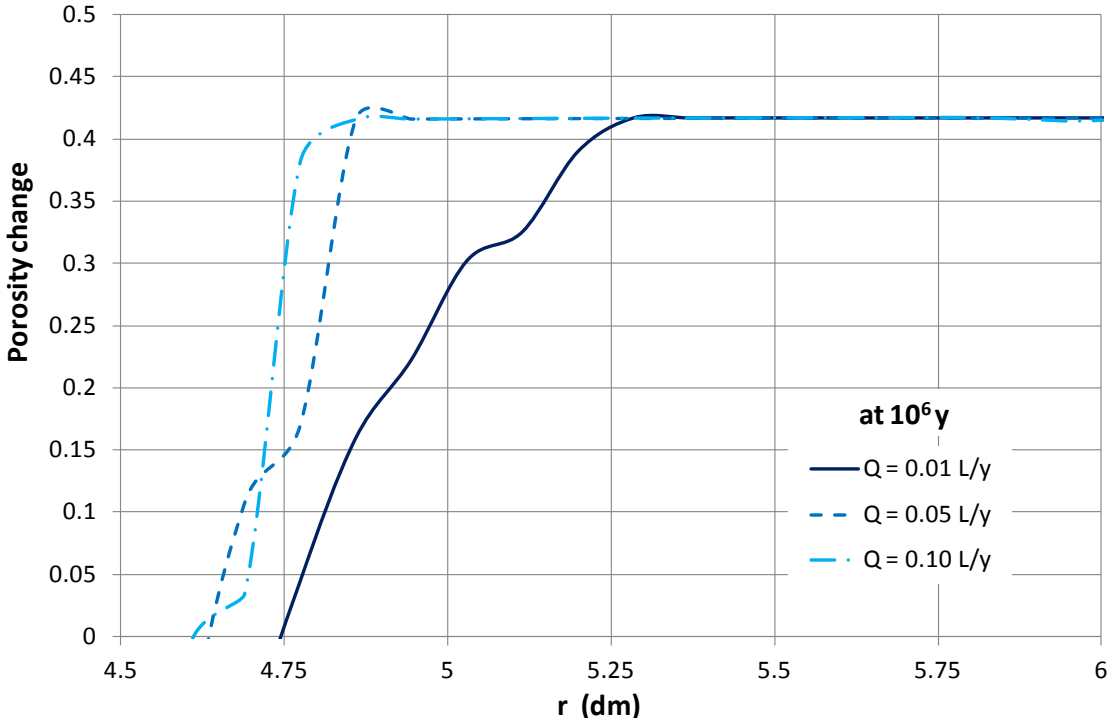

Figure 5.62. Spatial distribution of the changes in bentonite porosity at t = 10^6 years due to mineral dissolution/precipitation for several values of the groundwater flow, Q (L/year). r is the radial distance to the axis of the disposal cell.

5.4.3 Conclusions

The main conclusions of the sensitivity analysis to the groundwater flow Q include:

1. The computed concentrations of dissolved species are very sensitive to the changes in the water flow Q because the solute flux from the bentonite into the granite is controlled mostly by the advective transport of the granite water flow. The larger the Q, the faster the decrease of the concentrations. In fact, the time needed for the concentrations to decrease to a half, $T_{1/2}$, is proportional to Q.

2. The computed pH is slightly sensitive to the change in Q after 400 years. The larger the Q, the larger the pH from 400 to $6 \cdot 10^4$ years. After $6 \cdot 10^4$ years, the computed pH is largest for the smallest groundwater flow.

3. The computed Eh is not sensitive to the change in the groundwater flow Q.

4. The concentration of precipitated magnetite in the bentonite is strongly sensitive to the increase in the groundwater flow, Q. The larger the Q, the smaller the concentration of precipitated magnetite and the smaller the thickness of the zone where magnetite precipitates. Such thickness decreases from 6 cm to less than 2 cm when Q increases by a factor of 10.

5. The concentration of precipitated siderite is very sensitive to Q. The larger the Q, the larger the precipitation of siderite and the smaller the thickness of the zone where siderite precipitates.
6. The concentration of precipitated calcite near the canister/bentonite interface is very sensitive to the changes in groundwater flow, Q. The larger the Q, the smaller the zone where calcite precipitates.
7. The concentration of the exchanged Fe^{2+} is sensitive to Q after $t = 4 \cdot 10^3$ years. The larger the Q, the lager the concentration of the exchanged Fe^{2+}.
8. Sorption fronts are less pronounced when the groundwater flow increases.
9. The $H_2(g)$ partial pressure is very sensitive to the groundwater flow. The larger the Q, the smaller the $H_2(g)$ partial pressure.
10. The larger the groundwater flow Q, the smaller the zone affected by the porosity reduction and the smaller the thickness of bentonite affected by pore clogging.

5.5. Sensitivity to changes in the selectivity coefficients

5.5.1 Introduction

Cation selectivity coefficients for exchanged Ca^{2+}, Mg^{2+} and K^+ were derived from Samper et al. (2008a). The selectivity coefficient for the exchange of iron was taken from Tournassat (2003). Cation selectivities were calibrated in order to reproduce the reported concentrations of exchanged cations for the FEBEX bentonite by Fernández et al. (2004) and ENRESA (2004). The base run was performed with the selectivities used by Samper et al. (2008a). This section presents the sensitivity analysis of model results to change in the cation selectivities. The original and the calibrated selectivities are listed in Table 3.3.

5.5.2 Results of the sensitivity run

Table 5.1 lists the computed initial concentrations of the exchanged cations in the base run and the sensitivity run. The changes in the selectivities affect strongly the concentrations of the exchanged Ca^{2+} and Mg^{2+}.

Figure 5.63 shows the time evolution of computed concentrations of exchanged cations in the bentonite at r = 4.6 dm for the base and the sensitivity runs with the calibrated

selectivities. Clearly, the concentrations of exchanged cations are very sensitive to the cation selectivities.

Table 5.1. Initial concentrations of the exchanged cations in the base and sensitivity runs

Exchanged cation	Initial concentration of exchanged cátion (meq/100g)	
	Base run	Sensitivity run
Na^{+}	25.4	23.95
Ca^{2+}	40.5	33.6
Mg^{2+}	33.7	42.9
K^{+}	2.2	1.35
Fe^{2+}	0.022	0.025

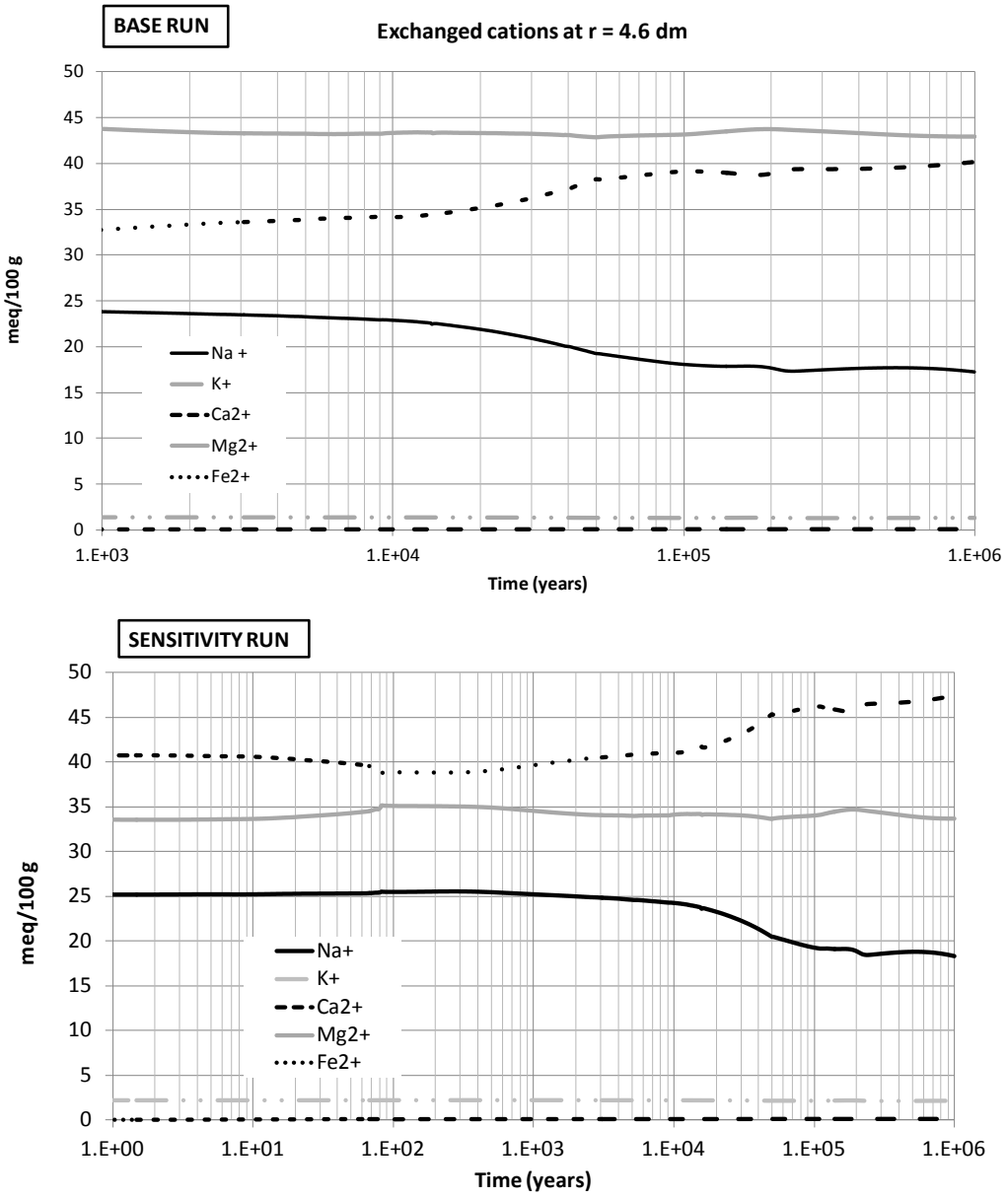

Figure 5.63. Time evolution of computed concentrations of exchanged cations in the bentonite at r = 4.6 dm for the base run and the sensitivity run with the calibrated selectivities (see Table 5.1).

However, the concentrations of dissolved species are not sensitive to the change in the selectivities (Figure 5.64).

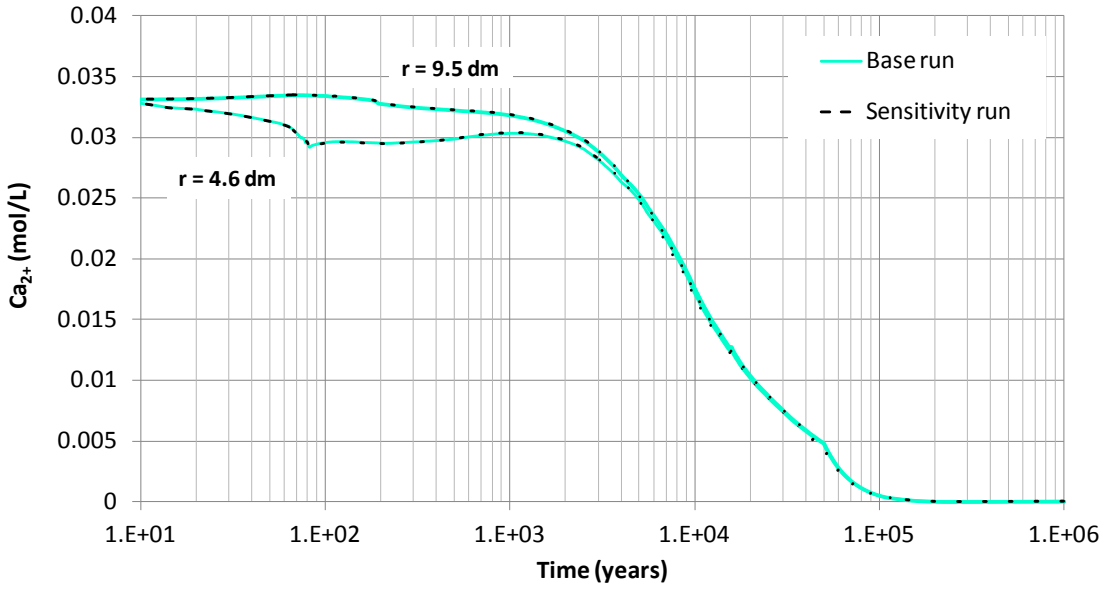

Figure 5.64. Computed concentration of dissolved Ca^{2+} in the bentonite for the base run and the sensitivity with the calibrated selectivities.

5.5.3 Conclusions

The change in the cation selectivities affect mostly the concentrations of exchanged cations, especially Mg^{2+} and Ca^{2+}. However, the computed pH, Eh and the concentrations of dissolved and precipitated species lack sensitivity to the selectivities.

5.6. Sensitivity to chemical composition of bentonite and granite porewater

5.6.1 Introduction

The conceptual model assumes that the bentonite is initially water-saturated and granite porewater will transport away the solutes at the bentonite/granite interface (see Section 3.4). The initial chemical composition of the bentonite porewater and the composition of the boundary granite porewater were taken from Samper et al. (2008a; 2011) and Samper et al. (2007) (see Table 3.5). Such compositions were also used by Lu et al. (2011, 2012) for the long-term geochemical simulation and the reactive transport of Ni from a HLW repository in granite.

Given the difficulties of deriving reliable data on saturated bentonite porewater chemistry, a sensitivity run was performed by changing the chemical compositions of the initial bentonite porewater and the granitic boundary (see Table 5.2). These compositions were derived by Samper et al. (2005) from a squeezing experiment at 23.8% water content and were previously used by Samper et al. (2008b). Appendix 2 presents a compilation of the chemical composition data for FEBEX bentonite.

Table 5.2. Chemical composition of the initial bentonite porewater and the granitic boundary water at the bentonite/granite interface used for the sensitivity run. They were taken from Samper et al. (2005). The values of Eh and the concentrations of Fe^{2+} and SiO_2(aq) in the bentonite are not available in Samper et al. (2005) and, therefore, they were taken equal to those of the granite pore water of Samper et al. (2008a; 2011).

	Bentonite porewater	**Granite porewater**
pH	7.94	8.15
Eh (V)	-0.188	-0.188
Ca^{2+} (mol/L)	$6.34 \cdot 10^{-3}$	$9.98 \cdot 10^{-4}$
Mg^{2+} (mol/L)	$8.82 \cdot 10^{-2}$	$3.67 \cdot 10^{-4}$
Na^{+} (mol/L)	$1.14 \cdot 10^{-1}$	$5 \cdot 10^{-4}$
K^{+} (mol/L)	$1.04 \cdot 10^{-3}$	$2.56 \cdot 10^{-5}$
Fe^{2+} (mol/L)	$1.791 \cdot 10^{-8}$	$1.791 \cdot 10^{-8}$
Cl^{-} (mol/L)	$1.12 \cdot 10^{-1}$	$3.81 \cdot 10^{-4}$
HCO_3^{-} (mol/L)	$6.45 \cdot 10^{-4}$	$2.37 \cdot 10^{-3}$
SO_4^{2-} (mol/L)	$1.27 \cdot 10^{-2}$	$146 \cdot 10^{-4}$
SiO_2 (aq) (mol/L)	$3.761 \cdot 10^{-4}$	$3.761 \cdot 10^{-4}$

5.6.2 Results of the sensitivity run

Aqueous species

The computed concentrations of dissolved species are very sensitive to the changes in the chemical composition of the bentonite and granite porewaters.

Figure 5.65 shows the time evolution of the computed concentration of dissolved Fe^{2+} in the sensitivity run at r = 4.6 and 9.5 dm. The concentration of dissolved Fe^{2+} increases due to the release of iron from the canister. It reaches its maximum at 1500 years. Then, it decreases to very small values due to diffusion to the granite. The computed concentration of dissolved Fe^{2+} shows some oscillations at $2 \cdot 10^4$ and $5 \cdot 10^4$ years which are also present in the curves of pH, Eh and sorbed species (Figure 5.68, Figure 5.71, Figure 5.84 and Figure 5.85) and are

related to the competition of Fe sorption and siderite and calcite precipitation (Figure 5.79 and Figure 5.81).

The concentration of dissolved Fe^{2+} in the bentonite in the sensitivity run is significantly smaller than that of the base run (Figure 5.66). Similar to the base run, the concentration of dissolved Fe^{2+} is related to that of the sorbed Fe^{2+}. However, in the sensitivity run, the results are different because: 1) The initial concentration of dissolved Fe^{2+} is smaller than that of the base run; and 2) The initial pH in the sensitivity run is larger than that of the base run.

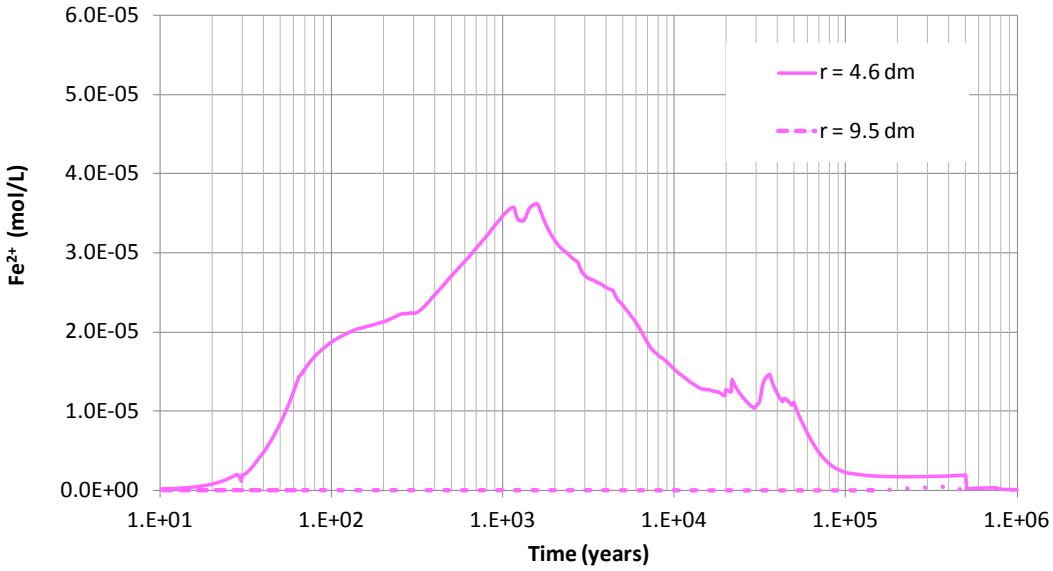

Figure 5.65. Time evolution of the computed concentration of dissolved Fe^{2+} in the bentonite at r = 4.6 and 9.5 dm for the sensitivity run in which the chemical compositions of the bentonite and granite porewaters are changed.

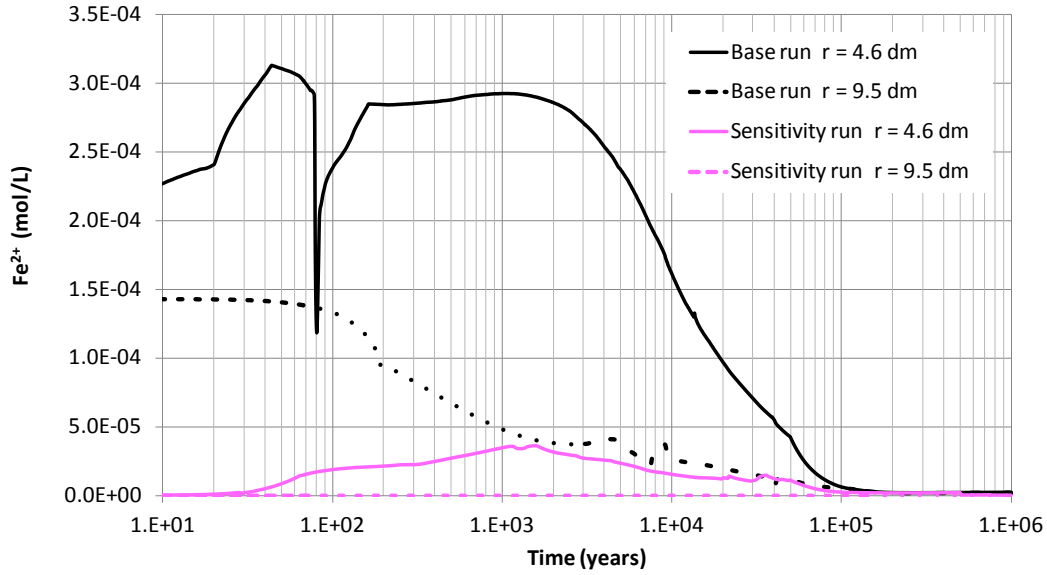

Figure 5.66. Time evolution of computed concentrations of dissolved Fe^{2+} in the bentonite at r = 4.6 and 9.5 dm for the base run and the sensitivity run in which the chemical compositions of the bentonite and granite porewaters are changed.

Figure 5.67shows the spatial distribution of the concentration of dissolved Fe^{2+} in the bentonite at selected times. This figure shows clearly the fronts of the migration of Fe^{2+} which extend up to 15 cm from the canister.

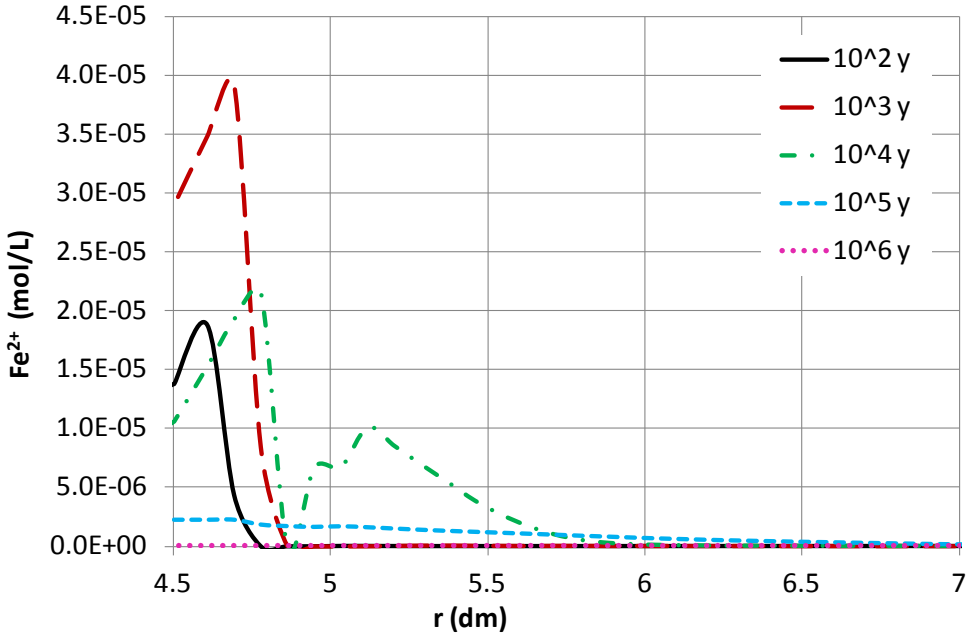

Figure 5.67. Spatial distribution of computed concentrations of dissolved Fe^{2+} in the bentonite at several times for the sensitivity run in which the chemical compositions of the bentonite and granite porewaters are changed.

Figure 5.68 shows time evolution of computed pH in the bentonite at r = 4.6, 4.9 and 9.5 dm for the sensitivity run. The initial pH is 1.5 units larger than that of the base run. The pH increases due to canister corrosion. The computed pH for the sensitivity run is generally larger than the pH of the base run and reaches its maximum of 9.8 at $t = 1.5 \cdot 10^5$ years. The time evolution of the computed pH is linked to that of proton sorption/desorption (compare Figure 5.68 and Figure 5.84). Similar to the base run, two pH fronts can be observed. However, for the sensitivity run they take place closer to the canister and sooner than for the base run. At r = 4.6 dm, a sharp increase of pH occurs at 30 years due to the first sorption front (see Figure 5.68). As the sorption front migrates through the bentonite, it gets smother (see Figure 5.88 and Figure 5.90). The second pH front takes places at r = 4.9 dm at $t = 1.5 \cdot 10^3$ years and extends at $t = 10^4$ years (see Figure 5.68 and Figure 5.70) which is related to the second sorption front (see Figure 5.85, Figure 5.88 and Figure 5.89). The computed pH is smaller than 7.5 during this period.

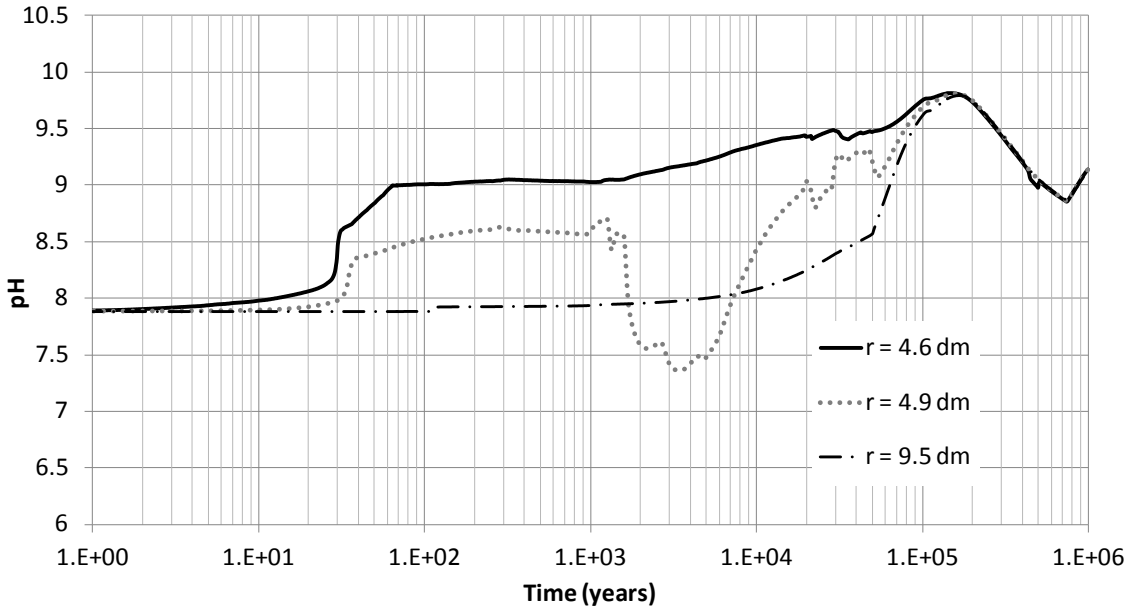

Figure 5.68. Time evolution of the computed pH in the bentonite at r = 4.6, 4.9 and 9.5 dm for the sensitivity run in which the chemical compositions of the bentonite and granite porewaters are changed.

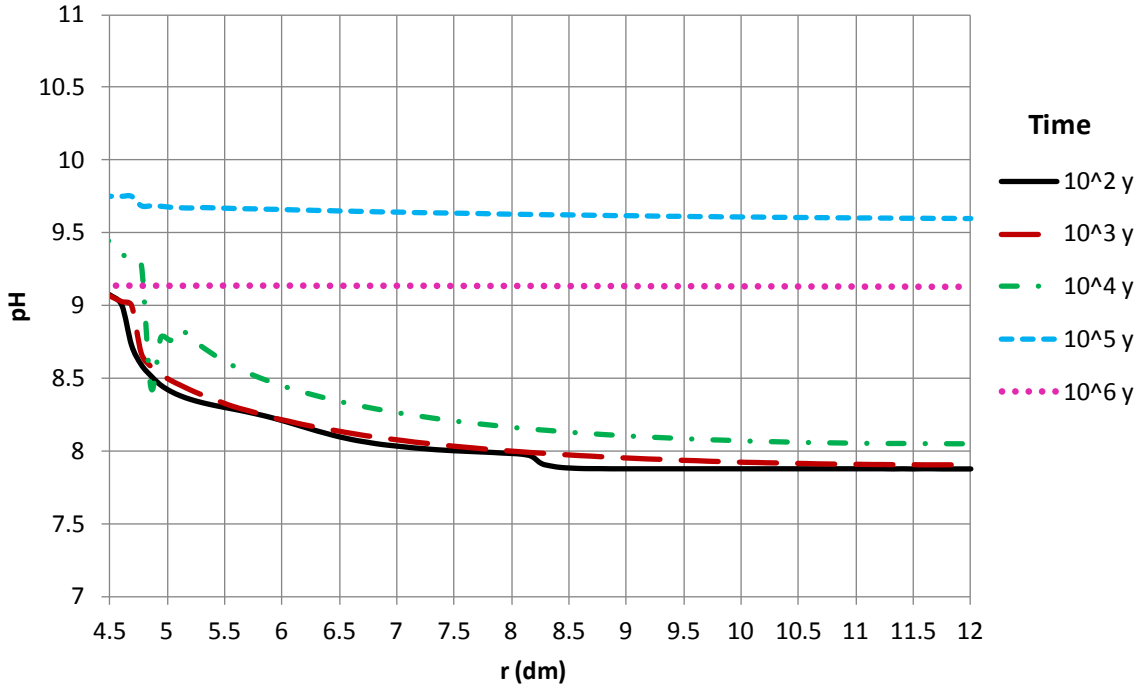

Figure 5.69. Spatial distribution of computed pH in the bentonite at selected times for the sensitivity run in which the chemical compositions of the bentonite and granite porewaters are changed.

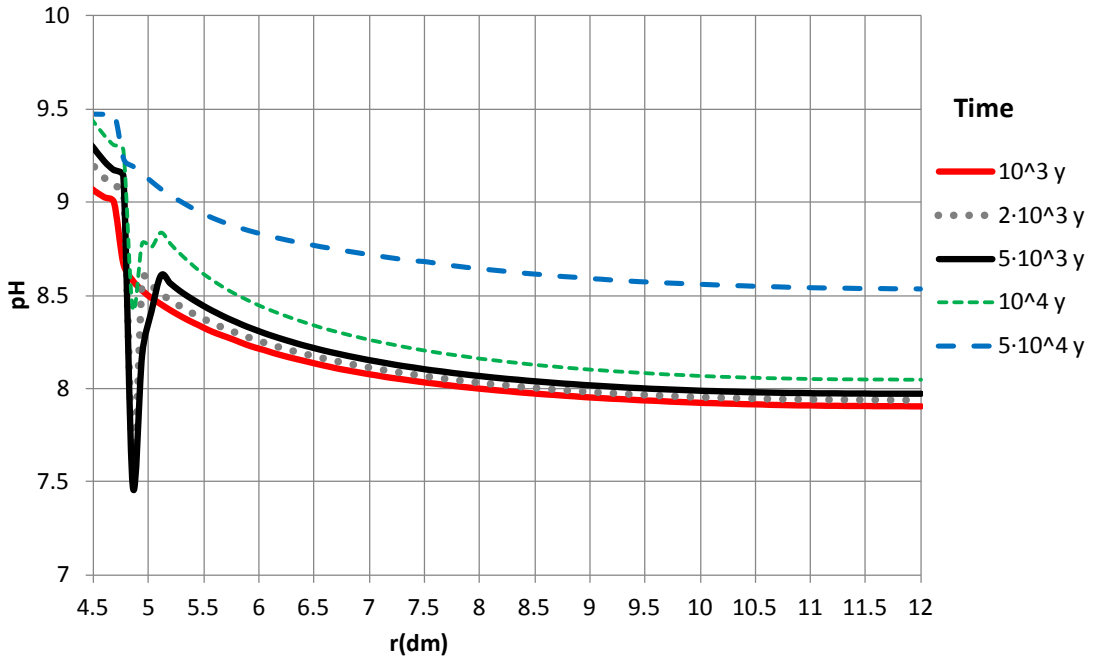

Figure 5.70. Spatial distribution of computed pH in the bentonite at selected times for the sensitivity run in which the chemical compositions of the bentonite and granite porewaters are changed. A front can be observed at r = 4.9 dm between 10^3 and 10^4 years.

Figure 5.7, Figure 5.72 and Figure 5.73 show the time evolution and spatial distribution of computed Eh in the bentonite at selected positions and times for the sensitivity run, respectively. Similar to the base run, the computed Eh is directly related to the pH which in turn is strongly influenced by the sorption fronts. The first sorption front is related to the sharp Eh decrease from -0.3 V to -0.5 V which can be observed at r = 4.6 dm at 30 years, at r = 4.9 dm at 35 years and at r = 8.25 dm at 100 years. The second Eh front occurs at r = 4.9 from $1.5 \cdot 10^3$ to $2 \cdot 10^4$ years. The Eh fronts take place at the same times and locations as those of pH.

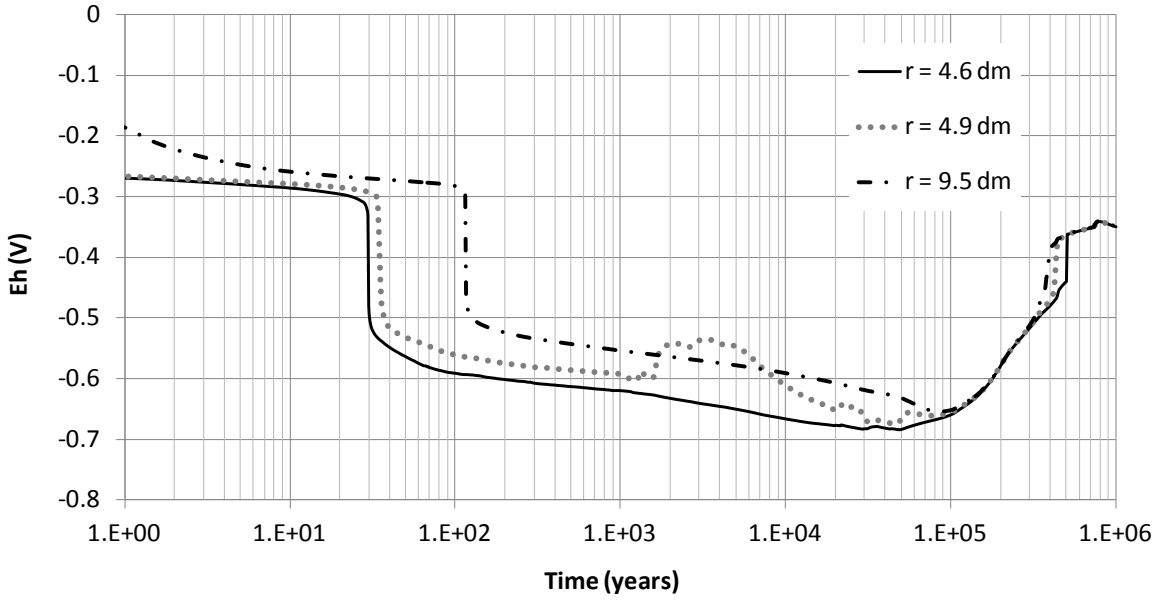

Figure 5.71. Time evolution of computed Eh in the bentonite at r equal to 4.6, 4.9 and 9.5 dm for the sensitivity run in which the chemical compositions of the bentonite and granite porewaters are changed.

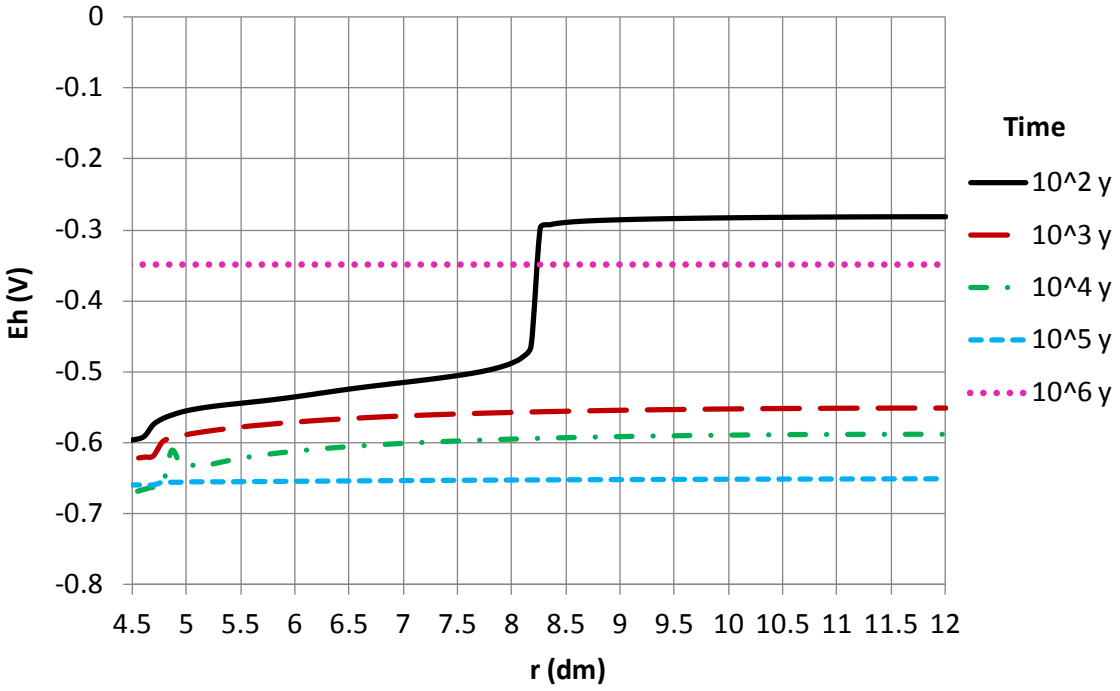

Figure 5.72. Spatial distribution of computed Eh in the bentonite at selected times for the sensitivity run in which the chemical compositions of the bentonite and granite porewaters are changed.

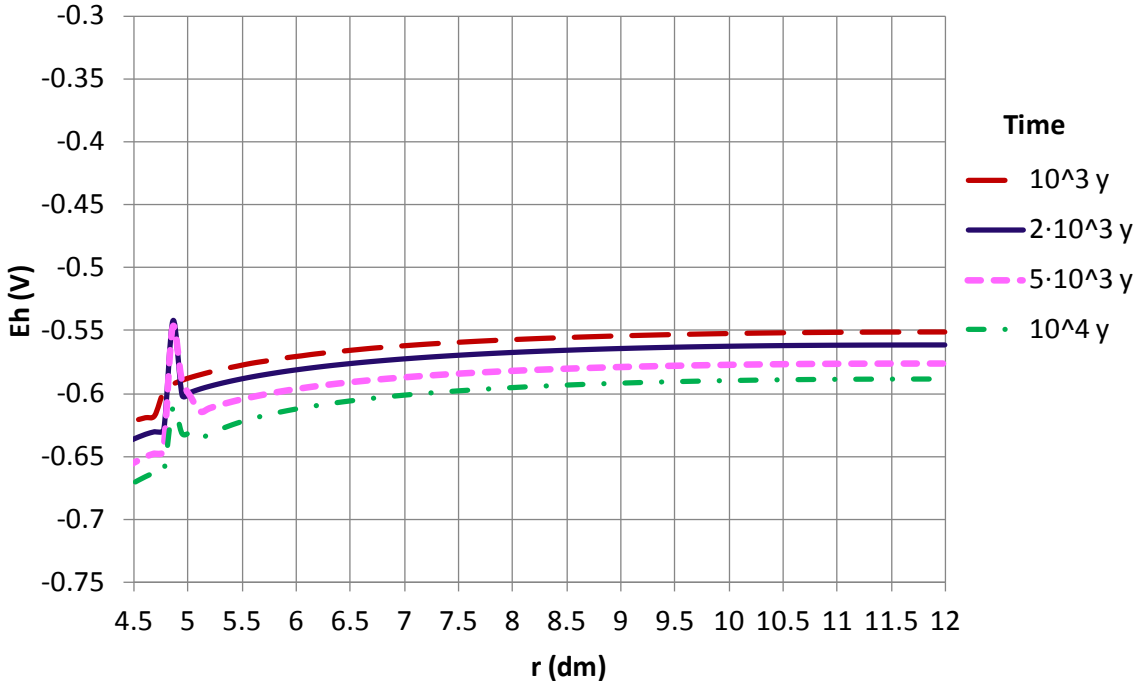

Figure 5.73. Spatial distribution of computed Eh in the bentonite at selected times for the sensitivity run in which the chemical compositions of the bentonite and granite porewaters are changed. A front can be observed at r = 4.9 dm and from $1.5 \cdot 10^3$ to 10^4 years.

Figure 5.74 shows the time evolution of the computed concentration of dissolved Cl^- in the bentonite for the base and sensitivity runs. The initial concentration of Cl^- in the sensitivity run is smaller than that in the base run and therefore, the computed Cl^- concentration in the sensitivity run is smaller and decreases slower than in the base run.

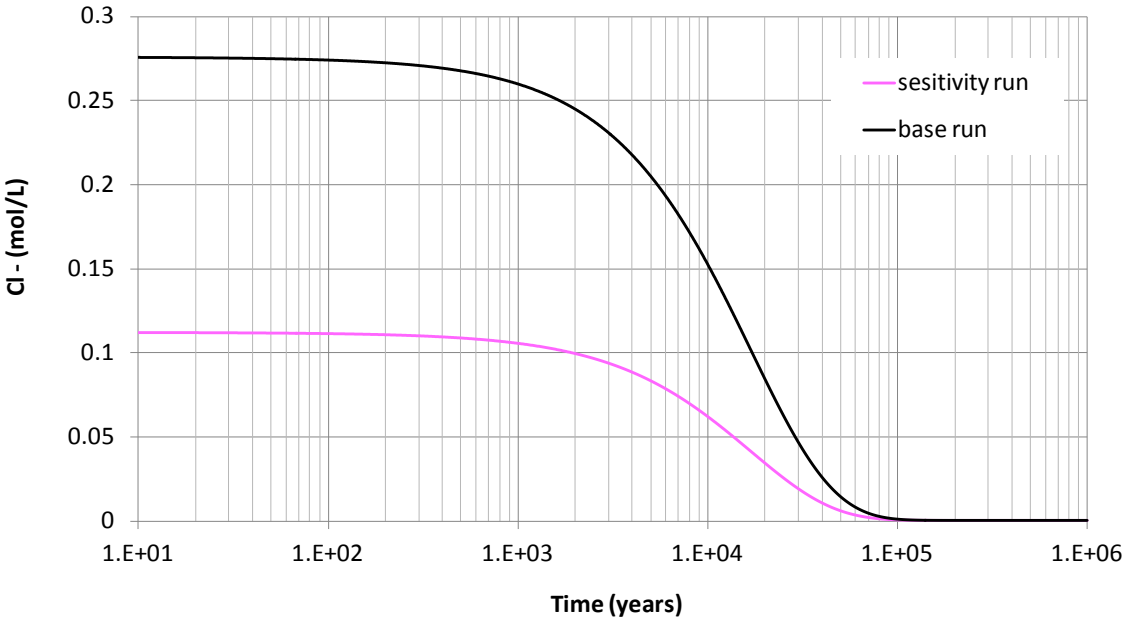

Figure 5.74. Time evolution of computed concentration of dissolved Cl^- in the bentonite for the base run and the sensitivity run in which the chemical compositions of the bentonite and granite porewaters are changed.

The time evolution of the concentrations of dissolved cations, Ca^{2+}, Mg^{2+}, Na^{+} and K^{+} in the sensitivity run is similar to that of the base run. Figure 5.75 shows the time evolution of the computed concentration of dissolved Ca^{2+} at r = 4.6, 4.9 and 9.5 dm. The concentration of dissolved Ca^{2+} is affected by calcite precipitation. A slight sudden decrease of Ca^{2+} concentration takes place at the pH front at r = 4.6 dm at t = 30 years and at r = 4.9 dm at 35 years. In addition, the concentration of dissolved Ca^{2+} shows oscillations from $2 \cdot 10^4$ to $5 \cdot 10^4$ years due to the competition of calcite and siderite precipitation.

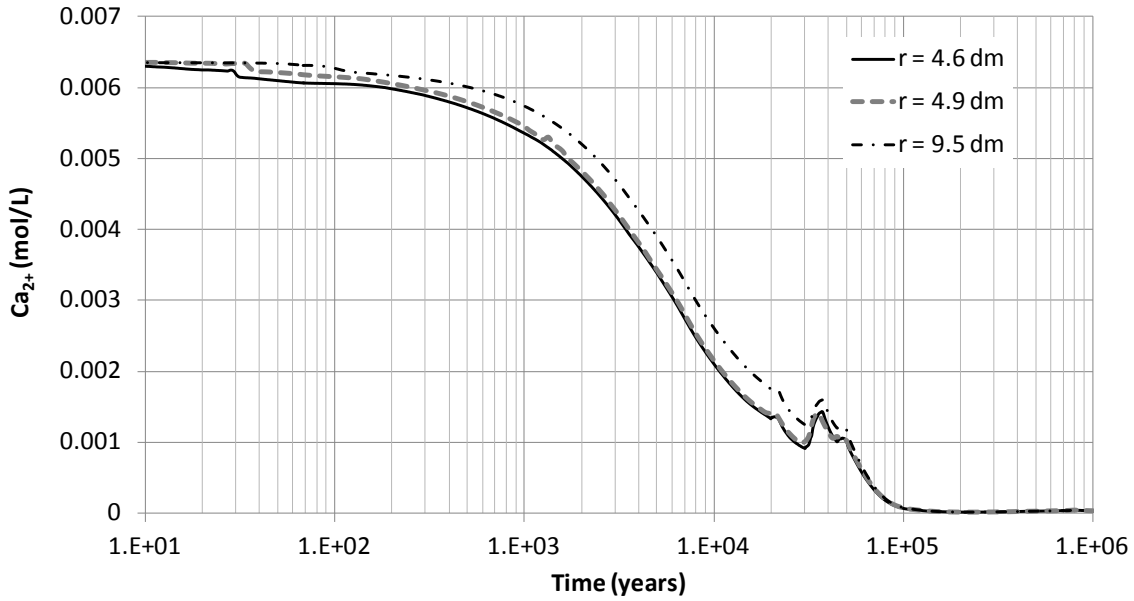

Figure 5.75. Time evolution of computed concentration of dissolved Ca^{2+} in the bentonite for the sensitivity run in which the chemical compositions of the bentonite and granite porewaters are changed.

Figure 5.76 shows the time evolution of the computed concentration of dissolved HCO_3^- in the bentonite at r = 4.6, 4.9 and 9.5 dm for the sensitivity run in which the chemical compositions of the bentonite and granite porewaters are changed. In this run, the dissolved HCO_3^- diffuses from the granite into the bentonite. The concentration of dissolved bicarbonate in the bentonite decreases due to calcite and siderite precipitation near the canister. Siderite and calcite compete for dissolved HCO_3^- which diffuses from the granite from t = $2 \cdot 10^4$ to t = $2 \cdot 10^5$ years. Siderite and calcite dissolve from t = $2 \cdot 10^5$ to t = $5 \cdot 10^5$ years, thus contributing to the increase of the concentration of dissolved HCO_3^- beyond the concentration of HCO_3^- in the granitic boundary water ($2.4 \cdot 10^{-3}$ mol/L). After t = $5 \cdot 10^5$ years, calcite dissolves slightly and dissolved HCO_3^- diffuses from the bentonite into the granite.

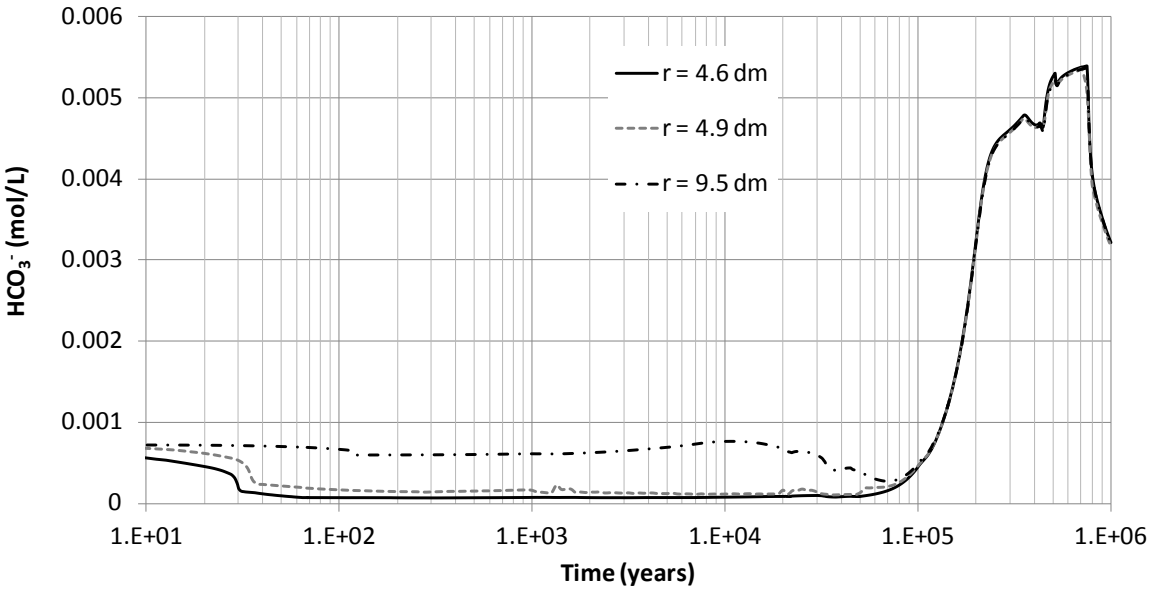

Figure 5.76. Time evolution of the computed concentration of dissolved HCO_3^- in the bentonite for the sensitivity run in which the chemical compositions of the bentonite and granite porewaters are changed.

Mineral phases

Magnetite is the main corrosion product in the bentonite for the sensitivity run. Figure 5.77 shows the time evolution of computed concentration of cumulative precipitated magnetite in the bentonite at r = 4.6 dm for the base and sensitivity runs. The amount of precipitated magnetite at r = 4.6 is significant smaller for the sensitivity run than that for the base run because: 1) The initial concentration of Fe^{2+} of the sensitivity run is smaller than that of the base run and 2) The initial pH of the sensitivity run is larger than that of the base run. Figure 5.78 shows the spatial distribution of the concentration of precipitated magnetite in the bentonite at selected times for the sensitivity and base runs. The computed concentration of magnetite near the canister/bentonite interface in the sensitivity run is much larger than in the base run while the thickness of the zone where magnetite penetrates (≈ 2.5 cm) is half of that computed for the base run.

Although most of the magnetite precipitates before $t = 5 \cdot 10^4$ years when the canister has been fully corroded, there is a small amount of magnetite precipitation after $t = 5 \cdot 10^5$ years due to the siderite dissolution and the release of exchanged Fe^{2+}.

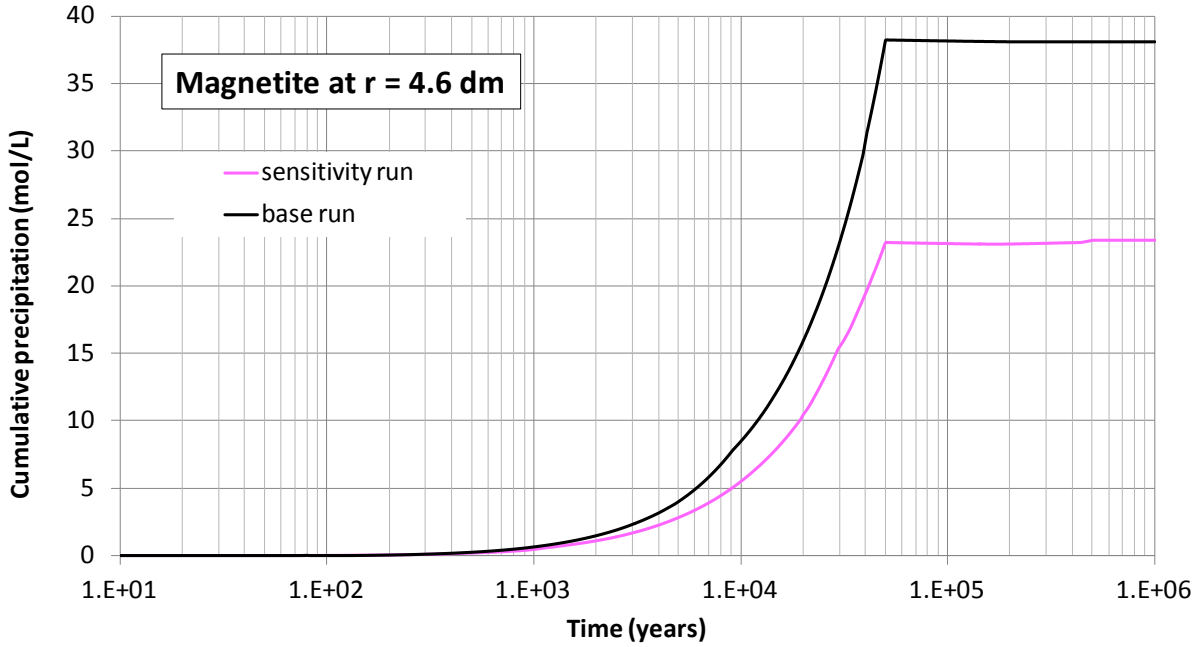

Figure 5.77. Time evolution of the computed concentration of precipitated magnetite in the bentonite at r = 4.6 dm for the base run and the sensitivity run in which the chemical compositions of the bentonite and granite porewaters are changed.

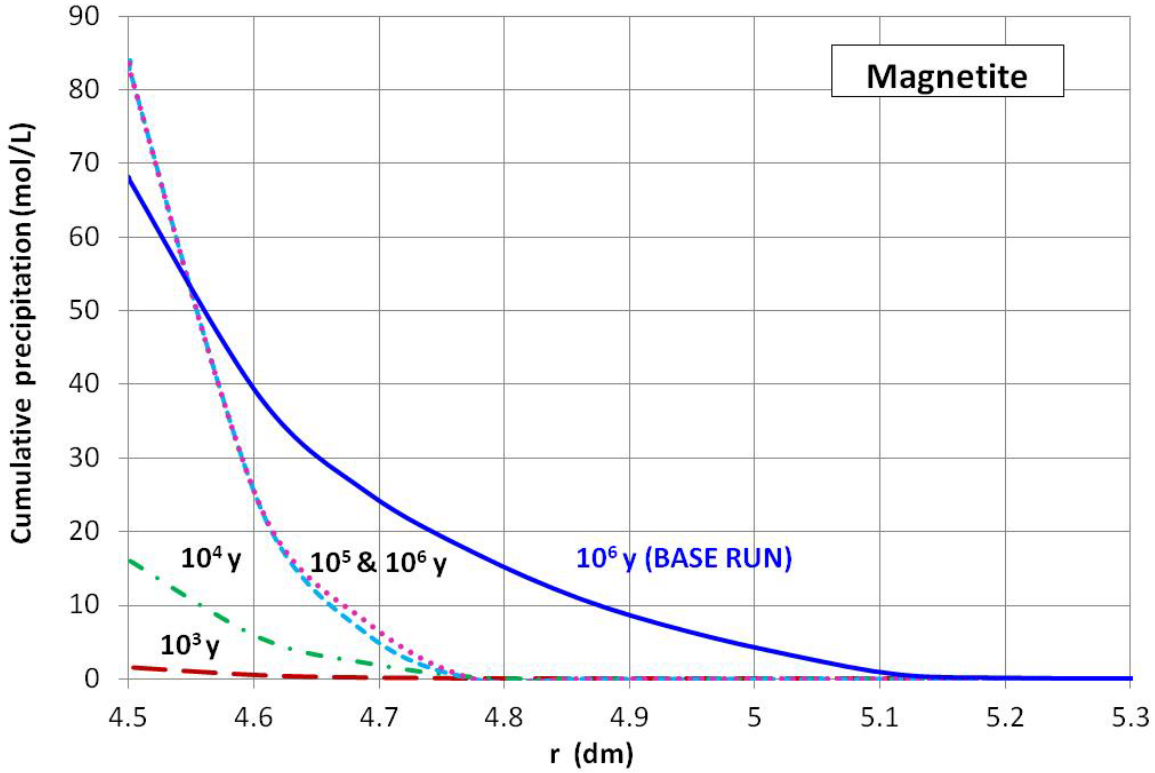

Figure 5.78. Spatial distribution of the computed concentration of precipitated magnetite in the bentonite at selected times for the base run and the sensitivity run in which the chemical compositions of the bentonite and granite porewaters are changed.

Figure 5.79 shows the time evolution of the computed concentration of cumulative precipitated siderite in the bentonite at r = 4.6 dm for the sensitivity and the base runs. Figure 5.80 shows the spatial distribution of the concentration of precipitated siderite in the bentonite at selected times for the sensitivity run. Siderite precipitation is controlled by the pH and the concentrations of dissolved Fe^{2+} and HCO_3^-. Siderite precipitation in the sensitivity run starts much later than in the base run. The thickness of the zone where siderite precipitates in the sensitivity run is always smaller than 4 cm and approximately half of that of the base run. All the precipitated siderite is subsequently dissolved and no siderite remains in the bentonite at the end of the simulation.

Figure 5.81 shows the time evolution of the concentration of cumulative calcite precipitation/dissolution for the sensitivity run at selected locations. Calcite dissolves slightly in the bentonite except near the canister/bentonite interface (r < 5 dm). Calcite precipitation at r = 4.6 dm in the sensitivity run is smaller than that in the base run for $t < 2 \cdot 10^4$ years. Figure 5.82 shows the spatial distribution of the concentration of precipitated calcite for the sensitivity run at selected times. From $2 \cdot 10^4$ years to $4 \cdot 10^4$ years, the precipitation rate increases notably. During this time period, siderite is also precipitating and both minerals compete for the dissolved HCO_3^-. A mild calcite dissolution is observed at $t = 10^5$ years, when the concentration of dissolved Ca^{2+} is small.

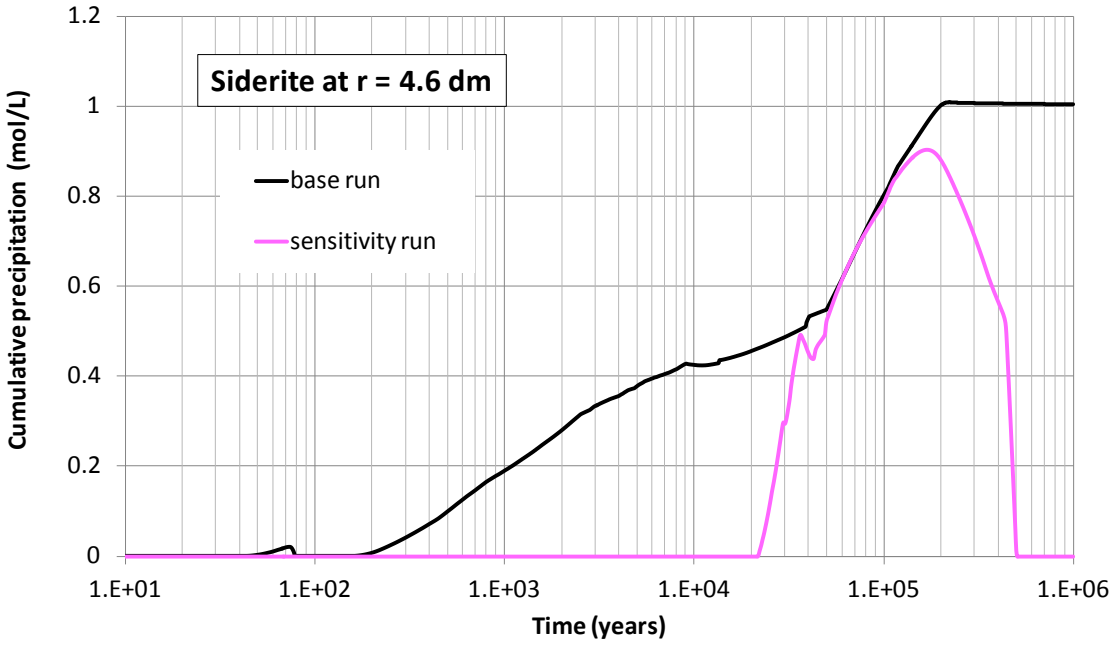

Figure 5.79. Time evolution of the computed concentration of precipitated siderite in the bentonite at r = 4.6 dm for the base run and the sensitivity run in which the chemical compositions of the bentonite and granite porewaters are changed.

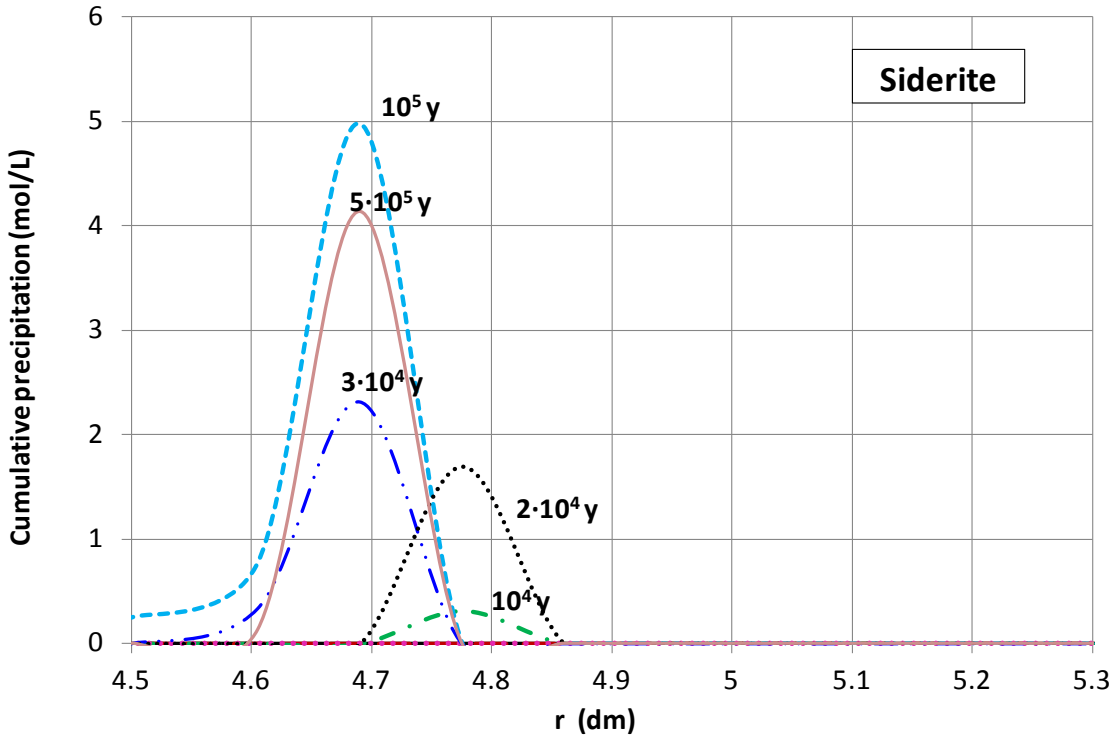

Figure 5.80. Spatial distribution of the computed concentration of precipitated siderite in the bentonite at selected times for the sensitivity run in which the chemical compositions of the bentonite and granite porewaters are changed. Computed siderite concentrations are not significant at 10^2, 10^3 and 10^6 years.

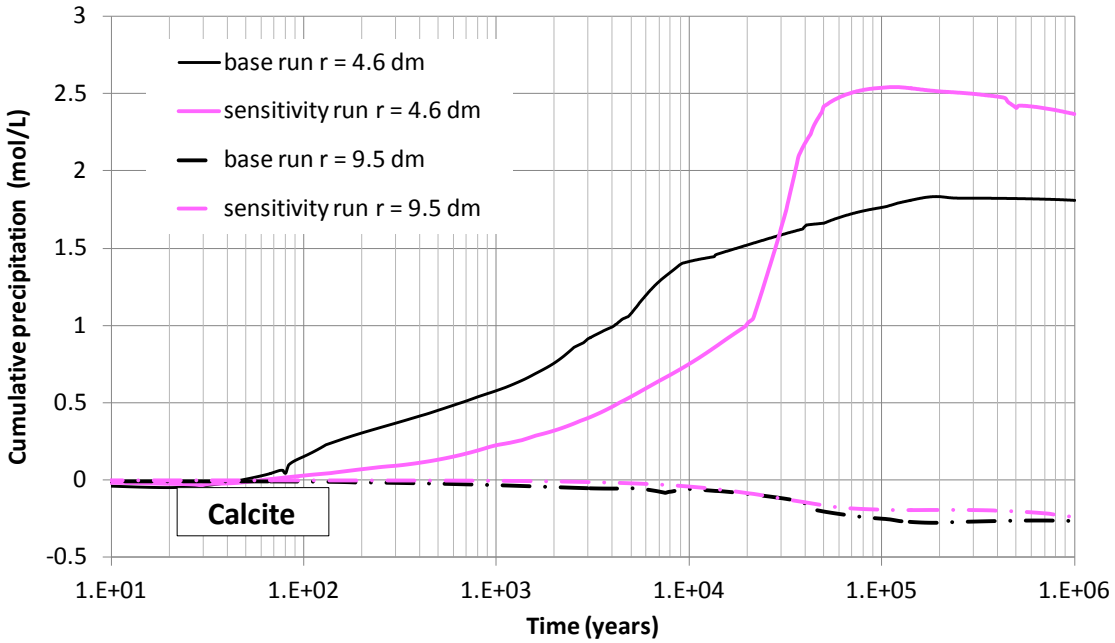

Figure 5.81. Time evolution of the computed concentration of precipitated calcite in the bentonite at r = 4.6 and 9.5 dm for the base run and the sensitivity run in which the chemical compositions of the bentonite and granite porewaters are changed.

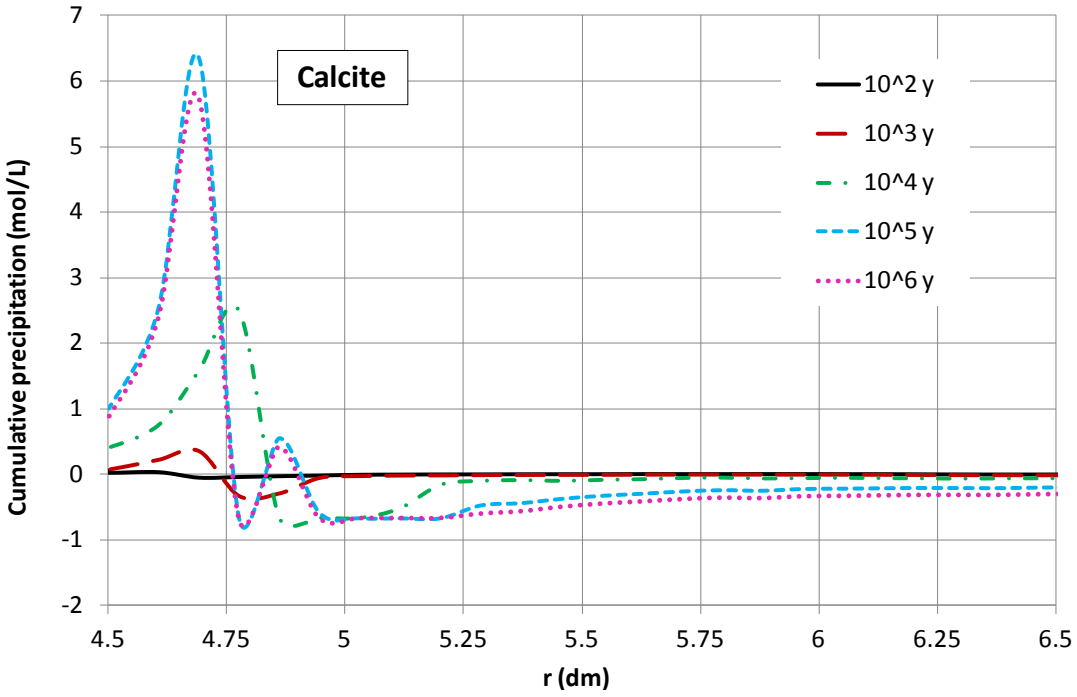

Figure 5.82. Spatial distribution of the computed concentration of precipitated calcite in the bentonite at selected times for the sensitivity run in which the chemical compositions of the bentonite and granite porewaters are changed.

Cation exchange

Selectivity coefficients for this sensitivity run are equal to those of the base run. The differences in the porewater chemistry lead to different initial concentrations of exchanged cations (not shown here). Figure 5.83 shows the time evolution of the concentration of exchanged Fe^{2+} in the sensitivity run. The concentration of exchanged Fe^{2+} increases in response to the increase in the concentration of dissolved Fe^{2+}. It should be noticed that most of the exchanged Fe^{2+} is released when the dissolved Fe^{2+} is used up for magnetite precipitation at $t = 5 \cdot 10^5$ years.

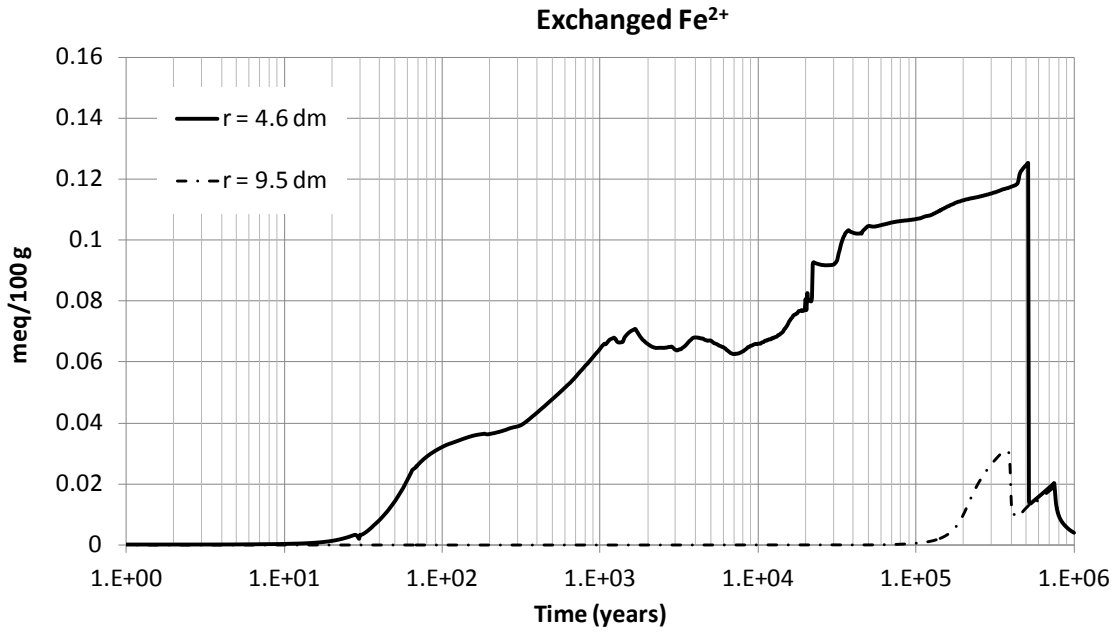

Figure 5.83. Time evolution of the computed concentration of exchanged Fe2+ calcite in the bentonite at r = 4.6 and 9.5 dm for the sensitivity run in which the chemical compositions of the bentonite and granite porewaters are changed.

Sorbed species

The results of the sensitivity run show that the competition for the sorption sites plays a relevant role in the geochemical evolution in the bentonite. Figure 5.84 shows the time evolution of computed concentration of sorbed species in the bentonite at r = 4.6 dm. The weak 1 sorption sites are initially occupied by $S^{W1}OH$ and $S^{W1}O^-$. The initial concentration of $S^{W1}OH$ for the sensitivity run is smaller than that of the base run due to differences on the initial pH. On the other hand, the initial concentration of $S^{W1}O^-$ for the sensitivity run is larger than that of the base run. $S^{W2}OH$ is the main sorbed species most of the time. The concentration of $S^{W1}OH$ decreases slowly while that of $S^{W1}O^-$ increases. The competition of these two sorption complexes for weak 1 sorption sites leads to a sorption front at t = 30 years. Dissolved Fe^{2+} competes with protons for the weak 1 sorption sites. The concentration of $S^{W1}OFe^+$ increases until t = 1500 years while that of $S^{W1}O^-$ decreases. Later, on the contrary, the concentration of $S^{W1}OFe^+$ decreases while that of $S^{W1}O^-$ increases. There is no competition of Fe^{2+} for the weak 2 sorption sites. The concentration of $S^{W2}OH$ decreases while that of $S^{W2}O^-$ increases. The concentrations of the four main complexes show oscillations from $2\cdot10^4$ to $5\cdot10^4$ years. After t = $1.5\cdot10^5$ years, H^+ sorbs on weak 1 and 2 sorption sites. Later, H^+ desorbs from the weak sorption sites.

Figure 5.85 shows the time evolution of computed concentration of sorbed species in the bentonite at r = 4.9 dm. The effect of the pH and Eh fronts can be observed (Figure 5.70

and Figure 5.73). The concentrations of sorbed complexes show trends similar to those observed at r = 4.6 dm. The sorption front on weak 1 sites takes place from 30 and 40 years.

Figure 5.86 and Figure 5.87 show the time evolution of the computed concentration of sorbed species in the bentonite at r = 9.5 and 11.9 dm. Dissolved Fe^{2+} does not sorb at these locations. Far from the canister, less H^{+} are released from the weak 1 sorption sites. No changes in species sorbed in weak 2 sorption sites are observed before t = $5 \cdot 10^4$ years. The behaviour of the sorbed species is identical throughout the bentonite after t = $5 \cdot 10^4$ years.

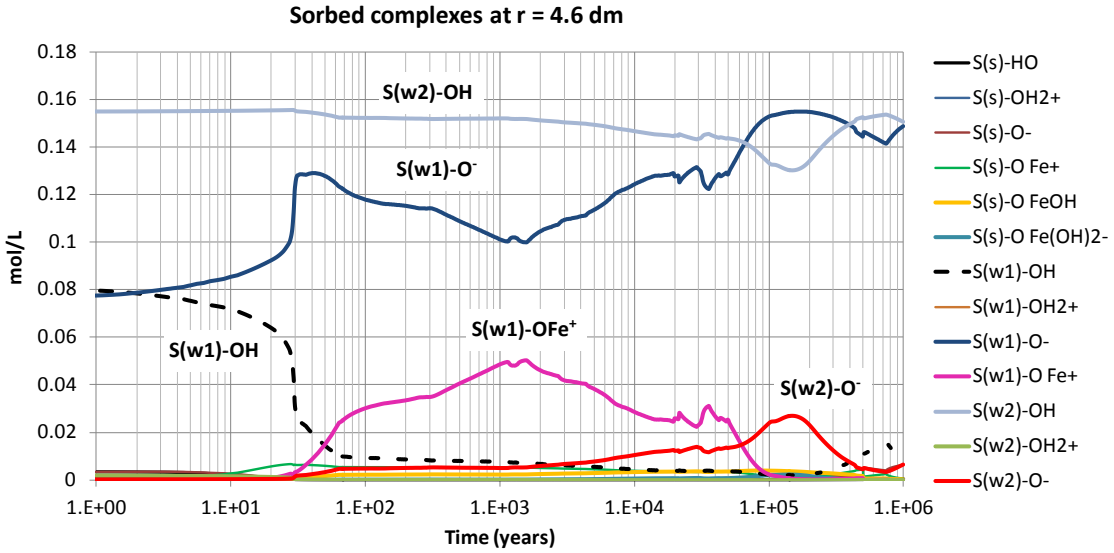

Figure 5.84. Time evolution of the concentrations of sorbed species in the bentonite at r = 4.6 dm for the sensitivity run in which the chemical compositions of the bentonite and granite porewaters are changed.

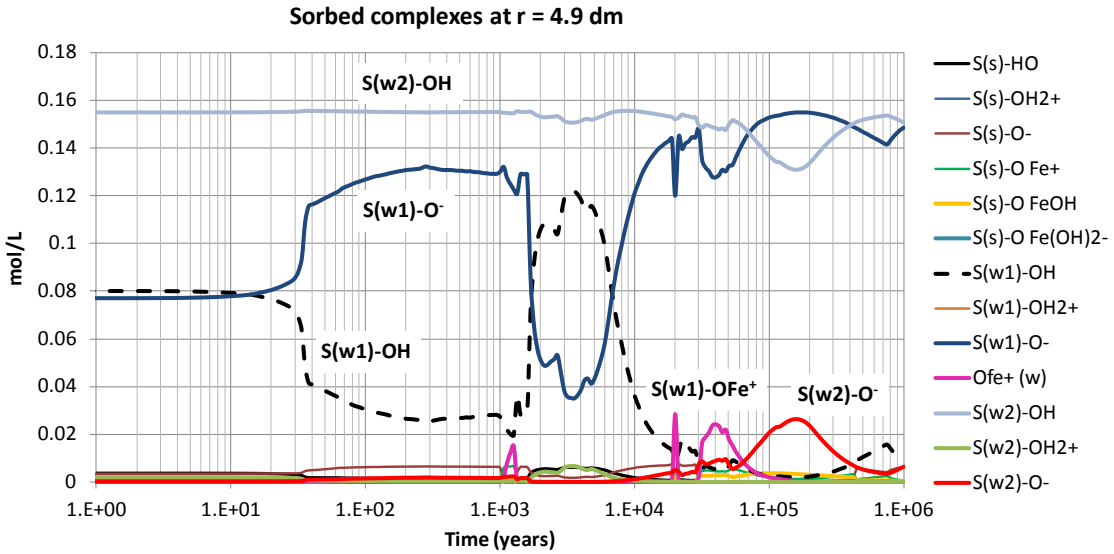

Figure 5.85. Time evolution of the concentrations of sorbed species in the bentonite at r = 4.9 dm for the sensitivity run in which the chemical compositions of the bentonite and granite porewaters are changed.

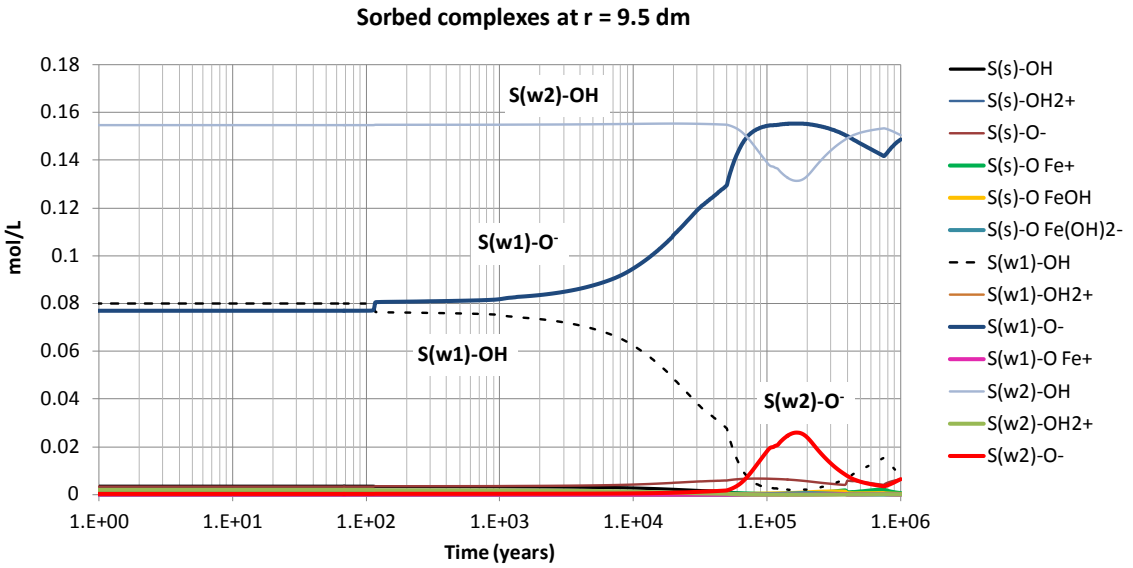

Figure 5.86. Time evolution of the concentrations of sorbed species in the bentonite at r = 9.5 dm for the sensitivity run in which the chemical compositions of the bentonite and granite porewaters are changed.

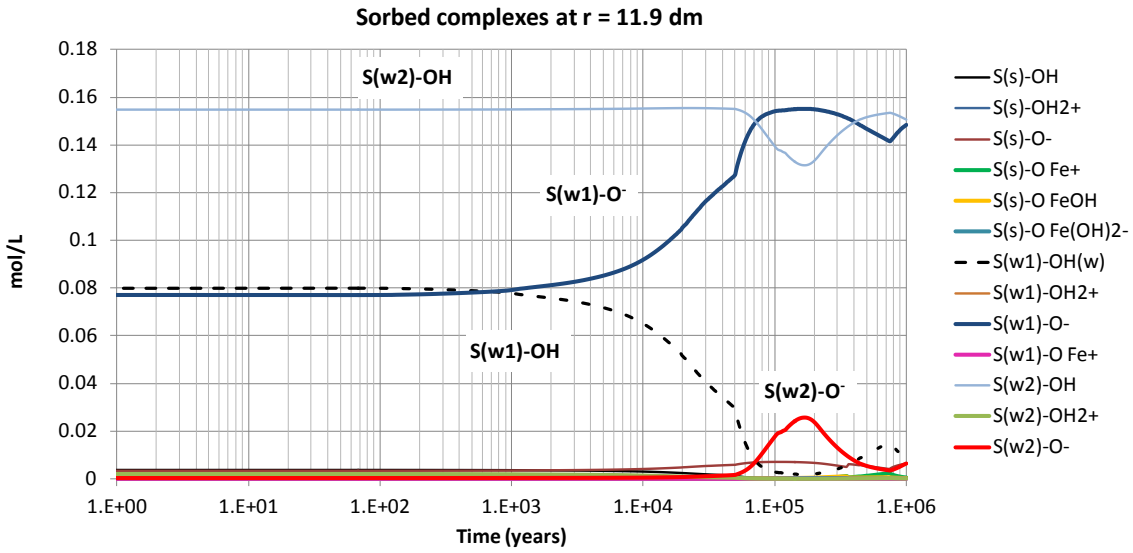

Figure 5.87. Time evolution of the concentrations of sorbed species in the bentonite at r = 11.9 dm for the sensitivity run in which the chemical compositions of the bentonite and granite porewaters are changed.

Figure 5.88 to Figure 5.90 show the spatial distribution of sorbed species in the bentonite at selected times. These figures show clearly the first sorption front in which the concentration of $S^{W1}OH$ decreases while that of $S^{W1}O^-$ increases. Such front at t = 35 years is located at r = 5 dm and at t = 100 years has arrived farther than r = 8 dm (Figure 5.92). A second sorption front appears close to the canister at t = 100 years and it grows up. It is very significant at r = 4.9 dm from $1.5 \cdot 10^3$ and $7 \cdot 10^3$ years (Figure 5.85and Figure 5.85). At t = 10^5 years the concentration of sorbed species is nearly uniform in the bentonite (Figure 5.90).

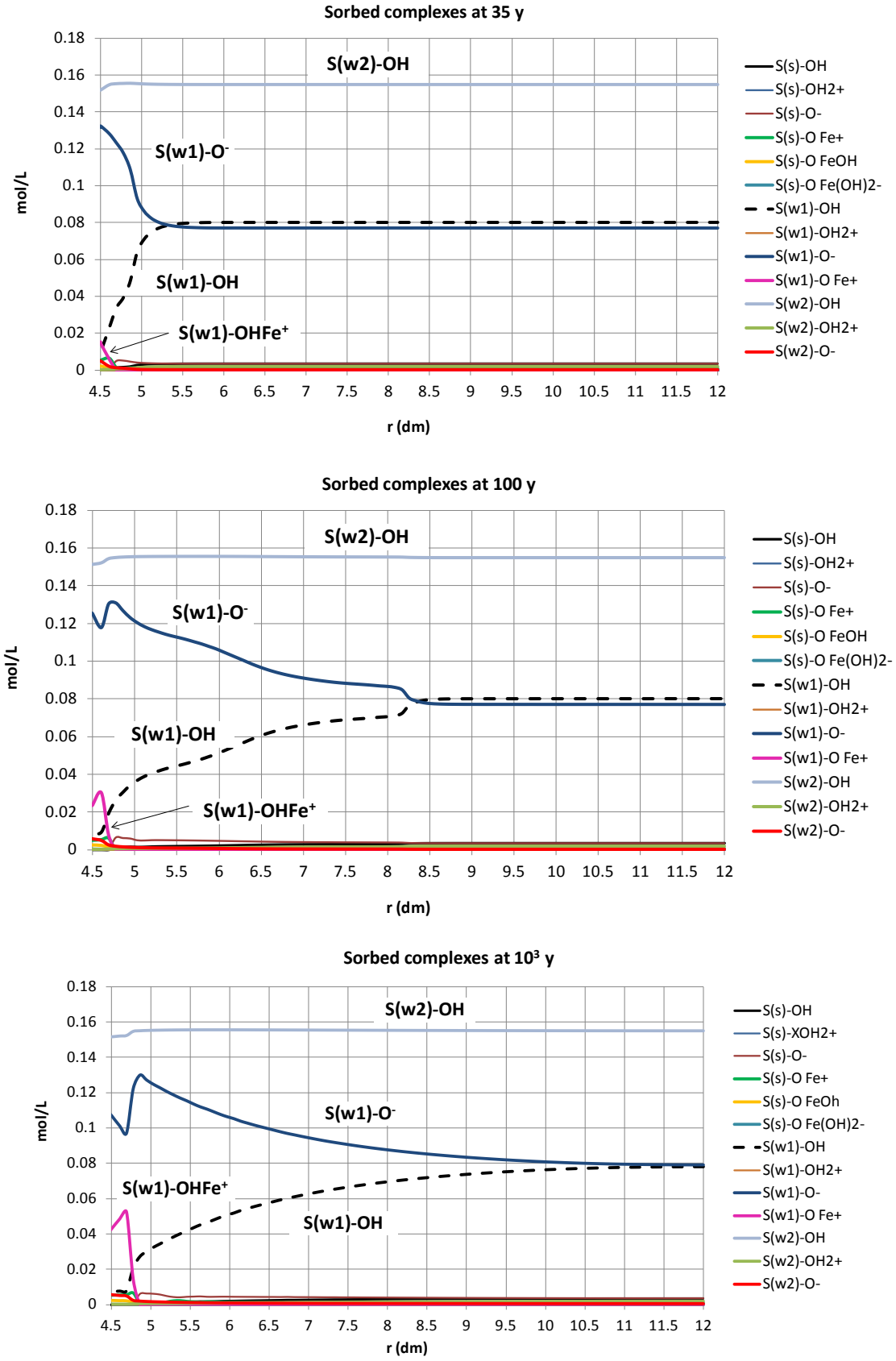

Figure 5.88. Spatial distribution of the concentrations of sorbed species in the bentonite at at t = 35, 100 and 10^3 years for the sensitivity run in which the chemical compositions of the bentonite and granite porewaters are changed.

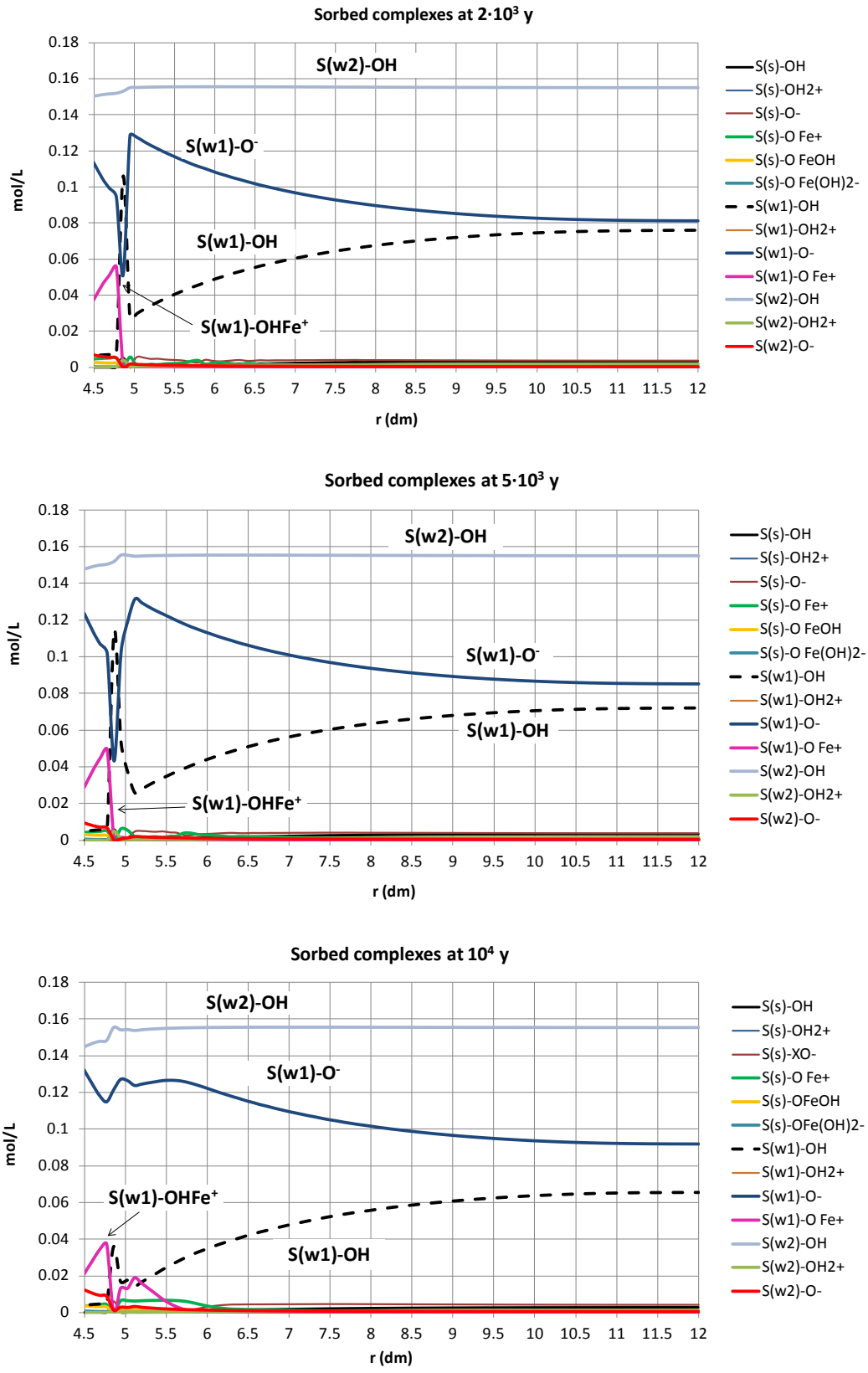

Figure 5.89. Spatial distribution of the concentrations of sorbed species in the bentonite at t = $2 \cdot 10^3$, $5 \cdot 10^3$ and 10^4 years for the sensitivity run in which the chemical compositions of the bentonite and granite porewaters are changed.

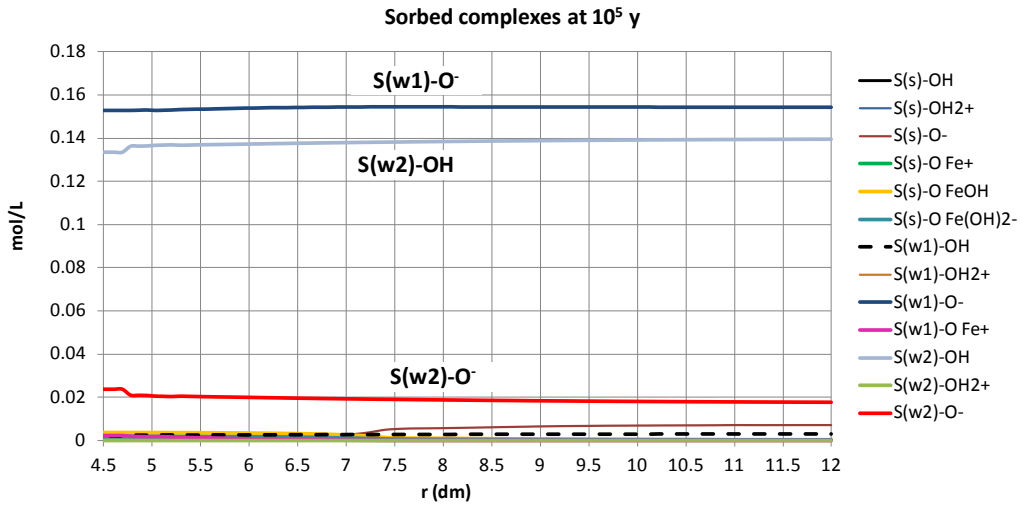

Figure 5.90. Spatial distribution of the concentrations of sorbed species in the bentonite at t = 10^5 years for the sensitivity run in which the chemical compositions of the bentonite and granite porewaters are changed.

The comparison of the concentrations of the sorbed species in the bentonite computed in the sensitivity and base runs shows that the concentration of sorbed iron in the sensitivity run is much smaller than that of the base run. This is linked to the initial Fe^{2+} concentration of the bentonite porewater. Two sorption fronts occur in both runs, but they take place sooner and closer to the canister in the sensitivity run.

Hydrogen pressure

The time evolution of the computed $H_2(g)$ for the sensitivity and base runs is shown in Figure 5.95. Pressure increases in both cases until the canister is fully corroded at $5 \cdot 10^4$ years. However, the peak pressure for the sensitivity run is smaller than that of the base run.

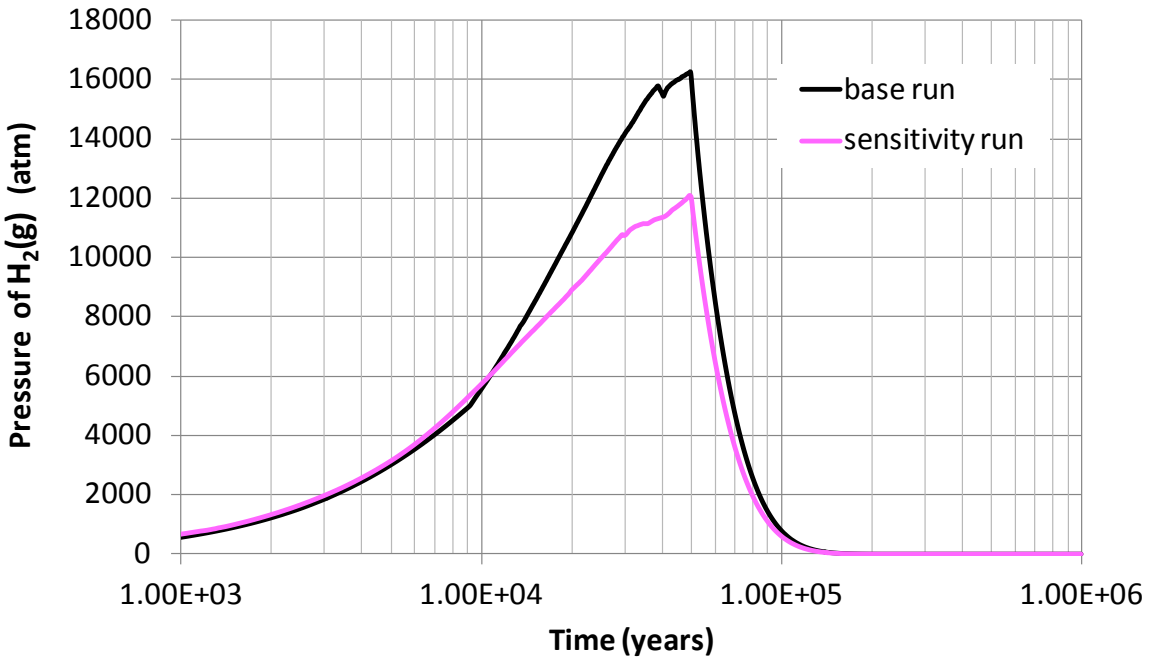

Figure 5.91. Time evolution of the hydrogen partial pressure in the bentonite for the base run and the sensitivity run in which the chemical compositions of the bentonite and granite porewaters are changed.

Changes in porosity

Figure 5.96 show the time evolution of the changes in bentonite porosity due to the mineral dissolution and precipitation at selected locations. Figure 5.97 shows the spatial distribution of the changes in porosity at selected times. Changes in porosity near the canister at t = 10^4 years are not relevant for the sensitivity run although they are for the base run However, magnetite and calcite precipitation causes a very relevant decrease of bentonite porosity afterwards. The thickness of bentonite zone affected by pore clogging in the sensitivity run is smaller than that of the base run.

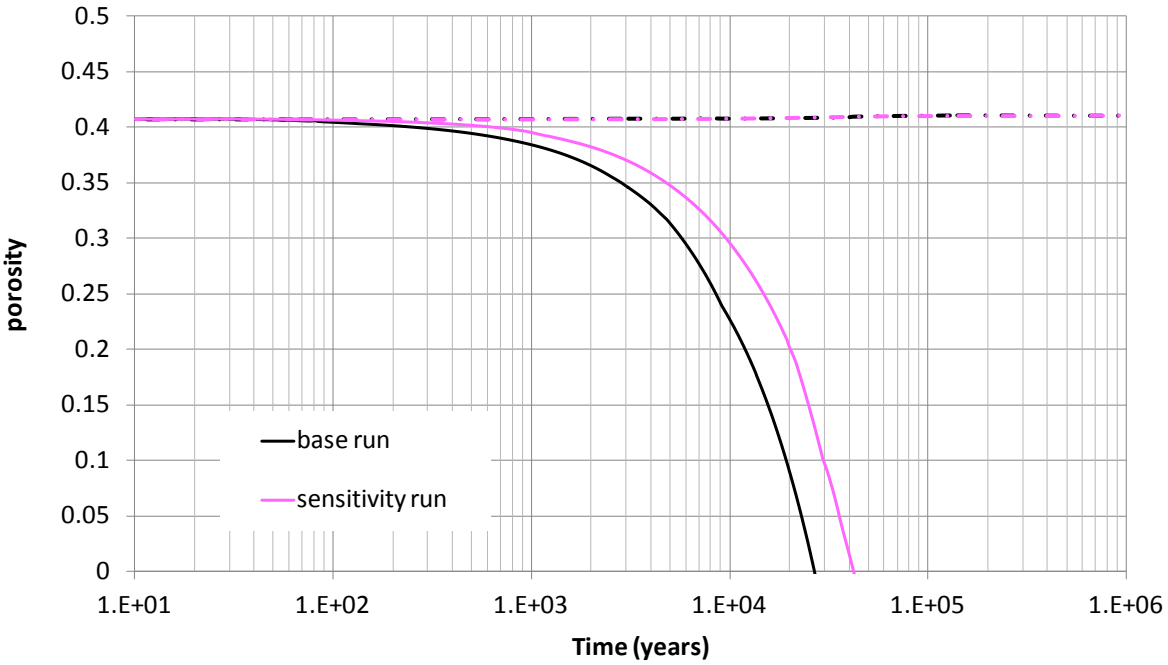

Figure 5.92. Time evolution of the change in porosity caused by mineral dissolution/precipitation at r = 4.6 and r = 9.5 dm for the base run and the sensitivity run in which the chemical compositions of the bentonite and granite porewaters are changed.

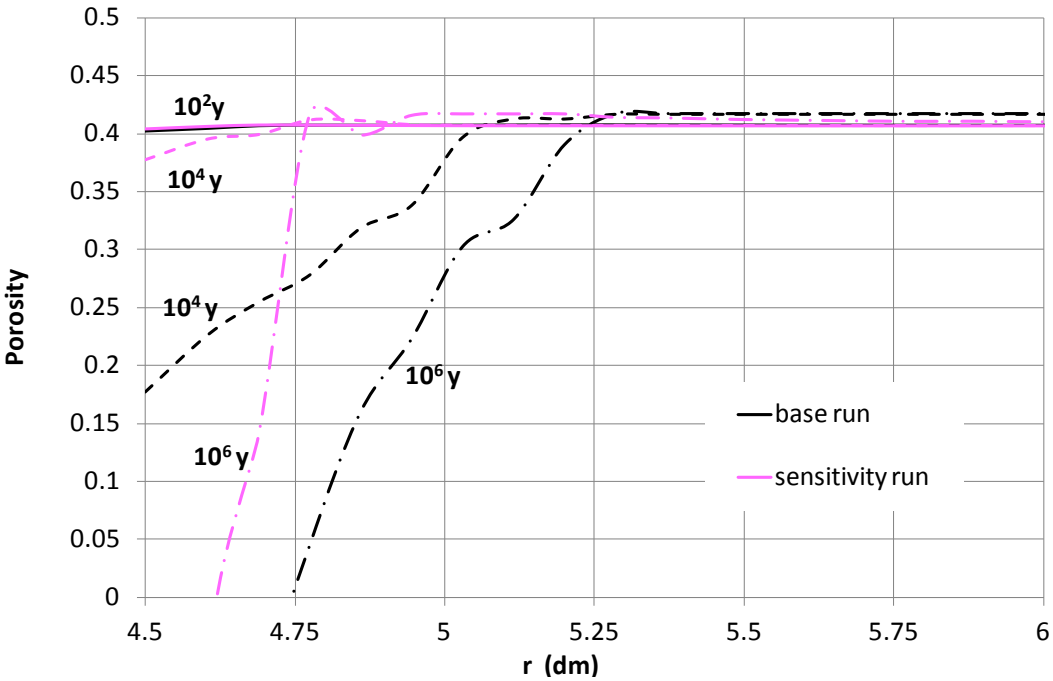

Figure 5.93. Spatial distribution of the change in porosity caused by mineral dissolution/precipitation at selected times for the base run and the sensitivity run in which the chemical compositions of the bentonite and ranite porewaters are changed.

5.6.3 Conclusions

The main conclusions of the sensitivity analysis to the change in the chemical compositions of the bentonite and granite porewaters are:

1. The initial concentration of Cl^- in the sensitivity run is smaller than that in the base run and therefore, the computed Cl^- concentration in the sensitivity run is smaller and decreases slower than in the base run.
2. The initial concentration of dissolved Fe^{2+} is smaller than that of the base run and the initial pH in the sensitivity run is larger than that of the base run.
3. The computed pH for the sensitivity run is generally larger than of the base run and reaches its maximum of 9.8 at $t = 1.5 \cdot 10^5$ years.
4. The computed concentration of magnetite in the sensitivity run near the canister/bentonite interface is much larger than in the base run while the thickness of the zone where magnetite precipitates (≈ 2.5 cm) is half of that computed for the base run.
5. Siderite precipitation in the sensitivity run starts much later than in the base run. The thickness of the zone of siderite precipitation in the sensitivity run is always smaller than 4 cm and half of that of the base run. All the precipitated siderite is subsequently dissolved and no siderite remains in the bentonite at the end of the simulation.
6. The concentration of sorbed Fe^{2+} and the thickness of the zone of sorption fronts in the sensitivity run are much smaller than those of the base run. The sorption fronts in the sensitivity run take place sooner and closer to the canister than in the base run.
7. The peak pressure of $H_2(g)$ for the sensitivity run is smaller than that of the base run.
8. The thickness of the bentonite zone affected by pore clogging in the sensitivity run with the modified chemical composition is smaller than that of the base run.

6. Recommendations for future research

The long-term model predictions presented here assumed that all the porewater is accessible to chemical species. The model could be improved by considering different types of waters: internal, external and free waters.

The canister is assumed to have the same transport properties of the bentonite. The uncertainties caused by this simplifying assumption should be evaluated in future studies.

The model assumes that bentonite porosity is constant and equal to its initial value based on the findings of Samper et al. (2008a) which were based on a corrosion rate of 0.2 μm/y. For a more realistic corrosion rate of 2 μm/y, the changes in porosity could be large near the canister/bentonite interface. A model with variable porosity would be more realistic.

The model could also be improved by:

1. Accounting for silicate aqueous complexes
2. Allowing for different effective diffusion coefficients for each chemical species

The model starts after the thermal pulse has been dissipated. Therefore, all chemical reactions were modelled at a constant temperature of 25ºC. Future studies should account for:

1. Bentonite hydration. The initial chemical composition of the bentonite porewater would then be that corresponding to the ambient conditions with a gravimetric water content of about 14%
2. The thermal field across the EBS which may last for some thousands of years.

The model presented here assumes that magnetite precipitation takes place at equilibrium conditions. However, magnetite precipitation may obey kinetics. The uncertainties caused by this assumption should be evaluated in future studies

The model could also be improved by:

1. Accounting for silicate aqueous complexes
2. Allowing for different effective diffusion coefficients for each chemical species
3. Incorporating smectite kinetic dissolution
4. Neoformation of Fe-clay minerals

7. Conclusions

The canister corrosion, the interactions of corrosion products with bentonite and the pH buffering mechanisms have been simulated during 1 Ma and at a constant temperature of 25ºC for a spent-fuel carbon-steel canister repository in granite.

The canister is fully corroded after $5 \cdot 10^4$ years for a constant corrosion rate of 2 μm/y. Canister corrosion causes an increase in the concentration of dissolved Fe^2 and pH, and a decrease in Eh. Most of the released Fe^{2+} diffuses from the canister into the bentonite where it precipitates or sorbs. The largest pH in the bentonite is almost 9.5 at $2 \cdot 10^5$ years. The evolution of the concentration of dissolved Fe^{2+}, pH and Eh are determined by the generation of corrosion products, the precipitation of magnetite and Fe sorption on weak sites.

Magnetite is the main corrosion product in the bentonite. Its precipitation progresses as Fe^{2+} diffuses into the bentonite. Siderite precipitation is much smaller than magnetite precipitation due to the limited availability of dissolved bicarbonate (smaller than 2 mol/L). The thickness of the bentonite zone where siderite precipitates is similar to that of the magnetite. The precipitation of the corrosion products contributes to the decrease in the concentration of dissolved Fe^2 and influences the pH evolution. Calcite dissolves in most of the bentonite except near the canister where it precipitates due to the increase in pH induced by canister corrosion. Dissolution/precipitation of quartz and gypsum are not significant.

Conservative species such as Cl^- present a pattern of decreasing concentration with time in the bentonite because their diffusion to granite. Dissolved cations, Ca^{2+}, Mg^{2+}, Na^+ and K^+ and show trends similar to those of conservative species but they are also subjected to mineral dissolution/precipitation and cation exchange processes.

The computed concentrations of exchanged cations in the bentonite vary with time due to changes in cation porewater concentration. The concentration of exchanged Ca^{2+} increases after 1 Ma while those of Na^+ and Mg^+ decrease. Only a small part of the Fe released by canister corrosion is sorbed at exchanged sites. The evolution of the concentration of exchanged Fe^{2+} is related to that of sorbed and dissolved Fe^{2+}.

Model results show that sorption play a very relevant role in the geochemical evolution of bentonite. Fe^{2+} and H^+ compete for the weak 1 sorption sites near the canister. Such competition leads to the several sorption fronts and is relevant only at distances smaller than 8 cm from the canister. There is no competition between Fe^2 and H^+ for weak 2 sorption sites because the model does not consider for sorption of Fe on weak 2 sites.

The time evolution of the $H_2(g)$ pressures generated has been calculated from computed the computed activities. The partial pressure of $H_2(g)$ increases while the canister is being corroded until 16200 atm and decreases once the canister has been fully corroded.

The effects of mineral dissolution and precipitation in porosity have been evaluated. The precipitation of the corrosion products close to the canister leads to a very large decrease of bentonite porosity in a zone of ≈ 6 cm of thickness. A negligible increase of the porosity is observed in the rest of the buffer.

The main conclusions of the sensitivity analysis to the corrosion rate include:

1. The increase in pH takes place sooner the larger the corrosion rate.
2. The larger the corrosion rate, the larger the magnetite concentration close to the canister/bentonite interface but the smaller its penetration in the bentonite.
3. Similar to magnetite, the larger the corrosion rate the smaller the penetration of the siderite front into the bentonite.
4. The thickness of the zone where calcite precipitates in the bentonite decreases with the corrosion rate and ranges from 4 to 10 cm for corrosion rates from 5 to 0.5 μm/y. For the smallest corrosion rate calcite precipitates everywhere in the bentonite.
5. The computed concentrations of exchanged cations in the bentonite are not sensitive to changes in the corrosion rate.
6. The larger the corrosion rate, the faster the porosity reduction near the canister interface. The larger the corrosion rate, the smaller the thickness of bentonite affected by pore clogging.

The main conclusions of the sensitivity analysis to the D_e of the bentonite include:

1. The computed concentrations of most dissolved species, except for the dissolved Fe^{2+} are not sensitive to the changes in D_e. The larger the D_e, the smoother is the increase of the curve if the concentration of dissolved Fe^{2+}.
2. The computed pH is not very sensitive to the change in the D_e of the bentonite.
3. The larger the D_e, the larger the thickness of the zone where magnetite, siderite and calcite precipitate. The thickness of magnetite precipitation increases from 4 to 9 cm when the D_e increases from *0.5De* to *2De*.

4. The computed concentrations of exchanged cations in the bentonite and the $H_2(g)$ partial pressure are not sensitive to changes in the D_e of the bentonite.
5. The larger the D_e of the bentonite, the larger the zone affected by the porosity reduction and the larger the thickness of bentonite affected by pore clogging.

The main conclusions of the sensitivity analysis to the groundwater flow Q include:

1. The computed concentrations of most dissolved species are very sensitive to the changes in the water flow Q because the solute flux from the bentonite into the granite is controlled mostly by the advective transport of the granite water flow. The larger the Q, the faster the decrease of the concentrations.
2. The computed pH is slightly sensitive to the change in Q after 400 years. The larger the Q the larger the pH from 400 to $6 \cdot 10^4$ years. After $6 \cdot 10^4$ years, the computed pH is largest for the smallest groundwater flow.
3. The computed Eh is not sensitive to changes in Q.
4. The concentration of precipitated magnetite in the bentonite is strongly sensitive to the increase in the groundwater flow, Q. The larger the Q, the smaller the concentration of precipitated magnetite and the smaller the thickness of the zone where magnetite precipitates.
5. The concentration of precipitated siderite is very sensitive to Q. The larger the Q, the larger the precipitation of siderite and the smaller the thickness of the zone where siderite precipitates.
6. The concentration of precipitated calcite near the canister/bentonite interface is very sensitive to the changes in groundwater flow, Q. The larger the Q, the smaller the zone where calcite precipitates.
7. The concentration of the exchanged Fe^{2+} is sensitive to Q after $t = 4 \cdot 10^3$ years. The larger the Q, the lager the concentration of the exchanged Fe^{2+}.
8. Sorption fronts are less pronounced when the groundwater flow increases.
9. The $H_2(g)$ partial pressure is very sensitive to the groundwater flow. The larger the Q, the smaller the $H_2(g)$ partial pressure.
10. The larger the groundwater flow Q, the smaller the zone affected by the porosity reduction and the smaller the thickness of bentonite affected by pore clogging.

The change in the cation selectivities affect mostly the concentrations of exchanged cations, especially Mg^{2+} and Ca^{2+}. However, the computed pH, Eh and the concentrations of dissolved and precipitated species lack sensitivity to the selectivities.

The main conclusions of the sensitivity analysis to the change in the chemical compositions of the bentonite and granite porewaters are:

1. The initial concentration of Cl^- in the sensitivity run is smaller than that in the base run and therefore, the computed Cl^- concentration in the sensitivity run is smaller and decreases slower than in the base run.
2. The initial concentration of dissolved Fe^{2+} is smaller than that of the base run and the initial pH in the sensitivity run is larger than that of the base run.
3. The computed pH for the sensitivity run is generally larger than of the base run.
4. The computed concentration of magnetite in the sensitivity run near the canister/bentonite interface is much larger than in the base run while the thickness of the zone where magnetite penetrates (≈ 2.5 cm) is half of that computed for the base run.
5. Siderite precipitation in the sensitivity run starts much later than in the base run. The thickness of the zone of siderite precipitation in the sensitivity run is always smaller than 4 cm and half of that of the base run. All the precipitated siderite is subsequently dissolved and no siderite remains in the bentonite at the end of the simulation.
6. The concentration of sorbed Fe^{2+} and the thickness of the zone of sorption fronts in the sensitivity run are much smaller than those of the base run.
7. The peak pressure of $H_2(g)$ for the sensitivity run is smaller than that of the base run.
8. The thickness of the bentonite zone affected by pore clogging in the sensitivity run with the modified chemical composition is smaller than that of the base run.

Possible ways to improve the model have been identified and recommendations for future research have been provided, including:

1. Considering different types of waters: internal, external and free waters;

2. Allow for the canister void space to have properties other than those of the bentonite;
3. Allowing for the dynamic update of bentonite porosity to account for the possible pore clogging. This will require the use of kinetics for mineral precipitation;
4. Accounting for silicate aqueous complexes;
5. Allowing for different effective diffusion coefficients for each chemical species;
6. Accounting for bentonite hydration and the thermal field across the EBS;
7. Taking into account kinetic magnetite precipitation;
8. Incorporating smectite kinetic dissolution and the neoformation of Fe-clay minerals

8. References

Bradbury, M.H., Baeyens, B., 1997. A mechanistic description of Ni and Zn sorption on Na-montmorillonite. Part II: Modelling. Journal of Contaminant Hydrology 27, 223-248.

Bradbury, M.H, Baeyens, B., 2002. Porewater chemistry in compacted re-saturated MX-80 bentonite: Physico-chemical characterisation and geochemical modelling. PSI Bericht 02-10, Villigen PSI and NTB 01-08, Nagra, Wettingen, Switzerland.

Bradbury, M.H., Baeyens, B., 2003. Porewater chemistry in compacted re-saturated MX-80 bentonite. Journal of Contaminant Hydrology 61, 329-338.

Bradbury, M.H., and Baeyens, B., 2005. Modelling the sorption of Mn(II), Co(II), Ni(II), Zn(II), Cd(II), Eu(III), Am(III), Sn(IV), Th(IV), Np(V) and U(VI) on montmorillonite: Linear free energy relationships and estimates of surface binding constants for some selected heavy metals and actinides. Geochimica et Cosmochimica Acta 69, 875-892.

BENIPA, 2003. Final Report of BENIPA Project: Bentonite Barriers in Integrated Performance Assessment. Final Technical Report EUR 21023.

Drissi, S.H., Refait, Ph., Abdelmoula, M., Génin, J.M.R., 1995. The preparation and thermodynamic properties of Fe(II)–Fe(III) hydroxide carbonate (green rust 1); pourbaix diagram of iron in carbonate-containing aqueous media. Corrosion Science 37, 2025–2041.

ENRESA, 2000a. Full-scale engineered barriers experiment for a deep geological repository in crystalline host rock FEBEX Project. EUR 19147 EN, European Commission.

ENRESA 2000b. Evaluación del comportamiento y de la seguridad de un almacenamiento de combustible gastado en una formación granítica. ENRESA Informe 49-1PP-M-15-01. Madrid, 2001.

ENRESA, 2004. Evaluación del comportamiento y de la seguridad de un almacén geológico profundo de residuos radiactivos en arcilla. Clave: 49-1PP-M-A1-01. ENRESA (In Spanish).

ENRESA, 2005. NF-PRO Project. Phenomenological description. Reference Concept (Spent Fuel–Carbon Steel Canister–Bentonite–Granite). Deliverable D5.1.1. Part 1.

ENRESA, 2006. Full-Scale Engineered Barriers Experiment: Updated Final Report 1994-2004. ENRESA Tech. Publ. PT 05-02/2006, 589 pp.

Fernández, A., Cuevas, J., Rivas, P., 2001. Pore water chemistry of the FEBEX bentonite. Materials Research Society Symposium Proceedings, 663, 573-588.

Fernández, A., Baeyens, B., Bradbury, M., Rivas, P., 2004. Analyses of the porewater chemical composition of a Spanish compacted bentonite used in a engineered barrier. Physics and Chemistry of the Earth 29, 105-118.

Gaines, G.I., Thomas, H.C., 1953. Adsorption studies on clay minerals II. A formulation of the thermodynamics of exchange adsorption. Journal of Chemical Physics 21, 714–718.

Génin, J.R.M., Olowe, A.A., Refait, Ph., Simon, L., 1996. On the stoichiometry and Pourbaix diagram of Fe(II)–Fe(III) hydroxy-sulphate or sulphate containing green rust: 2. An electrochemical and Mössbauer spectroscopy study. Corrosion Science 38, 1751–1762.

JNC, 2000. H12: Project to establish the scientific and technical basis for HLW disposal in Japan. Japan Nuclear Cycle Development Institute, Supporting Report 2, Repository Design and Engineering Technology.

King, F., 2008. Corrosion of carbon steel under anaerobic conditions in a repository for SF and HLW in Opalinus Clay, NAGRA Technical Report 08-12, October 2008.

Lu, C., Samper, J., Fritz, B., Clement, A., Montenegro, L., 2011. Interactions of corrosion products and bentonite: An extended multicomponent reactive transport model, Physics and Chemistry of the Earth 36, 1661–1668, doi: 10.1016/j.pce.2011.07.013.

Lu, C., Samper, J., Cormenzana, J.L., Ma, H., Montenegro, L., Cuñado, M.A., 2012. Reactive transport model and apparent K_d of Ni in the near field of a HLW repository in granite. Computers and Geosciences 49, 256-266, doi: 10.1016/j.cageo.2012.06.003

Ma, H., 2010. Reactive transport models in acid mine drainage and nuclear waste disposal, Ph.D. Dissertation, Universidad de A Coruña.

Miyata, S., 1983. Anion-exchange properties of hydrotalcite-like compounds. Clays and Clay Minerals 31, 305–311.

Molinero, J., Samper, J., 2006. Modeling of reactive solute transport in fracture zones of granitic bedrocks. Journal of contaminant Hydrology 82, 293-318.

Refait, Ph., Drissi, S.H., Pytkiwicz, J., Génin, J.M.R., 1997. The anionic species competition in iron aqueous corrosion: role of various green rust compounds. Corrosion Science 39, 1699–1710.

Samper, J., Yang, C., Montenegro, L., 2003. CORE^{2D} V4: a code for non-isothermal water flow and reactive solute transport. Users Manual. University of La Coruña, Spain.

Samper, J., Zheng, Montenegro, L. , Vázquez, A., Fernández, A.M., Rivas, P., 2005. Testing coupled thermo-hydro-geochemical models with geochemical data from FEBEX in situ test, En: Advances in Understanding Engineered Clay Barriers, , E. Alonso and A. Ledesma Eds, Balkema Pub. ISBN 04 1536 5449, 565-576, 2005.

Samper, J., Vázquez, A., Montenegro, L., 2005b. Inverse hydrochemical modelling of aqueous extracts experiments for the estimation of FEBEX bentonite pore water chemistry. In: Alonso, E.E., Ledesma, A. (Eds.), Advances in Understanding Engineered Clay Barriers. A.A. Balkema Publishers, Leiden, The Netherlands, pp. 553-563.

Samper, J., Yang, Ch., Montenegro, L., Bonilla, M., Lu, C., Yang, Q., Zheng, L., 2007. Mass and energy balance and flux calculations for radionuclide release and geochemical evolution for SF carbon steel HLW repositories in clay and granite. NF-PRO project, Deliverable D5.1.13. University of A Coruña, Spain.

Samper, J., Lu, C., Montenegro, L., 2008a. Coupled hydrogeochemical calculations of the interactions of corrosion products and bentonite. Physics and Chemistry of the Earth 33, S306–S316, doi:10.1016/j.pce.2008.10.009.

Samper, J., Zheng, L., Fernández, A.M., Montenegro, L., 2008b. Inverse modeling of multicomponent reactive transport through single and dual porosity media. Journal of Contaminant Hydrology 98, 115–127.

Samper, J., Zheng, L., Montenegro, L., Fernández, A.M., Rivas, P., 2008c. Testing coupled thermo-hydro-chemical models of compacted bentonite after dismantling the FEBEX in situ test. Applied Geochemistry 23, 1186–1201, doi:10.1016/j.apgeochem.2007.11.010.

Samper, J., Xu, T., Yang, C., 2009b. A sequential partly iterative approach for multicomponent reactive transport with CORE2D. Computational Geosciences. doi: 10.1007/s10596-008-9119-5.

Samper, J., Lu, C., Cormenzana, J.L., Ma, H., Montenegro, L., Cuñado, M.A., 2010. Testing K_d models of Cs+ in the near field of a HLW repository in granite with a reactive transport model. Physics and Chemistry of the Earth 35, 278–283, doi:10.1016/j.pce.2010.04.002.

Samper, J., Lu, C., Fritz, B., Clement, A., Montenegro, L., 2011. Interactions of corrosion products and bentonite: An extended multicomponent reactive transport model. Physics and Chemistry of the Earth, 36, 1661–1668, doi: 10.1016/j.bbr.2011.03.031

Smart, N.R., Rance, A.P., Carlson, L., Werme, L.O., 2006. Further studies of the anaerobic corrosion of steel in bentonite. Material Research Society Symposium Proceedings 932, 813–820.

Taniguchi, N., Kawasaki, M., Kawakami, S., Kubota, M., 2004. Corrosion behaviour of carbon steel in contact with bentonite under anaerobic condition. In: Prediction of Long Term Corrosion in Nuclear Waste Systems Proceedings 2nd International Workshop, Nice, September 2004, p. 24–34.

Tournassat, C., 2003. Cations–clay interactions: The Fe(II) case. Application to the problematic of the French deep nuclear repository field concept. Ph.D. Dissert. Grenoble, France.

Wolery, T.J., 1992. EQ3/6, a software package for geochemical modeling of aqueous systems: Package overview and installation guide (version 7.0). Technical Report UCRL-MA-110662-Pt 1. Lawrence Livermore National Laboratory, CA, USA.

Xu, T., Samper, J., Ayora, C., Manzano, M., Custodio, E., 1999. Modeling of nonisothermal multicomponent reactive transport in field scale porous media flow systems. Journal of Hydrology 214, 144–164.

Yang, C., Samper, J., Montenegro, L., 2008. A coupled non-isothermal reactive transport model for long-term geochemical evolution of a HLW repository in clay. Environmental Geology 53, 1627–1638, doi: 10.1007/s00254-007-0770-2.

Zheng, L., Samper, J., 2008. Coupled THMC model of FEBEX mock-up test. Physics and Chemistry of the Earth 33, S486–S498, doi:10.1016/j.pce.2008.10.023.

Zheng, L., Samper, J., Montenegro, L., Mayor J.C., 2008. Flow and reactive transport model of a ventilation experiment in Opalinus clay. Physics and Chemistry of the Earth 33, 1009-1018, doi: 10.1016/j.pce.2008.05.012

Zheng, L, Samper, J., Montenegro, L., Fernández, AM., 2010. A coupled THMC model of a heating and hydration laboratory experiment in unsaturated compacted FEBEX bentonite. Journal of Hydrology 386, 80-94, doi: 10.1016/j.jhydrol.2010.03.009.

Zheng et al. (2011). A coupled THC model of the FEBEX in situ test with bentonite swelling and chemical and thermal osmosis. Journal of Contaminant Hydrology 126, 45-60.

Appendix 1. Improvements and verification of the code CORE^{2D} V5

CORE^{2D} V5 is a finite element code for modelling water flow (saturated and unsaturated), heat transport and multicomponent reactive solute transport under both chemical equilibrium and kinetic conditions. The code has been updated, improved, tested and verified during the course of the PEBS project. This appendix describes such improvements and the verification of the code. The improvements, corrections and verifications include:

1. The correction of a bug in the reading of sorption data. This bug did not affect the calculations involving sorption reactions and was relevant only when such reactions were not considered. It has been fixed.
2. The correction of a typo in the CORE^{2D} User's Manual. The right units of the specific surface of the minerals should be "dm^2/dm^3 of pore water" instead of "dm^2/dm^3 of bulk medium". It has been fixed.
3. The correction of the calculation of the kinetic rate, r, of mineral dissolution/precipitation. In the previous version of the code the rate r was expressed as "mol of mineral per dm^3 of medium". However, the rate r should be expressed in terms of "mol of mineral per dm^3 of pore water". This correction has been implemented in the code.
4. The improvement of the equation used to calculate the change in porosity caused by the dissolution/precipitation of mineral phases.

The first two corrections were implemented in a straightforward manner. The other two require the verification of the code.

1. Verification of the calculation of the kinetic rate of mineral dissolution/precipitation

The general kinetic rate expression of mineral dissolution/precipitation used in CORE^{2D} is given by (Samper et al., 2011):

$$r_m = s_m e^{\frac{-Ea}{RT}} \sum_{i=1}^{N_k} K_{mk} \prod_{i=1}^{N_c+N_x} a_i^{p_{mki}} \left(\Omega_m^{\theta_{mk}} - 1\right)^{\eta_{mk}} \qquad (1)$$

where:

r_m is the dissolution/precipitation rate

s_m is a function which can take a value of 1 or -1 depending on whether the term involving the saturation index is positive or negative,

Ω_m is the ratio between the ionic activity product and the equilibrium constant

θ_{mk} and η_{mk} are parameters of the k-th kinetic reaction of the m-th mineral, which are usually determined by experiments

$e^{\frac{-Ea}{RT}}$ is the thermodynamic factor, which takes into account the apparent activation energy of the overall reaction, Ea_m. R and T are the gas constant and the absolute temperature, respectively.

$\prod_{i=1}^{N_c+N_x} a_i^{p_{mki}}$ is a factor which accounts for the catalytic effect of some species (usually for H^+).

K_m is the kinetic rate constant of the k-th kinetic reaction of the m-th mineral.

N_k is the number of kinetic reactions of the m-th mineral

N_c and N_x are the number of primary and secondary species, respectively

The code computed r_m as mol/L of medium. These units are not consistent with the rest of the units of other variables. The code has been modified so that the units of mineral dissolution/precipitation in "mol/L of water". A simple example was used for the verification of the revised version of the code. The example involves 4 nodes and 3 one dimensional elements. The total length is 3 dm. It corresponds to isothermal saturated flow. The chemical system is defined in terms of Ca^{2+}, HCO_3^-, H_2O, H^+ and calcite which dissolves kinetically with a kinetic constant of $5 \cdot 10^{-6}$ mol/(dm^2 y). Figure A1-1 shows the scheme of the example.

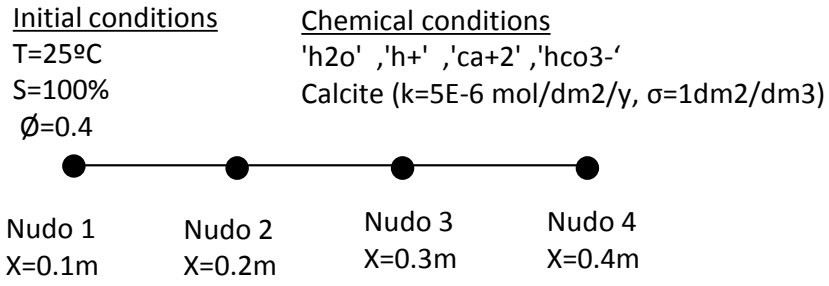

Figure A1-1. Scheme of the example used for the verification.

The verification was performed by comparing the numerical solution with an analytical solution. The analytical solution for calcite dissolution is given by:

$$R = -\frac{dM}{dt} = -\frac{d(PV)}{dt} \rightarrow P = -\frac{R}{\emptyset V}t \qquad (2)$$

where R is the dissolution rate (mol/y), M is the mass of dissolved mineral (mol), P is the concentration of the precipitated species or mineral (mol/L), V is the volume of the porous medium (L) and t is the time (y).

The analytical solution of the concentration c of the dissolved species is given by:

$$c = c_o + \frac{R}{\emptyset V}t \qquad (3)$$

where c_o is the initial concentration (mol/L).

For this example, the volume of the medium is 3 L and the volume of water is 1.2 L. The dissolution rate R is $6 \cdot 10^6$ mol/y. The concentration of the mineral after 70.000 years is 3.4 mol/L.

Figure A1-2 and Figure A1-3 show the comparison of the analytical and numerical solutions of the concentrations of the mineral, P, and dissolved species, c. The numerical solution coincides with the analytical solution for both variables. Therefore, the calculated dissolution rates can be considered to be verified.

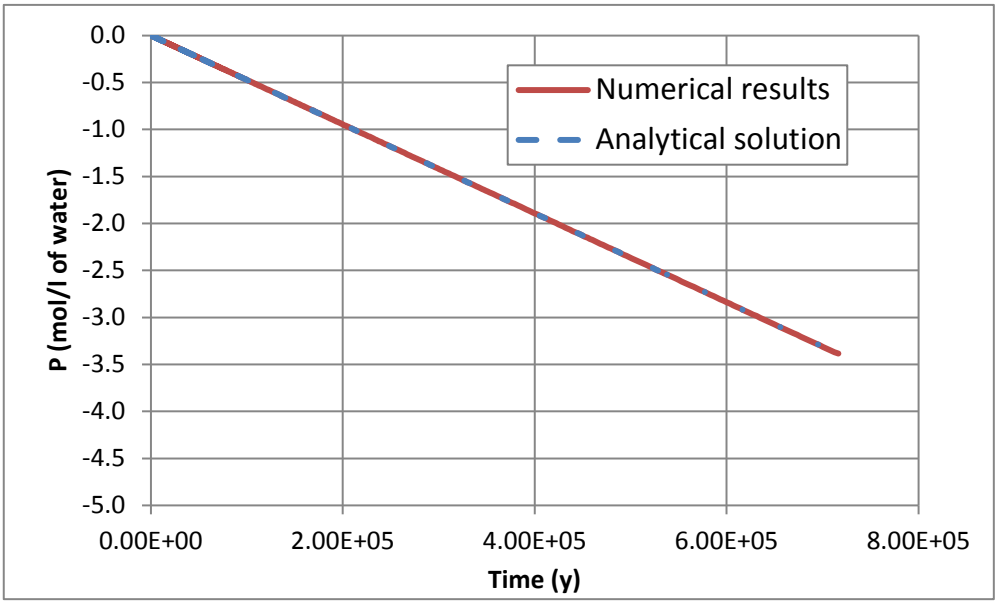

Figure A1-94. Comparison of the analytical and numerical solutions for the concentration of mineral (mol/L).

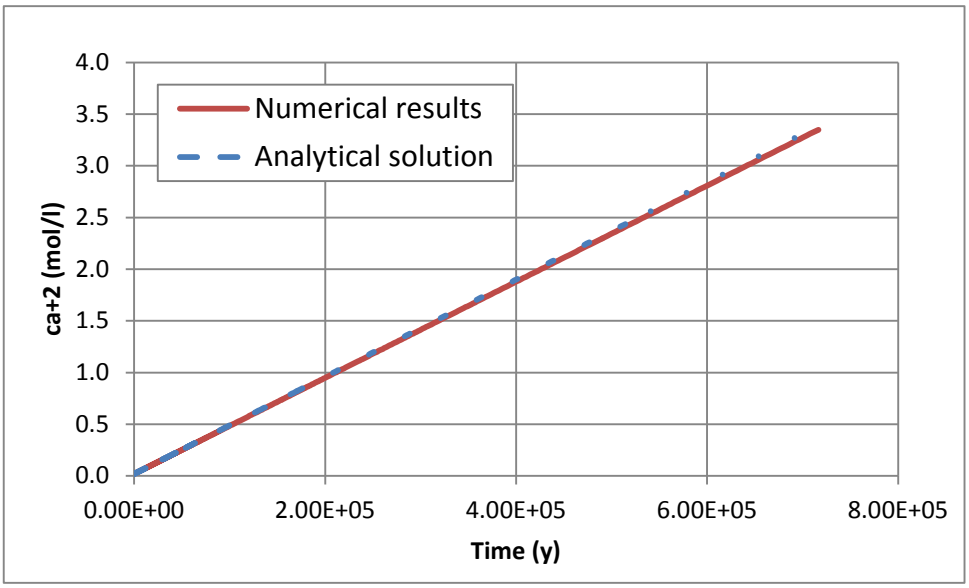

Figure A1-95. Comparison of the analytical and numerical solutions for the concentration of dissolved Ca^{2+} (mol/L).

2. Verification of the calculation of the changes in porosity caused by mineral dissolution/precipitation

The code calculates the changes in the porosity due to mineral dissolution/precipitation at the end of each time step. The total amount of mineral per unit volume of the medium, p, can be related to the porosity ∅ and the concentration of the mineral P by means of:

$$p = \emptyset P \qquad (4)$$

The time derivative of the porosity can be related to the time derivative of p according to:

$$\frac{d\emptyset}{dt} = -\frac{d\emptyset}{dp}\frac{dp}{dt} \qquad (5)$$

Then, the change in porosity, $\Delta\emptyset$, can be computed from:

$$\Delta\emptyset = -\frac{d\emptyset}{dp}\Delta p \qquad (6)$$

where the change of p can be calculated from (4) as:

$$\Delta p = P\Delta\emptyset + \Delta P\emptyset \qquad (7)$$

where ΔP is change of P. By substituting Equation (7) into (6), and recalling that $\frac{d\emptyset}{dp}$ is equal to the molar volume of the mineral, ϑ, one obtains:

$$\Delta\emptyset = \frac{\vartheta\emptyset\Delta P}{1-\vartheta P} \qquad (8)$$

This equation has been implemented in the code to update the porosity at the end of each time step. This method to calculate the porosity has been tested and verified by using the previous test case.

The analytical solution for p is given by:

$$V\,\frac{dp}{dt} = -R \rightarrow p = p_o - \frac{R}{V}t \qquad (9)$$

The analytical solution of the porosity can be derived from Equation 5. By substituting Equation (9) into (5), and after integration, one obtains:

$$\emptyset = \emptyset_o + \frac{R}{V}\vartheta t \qquad (10)$$

The analytical solution for P can be derived by combining Equations (4), (8) and (9):

$$P = \frac{P_0 - Rt/V}{\emptyset} \qquad (11)$$

The analytical solution of the concentration of the dissolved species, c, can be derived from:

$$\frac{dc\emptyset V}{dt} = R \qquad (12)$$

Integrating this differential equation, one has:

$$c = \frac{Rt/V + c_o\emptyset_o}{\emptyset} \qquad (13)$$

where P_o is the initial mineral concentration (mol/L) and $\emptyset_o$ is the initial porosity.

Figure A1-4, Figure A1-5 and Figure A1-6 show the comparison of the analytical and numerical solutions for the concentration of the mineral, P, the concentration of the dissolved species, c, and the porosity, respectively. For the most part, the analytical and numerical solutions coincide. There are small differences at late times which could be due to numerical truncation errors.

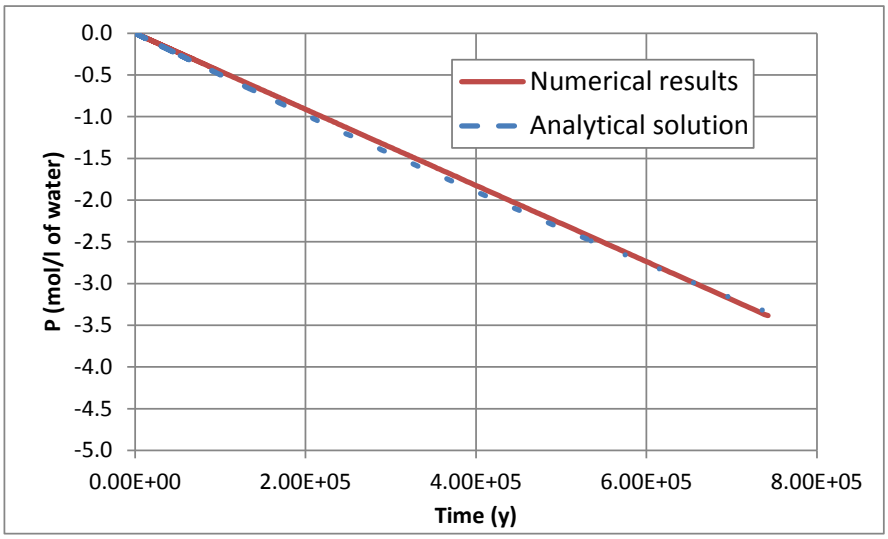

Figure A1-96. Comparison of the analytical and numerical solutions for the concentration of the mineral (mol/l).

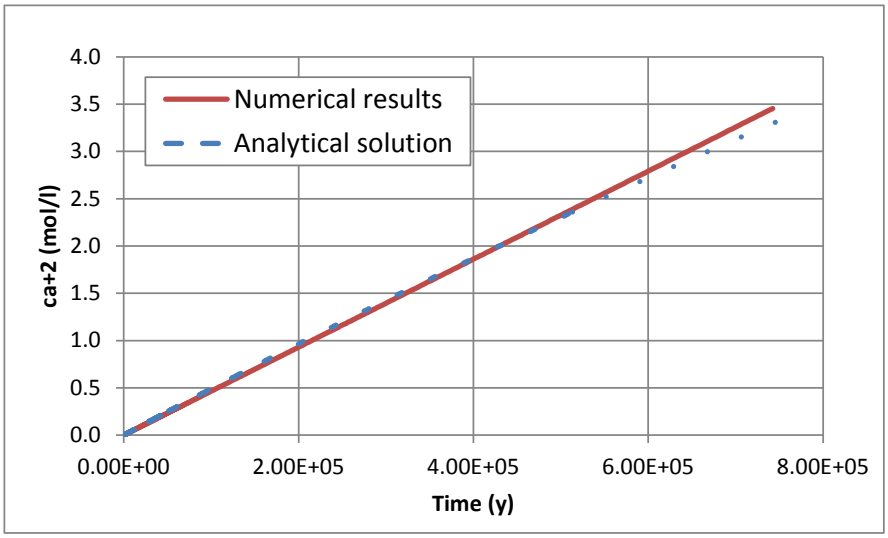

Figure A1-97. Comparison of the analytical and numerical solutions for the concentration of dissolved Ca^{2+} (mol/l).

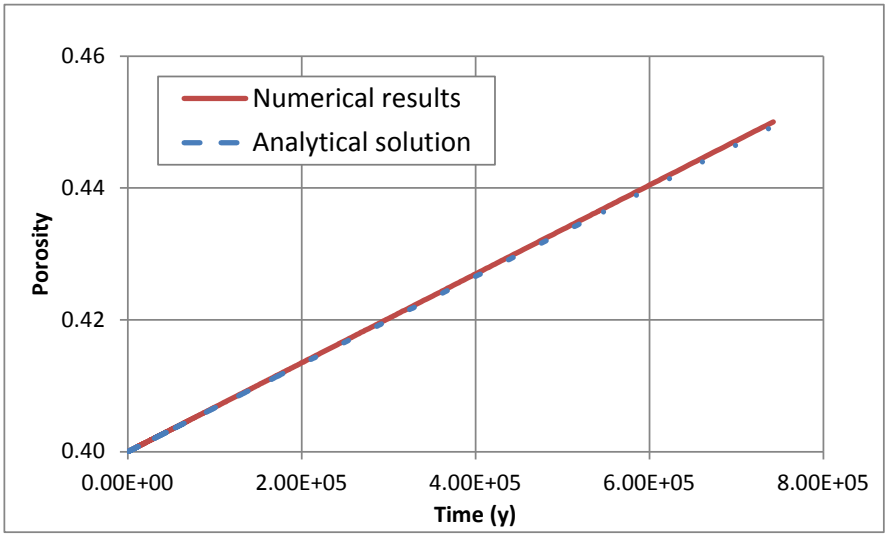

Figure A1-6. Comparison of the analytical and numerical solutions for the porosity.

Appendix 2. Compilation of saturated and unsaturated initial pore water chemical composition used in the UDC THMC models and suggested values

1. Introduction

This Appendix presents a compilation of the bentonite porewater chemical compositions used by in the UDC THMC models. They include the chemical composition of the bentonite at saturated and ambient conditions.

2. Saturated bentonite initial porewater chemical composition

According to ENRESA (2005, 2006) the bentonite barrier for the Spanish reference concept will become fully water-saturated after about 50 years.

For the long-term modeling of the geochemical conditions in the EBS barrier in a repository in granite, most of the models performed by UDC assume that the bentonite is initially water-saturated. Chemical data of the bentonite have been compiled from the following four papers published by UDC:

[1] Samper et al. (2008a). Reactive transport model of interactions of corrosion products and bentonite. Phys. Chem. Earth 33, S306-S316.

[2] Lu et al. (2011). Interactions of corrosion products and bentonite: An Extended multicomponent reactive transport model. Phys. Chem. Earth 36, 1661-1668.

[3] Samper et al. (2010). Testing Kd models of Cs+ in the near field of a HLW repository in granite with a reactive transport model. Phys. Chem. Earth 35, 278-283.

[4] Lu, C, J Samper, JL Cormenzana, H Ma, L Montenegro & MA Cuñado, 2012, Reactive transport model and apparent Kd of Ni in the near field of a HLW repository in granite, Computers and Geosciences, http://dx.doi.org/10.1016/j.cageo.2012.06.003

Table A2-1 shows the chemical compositions of the saturated bentonite porewater and granite porewater chemical used in such papers. In general, the values used in the different papers coincide. There are small differences in pH and silica. The original source of this chemical composition is BENIPA (2003) and Samper et al. (2007). It should be pointed out

that the geochemical model used in these papers accounts for the following geochemical reactions: aqueous complexation, acid-base, redox, mineral dissolution/precipitation, cation exchange and surface complexation.

Table A2-3. Chemical compositions of the saturated bentonite porewater and granite pore water chemical used in the long-term UDC reactive transport models. Numbers within parentheses indicate the reference from which the data come from.

	Bentonite	**Granite**
pH	6.4 [1][2] - 6.435 [3][4]	7.825 [2][3][4]- 8.0 [1]
Eh (V)	-0.059	-0.188
Ca^{2+} (mol/L)	$3.101 \cdot 10^{-2}$	$1.522 \cdot 10^{-4}$
Mg^{2+} (mol/L)	$3.473 \cdot 10^{-2}$	$1.604 \cdot 10^{-4}$
Na^{+} (mol/L)	$1.841 \cdot 10^{-1}$	$4.350 \cdot 10^{-3}$
K^{+} (mol/L)	$1.507 \cdot 10^{-3}$	$5.371 \cdot 10^{-5}$
Fe^{2+} (mol/L)	$6.583 \cdot 10^{-5}$	$1.791 \cdot 10^{-8}$
Cl^{-} (mol/L)	$2.756 \cdot 10^{-1}$	$3.949 \cdot 10^{-4}$
HCO_3^{-} (mol/L)	$1.689 \cdot 10^{-3}$	$5.049 \cdot 10^{-3}$
SO_4^{2-} (mol/L)	$2.049 \cdot 10^{-2}$	$1.561 \cdot 10^{-5}$
$SiO_2(aq)$ (mol/L)	$8.426 \cdot 10^{-4}$, $3.761 \cdot 10^{-4}$ [3]	$3.761 \cdot 10^{-4}$

In addition to the previous papers, Samper et al. (2008b) presented inverse single and dual-continuum multicomponent reactive transport models for a long-term permeation test performed on a 2.5 cm long sample of saturated FEBEX bentonite. The geochemical model accounts for aqueous complexation, acid-base, mineral disolution/precipitation, surface protonation/deprotonation and cation exchange. Redox reactions are not considered in the model. In this test, the porewater solution of the saturated bentonite sample was flushed with granitic water. Given the difficulties of deriving reliable data on bentonite porewater chemistry, they adopted as prior estimate of the initial composition of the bentonite porewater the composition of Samper et al. (2005) derived from squeezing experiments (CGM-0) at a 23.8% water content. Those compositions are listed in Table A2-1. The values used by Samper et al. (2008b) are listed in Table A2-3. One can see that the concentrations of the base run of the direct single-continuum model (SCM) coincide with those of the bentonite in Table

A2-2. Table A2-3 presents also the compositions estimated for the inverse SCM models (steps 1 and 2). The initial concentrations used in the two domains of the inverse dual-continuum model (DCM) are indentical and are taken from obtained with the inverse SCM in step 1. The breakthrough curves of the reactive species computed with a single-continuum model (SCM) reproduce the general trends of measured data, but show discrepancies at early times and fail to fit the long tails of measured data. These deviations are overcome by inverse estimation of initial porewater concentrations and effective diffusion coefficient. The estimation is performed in two steps. The initial concentrations of Ca^{2+}, Mg^{2+}, Na^{+}, K^{+}, SO_4^{2-} and pH are estimated in step 1 while step 2 is devoted to the simultaneous estimation of effective diffusion coefficient and initial concentrations and pH. It should be noticed that initial HCO_3^{-} concentrations in steps 1 and 2 are not estimated, but computed from chemical equilibrium with respect to calcite. The estimation of initial concentrations leads to a significant improvement in the fit to the measured breakthrough curves of almost all species. The DCM overcomes most of the limitations of the SCM.

Table A2-4. Chemical composition (in mol/L) of the inflow granitic water and the initial bentonite porewater composition at a 23.8% water content (taken from Samper et al., 2005).

	Bentonite CGM-0	**Granitic water**
pH	7.94	8.15
Cl^-	$1.12\cdot10^{-1}$	$3.81\cdot10^{-4}$
SO_4^{2-}	$1.27\cdot10^{-2}$	$1.46\cdot10^{-4}$
HCO_3^-	$6.45\cdot10^{-4}$	$2.37\cdot10^{-3}$
Ca^{2+}	$6.34\cdot10^{-3}$	$9.98\cdot10^{-4}$
Mg^{2+}	$8.82\cdot10^{-3}$	$3.67\cdot10^{-4}$
Na^+	$1.14\cdot10^{-1}$	$5\cdot10^{-4}$
K^+	$1.04\cdot10^{-3}$	$2.56\cdot10^{-4}$

Table A2-5. Effective diffusion coefficients, D_e (m^2/s), initial concentrations, c_i, (mol/L) and pH for the base run of the direct SCM (single-continuum model) and estimated concentrations in steps 1 and 2 of the inverse SCM (from Samper et al., 2008b). The initial concentrations of HCO_3^- in steps 1 and 2 are computed from equilibrium with calcite. The last column corresponds to the case when K^+ and HCO_3^- data are given smaller weights.

Parameters	**Base run (direct SCM)**	**Estimates for inverse SCM step 1**	**Estimates for inverse SCM step 2**	**Estimates for inverse SCM step 2 (smaller weights for K^+ and HCO_3^-)**
D_e	$5.7\cdot10^{-11}$	-	$9.51\cdot10^{-12}$	$8.43\cdot10^{-12}$
c_i of Ca^{2+}	$6.34\cdot10^{-3}$	$1.34\cdot10^{-2}$	$1.24\cdot10^{-2}$	$1.22\cdot10^{-2}$
c_i of Mg^{2+}	$8.82\cdot10^{-3}$	$2\cdot10^{-2}$	$1.6\cdot10^{-2}$	$1.56\cdot10^{-2}$
c_i of Na^+	$1.14\cdot10^{-1}$	$1.14\cdot10^{-1}$	$1.18\cdot10^{-1}$	$1.13\cdot10^{-1}$
c_i of K^+	$1.04\cdot10^{-3}$	$5.74\cdot10^{-4}$	$5.94\cdot10^{-4}$	$5.61\cdot10^{-4}$
c_i of SO_4^{2-}	$1.27\cdot10^{-2}$	$3.84\cdot10^{-2}$	$3.5\cdot10^{-2}$	$3.6\cdot10^{-2}$
c_i of HCO_3^-	$6.45\cdot10^{-4}$	$4.02\cdot10^{-4}$	$4.24\cdot10^{-4}$	$3.6\cdot10^{-4}$
Initial pH	7.94	7.92	7.92	7.92

3. Unsaturated bentonite initial porewater chemical composition

UDC has performed THC and THMC numerical models of laboratory, mock-up and in-situ experiments. Such models cover a short time horizon (less than 50 years) and assume that the bentonite is initially unsaturated. We have compiled the chemical composition data of the following four papers:

[1] Samper et al. (2008c). Coupled THC models of compacted bentonite after FEBEX in situ test. App. Geochem. 23,1186-1201.

[2] Zheng et al. (2011). A coupled THC model of the FEBEX in situ test with bentonite swelling and chemical and thermal osmosis. J. Cont. Hydrol. 126, 45-60.

[3] Zheng et al. (2010). A coupled THMC model of a heating and hydration laboratory experiment in unsaturated compacted FEBEX bentonite. J. Hydrol 386, 80-94.

[4] Zheng and Samper. (2008). A coupled THMC model of FEBEX mock-up test. Physics and Chemistry of the Earth 33,S486-S498.

Samper et al. (2008c) presented a THC model of the FEBEX in situ test. Several conceptual geochemical models (CGM) were used for the FEBEX bentonite. They differ on the type of test used to obtain chemical data: squeezing and aqueous extracts tests (AET). Conceptual model CGM-0 was derived from a squeezing test performed on a bentonite

sample having a gravimetric water content of 26.5% (ENRESA, 2000a). Geochemical models were used to derive the chemical composition at 14% water content. The chemical species considered in model CGM-0 are listed in Table A2-4. Later, Samper et al. (2005b) presented a model derived from aqueous extract tests (model CGM-1) which assumes that bentonite porewater is at equilibrium with gypsum. On the other hand, calcite and dolomite are assumed to dissolve/precipitate kinetically with a $CO_2(g)$ pressure of $10^{-3.5}$ bar. This model reproduces adequately the measured aqueous extract data performed at different durations and S/L ratios. However, it fails to reproduce bicarbonate and pH data, possibly due to changes in $CO_2(g)$ pressure which are not considered in the model. In general, calculated results with model CGM-1 could not fit sulfate squeezing data. Samper et al. (2005b) presented a modified model (CGM-2) based on data from both aqueous extract and squeezing tests. This model does not consider an initial amount of gypsum in the system but allows for its precipitation. Models CGM-1 and CGM-2 fit simultaneously both squeezing and aqueous extract data for most chemical species, although they present discrepancies for sulfate and bicarbonate data.

Models CGM-0, CGM-1 and CGM-2 account for aqueous complexation, acid-base, mineral dissolution/precipitation, gas dissolution/exsolution and cation exchange. These processes are assumed at local equilibrium except for calcite and dolomite which may dissolve or precipitate under kinetic conditions in models CGM-1 and CGM-2 (see Table A2-4). These models account neither for redox nor for surface complexation reactions. Table A2-5 lists the initial concentrations of granite and FEBEX bentonite at a gravimetric water content of 14% for CGM-0, CGM-1 and CGM-2.

Table A2-6. Chemical species considered in models CGM-0, CGM-1 and CGM-2 (from Samper et al., 2005b).

Geochemical models	CGM-0	CGM-1	CGM-2
Primary species	H_2O, H^+, Ca^{2+}, Mg^{2+}, Na^+, K^+, Cl^-, SO_4^{2-}, HCO_3^-, $SiO_{2(aq)}$,		
Aqueous complexes	OH^-, $CaSO_{4(aq)}$, $CaCl^+$, $MgCl^+$, $NaCl_{(aq)}$, $MgHCO_3^+$, $NaHCO_{3(aq)}$, $CaHCO_3^+$, $MgCO_{3(aq)}$, $CaCO_{3(aq)}$, $CO_{2(aq)}$, CO_3^{-2}, KSO_4^-, $MgSO_{4(aq)}$, $NaSO_4^-$, $H_2SiO_4^{2-}$, $HSiO_3^-$		
Minerals	Calcite (equilibrium) Chalcedony (equilibrium) Gypsum/anhydrite (equilibrium, only precipitation)	Calcite (kinetic) Chalcedony (equilibrium) Gypsum/anhydrite (equilibrium) Dis-dolomite (kinetic)	Calcite (kinetic) Chalcedony (equilibrium) Gypsum/anhydrite (equilibrium, only precipitation) Dis-dolomite (kinetic)
Exchangeable cations	Ca^{2+}, Mg^{2+}, Na^+, K^+	Ca^{2+}, Mg^{2+}, Na^+, K^+, H^+	Ca^{2+}, Mg^{2+}, Na^+, K^+, H^+
Gases	No condition on $CO_{2(g)}$	Fixed $CO_{2(g)}$ pressure	Fixed $CO_{2(g)}$ pressure

Table A2-7. Chemical initial composition at 14% water content of FEBEX bentonite and granite for CGM0, CGM1 and CGM2.

	Conceptual geochemical models for bentonite			**Granite**
	CGM-0	**CGM-1**	**CGM-2**	
T (ºC)	12	12	12	12
pH	7.86	7.62	7.62	9.25
Na^+ (mol/L)	$1.88\cdot10^{-1}$	$1.28\cdot10^{-1}$	$1.28\cdot10^{-1}$	$3.76\cdot10^{-4}$
K^+ (mol/L)	$1.68\cdot10^{-3}$	$2.00\cdot10^{-3}$	$2.30\cdot10^{-3}$	$7.80\cdot10^{-6}$
Ca^{2+} (mol/L)	$1.13\cdot10^{-2}$	$2.10\cdot10^{-2}$	$2.5\cdot10^{-2}$	$2.16\cdot10^{-4}$
Mg^{2+} (mol/L)	$1.44\cdot10^{-2}$	$2.20\cdot10^{-2}$	$3.2\cdot10^{-2}$	$1.32\cdot10^{-6}$
HCO_3^- (mol/L)	$5.80\cdot10^{-4}$	$3.90\cdot10^{-4}$	$4.1\cdot10^{-4}$	$3.97\cdot10^{-4}$
SO_4^{2-} (mol/L)	$2.12\cdot10^{-2}$	$3.10\cdot10^{-2}$	$2.2\cdot10^{-2}$	$7.86\cdot10^{-5}$
Cl^- (mol/L)	$1.87\cdot10^{-1}$	$1.55\cdot10^{-1}$	$1.85\cdot10^{-1}$	$1.31\cdot10^{-5}$
$SiO_{2(aq)}$ (mol/L)	$1.05\cdot10^{-4}$	$2.8\cdot10^{-4}$	$2.8\cdot10^{-4}$	$6.07\cdot10^{-4}$

Zheng et al. (2011) presented a coupled THC model of the FEBEX in situ test which accounts for bentonite swelling and chemical and thermal osmosis. The model accounts for: aqueous complexation, acid-base, mineral dissolution/precipitation, cation exchange and surface complexation. Calcite, anhydrite and chalcedony are assumed at chemical equilibrium. Three types of protolysis sites S^SOH, $S^{W1}OH$ and $S^{W2}OH$ (Bradbury and Baeyens, 1997) are considered for surface complexation reactions. Redox reactions are not considered in this model. The initial chemical composition of the granite water and the FEBEX bentonite porewater at the initial gravimetric water content of 14% inferred from aqueous extract data (Fernández et al., 2001) are listed in Table A2-6. They used a conceptual model denoted here as CGM-Ciemat. They also performed model predictions for a second initial chemical composition of the FEBEX bentonite at a water content of 13.3% (see Table A2-7) estimated from squeezing data (Samper et al., 2008c). This chemical composition corresponds to CGM-0.

Table A2-8. Initial chemical composition of the bentonite at 14% water content (Fenández et al., 2001) and granite porewaters (Samper et al., 2008c)

	Bentonite (CGM-Ciemat)	**Granite**
pH	7.72	8.35
Na^+ (mol/kg)	$1.3 \cdot 10^{-2}$	$3.8 \cdot 10^{-4}$
K^+ (mol/kg)	$1.7 \cdot 10^{-3}$	$7.8 \cdot 10^{-6}$
Ca^{2+} (mol/kg)	$2.2 \cdot 10^{-2}$	$1.8 \cdot 10^{-4}$
Mg^{2+} (mol/kg)	$2.3 \cdot 10^{-2}$	$1.3 \cdot 10^{-6}$
HCO_3^- (mol/kg)	$4.1 \cdot 10^{-4}$	$3.9 \cdot 10^{-4}$
SO_4^{2-} (mol/kg)	$3.2 \cdot 10^{-2}$	$7.9 \cdot 10^{-5}$
Cl^- (mol/kg)	$1.6 \cdot 10^{-1}$	$1.3 \cdot 10^{-5}$
$SiO_{2(aq)}$ (mol/kg)	$1.1 \cdot 10^{-4}$	$1.4 \cdot 10^{-4}$

Table A2-9. FEBEX bentonite porewater composition at water a content of 13.3% estimated from squeezing data with model CGM-0 (Samper et al., 2008c). Units in mol/L.

Component	**Cl^-**	**SO_4^{2-}**	**HCO_3^-**	**Ca^{2+}**	**Mg^{2+}**	**Na^+**	**K^+**	**pH**
CGM-0	$1.87 \cdot 10^{-1}$	$2.12 \cdot 10^{-2}$	$6.65 \cdot 10^{-4}$	$1.14 \cdot 10^{-2}$	$1.44 \cdot 10^{-2}$	$1.88 \cdot 10^{-1}$	$1.68 \cdot 10^{-3}$	7.86

Zheng et al. (2010) presented a coupled THMC model of a heating and hydration laboratory experiment (cell CT23) performed on a sample of unsaturated compacted FEBEX bentonite. The chemical model accounts for: aqueous complexation, acid-base, mineral dissolution/precipitation, cation exchange and surface complexation. Redox reactions are not considered in the model. They compared the predictions obtained with two bentonite porewater compositions (at a water content of 13.3%). One corresponds to the composition derived by Fernández et al. (2001) from aqueous extract data and the second one was taken from Samper et al. (2008c) who derived the composition from squeezing data (see Table A2-8).

Table A2-10. FEBEX bentonite porewater composition (mol/L) at a water content of 13.3% estimated by Fernández et al. (2001) from aqueous extract data and Samper et al. (2008c) from squeezing data.

Component	**Cl^-**	**SO_4^{2-}**	**HCO_3^-**	**Ca^{2+}**	**Mg^{2+}**	**Na^+**	**K^+**	**pH**
CGM-Ciemat	$1.6 \cdot 10^{-1}$	$3.2 \cdot 10^{-2}$	$5 \cdot 10^{-4}$	$2.2 \cdot 10^{-2}$	$2.3 \cdot 10^{-2}$	$1.3 \cdot 10^{-1}$	$1.7 \cdot 10^{-3}$	7.72
CGM-0	$1.87 \cdot 10^{-1}$	$2.12 \cdot 10^{-2}$	$6.65 \cdot 10^{-4}$	$1.14 \cdot 10^{-2}$	$1.44 \cdot 10^{-2}$	$1.88 \cdot 10^{-1}$	$1.68 \cdot 10^{-3}$	7.86

Zheng and Samper (2008) presented a coupled THMC model of the FEBEX mock-up test which accounts for aqueous complexation, acid-base, cation exchange, protonation/deprotonation by surface complexation and dissolution/precipitation of calcite, anhydrite, gypsum and chalcedony. All of them are assumed at local equilibrium. Redox reactions are not considered in the model. Table A2-9 shows the chemical composition of FEBEX bentonite porewater at a water content of 13.3% taken from CGM-0 of Samper et al. (2008c).

Table A2-11. FEBEX bentonite porewater composition (mol/L) at water content of 13.3% estimated by Samper et al. (2008c) from squeezing data.

Component	Cl^-	SO_4^{2-}	HCO_3^-	Ca^{2+}	Mg^{2+}	Na^+	K^+	$SiO_2(aq)$	pH
Hydration water	$4.23 \cdot 10^{-4}$	$1.56 \cdot 10^{-4}$	$2.53 \cdot 10^{-3}$	$9.5 \cdot 10^{-4}$	$3.92 \cdot 10^{-4}$	$6.08 \cdot 10^{-4}$	$3.32 \cdot 10^{-5}$	$3.62 \cdot 10^{-4}$	8.1
CGM-0	$1.87 \cdot 10^{-1}$	$2.12 \cdot 10^{-2}$	$6.65 \cdot 10^{-4}$	$1.14 \cdot 10^{-2}$	$1.44 \cdot 10^{-2}$	$1.88 \cdot 10^{-1}$	$1.68 \cdot 10^{-3}$	$1.05 \cdot 10^{-4}$	7.86

4. Evolution of the bentonite pore water composition during bentonite hydration

Yang et al. (2008) presented a coupled non-isothermal reactive transport model for the long-term geochemical evolution of a HLW repository in clay. The model domain includes 3 material zones: bentonite buffer, concrete and the clay formation with a total length of 25 m. Initially, the bentonite buffer is unsaturated with a gravimetric water content of 14%. Water flow is assumed negligible once the bentonite buffer is saturated. Then, solute transport in the domain occurs mainly by diffusion. Table A2-10 shows the initial porewater composition in bentonite, concrete and clay. The chemical model considers aqueous complexation, acid-base, mineral dissolution/precipitation and cation exchange reactions (see Table A2-11). All mineral reactions are assumed at local equilibrium. Table A2-12 lists the initial volume fraction of the mineral phases at each material zone included in the model. Redox and surface complexation reactions are not considered in the model.

The initial porewater composition of the bentonite (see Table A2-10) was calculated with the geochemical model of Bradbury and Baeyens (2003). They presented a geochemical model to calculate porewater composition in compacted bentonites taking into account such factors as montmorillonite swelling, semi-permeable membrane effects, very low free water volumes, and the highly effective buffering characteristics of the exchangeable cations and the amphoteric edge sites. These considerations are used in conjunction with previously measured

physico-chemical characterisation data on MX-80 powder to calculate porewater compositions in compacted bentonites. Fernández et al. (2004) used a similar methodology to derive the porewater chemical composition of the Febex bentonite. The conceptual geochemical model of Bradbury and Baeyens (2003) and Fernández et al. (2004) considers three types of waters: (1) Internal water as interlayer water, (2) External water as double layer and (3) External water as free water.

Table A2-12. Initial porewater composition (mol/L) in bentonite at a water content of 14%, concrete and clay (ENRESA, 2004; Yang et al., 2008)

	Bentonite (ENRESA 2004)	**Concrete**	**Clay**
pH	7.462	13.25	7.54
Cl^-	1.30	-	2.30×10^{-2}
HCO_3^-	2.70×10^{-4}	-	1.80×10^{-3}
SO_4^{2-}	1.62×10^{-2}	2.0×10^{-3}	7.00×10^{-2}
Na^+	5.93×10^{-1}	1.60×10^{-2}	1.30×10^{-1}
K^+	4.27×10^{-3}	1.00×10^{-1}	8.20×10^{-4}
Mg^{2+}	1.60×10^{-1}	4.10×10^{-9}	8.20×10^{-3}
Ca^{2+}	2.02×10^{-1}	1.10×10^{-2}	1.10×10^{-2}
$SiO_{2(aq)}$	1.93×10^{-4}	2.00×10^{-5}	2.70×10^{-4}

Table A2-13. Components, aqueous complexes, minerals and exchangeable cations considered in the coupled hydrogeochemical model (Yang et al., 2008)

Components	Ca^{2+}, Mg^{2+}, Na^+, K^+, H^+, Cl^-, HCO_3^-, SO_4^{2-}, $SiO_{2(aq)}$, H_2O
Aqueous complexes	CO_3^{2-}, $CaCO_{3(aq)}$, $CaHCO_3^+$, $CaSO_{4(aq)}$, $CaOH^+$, $CaCl^+$, $CaCl_{2(aq)}$, $Ca(H_3SiO_4)_{2(aq)}$, $CaH_2SiO_{4(aq)}$, $CaH3SiO_4^+$, $MgCO_{3(aq)}$, $MgHCO_3^+$, $MgSO_{4(aq)}$, $MgCl^+$, $MgOH^+$, $MgH_2SiO_{4(aq)}$, $MgH_3SiO_4^+$, $NaOH_{(aq)}$, $NaCO_3^-$, $NaHCO_{3(aq)}$, $NaCl_{(aq)}$, $NaH_3Si_{4(aq)}$, $NaHSiO_{3(aq)}$, $CO_{2(aq)}$, $KOH_{(aq)}$, $KCl_{(aq)}$, KSO_4^-, $KHSO_{4(aq)}$, $NaSO_4^-$, $H_3SIO_4^-$, $H_2SiO_4^{2-}$, $H_4(H_2SiO_4)_4^{4-}$, $HSiO_3^-$, $H_6(H_2SiO_4)_4^{2-}$, $HCl_{(aq)}$, HSO_4^-, OH^-
Minerals	Calcite, Brucite, Gyrolite, Tobermorite, Quartz, Dolomite, Portlandite, Sepiolite, Gypsum
Exchangeable cations	Ca^{2+}, Mg^{2+}, Na^+, K^+, H^+

Table A2-14. Initial volume fractions (% in volume) of mineral phases at each material zone (ENRESA, 2004; Yang et al., 2008).

Bentonite		**Concrete**		**Clay**	
Calcite	0.36	Calcite	0.1	Calcite	11.3
Gypsum	0.083	Brucite	1	Gypsum	1.2
Quartz	1.19	Portlandite	16.5	Quartz	2.4
		Tobermorite	36.6	Dolomite	2.4

The model was run for 2 stages, from initial time to the time that the bentonite is saturated and then to 1 Ma. For the first stage (saturation of bentonite), the model accounts only for the bentonite buffer and the concrete. The pore fluid from the host rock (clay formation) is taken as boundary water and infiltrates into the concrete. Then the results of the first stage are taken as initial conditions for the model of the second stage. In the second stage (geochemical evolution after saturation of bentonite), the clay formation is included in the model domain.

5. Conclusions

In saturated conditions, the geochemical model used in the long-term UDC reactive transport models accounts for the following geochemical reactions: aqueous complexation, acid-base, redox, mineral dissolution/precipitation, cation exchage and surface complexation. The saturated bentonite initial porewater chemical composition used in the long-term UDC reactive transport models is shown in Table A2-1. It is important to point out that the Eh and the Fe^{2+} concentration are not at equilibrium with the mineral assemblage used in the model. Other two compositions are listed in Table A2-2 and Table A2-3. Table A2-2 presents the bentonite porewater chemical composition at 23.8% water content derived by Samper et al. (2005) from squeezing tests (CGM-0). Table A2-3 shows the bentonite porewater chemical composition estimated for the inverse analysis of a permeation test using a single porosity model (step 1). There are no values of Eh and Fe^{2+} in these two tables because their corresponding models did not consider redox reactions.

The three reported chemical compositions of the FEBEX bentonite porewater at saturated conditions are listed in Table A2-13.

Table A2-15. Chemical compositions of the FEBEX bentonite porewater at saturated conditions: 1) Used in the long-term UDC reactive transport models; 2) Derived from squeezing tests; and 3) Estimated from a permeation test

	Long-term models	**Squeezing tests (model CGM-0)**	**Estimates from a permeation test (inverse SCM step 1)**
pH	6.4 - 6.435	7.94	7.92
Eh (V)	-0.059	-	-
Ca^{2+} (mol/L)	$3.101 \cdot 10^{-2}$	$6.34 \cdot 10^{-3}$	$1.34 \cdot 10^{-2}$
Mg^{2+} (mol/L)	$3.473 \cdot 10^{-2}$	$8.82 \cdot 10^{-3}$	$2.0 \cdot 10^{-2}$
Na^{+} (mol/L)	$1.841 \cdot 10^{-1}$	$1.14 \cdot 10^{-1}$	$1.14 \cdot 10^{-1}$
K^{+} (mol/L)	$1.507 \cdot 10^{-3}$	$1.04 \cdot 10^{-3}$	$5.74 \cdot 10^{-4}$
Fe^{2+} (mol/L)	$6.583 \cdot 10^{-5}$	-	-
Cl^{-} (mol/L)	$2.756 \cdot 10^{-1}$	$1.12 \cdot 10^{-1}$	$1.12 \cdot 10^{-1}$
HCO_3^{-} (mol/L)	$1.689 \cdot 10^{-3}$	$6.45 \cdot 10^{-4}$	$4.02 \cdot 10^{-4}$
SO_4^{2-} (mol/L)	$2.049 \cdot 10^{-2}$	$1.27 \cdot 10^{-2}$	$3.84 \cdot 10^{-2}$
$SiO_2(aq)$ (mol/L)	$3.761 - 8.426 \cdot 10^{-4}$	-	-

In unsaturated conditions, the suggested initial FEBEX bentonite porewater composition at water content of 13.3-14% is shown in Table A2-14. Three different compositions can be used. The first one (Table A2-8) was estimated by Fernández et al. (2001) from aqueous extract data (CGM-Ciemat). The second one (Table A2-8) was estimated by Samper et al. (2008c) from squeezing data (CGM-0). Both of these compositions were derived by assuming that the volume of water accessible for geochemical reactions is equal to the total water content. The last composition (Table A2-10) of ENRESA (2004) was calculated by assuming that the volume of water accessible for geochemical reactions is only the free water and using the geochemical model of Bradbury and Baeyens (2002, 2003) which considers three types of waters: internal water, external water as double layer water and free water. None of these models consider redox reactions and therefore, they provide no Eh and Fe^{2+} data.

Table A2-16. FEBEX bentonite porewater composition (mol/L) at a water content of 13.3% estimated by Fernández et al. (2001) from aqueous extract data (CGM-Ciemat), Samper et al. (2008c) from squeezing data (CGM-0) and at a water content of 14% estimated by ENRESA (2004).

Component	Cl^-	SO_4^{2-}	HCO_3^-	Ca^{2+}	Mg^{2+}	Na^+	K^+	$SiO_2(aq)$	pH
CGM-Ciemat	$1.6.10^{-1}$	$3.2.10^{-2}$	5.10^{-4}	$2.2.10^{-2}$	$2.3.10^{-2}$	$1.3.10^{-1}$	$1.7.10^{-3}$	$1.1.10^{-4}$	7.72
CGM-0	$1.87.10^{-1}$	$2.12.10^{-2}$	$6.65.10^{-4}$	$1.14.10^{-2}$	$1.44.10^{-2}$	$1.88.10^{-1}$	$1.68.10^{-3}$	$1.05.10^{-4}$	7.86
ENRESA 2004	1.3	$1.62.10^{-2}$	$2.70.10^{-4}$	$2.02.10^{-1}$	$1.60.10^{-1}$	$5.93.10^{-1}$	$4.27.10^{-3}$	$1.93.10^{-4}$	7.462

Bradbury and Baeyens (2002, 2003) presented a geochemical model to calculate porewater composition in compacted bentonites taking into account such factors as montmorillonite swelling, semi-permeable membrane effects, very low free water volumes, and the highly effective buffering characteristics of the exchangeable cations and the amphoteric edge sites. These considerations were used in conjunction with previously measured physico-chemical characterisation data on MX-80 powder to calculate porewater compositions in compacted bentonites.

Fernández et al. (2004) used the methodology of Bradbury and Baeyens (2002, 2003) to analyze the porewater chemical composition of the FEBEX bentonite. Table 15 shows the calculated initial porewater chemistry in a re-saturated FEBEX bentonite having an initial dry density o f 1650 kg/m^3. They assumed that the chloride accessible porosity at this density is 5 vol%. With this value and the dry density they got a value of 0.0303 L of water per kg of dry FEBEX bentonite (i.e., a S:L ratio of 33 kg of dry bentonite/L). Cl^- cannot move through the interlayer and overlapping double layer regions due to anion exclusion effects. Therefore, it is assumed that the accessible porosity for Cl^- is the free water. Its amount is equal to 0.0303 L of water per kg of dry FEBEX bentonite. This together with the value of the chloride inventory (20 mmol of Cl^- per kg of bentonite) yields a Cl^- concentration of 0.73 mol/L (see Table A2-15).

Table A2-17. Calculated initial porewater chemistry in a re-saturated FEBEX bentonite having an initial dry density o f 1650 kg/m3 by Fernández et al. (2004) taking into account three types of water.

Component	Cl^-	SO_4^{2-}	HCO_3^-	Ca^{2+}	Mg^{2+}	Na^+	K^+	$SiO_2(aq)$	pH
Fernández et al. (2004)	$7.3.10^{-1}$	$1.7.10^{-2}$	$2.4.10^{-4}$	$8.2.10^{-2}$	$9.7.10^{-2}$	$3.9.10^{-1}$	$3.0.10^{-3}$	$1.8.10^{-4}$	7.44